Numerical studies on vortex dynamics : helical vortices and two-phase vortices

Yonghui Xu

Sorbonne Université

Institut Jean Le Rond d'Alembert

Doctoral School **391 : Sciences mécaniques, acoustique, électronique et robotique de Paris (SMAER)**

University Department **Institut Jean Le Rond d'Alembert**

Thesis defended by **Yonghui Xu**

Defended on **30th September, 2022**

In order to become Doctor from Sorbonne Université

Academic Field **Mechanics**

Speciality **Numerical simulation**

Numerical studies on vortex dynamics

helical vortices and two-phase vortices

Thesis supervised by Maurice Rossi — Supervisor
Ivan Delbende — Co-Supervisor

Committee members

Referees	Pierre Brancher	Professor at IMFT
	Stéphane Le Dizès	Senior Researcher at IRPHE
Examiners	Arnaud Antkowiak	Professor at Sorbonne Université
	Vincent Brion	lbl-mcf2 at ONERA
Guest	Daniel Fuster	Senior Researcher at CNRS
Supervisors	Maurice Rossi	Senior Researcher at CNRS
	Ivan Delbende	Associate Professor at Sorbonne Université

SORBONNE UNIVERSITÉ

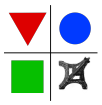

∂'Alembert
Institut Jean le Rond d'Alembert

Colophon

Doctoral dissertation entitled "Numerical studies on vortex dynamics", written by Yonghui Xu, completed on 15th November, 2022, typeset with the document preparation system LaTeX and the yathesis class dedicated to theses prepared in France.

Sorbonne Université

Institut Jean Le Rond d'Alembert

Doctoral School **391 : Sciences mécaniques, acoustique, électronique et robotique de Paris (SMAER)**

University Department **Institut Jean Le Rond d'Alembert**

Thesis defended by **Yonghui Xu**

Defended on **30th September, 2022**

In order to become Doctor from Sorbonne Université

Academic Field **Mechanics**

Speciality **Numerical simulation**

Numerical studies on vortex dynamics

helical vortices and two-phase vortices

Thesis supervised by Maurice Rossi — Supervisor
Ivan Delbende — Co-Supervisor

Committee members

Referees	Pierre Brancher	Professor at IMFT
	Stéphane Le Dizès	Senior Researcher at IRPHE
Examiners	Arnaud Antkowiak	Professor at Sorbonne Université
	Vincent Brion	lbl-mcf2 at ONERA
Guest	Daniel Fuster	Senior Researcher at CNRS
Supervisors	Maurice Rossi	Senior Researcher at CNRS
	Ivan Delbende	Associate Professor at Sorbonne Université

Sorbonne Université

Institut Jean Le Rond d'Alembert

École doctorale **391 : Sciences mécaniques, acoustique, électronique et robotique de Paris (SMAER)**

Unité de recherche **Institut Jean Le Rond d'Alembert**

Thèse présentée par **Yonghui Xu**

Soutenue le **30 septembre 2022**

En vue de l'obtention du grade de docteur de l'Sorbonne Université

Discipline **Mécanique**

Spécialité **Simulation numérique**

Études numériques sur la dynamique des vortex

Vortex hélicoïdaux et Vortex diphasiques

Thèse dirigée par Maurice Rossi directeur
Ivan Delbende co-directeur

Composition du jury

Rapporteurs	Pierre Brancher	professeur à l'IMFT
	Stéphane Le Dizès	directeur de recherche à l'IRPHE
Examinateurs	Arnaud Antkowiak	professeur à Sorbonne Université
	Vincent Brion	lbl-mcf2 à l'ONERA
Invité	Daniel Fuster	directeur de recherche au CNRS
Directeurs de thèse	Maurice Rossi	directeur de recherche au CNRS
	Ivan Delbende	mcf à Sorbonne Université

This thesis has been prepared at

Institut Jean Le Rond d'Alembert
Sorbonne Université
Campus Pierre et Marie Curie
4 place Jussieu
75005 Paris
France

☎ +33 01 44 27 37 90
Web Site `https://http://www.dalembert.upmc.fr/ijlrda/`

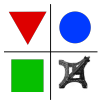

∂'Alembert
Institut Jean le Rond d'Alembert

I dedicate this job to my parents Xu Jisheng and Chen Dongyun,
thank them for supporting me with love.

Remerciements

I would like to take advantage of this chapter to thank all the people who have supported me during the past three years, you made this thesis possible and allowed me to complete it.

At start, I would like to thank my jury. Thanks to Pierre and Stéphane for being the rapporteurs of this manuscript. Pierre's study on vortex dynamics has been a real source of inspiration for the topic of this thesis. The works from Stéphane's group provide a very solid theoretical support for the numerical simulations on helical vortices. Thanks to Arnaud and Vincent for the perfect courses during my master's study, they give me the resolve to keep studying on fluid mechanics. Special thanks to Arnaud and Sébastien Neukirch for their guidance during my M1 internship, from which I learned a lot, and the experience continues to help me during my thesis. Special thanks to Suzie and Laurent as the member of my "comité de suivi", thanks for your following of my works during previous three years.

This thesis would never have been possible without my three supervisors, Maurice Rossi, Ivan Delbende and Daniel Fuster, thank you for agreeing to be my supervisor and helping me along the path, this thesis could not have been accomplished without your help. A special thanks to Maurice, your deep theoretical understanding has led the research for past three years and solved many serious problems we have encountered. In addition, you have been helping me improve my shortcomings with your inexhaustible enthusiasm, especially my lack of clarity and rigor. Even though I've "sticked" to some bad habits for a long time, you always trust me and didn't give up on me, I learned a lot from your pedagogy and your infinite patience, I'm sure it will help me for the rest of my life. Thank you, Ivan, for all the helps from the start of my master until the end of my thesis. we spend a long time on the discussion of code HELIX and HELIKZ, thank you for sharing with me your genius ideas, your kindness, scientific rigor and analytical capacity. Finally, thanks to Daniel for all the discussion on Basilisk, we dived into the code and you were so kind to explain all the physics related to it. It's a huge misfortune that we did not delve into this thesis with Basilisk due to time constraints. Also big thanks to Can Selcuk, who was the previous PHD Student of this group, your results provided a very solid foundation for this thesis.

Of course, I cannot say thank you without thanking the whole team of the Jean le Rond D'Alembert Institute, both among permanent staff and among doctoral students. This thesis would have been much difficult if I hadn't shared many great moments with you. Special thanks to Olivier and Simona for the administrative helps. Thanks to Pascal, Patrick and Élisée for the IT advisors. Thanks to Yutao, Guangjing, Boyang and Guo as "comrade" in this lab, because of the COVID we all stay in France for years, you helped me a lot with my homesickness. Finally, I want to thank my co-offices of Bureau 311, Thomas, Priscilla, Gonzalo, Ikram, Serena, Theo, Goustan, Francois, and Gerald, for their accompanying during the three years. I also thank all the others who have left their mark at D'alembert, It is a pleasure for me to have the precious

opportunity to join this big family.

I would also like to salute my college "brothers", those with whom I have lived together since the first day of my arrival in France: Linghua, Rui and Hao for their unique and quirky humor, and Yingzheng for being a good roommate for years. We spent 7 years together in France and every moment of my life is filled with memories of being with you. Thanks also to Xiaoyang, Yifan, Jie, Danxuan and other "Zhongfa" classmates for the time we spent together in France. I will never forget to thank my two best friends with whom I spend most of my off hours: Wenzhi and Lingtao in the UK, even the English Channel cannot separate us.

Finally, I would like to express my deepest gratitude to my family: I would like to thank my mom Dongyun and my dad Jisheng, you have sacrificed so much for me and always been solid in the most difficult moments of my history. Thank you for your constant encouragement, I really don't know what I would do without you.

... à tous et à toutes, un grand grand merci.

Numerical studies on vortex dynamics
helical vortices and two-phase vortices

Abstract

Nous présentons des études numériques sur la dynamique des vortex homogènes et diphasiques. Dans une première partie, nous étudions la structure des vortex hélicoïdaux homogènes tels qu'on peut les trouver dans le sillage des hélices ou des turbines. Certaines propriétés des états d'équilibre non visqueux sont dérivées théoriquement et confirmées numériquement sur des états de quasi-équilibre en utilisant des simulations numériques directes dans le cadre de la symétrie hélicoïdale. Les modes d'instabilité de grandes et petites longueurs d'onde qui se développent sur ces états sont ensuite étudiés et comparés aux théories asymptotiques existantes, avec un bon accord. L'intensité du jet axial au cœur du vortex joue un rôle prépondérant, mais l'influence d'autres paramètres tels que le pas des vortex hélicoïdaux et la taille du cœur est également étudiée. Dans une deuxième partie, nous étudions deux problèmes de dynamique des vortex diphasiques. D'une part, on traite les instabilités se produisant dans les tourbillons diphasiques droits en utilisant un code d'instabilité maison. En particulier, l'effet de stabilisation par la rotation sur les instabilités capillaires avec un vortex dans le cœur gazeux est mis en évidence. D'autre part, on étudie la génération de bulles tourbillonnaires toroïdales comme celles produites par les plongeurs, les bélugas ou les dauphins par des simulations directes à deux phases. Les résultats d'instabilité sont utilisés pour expliquer la très grande robustesse de telles structures vis-à-vis des perturbations.

Keywords: ⟨ vortex; hélicoïdal; stabilité; écoulement diphasique ⟩

Études numériques sur la dynamique des vortex
Vortex hélicoïdaux et Vortex diphasiques

Résumé

We present numerical studies on the dynamics of homogeneous and two-phase vortices. In a first part, we study the structure of homogeneous helical vortices as can be found in the wake of propellers or turbines. Some properties of inviscid steady states are derived theoretically and confirmed numerically on quasi-equilibria using direct numerical simulations in the helical symmetry framework. Long- and short-wave instability modes growing on these states are then investigated and compared favourably to existing asymptotic theories. Axial jet intensity within the core has a prominent role, but the influence of other parameters such as helical vortex pitch and core size are also investigated. In a second part, we study two problems concerning the dynamics of two-phase vortices. On the one hand, we investigate the instabilities occurring in straight two-phase vortices using an original in-house instability code. In particular, the stabilizing effect of rotation on capillary instabilities in vortices with a gaseous core is evidenced. On the other hand, we study the generation of toroidal vortex bubbles as those produced by scuba divers, beluga whales or dolphins by direct two-phase simulations. Previous instability results are used to explain the remarkable robustness of such structures with respect to perturbations.

Mots clés : ⟨ vortex ; helical ; stability ; two-phase flow ⟩

Institut Jean Le Rond d'Alembert
Sorbonne Université – Campus Pierre et Marie Curie – 4 place Jussieu – 75005 Paris – France

Contents

Chapter 1

General Introduction

A vortex is a type of fluid motion in which fluid particles revolve around an axis. Such an organized structure appears everywhere in nature, from water behind a bridge pier, tornadoes in the atmosphere to spiral galaxies in the universe. Many industrial applications are designed based on properties of vortices to transfer energy, momentum or mass. The importance of vortices has been recognized at both fundamental and applied levels of fluid dynamics since they are described as the *sinews and muscles of fluid motion* [Küchemann, 1965] as well as the *sound of flow* [Müller and Obermeier, 1988]. Vortices can be of different scales: in geophysics they may be of a scale $100 - 1000$km, in a wake of a car from 0.01 to 10m. More generally, turbulent flows are characterized by a large ratio between sizes of the smallest and largest eddies.

A more precise definition for a vortex is based on the physical quantity called *vorticity*: vorticity is mathematically defined as the curl of velocity $\boldsymbol{\omega} = \nabla \times \boldsymbol{u}$, where ∇ is the nabla operator and $\boldsymbol{u}$ is the velocity field. A vortex is a region where vorticity is concentrated in tube like regions. Other structures related to vorticity are vorticity layers: they are usually attached to velocity differences appearing at a solid surface, or at the interface between two fluids. Such a finite-thickness vorticity layer may roll up generating a unique vortex *via* a starting vortex or an array of vortices *via* the Kelvin-Helmholtz instability. For instance, a constant velocity flow impinging a solid body produces a repetitive vortex pattern, the von Kármán vortex street (figure 1.1) by shedding vorticity at an unsteady separation point on a solid body. The subject of *vorticity dynamics* was initiated by [Helmholtz, 1858] and [Kelvin, 1869] as an ideal inviscid fluid. This topic was then considerably developed: one may refer to classical texts such as *Théorie des tourbillons* [Poincaré, 1893], *Hydrodynamics* [Lamb, 1932], *Introduction to Fluid Dynamics* [Batchelor, 1967], *Vortex Dynamics* [Saffman, 1992]. This literature covers the generation, motion of vortices, interaction between vortices, or between vortices and its surrounding environment.

Vortices may induce unwanted effects and sometimes we would like to eliminate such flow patterns. For instance the Karman vortex street generates periodic forces on the solid body which may cause problems. This is why the control of vortex shedding has been studied experimentally [Strykowski and Sreenivasan, 1990] and numerically [Marquet et al., 2008]. Similarly, the wingtip vortices behind an aircraft should be eliminated as much as possible because they constitute a danger for following aircrafts. Vortex destruction can be due to different mechanisms: for instance, vortex breakdown [Hall, 1972] which is linked to the presence of an axial flow in the vortex causing a backflow and an abrupt increase of the vortex core, or various instabilities such as the Crow instability or the elliptical instability due to the deformation exerted

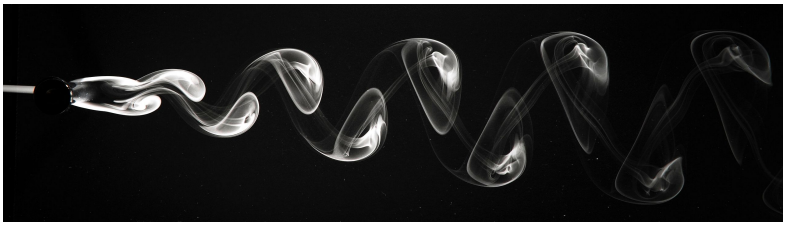

Figure 1.1 – Visualisation of a von Kármán vortex street behind a circular cylinder in air using smoke. Source: Wikipedia.

by other vortices or by boundaries. Many procedures to eliminate wingtip vortices behind an aircraft are based on increasing the initial amplitude of a perturbation mode at the origin of the Crow instability. The first part of the present Ph.D. thesis is dedicated to the study of helical vortices which are often observed in the wake of rotating blades. It includes computations and characterisations of helical vortices with an axial flow inside the core: the governing equations can be found in chapter 3, quasi-steady solutions in chapter 4. Their linear stability analyses are performed in chapters 5–7).

A flow with more than one phase, is known as a *multiphase flow*. It is called *disperse* when many solid particles or bubbles are present inside another fluid, or *separated* when two or more fluids domains are separated by a large scale *interface* [Brennen, 2005], for instance the air-sea interface. Two-fluid flows are present everywhere in our daily life: when pouring sparkling water into a glass, spherical bubbles form inside the glass, while liquid drops with a tear shape can slide down outside the glass. The dynamics of multiphase flows often depend on surface tension (or capillary forces) since pressure takes different values across a curved interface. This phenomenon was first studied by Pierre Simon de Laplace (1749-1827) and Thomas Young (1773-1829). It can be reduced for inviscid flows to equality

$$P_1 - P_2 = \gamma\kappa \tag{1.1}$$

between pressure P_1 in fluid 1 at the interface, and pressure P_2 of fluid 2 at the same point across the interface. The mean curvature κ equals the sum of the inverse maximum radius R_1 and inverse minimum radius R_2 of the interface

$$\kappa \equiv \left(\frac{1}{R_1} + \frac{1}{R_2} \right).$$

The surface tension γ depends on the characteristic of both fluids, on temperature or on the presence of surfactants. Some typical values are given in Table 1.1.

Interface	Water–air	Benzene–air	Nonane–air
Temperature (°C)	20	30	20
γ (mN m^{-1})	72.86	27.56	22.85

Table 1.1 – Values of surface tension for various substances.

The fluid-fluid interface is deformable: for instance a soap bubble with different pressures across the interface, evolves spontaneously towards a spherical shape. This is explained by the minimization of surface energy. This mechanism is also responsible for the famous Rayleigh-Plateau instability: the stream

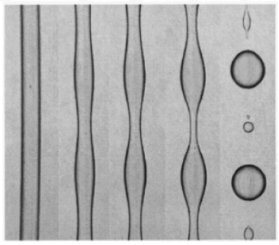

Figure 1.2 – Temporal evolution of non rotating Rayleigh-Plateau instability [enseeiht, 2013].

of tap water breaks into smaller droplets (see figure 1.2). Indeed, the cylinder liquid jet of radius R_0 and length L has a total surface of $2\pi R_0 L$, larger than the more favorable situation of n droplets of radius $r = (3R_0^2 L/(4n))^{-1/3}$ if $r > 1.5R_0$. This behaviour is very different from a monophasic jet often dominated by the Kelvin–Helmholtz instability leading to vortex rings and secondary instabilities [Brancher et al., 1994]. Lord Rayleigh gave the general stability analysis of an axisymmetric inviscid liquid jet [Rayleigh, 1892b] and viscous jet [Rayleigh, 1892a]. In the linear framework, the growth of perturbation reads:

$$f' = \hat{f}\, \mathrm{e}^{st+\mathrm{i}(kx+m\theta)} \tag{1.2}$$

where f' is the perturbation term with $\hat{f}$ its amplitude, s the growth rate, k the axial wavenumber and m the azimuthal wavenumber. Even limited to an axisymmetric case, the stability of liquid jet can be affected by various parameters, such as: *(i)* density ratio of the two phases; *(ii)* viscosity. The effect of the above two parameters are rapidly recalled below.

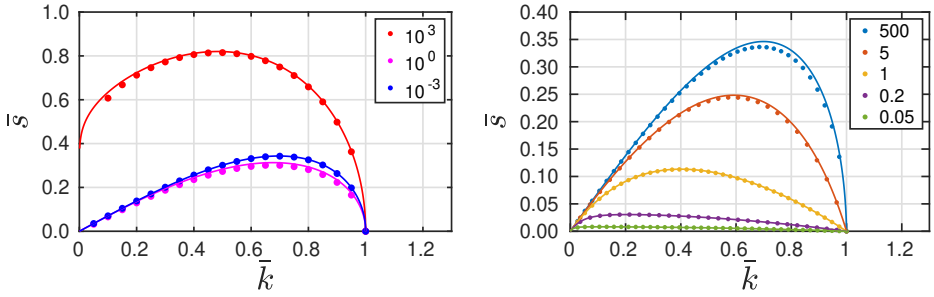

Figure 1.3 – Left: inviscid case for three density ratios ρ_2/ρ_1 (red: air column in water, blue: water column in air). Right: viscous liquid column in air, for different *Re* values as indicated. Solid lines in left (resp. right) graph: theoretical dispersion relation (1.5) (resp. 1.10); symbols: results from the instability code used in part II.

In the inviscid framework, a two-phase jet of radius R_0 at rest is unstable [Rayleigh, 1892b]. Indeed its analytical dispersion relation reads

$$\left(1 - \frac{\rho_2}{\rho_1}\frac{K_m(\bar{k})I'_m(\bar{k})}{K'_m(\bar{k})I_m(\bar{k})}\right)s^2 = \frac{\gamma}{R_0^3\rho_1}\frac{\bar{k}I'_m(\bar{k})}{I_m(\bar{k})}\left(1-\bar{k}^2-m^2\right) \tag{1.3}$$

with ρ_1 (resp. ρ_2) the density of inner phase (resp. for ambient phase), s the growth rate and $\bar{k} \equiv kR_0$.

When $\bar{k}$ is small (typically smaller than 1), the dispersion relation reduces to:

$$s^2 \approx \frac{\gamma}{(\rho_1+\rho_2)R_0^3}\frac{\bar{k}I_m^{'}(\bar{k})}{I_m(\bar{k})}\left(1-\bar{k}^2-m^2\right). \tag{1.4}$$

showing that the sign of growth rate s depends only on the term $(1-\bar{k}^2-m^2)$. This also imposes that the most unstable modes are axisymmetric ($m=0$) and satisfy:

$$\frac{R_0^3\rho_1}{\gamma}s^2\left(1+\frac{\rho_2}{\rho_1}\frac{K_0(\bar{k})I_0'(\bar{k})}{K_1(\bar{k})I_0(\bar{k})}\right)=\bar{k}\left(1-\bar{k}^2\right)\frac{I_0'(\bar{k})}{I_0(\bar{k})}. \tag{1.5}$$

For $0\leq\bar{k}\leq 1$, the growth rate s is positive hence the jet is unstable. For a liquid jet (say of water, $\rho_1=\rho^{(w)}$) without external fluid ($\rho_2\simeq 0$), the dispersion relation, in the vicinity of small $\bar{k}$, takes a simplified form

$$\bar{s}\equiv\sqrt{\frac{R_0^3\rho^{(w)}}{\gamma}}s=\sqrt{\bar{k}(1-\bar{k}^2)\frac{I_1(\bar{k})}{I_0(\bar{k})}}\simeq\sqrt{\frac{\bar{k}^2-\bar{k}^4}{2}}. \tag{1.6}$$

The initial perturbation with $\bar{k}_m\simeq 0.7$ has the largest growth rate close to 0.35 (see blue curve in figure 1.3, left). For a hollow jet in water ($\rho_1\simeq 0$, $\rho_2=\rho^{(w)}$) the dispersion relation becomes

$$\bar{s}\equiv\sqrt{\frac{R_0^3\rho^{(w)}}{\gamma}}s=\sqrt{\bar{k}(1-\bar{k}^2)\frac{K_1(\bar{k})}{K_0(\bar{k})}}\simeq\sqrt{\frac{(1-\bar{k}^2)}{\ln(1+1/\bar{k})}} \tag{1.7}$$

and the initial perturbation with $\bar{k}_m\simeq 0.48$ has the biggest growth rate close to 0.80 (see red curve in figure 1.3, left). When the densities of the two phases are equal ($\rho_1=\rho_2=\rho^{(w)}$), we get, for small $\bar{k}$:

$$\bar{s}\equiv\sqrt{\frac{R_0^3\rho^{(w)}}{\gamma}}s=\sqrt{\frac{\bar{k}(1-\bar{k}^2)}{\frac{I_0(\bar{k})}{I_1(\bar{k})}+\frac{K_0(\bar{k})}{K_1(\bar{k})}}}\simeq\sqrt{\frac{\bar{k}^2(1-\bar{k}^2)}{2+\bar{k}^2\ln(1+1/\bar{k})}}. \tag{1.8}$$

In this case the initial perturbation with $\bar{k}_m\simeq 0.7$ has the maximum growth rate close to 0.31 (see magenta curve in figure 1.3, left). The presence of a surrounding fluid slows down the instability and shifts the wavenumber of maximal growth $\bar{k}_m$ to a smaller value [Eggers and Villermaux, 2008].

Viscosity is also important for stability. From equation (1.6), viscosity may be taken into account [Rayleigh, 1892b, Eggers and Villermaux, 2008], for small $\bar{k}$ and $\rho_2\ll\rho_1=\rho^{(w)}$ it yields:

$$s^2=\frac{1}{2}\frac{\gamma}{\rho^{(w)}R_0^3}\left(\bar{k}^2-\bar{k}^4\right)-s\frac{3\nu}{R_0^2}\bar{k}^2 \tag{1.9}$$

where $\nu=\mu/\rho$ is the kinematic viscosity of the liquid, with μ the dynamic viscosity. Its importance compared to surface tension is quantified by the Ohnesorge number

$$Oh=\mu/\sqrt{\rho\gamma R_0}.$$

A larger Ohnesorge number corresponds to a greater influence of viscosity. For a rain drop with a radius of nearly 3 mm, the Ohnesorge number is typically 0.002. Put in nondimensional form, the dispersion relation

reads

$$\bar{s} \equiv \sqrt{\frac{R_0^3 \rho^{(w)}}{\gamma}} s \simeq \sqrt{\frac{1}{2}\left(\bar{k}^2 - \bar{k}^4\right) + \frac{9\bar{k}^4}{4Re^2}} - \frac{3\bar{k}^2}{2Re}, \tag{1.10}$$

where $Re \equiv 1/Oh$. Viscosity thus stabilizes the system and shifts the most amplified wavenumber to a smaller value. The growth rate remains positive for $0 \leq \bar{k} \leq 1$, but viscosity attenuates the instability, while the most unstable wavenumber $\bar{k}_m$ decreases as Re decreases. This is shown in figure 1.3 (right), where asymptotic theory and exact values obtained numerically agree quite well, especially at low Re.

Another mechanism may alter the Rayleigh-Plateau instability: the presence of azimuthal velocity. The second part of this thesis is precisely devoted to the influence of an azimuthal velocity profile on the dynamics of two-phase liquid columns (chapters 9–12). A second problem is also studied: the formation and time evolution (stretching and instability) of a two-phase vortex ring (chapter 13).

Part I

Instabilities of monophasic helical vortices

Chapter 2

Introduction to wind turbines and helical vortices

The world electricity consumption increased from 16.8 GWh in 2008 to 23.4 GWh in 2018. As a consequence, the global energy-related CO_2 emissions increased from 29.1 Gt (2008) to 33.5 Gt (2018). As the supply of fossil fuels is declining every day and CO_2 concentration in the atmosphere continues to increase, governments and companies are investing heavily in sustainable and environmentally friendly energy sources. As a consequence, renewable energy (wind power, solar power, hydro-power, ...) has become a research hot-spot in the past decades with its many advantages: first, contrary to fossil fuels which are often concentrated in a few countries, renewable energy resources exist in a large geographical area, bringing more energy safety. Second, renewable energies generate less air pollution, as their emission rates are much lower than for fossil fuels. According to the international renewable energy agency (IRENA), from 2000 to 2019, world total electricity generation by renewable energy has increased from 3000 TWh to 7000 TWh, of which wind energy is one of the fastest-growing energy sources. In France, wind energy provided 5.7 TWh electricity generation in 2008 (out of 80 TWh for all renewable energy sources), which increased to 34.7 TWh in 2018 (out of 115 TWh). The potential amount of wind energy however is greater. Much wind energy is wasted because of the time lag between domestic electricity demand and natural wind peaks. Improvements have been developed in recent years due to new technologies (hydrolysis): wind energy is used to split water into hydrogen and oxygen in periods of low electricity demand and this process can be reversed to recover energy in periods of high demand. In this context, more wind energy will be generated in the coming years, especially with the growing use of off-shore windfarms. Off-shore capacity represented in 2008 less than 1% of the total wind energy capacity installed over the world. In 2020, it represented 4.7% at a level of 35 GW (out of 743 GW for the total wind capacity). The annual growth rate of wind energy capacity worldwide exceeds 10%.

Wind energy technology uses wind turbines to extract wind resources. A wind turbine is a rotor system that combines several evenly distributed rotating blades. As the wind passes through the turbine, the shape of the blades generates asymmetric forces at the two blade sides. This effect is similar to what brings lift for an airplane wing and, in that instance, causes the rotation of the rotor system. Vortices are generated both at the root (hub vortices) and at the tip of each blade. Tip vortices dominate the flow behind the rotor and

form a system of interlaced helical vortices. According to the distance from the rotor plane, one can define a near-wake region and a far-wake region. The near wake refers to the vortices close to the rotor, where the flow is governed by interaction dynamics. The topic of part 1 belongs to this regime. The far-wake is a fully developed turbulent tail, which can be considered to be widely independent of the near wake, but results from its spatial evolution: diffusion of the vortex filaments, growth of instabilities, reconnection events, transition to turbulence... Such a transition is beneficial as it improves wake recovery: in a wind farm, other wind turbines in the wake are more able to produce energy since the velocity deficit due to the leading wind turbine weakens on shorter distances, thanks to the mixing which is enhanced with the surrounding more energetic flow. Such wakes also exist behind helicopters or ship propellers, and can cause serious problems, such as possible dangerous flight conditions, noise generation, cavitation and material fatigue. With a better understanding of helical vortices, one may guide the layout of wind turbines in the field, thus improving the efficiency of wind energy extraction, or a better control strategy for helicopters or ship propellers.

Experiments on helical vortices

The studies on full-scale wind turbine experiments is limited due to the high cost of wind tunnel experiments and the difficulty of controlling inflow conditions [Maeda et al., 2016]. Most experiments are obtained from small-scale models conducted in a ideal environment. Figure 2.1 (a) shows a full size wind tunnel

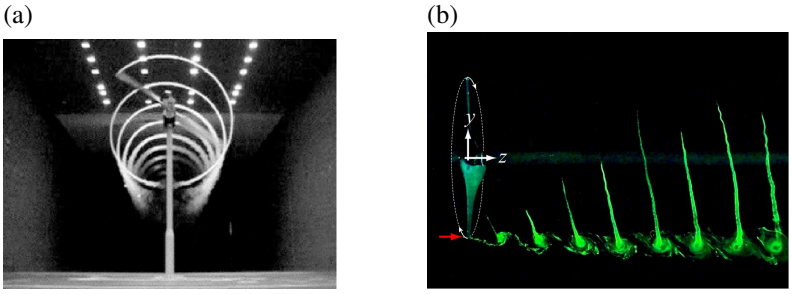

Figure 2.1 – (a): Visualisation of helical vortices with smoke in a wind tunnel test [Hand et al., 2001]. (b): Visualisation of the axial flow within the vortex cores of the helical vortices [Quaranta et al., 2015].

test with a two-bladed turbine [Hand et al., 2001], where the wind comes from the forward direction, the vortices generated at the tip are visualized by smoke, the helical-similar structure is observed in the near wake, as well as the turbulence formation at the far end. This flow is almost periodic along the axis perpendicular to the rotation plane : at each blade, a tip vortex is generated at a given radial position of core size a taking the geometry of an almost perfect helix of spatial period $2\pi L$ which is called the helix pitch. Figure 2.1 (b) shows a hydraulic channel experiment of a small-size rotor with one blade [Quaranta et al., 2015, Quaranta et al., 2019]. The flow comes from the left side, and dye is injected at the bottom near the edge of the rotor disk. The cross-sectional view shows the local vortex structure. In addition to their rotation around the helical vortex centerline, fluid particles translate along this centerline : this indicates the existence of an internal jet flow in the vortex core. The local flow velocity within the core of helical vortices has been measured in different experiments, namely helical tip vortices generated by a three-bladed rotor [Okulov et al., 2019] and a stationary vortex produced in a hydrodynamic vortex chamber [Shtork et al., 2020]. In both instances, an axial velocity component is found.

Theory on helical vortices

Theoretical studies on helical vortices go back to the works of [Joukowsky and Vetchinkin, 1929] and [Levy and Forsdyke, 1928]. The shape of an inviscid pure helical vortex filament remains invariant, as

recalled by [Kida, 1981] using the local induction approximation. Later, [Kuibin and Okulov, 1998] determined the motion of a helical filament with arbitrary pitches, using the induced velocity provided by [Hardin, 1982]. The results were extended to multiple helical vortices [Okulov, 2004]. Torsion effects were characterized by [Ricca, 1994] and shown to generate a dipolar correction at second order. Finite-core helical vortices were considered by [Fukumoto and Okulov, 2005]: these authors used an asymptotic expansion of the Biot–Savart law allowing to represent correction terms as a filament of dipoles and of quadrupoles, correcting the monopole filament solution of Hardin. In the context of vortex rings, [Fukumoto and Miyazaki, 1991] and [Fukumoto and Moffatt, 2000] showed the influence of such corrections on the ring velocity. Most of these studies do not consider the presence of internal jet in the basic flow, which leads to a more complex structure of the vortex [Blanco-Rodríguez et al., 2015]. In the past few decades, theoretical and numerical studies have been conducted on the formation of helical tip vortices behind blades, which forms the base state of subsequent stability studies explaining their evolution in the wake and the transition to turbulence.

Present work on helical vortices

The present work numerically investigates the helically symmetric quasi-equilibrium state of tip vortices with the presence of axial velocity and related instabilities using linearized Navier-Stokes equations. The numerical code HELIX and the second nonlinear and linearized code HELIKZ were available and have been exploited by the previous PhD students Benjamin Piton [Piton, 2011] and Can Selçuk [Selçuk, 2016]. During this thesis, more precise methods to generate specific base states in HELIX have been developed, which enables to obtain helical vortices with prescribed stronger axial velocity. Some useful routines were developed in HELIKZ for the post-processing of simulation results.

Part1 is organized as follows. The chapter 3 is dedicated to Navier-Stokes equations for general cases using helical variables and the special case of helical symmetry. The chapter 4 is dedicated to the characterisation of quasi-equilibrium states of a helical vortex with a jet component inside the core. In chapter 5, we linearize the governing equations in the neighborhood of the base states, and present the numerical methods of resolution. Numerical results are presented in chapter 6 for long-wave instability modes and in chapter 7 for short-wave instabilities, namely elliptical modes and curvature modes. When available, a comparison between theoretical and numerical results is performed.

Chapter 3

Equations for helical vortices

Contents

The dynamics of vortices found in the near wake of a rotor system such as a wind turbine and a propeller may be well approximated by a flow with *helical symmetry* of *helix pitch* $2\pi L$ along a given axis. In the inertial reference frame fixed with the wind turbine (called the laboratory frame ($\mathrm{L_B}$) in the sequel), such a helical vortex is also characterized by a circulation Γ (resp. an external velocity U_z^∞). For a system with N helical vortices, the total circulation becomes $N\Gamma$. The quantity $2\pi r u_\theta$ (resp. u_z) tends as $r \to \infty$ to $N\Gamma$ (resp. U_z^∞). Experimentally a helical vortex found in the wake of a rotor system is also characterized by an internal jet component. This feature is important as it is known that for *straight vortices*, an internal jet component may change the stability properties, in particular causing the famous swirling jet instability [Lessen et al., 1974, Mayer and Powell, 1992]. In that framework, the evolution of realistic helical vortices in the near-wake can be studied in terms of instability of a *strict helical base flow* consisting of a *quasi-equilibrium state*. Let us define these two concepts more precisely.

An equilibrium state is a fixed point of the governing equations, i.e. an exact steady solution of the Navier–Stokes equations. If one excepts spatially uniform and solid-body rotation flows, an unbounded viscous flow without external forcing never remains steady, as its kinetic energy is converted into thermal energy by viscosity. Nevertheless, it is standard to use the classical instability theory for a base solution which is steady for the Euler equations, but unsteady for the Navier–Stokes equations. In such an instance, for high Reynolds number, this base flow slowly changes over time by viscous diffusion. This flow will be called a quasi-equilibrium state. Disturbances superimposed on this quasi-equilibrium state generally evolve on a much faster scale than the diffusion time. Consequently, it is possible to freeze this time-dependent base state and to treat its instability in a classical manner.

A strict helical vortex of *helix pitch* $2\pi L$ along a given axis (in the following, this axis is called the z-axis), means a *helically symmetric* flow along this axis that is a flow invariant with respect to a rotation of any angle θ_s around the z-axis coupled with a translation of $L\theta_s$ along the same axis (see f.i. [Selçuk et al., 2017b]). This actually implies that a scalar field G such as the pressure field, depends only on two variables r and $\varphi \equiv \theta - z/L$, namely:

$$\boxed{G = G(r, \varphi, t)} \tag{3.1}$$

and the velocity field is such that

$$\boxed{\boldsymbol{u} = u_r(r, \varphi, t)\boldsymbol{e}_r(\theta) + u_\theta(r, \varphi, t)\boldsymbol{e}_\theta(\theta) + u_z(r, \varphi, t)\boldsymbol{e}_z} \tag{3.2}$$

where the basis $(\boldsymbol{e}_r, \boldsymbol{e}_\theta, \boldsymbol{e}_z)$ is the usual cylindrical coordinate basis. In the following work, we study such a base state of *pitch* $2\pi L$ and its stability. It is hence worth changing variables from the standard cylindrical coordinates (r, θ, z) to helical coordinates

$$\boxed{\tilde{r} = r, \quad \varphi \equiv \theta - z/L, \quad \tilde{z} = z,} \tag{3.3}$$

and writing the Navier-stokes equations in this new coordinate system.

3.1 Governing equations for general flows written with helical variables

One considers the Navier–Stokes equations in velocity–pressure formulation, where velocity $\boldsymbol{u}$ satisfy

$$\boldsymbol{\nabla} \cdot \boldsymbol{u} = 0\,, \tag{3.4}$$

$$\frac{\partial \boldsymbol{u}}{\partial t} + \mathbf{NL} = -\boldsymbol{\nabla} G + \nu \mathbf{VT} \quad \text{with} \quad \mathbf{VT} \equiv \Delta \boldsymbol{u} \quad \text{and} \quad \mathbf{NL} \equiv \boldsymbol{\omega} \times \boldsymbol{u}\,, \tag{3.5}$$

where $\boldsymbol{\omega}$ stands for vorticity, ν for the kinematic viscosity and the scalar field G for

$$G \equiv \frac{p}{\rho} + \frac{1}{2}\boldsymbol{u}^2, \tag{3.6}$$

ρ for the fluid density and p for the pressure field. Let us change variables from the standard cylindrical coordinates (r, θ, z) to helical coordinates $(\tilde{r},\ \varphi,\ \tilde{z})$. The first order and second order derivatives with respect to the cylindrical coordinates in equation (3.5) can be expressed with the helical coordinates using the relations:

$$\frac{\partial}{\partial r} = \frac{\partial}{\partial \tilde{r}}\,, \quad \frac{\partial}{\partial \theta} = \frac{\partial}{\partial \varphi}\,, \quad \frac{\partial}{\partial z} = \frac{\partial}{\partial \tilde{z}} - \frac{1}{L}\frac{\partial}{\partial \varphi}\,; \tag{3.7}$$

$$\frac{\partial^2}{\partial r^2} = \frac{\partial^2}{\partial \tilde{r}^2}\,, \quad \frac{\partial^2}{\partial \theta^2} = \frac{\partial^2}{\partial \varphi^2}\,, \quad \frac{\partial^2}{\partial z^2} = \frac{\partial^2}{\partial \tilde{z}^2} - \frac{2}{L}\frac{\partial^2}{\partial \tilde{z}\partial \varphi} + \frac{1}{L^2}\frac{\partial^2}{\partial \varphi^2}\,. \tag{3.8}$$

The expression of operators in equation 3.5 changes accordingly. **From now on, we only use the coordinates $(\tilde{r}, \varphi, \tilde{z})$ and for the sake of simplicity, we remove the tilde.** The divergence $\boldsymbol{\nabla} \cdot \boldsymbol{u}$ of velocity

vector $\boldsymbol{u}$ reads:

$$\boldsymbol{\nabla}\cdot\boldsymbol{u} = \frac{1}{r}\frac{\partial(ru_r)}{\partial r} + \frac{1}{r}\frac{\partial u_\theta}{\partial\varphi} + \frac{\partial u_z}{\partial z} - \frac{1}{L}\frac{\partial u_z}{\partial\varphi}\,. \tag{3.9}$$

Similarly, the gradient $\boldsymbol{\nabla}G$ of the scalar G, now becomes

$$\boldsymbol{\nabla}G = \left(\frac{\partial G}{\partial r},\ \frac{1}{r}\frac{\partial G}{\partial\varphi},\ \frac{\partial G}{\partial z} - \frac{1}{L}\frac{\partial G}{\partial\varphi}\right). \tag{3.10}$$

The three components of the Laplacian operator $\boldsymbol{\Delta u}$ of velocity field denoted as $\mathrm{VT}_r, \mathrm{VT}_\theta, \mathrm{VT}_z$ take the following form:

$$\mathrm{VT}_r \equiv \frac{\partial}{\partial r}\left(\frac{1}{r}\frac{\partial(ru_r)}{\partial r}\right) + \frac{1}{r^2}\frac{\partial^2 u_r}{\partial\varphi^2} + \frac{\partial^2 u_r}{\partial z^2} - \frac{2}{L}\frac{\partial^2 u_r}{\partial z\partial\varphi} + \frac{1}{L^2}\frac{\partial^2 u_r}{\partial\varphi^2} - \frac{2}{r^2}\frac{\partial u_\theta}{\partial\varphi} \tag{3.11}$$

$$\mathrm{VT}_\theta \equiv \frac{\partial}{\partial r}\left(\frac{1}{r}\frac{\partial(ru_\theta)}{\partial r}\right) + \frac{1}{r^2}\frac{\partial^2 u_\theta}{\partial\varphi^2} + \frac{\partial^2 u_\theta}{\partial z^2} - \frac{2}{L}\frac{\partial^2 u_\theta}{\partial z\partial\varphi} + \frac{1}{L^2}\frac{\partial^2 u_\theta}{\partial\varphi^2} + \frac{2}{r^2}\frac{\partial u_r}{\partial\varphi} \tag{3.12}$$

$$\mathrm{VT}_z \equiv \frac{1}{r}\frac{\partial}{\partial r}\left(r\frac{\partial u_z}{\partial r}\right) + \frac{1}{r^2}\frac{\partial^2 u_z}{\partial\varphi^2} + \frac{\partial^2 u_z}{\partial z^2} - \frac{2}{L}\frac{\partial^2 u_z}{\partial z\partial\varphi} + \frac{1}{L^2}\frac{\partial^2 u_z}{\partial\varphi^2}\,. \tag{3.13}$$

Equation (3.13) also defines as the Laplacian $\boldsymbol{\Delta}$ of a *scalar* field in helical coordinates. Taking the curl of velocity provides the vorticity components expressed with the helical variables

$$\omega_r = \frac{1}{r}\frac{\partial u_z}{\partial\varphi} + \frac{1}{L}\frac{\partial u_\theta}{\partial\varphi} - \frac{\partial u_\theta}{\partial z} \tag{3.14}$$

$$\omega_\theta = \frac{\partial u_r}{\partial z} - \frac{1}{L}\frac{\partial u_r}{\partial\varphi} - \frac{\partial u_z}{\partial r} \tag{3.15}$$

$$\omega_z = \frac{1}{r}\frac{\partial}{\partial r}(r\,u_\theta) - \frac{1}{r}\frac{\partial u_r}{\partial\varphi}\,. \tag{3.16}$$

Finally, each component of the non-linear part **NL** is a sum of two elements which are themselves products of velocity and vorticity components namely

$$\mathrm{NL}_r = \omega_\theta u_z - \omega_z u_\theta\,, \tag{3.17}$$

$$\mathrm{NL}_\theta = \omega_z u_r - \omega_r u_z\,, \tag{3.18}$$

$$\mathrm{NL}_z = \omega_r u_\theta - \omega_\theta u_r\,. \tag{3.19}$$

3.2 Governing equations for strict helically symmetric flows

For flows with strict *helical symmetry* of *helical pitch* $2\pi L$, the velocity components or the scalar field written in helical coordinates do not depend on z. As a consequence, the derivative of $\partial/\partial z$ in the Navier-Stokes equation (3.4)–(3.5) vanishes. In addition, one changes basis as well: instead of the cylindrical coordinate basis $(\boldsymbol{e}_r, \boldsymbol{e}_\theta, \boldsymbol{e}_z)$, one may use the orthonormal Beltrami basis $(\boldsymbol{e}_r, \boldsymbol{e}_\varphi, \boldsymbol{e}_B)$, where $\boldsymbol{e}_B$ is directed along the tangent of helical lines $\varphi = \mathrm{cst}$ and $\boldsymbol{e}_\varphi = \boldsymbol{e}_B \times \boldsymbol{e}_r$:

$$\boldsymbol{e}_B(r,\theta) = \alpha(r)\left[\boldsymbol{e}_z + \frac{r}{L}\boldsymbol{e}_\theta(\theta)\right], \quad \boldsymbol{e}_\varphi(r,\theta) = \alpha(r)\left[\boldsymbol{e}_\theta(\theta) - \frac{r}{L}\boldsymbol{e}_z\right] \tag{3.20}$$

with the normalisation dimensionless factor

$$\alpha(r) \equiv (1 + r^2/L^2)^{-1/2}. \tag{3.21}$$

In this new basis, a helically symmetric velocity field is expressed as:

$$\boldsymbol{u}(r,\varphi,t) = u_r(r,\varphi,t)\boldsymbol{e}_r(\theta) + u_B(r,\varphi,t)\boldsymbol{e}_B(r,\theta) + u_\varphi(r,\varphi,t)\boldsymbol{e}_\varphi(r,\theta), \tag{3.22}$$

with the relations

$$u_B = \alpha(u_z + \frac{r}{L}u_\theta), \quad u_\varphi = \alpha(u_\theta - \frac{r}{L}u_z) \tag{3.23}$$

$$u_\theta = \alpha(u_\varphi + \frac{r}{L}u_B), \quad u_z = \alpha(u_B - \frac{r}{L}u_\varphi) \tag{3.24}$$

The divergence operator in this new basis takes a simplified form as

$$\boldsymbol{\nabla}\cdot\boldsymbol{u} = \frac{1}{r}\frac{\partial(ru_r)}{\partial r} + \frac{1}{r\alpha}\frac{\partial u_\varphi}{\partial\varphi}. \tag{3.25}$$

This ensures that a stream function Ψ exists satisfying

$$ru_r = \partial_\varphi\Psi, \quad u_\varphi = -\alpha(r)\partial_r\Psi. \tag{3.26}$$

As a consequence, only the helical velocity u_B and the stream function Ψ are necessary to describe a helically symmetric velocity field:

$$\boldsymbol{u}(r,\varphi,t) = u_B(r,\varphi,t)\boldsymbol{e}_B + \alpha\boldsymbol{\nabla}\Psi(r,\varphi,t)\times\boldsymbol{e}_B. \tag{3.27}$$

By taking the curl of equation (3.27), one obtains

$$\omega_r = \frac{1}{r}\frac{\partial}{\partial\varphi}\left(\frac{u_B}{\alpha}\right), \quad \omega_\varphi = -\alpha\frac{\partial}{\partial r}\left(\frac{u_B}{\alpha}\right), \quad \omega_B = -\mathbb{L}\Psi + \frac{2\alpha^2}{L}u_B, \tag{3.28}$$

where $\mathbb{L}$ denotes a generalized Laplace operator:

$$\mathbb{L}(\bullet) \equiv \frac{1}{r\alpha}\partial_r[r\alpha^2\partial_r(\bullet)] + \frac{1}{r^2\alpha}\partial_{\varphi\varphi}(\bullet). \tag{3.29}$$

It can be checked that u_B/α plays for the vorticity field $\boldsymbol{\omega}$ the role played by Ψ for the velocity field. Furthermore, the last equation in (3.28) connects these two fields Ψ–u_B with ω_B. Reversely, if fields ω_B and u_B are known, the other flow components are obtained through the above set of equations.

If vorticity is localized in a bounded region of the (r,φ) plane — this occurs for instance when one or several helical vortices are present— it is worth, instead of u_B, to use the velocity u_H defined by

$$u_H \equiv \frac{u_B}{\alpha} - C_\infty, \quad \text{with} \quad C_\infty \equiv \frac{N\Gamma}{2\pi L} + U_z^\infty. \tag{3.30}$$

Indeed u_H must vanish away from the vortices: velocity u_H is bound to be constant away from the vorticity region since $\partial_r u_H = -\omega_\varphi/\alpha$ and $\partial_\varphi u_H = r\omega_r$ both vanish, and this constant is zero by construction since $u_B/\alpha \to C_\infty$ as $r \to \infty$. The dynamical equation for field u_H is obtained as follows. First one rewrites the

Navier–Stokes equation (3.5) introducing the vectorial relation $\boldsymbol{\nabla}^2\boldsymbol{u} = -\boldsymbol{\nabla}\times\boldsymbol{\omega}$:

$$\frac{\partial}{\partial t}\boldsymbol{u} + \boldsymbol{\omega}\times\boldsymbol{u} = -\nabla G - \nu\boldsymbol{\nabla}\times\boldsymbol{\omega}. \tag{3.31}$$

The above equation is then projected along the direction $\boldsymbol{e}_B$ and divided by α yielding an equation for u_H:

$$\partial_t u_H + \mathrm{NL}_{u_H} = \nu \mathrm{VT}_{u_H}, \tag{3.32}$$

where the viscous term takes the form

$$\mathrm{VT}_{u_H} \equiv -\frac{1}{\alpha}\boldsymbol{e}_B\cdot[\boldsymbol{\nabla}\times\boldsymbol{\omega}] = \frac{1}{\alpha}\mathbb{L}u_H - \frac{2}{L}\alpha\omega_B \tag{3.33}$$

and the nonlinear term NL_{u_H}

$$\mathrm{NL}_{u_H} = \frac{1}{\alpha}\boldsymbol{e}_B\cdot[\boldsymbol{\omega}\times\boldsymbol{u}] = \frac{1}{\alpha}[\omega_r u_\varphi - \omega_\varphi u_r] = \frac{u_\varphi}{\alpha r}\partial_\varphi u_H + u_r\partial_r u_H.$$

The scalar function G does not appear in the projection along $\boldsymbol{e}_B$ since for any helically symmetric scalar function, the property $\boldsymbol{e}_B\cdot\boldsymbol{\nabla}G = 0$ holds. Finally, the nonlinear term can be also rewritten using a Jacobian $J(f,g)$

$$\mathrm{NL}_{u_H} = J(u_H,\Psi) \quad \text{with} \quad J(f,g) \equiv \frac{1}{r}\left(\partial_r f\,\partial_\varphi g - \partial_\varphi f\,\partial_r g\right). \tag{3.34}$$

The dynamical equation for vorticity ω_B is obtained first by taking the curl of equation (3.31)

$$\frac{\partial}{\partial t}\boldsymbol{\omega} + \boldsymbol{\nabla}\times(\boldsymbol{\omega}\times\boldsymbol{u}) = -\nu\boldsymbol{\nabla}\times(\boldsymbol{\nabla}\times\boldsymbol{\omega}) \tag{3.35}$$

and second by projecting this equation along $\boldsymbol{e}_B$. This yields

$$\partial_t\omega_B + \mathrm{NL}_\omega = \nu\mathrm{VT}_\omega, \tag{3.36}$$

with the viscous term is

$$\mathrm{VT}_\omega \equiv -\boldsymbol{e}_B\cdot\boldsymbol{\nabla}\times[\boldsymbol{\nabla}\times\boldsymbol{\omega}] = \mathbb{L}(\frac{\omega_B}{\alpha}) - \left(\frac{2\alpha^2}{L}\right)^2\omega_B + \frac{2\alpha^2}{L}\mathbb{L}(u_H) \tag{3.37}$$

and the nonlinear term

$$\mathrm{NL}_\omega = \frac{1}{r\alpha}[\partial_r(r\alpha\omega_B u_r) + \partial_\varphi(\omega_B u_\varphi)] + \frac{2\alpha^2}{L}(\omega_r u_\varphi - \omega_\varphi u_r) + \frac{2\alpha^3}{L^2}(u_H + C_\infty)\partial_\varphi u_H. \tag{3.38}$$

This latter expression can be further simplified using incompressibility to yield

$$\mathrm{NL}_\omega = \frac{1}{\alpha}J(\alpha\omega_B,\Psi) + \frac{2\alpha^3}{L}J(u_H,\Psi) + \frac{\alpha^3}{L^2}\partial_\varphi[(u_H + C_\infty)^2]. \tag{3.39}$$

As a summary, the two governing equations (3.32) and (3.36) together with

$$\omega_B = -\mathbb{L}\Psi + \frac{2\alpha^3}{L}(u_H + C_\infty), \tag{3.40}$$

generalise the standard two-dimensional ψ–ω formulation. This Ψ–ω_B–u_H problem is solved numerically using **the numerical code HELIX**. This code uses 2nd-order finite differences along r, Fourier expansions along φ, 2nd-order time discretization and fully implicit viscous terms. Computation details can be found in [Delbende et al., 2012b].

3.2.1 Boundary condition at $r = R_{\mathbf{ext}}$ for mode $m = 0$

To impose boundary condition on HELIX, we made a slight change. Away from the vortex, the flow in potential, and thus equation (3.28) reads:

$$\partial_r\left[r\alpha^2\partial_r(\psi)\right] = 2\frac{r\alpha^4}{L}C_\infty \quad \text{with} \quad C_\infty = \frac{N\Gamma}{2\pi L} + u_z^\infty, \tag{3.41}$$

which can be written as

$$\partial_x(2x\alpha^2\partial_x\psi) = \alpha^4 L C_\infty \quad \text{with} \quad x = r^2/L^2. \tag{3.42}$$

By integrating the above equation, one obtains:

$$\frac{2x}{1+x}\partial_x\psi = -\frac{LC_\infty}{(x+1)} + A, \quad \text{that is} \quad \partial_x\psi = -\frac{LC_\infty}{2x} + A\frac{1+x}{2x}, \tag{3.43}$$

where A is a constant to be determined. The zero order of velocity $u_\varphi^{(0)}$ must satisfied:

$$u_\varphi^{(0)} = -\alpha\partial_r\psi = -\alpha\frac{2r}{L^2}\partial_x\psi = -\frac{A}{L}\sqrt{\frac{1+x}{x}} + \frac{C_\infty}{\sqrt{x(x+1)}} \tag{3.44}$$

then the expression of velocity $u_B^{(0)}$ can be obtained through relation:

$$\frac{2}{L}\alpha u_B^{(0)} + \frac{1}{r\alpha^2}\frac{\partial}{\partial r}\left(r\alpha u_\varphi^{(0)}\right) = 0, \tag{3.45}$$

leading to

$$u_B^{(0)} = \alpha C_\infty. \tag{3.46}$$

Finally the azimuthal velocity reads:

$$u_\theta^{(0)} = \alpha(u_\varphi + \frac{r}{L}u_B) = -\frac{A}{r} + C_\infty\alpha^2(\frac{L}{r} + \frac{r}{L}), \tag{3.47}$$

since it must equal $N\Gamma/(2\pi r)$ at infinity, the constant A must equal

$$A = u_z^\infty L \tag{3.48}$$

which lead to the final condition of velocity $u_\varphi^{(0)}$ at boundary:

$$u_\varphi^{(0)} = -u_z^\infty + C_\infty\frac{L\alpha}{r} \tag{3.49}$$

3.2.2 Boundary condition for $\Psi^{(m)}$ at $r = R_{\mathbf{ext}}$ for $m \neq 0$

For all modes $m \neq 0$, in the potential region, the stream function $\Psi^{(m)}$ satisfied $\mathbb{L}^{(m)}(\Psi^{(m)}) = 0$, where

$$L^{(m)}\Psi^{(m)} = \frac{1}{r\alpha}\frac{\partial}{\partial r}\left[r\alpha^2\frac{\partial}{\partial r}(\Psi^{(m)})\right] - \frac{m^2}{\alpha r^2}\Psi^{(m)} \tag{3.50}$$

Concerning the outer boundary condition at boundary $r = R_{\text{ext}}$, one consider three cases: $r/L \gg 1$, $r/L \sim 1$ and $r/L \ll 1$.

In the case $r/L \gg 1$, one replaces the operator α with L/r into equation (3.50):

$$L^{(m)}\Psi^{(m)} = \frac{L}{r}\left(\frac{\partial^2\Psi^{(m)}}{\partial r^2} - \frac{1}{r}\frac{\partial\Psi^{(m)}}{\partial r} - \frac{m^2}{L^2}\Psi^{(m)}\right) = 0 \tag{3.51}$$

the asymptotic behaviour of streamfunction $\Psi^{(m)}$ can be written in form:

$$\hat{r}^2\frac{\partial^2\Psi^{(m)}}{\partial\hat{r}^2} - \hat{r}\frac{\partial\Psi^{(m)}}{\partial\hat{r}} - \hat{r}^2\Psi^{(m)} = 0 \tag{3.52}$$

with

$$\hat{r} = kr, \quad k = |\frac{m}{L}|$$

The solution of equation (3.52) reads:

$$\Psi^{(m)}(\hat{r}) = A\,\hat{r}J_1(i\hat{r}) + B\,\hat{r}Y_1(-i\hat{r}) \tag{3.53}$$

where J and Y is the Bessel function of the first and second kind. This solution, with the property of Bessel function, is equivalent to:

$$\Psi^{(m)}(\hat{r}) = Ai\,\hat{r}I_1(\hat{r}) + B\,\hat{r}(I_1(\hat{r}) - \frac{2i}{\pi}K_1(\hat{r})) \tag{3.54}$$

where A, B are two unknown constants, and I, K denotes the modified Bessel function of first and second kind. Since the solution must decrease at infinity, the asymptotic behaviour of streamfunction with finite L reads:

$$\Psi^{(m)}(\hat{r}) = C\,\hat{r}K_1(\hat{r}) \tag{3.55}$$

with its derivative along r:

$$\partial_r[\Psi^{(m)}(\hat{r})] = Ck\,(K_1(\hat{r}) + \hat{r}\partial_{\hat{r}}[K_1(\hat{r})]) \tag{3.56}$$

where the derivative of Bessel function equals:

$$\partial_{\hat{r}}[K_1(\hat{r})] = -K_0(\hat{r}) - \frac{1}{\hat{r}}K_1(\hat{r}) \tag{3.57}$$

one has

$$\partial_r[\Psi^{(m)}(\hat{r})] = -\frac{\Psi^{(m)}(\hat{r})}{K_1(\hat{r})}kK_0(\hat{r}) \tag{3.58}$$

then the boundary condition on $\Psi^{(m)}$ is imposed through a Robin condition:

$$\partial_r[\Psi^{(m)}(R_{\text{ext}})] = -|m|C_m\Psi^{(m)}(R_{\text{ext}}) \quad \text{with} \quad C_m = \frac{1}{|L|}\frac{K_0(|m/L|R_{\text{ext}})}{K_1(|m/L|R_{\text{ext}})} \tag{3.59}$$

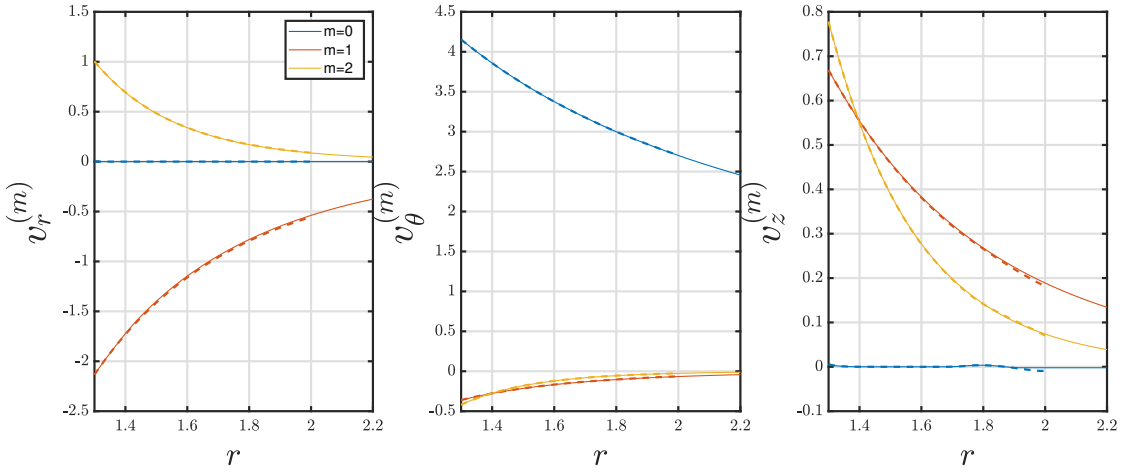

Figure 3.1 – Comparison between potential flow profile (line) and DNS results from HELIX (dashed line) for three velocity components in mode $m \in (0, 2)$, for base state with $L = 0.7$, $a = 0.15$, $W_0 = 0.2$ and $R_{\text{ext}} = 2$. The potential flow profile is obtained by the relations mentioned in the appendix B.2.

This condition of finite L replaces the previous condition used in [Delbende et al., 2012b] for finite L. **For the case** $r/L \ll 1$, or $L = \infty$ as the notion used in [Delbende et al., 2012b] , the boundary condition is obtained by replacing α with 1 in equation (3.50), which can be expressed as:

$$r^2 \frac{\partial^2 \Psi^{(m)}}{\partial r^2} + r \frac{\partial \Psi^{(m)}}{\partial r} - m^2 \Psi^{(m)} = 0\,, \tag{3.60}$$

The solution of $\Psi^{(m)}$ is given by

$$\Psi^{(m)}(\hat{r}) = \frac{A_m}{r^m} + B_m r^m\,, \tag{3.61}$$

The requirement that the solution remains finite imposes $B_m = 0$ since one needs a decaying function. The unknown coefficients A_m is eliminated using the same method, such that:

$$\partial_r[\Psi^{(m)}(R_{\text{ext}})] = -|m| C_m \Psi^{(m)}(R_{\text{ext}}) \quad \text{with} \quad C_m = \frac{1}{R_{\text{ext}}} \tag{3.62}$$

Chapter 4

Quasi-equilibrium base states for helical vortices with swirl

Contents

For axisymmetric vortex rings, a family of steady Euler flows can be found in classical text books [Batchelor, 1967]. It is given in terms of cylindrical coordinates (r,θ,z), by the velocity components

$$u_r(r,z,t) = -\frac{1}{r}\partial_z\Psi_S, \quad u_\theta = 0, \quad u_z(r,z,t) = \frac{1}{r}\partial_r\Psi_S, \tag{4.1}$$

where the streamfunction $\Psi_S(r,z)$ satisfies the nonlinear partial differential equation

$$\left(\partial_{rr} - \frac{1}{r}\partial_r + \partial_{zz}\right)\Psi_S(r,z) = -r^2 F_0(\Psi_S), \tag{4.2}$$

with $F_0(\Psi_S)$ an arbitrary function. The associated vorticity components are given by

$$(\omega_r, \omega_\theta(r,z,t), \omega_z) = (0, rF_0(\Psi_S), 0). \tag{4.3}$$

An example is the spherical Hill vortex [Batchelor, 1967], which is an exact solution of the Euler equations to model a vortex ring,. For such a vortex ring family, the azimuthal velocity component is zero but such a component can be introduced in the core along the vortex axis: the new family of vortex rings is then characterized by velocity components

$$u_r(r,z,t) = -\frac{1}{r}\partial_z \Psi_S\,, \quad u_\theta = \frac{1}{r}K(\Psi_S)\,, \quad u_z(r,z,t) = \frac{1}{r}\partial_r \Psi_S \tag{4.4}$$

and by vorticity components

$$\omega_\theta = rF(\Psi_S) + \frac{1}{2r}\frac{\mathrm{d}K^2}{\mathrm{d}\Psi_S}\,, \quad \omega_r = \omega_z = 0 \tag{4.5}$$

where $F(\Psi_S)$ and $K(\Psi_S)$ are two arbitrary functions. Given these two functions, an exact Euler equilibrium now satisfies the nonlinear partial differential equation

$$\left(\partial_{rr} - \frac{1}{r}\partial_r + \partial_{zz}\right)\Psi_S(r,z) = -r^2 F(\Psi_S) - \frac{1}{2}\frac{\mathrm{d}K^2}{\mathrm{d}\Psi_S}(\Psi_S)\,. \tag{4.6}$$

For instance, the family of Hicks solution [Hicks, 1884] is an extension of the Hill vortex with internal jet.

As mentioned in the previous chapter, experiments show that helical vortices in a rotor system are also characterized by an internal jet. In the first section of this chapter, our purpose is to find, for helical vortices, relations similar to those found for vortex rings that is to derive relations between vorticity, velocity and streamfunction satisfied by Euler equilibria of helical solutions with a jet velocity inside the core. This family of solutions of the Euler and Navier-Stokes equations contains the case of a single helical vortex with an axial flow component along the vortex core. Through Navier–Stokes simulations, it is then shown that these relations hold for quasi-steady viscous solutions and become independent of the Reynolds number when sufficiently large. In addition we elaborate a procedure which generates a quasi-equilibrium with prescribed characteristics (circulation, helix radius, helix pitch, vortex core size, swirl level). In section 4.4, this state is also compared to results of an asymptotic theory which provides the field structure for a small self-strain parameter. Finally in section 4.6, the effect of the intensity of the initial axial flow is discussed : we illustrate how a strong axial flow jeopardises such an evolution towards a quasi-equilibrium. This work has been accepted for publication in the Journal of Fluid Mechanics.

In the following, we use three inertial reference frames and one non-inertial reference frame:

- The laboratory frame ($\mathrm{L_B}$) in which the fluid velocity at infinity equals U_z^∞ and the vortex structure rotates with the angular velocity Ω_0 along the z-axis.
- The frame ($\mathrm{L_0}$) translating along the z-axis at velocity $U_z^\infty \boldsymbol{e}_z$ with respect to the frame ($\mathrm{L_B}$). In this frame, the fluid velocity at infinity vanishes and the vortex structure rotates with the angular velocity $\Omega_0 + U_z^\infty/L$ along the z-axis.
- The inertial frame (T) translating along the z-axis at velocity $U_0\boldsymbol{e}_z \equiv -\Omega_0 L\boldsymbol{e}_z$ with respect to the frame ($\mathrm{L_B}$). In this frame, the fluid velocity at infinity equals $U_z^{\infty(\mathrm{T})} = U_z^\infty - U_0 = U_z^\infty + \Omega_0 L$ and the vorticity structure is steady.
- The non-inertial frame (R) which rotates with the angular velocity Ω_0 with respect to frame ($\mathrm{L_B}$). In this frame, the vorticity structure is also steady.

4.1 A family of inviscid equilibria of helical vortices with swirl

Let us look for the conditions satisfied by an Euler equilibrium solution which is helically symmetric. Such an inviscid solution is not steady in the ($\mathrm{L_B}$) reference frame and is governed by equations (3.32) and (3.36) when the viscous terms (3.33) and (3.37) are neglected:

$$\partial_t u_H + J(u_H, \Psi) = 0\,, \tag{4.7}$$

and

$$\partial_t(\alpha\omega_B) + J(\alpha\omega_B, \Psi) + \frac{2\alpha^4}{L} J(u_H, \Psi) + \frac{\alpha^4}{L^2}\partial_\varphi\left[(u_H + C_\infty)^2\right] = 0\,. \tag{4.8}$$

In the reference frame (T), this inviscid state becomes steady and characterized by the following fields

$$\left\{\begin{array}{lcll} u_B^{(\mathrm{T})} & = & u_B - \alpha U_0, & U_0 \equiv -\Omega_0 L \\ u_\varphi^{(\mathrm{T})} & = & u_\varphi + \alpha U_0 r/L & \\ u_r^{(\mathrm{T})} & = & u_r & \end{array}\right. . \tag{4.9}$$

Since $z^{(\mathrm{T})} = z - U_0 t$, the variable $\varphi^{(\mathrm{T})}$ associated to the translating frame (T) is defined by

$$\varphi^{(\mathrm{T})} \equiv \theta - \frac{z^{(\mathrm{T})}}{L} = \theta - \frac{z}{L} + \frac{U_0 t}{L} = \varphi + \frac{U_0 t}{L}\,.$$

Since $U_z^{\infty(\mathrm{T})} = U_z^\infty - U_0$, neither quantity ω_B nor quantity u_H depend on the reference frame, as

$$u_H{}^{(\mathrm{T})} = \frac{u_B^{(\mathrm{T})}}{\alpha} - \left(U_z^{\infty(\mathrm{T})} + \frac{\Gamma}{2\pi L}\right) = u_H\,.$$

By contrast, the streamfunction is modified according to

$$\Psi^{(\mathrm{T})} = \Psi - \frac{U_0}{L}\frac{r^2}{2} = \Psi + \frac{1}{2}\Omega_0 r^2\,, \tag{4.10}$$

which imposes

$$J(u_H, \Psi) = J(u_H, \Psi^{(\mathrm{T})}) + \frac{U_0}{L} J(u_H, \frac{1}{2}r^2) = J(u_H, \Psi^{(\mathrm{T})}) - \frac{U_0}{L}\partial_{\varphi^{(\mathrm{T})}} u_H\,.$$

Using the identity

$$\partial_t u_H(r, \varphi, t) = \left(\partial_t + \frac{U_0}{L}\partial_{\varphi^{(\mathrm{T})}}\right) u_H(r, \varphi^{(\mathrm{T})}, t),$$

equation (4.7), re-written for a steady state ($\partial_t = 0$) in the translating frame, becomes

$$J(u_H, \Psi^{(\mathrm{T})}) = 0\,. \tag{4.11}$$

As a consequence, velocity u_H is a constant on any streamline $\Psi^{(\mathrm{T})} = \mathrm{cst}$.

Similarly, equation (4.8) for the same steady state yields

$$J(\alpha\omega_B, \Psi^{(\mathrm{T})}) + \frac{\alpha^4}{L^2}\partial_{\varphi^{(\mathrm{T})}}[(u_H + C)^2] = 0\,, \quad \text{with } C \equiv C_\infty - U_0\,. \tag{4.12}$$

Note that $u_H + C = u_B^{(\mathrm{T})}/\alpha$. Equation (4.11) imposes

$$J(\alpha^2(u_H + C), \Psi^{(\mathrm{T})}) + \frac{2\alpha^4}{L^2}(u_H + C)\partial_{\varphi^{(\mathrm{T})}}\Psi^{(\mathrm{T})} = 0\,,$$

hence

$$-\frac{\mathrm{d}(u_H + C)}{\mathrm{d}\Psi^{(\mathrm{T})}} J(\alpha^2(u_H + C), \Psi^{(\mathrm{T})}) - \frac{\alpha^4}{L^2}\partial_{\varphi^{(\mathrm{T})}}[(u_H + C)^2] = 0\,. \tag{4.13}$$

Due to equation (4.11), one can also derive:

$$\frac{\mathrm{d}(u_H + C)}{\mathrm{d}\Psi^{(\mathrm{T})}} J(\alpha^2(u_H + C), \Psi^{(\mathrm{T})}) + J\left(-\frac{\alpha^2}{2}\frac{\mathrm{d}(u_H + C)^2}{\mathrm{d}\Psi^{(\mathrm{T})}}, \Psi^{(\mathrm{T})}\right)$$
$$= -\alpha^2(u_H + C) J\left(\frac{\mathrm{d}(u_H + C)}{\mathrm{d}\Psi^{(\mathrm{T})}}, \Psi^{(\mathrm{T})}\right) = 0\,. \tag{4.14}$$

Summing relations (4.12), (4.13) and (4.14) yields

$$J(\varpi, \Psi^{(\mathrm{T})}) = 0\,, \quad \text{where } \varpi \equiv \alpha\omega_B - \frac{\alpha^2}{2}\frac{\mathrm{d}(u_H + C)^2}{\mathrm{d}\Psi^{(\mathrm{T})}}\,, \tag{4.15}$$

which indicates that quantity ϖ is a constant on any streamline $\Psi^{(\mathrm{T})} = \mathrm{cst}$. Equations (4.15) and (4.11) show that, in the reference frame (T) in which the flow is steady, there exist two functions f and g such that

$$\boxed{\omega_B = \frac{1}{\alpha} f(\Psi^{(\mathrm{T})}) + \frac{\alpha}{2}\frac{\mathrm{d}\, g^2}{\mathrm{d}\,\Psi^{(\mathrm{T})}}\,, \quad \frac{u_B^{(\mathrm{T})}}{\alpha} = u_H + C = g(\Psi^{(\mathrm{T})}).} \tag{4.16}$$

The above relations for helical equilibria extend the relation (4.5) valid for axisymmetric equilibria of the Euler equations, which is recovered in the limit $L \to 0$, since then $\alpha \sim 1/r$ and $\boldsymbol{e}_B \to \boldsymbol{e}_\theta$.

In the following, we show that such a family can be obtained as quasi-equilibria of the Navier–Stokes equations at large Reynolds number. In the computations, we set the fluid velocity at infinity to be zero $U_z^\infty = 0$: the laboratory frame ($\mathrm{L_B}$) and the frame ($\mathrm{L_0}$) are thus identical. This removes one parameter which has no impact on the dynamics because of Galilean invariance. From now on, we only consider the case with single helical vortex, that is $N = 1$.

4.2 From Euler equilibria to viscous quasi-equilibria

Let us consider an initial 2D vortex with an elliptical shape as in figure 4.1. The initial condition reads:

$$\omega_z(\boldsymbol{x}, 0) = \frac{\Gamma}{\pi a_1 a_2}\exp\left[-\frac{x^2}{a_1^2} - \frac{y^2}{a_2^2}\right] \quad \text{with} \quad a_1 = a\sqrt{1-\delta}\,, \quad a_2 = a\sqrt{1+\delta}\,. \tag{4.17}$$

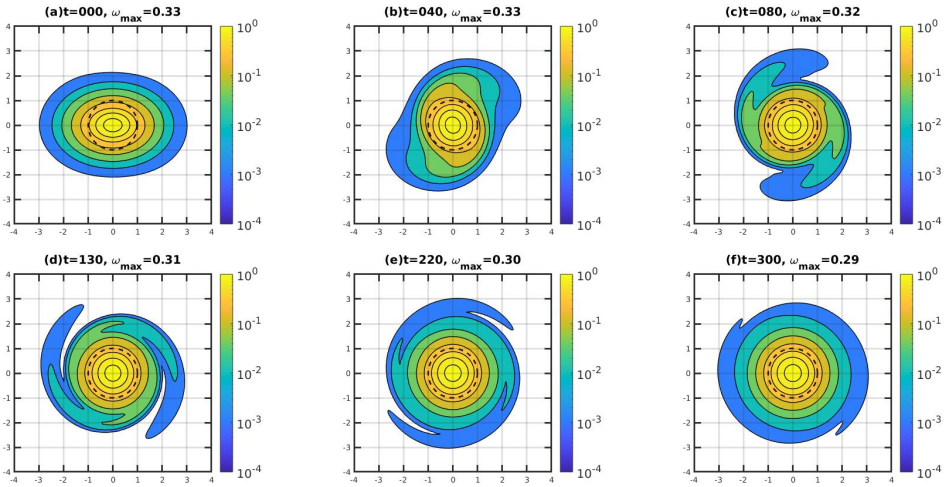

Figure 4.1 – Time evolution of a 2D elliptic vortex, with $Re_{2D} = \Gamma/(2\pi\nu) = 10^4$. Contours of $\omega/\omega_{\max}$ at (a) $t = 0$, (b) $t = 40$, (c) $t = 80$, (d) $t = 130$, (e) $t = 220$, (f) $t = 300$, with the black dashed circle indicates one unit radius.

The two-dimensional DNS simulation at $Re_{2D} = \Gamma/(2\pi\nu) = 10^4$ shows a two-stage process. First a transient called the relaxation stage is observed, where filaments form and decay towards an axisymmetric state. This axisymmetric flow profile is close to an Euler equilibrium profile. Second the velocity profile evolves approaching a typical Gaussian profile on a slow diffusion time scale. More generally, a two-dimensional initial flow with three velocity components evolves towards a viscous Batchelor vortex [Rossi, 2000]. Furthermore, when an external potential flow is imposed on top of the two-dimensional vortex, the initial vortex evolves by emitting filaments during a transient stage, and rapidly reaches a quasi-equilibrium state. This state is now characterized by a slightly elliptic shape due to presence of the external strain, which is small with respect to the characteristic vorticity of the vortex [Jiménez et al., 1996, Le Dizès and Verga, 2002].

Let us come back to viscous helical quasi-steady states. For large pitch L, the dynamics of each transversal section of a helical vortex can be approximated by a two-dimensional vortex with three velocity components subjected to a strain originating from the remaining part of the vortex. It is thus reasonable to assume that a similar process occurs for a helical vortex at finite L. The potential flow deforming the vortex core takes its origin from the three-dimensional geometry of the vortex itself: after a rapid relaxation process, a helical vortex with thin core evolves towards a generic quasi-equilibrium helical state. This solution approaches a slightly deformed Gaussian profile. The present section describes the relaxation process, starting from a helically axisymmetric vortex, and checks that a quasi-equilibrium is indeed reached after a transient.

4.2.1 Building an appropriate initial flow

In this subsection, we define an initial flow which is helically symmetric along the z-direction, of spatial period $2\pi L$ and characterized by a vorticity field $\boldsymbol{\omega}$ which tends at least exponentially to zero away from a given helical line. Let us first define this helical line. As illustrated in figure 4.2, the line intersects the $z = 0$ plane (thereafter called Π_0) at a point $\mathrm{A}^\star$ defined by its cylindrical coordinates $r_{\mathrm{A}^\star}$ and $\theta_{\mathrm{A}^\star}$, The angle is set to $\theta_{\mathrm{A}^\star} = 0$ without loss of generality. This helical line is thus located at

$$\boldsymbol{x}(\theta_s) = r_{\mathrm{A}^\star}\boldsymbol{e}_r(\theta_s) + L\theta_s\boldsymbol{e}_z\,, \qquad \theta_s \in \mathbb{R}. \tag{4.18}$$

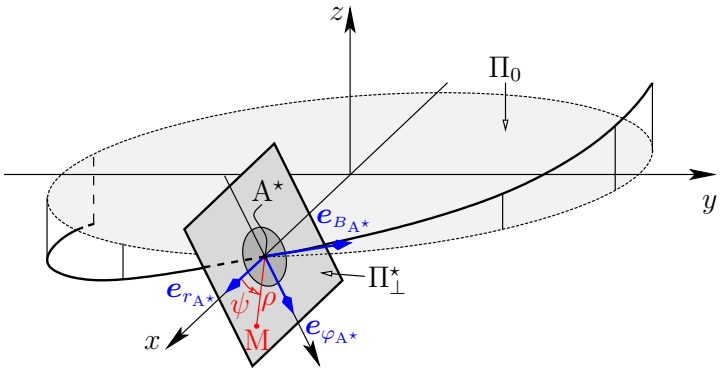

Figure 4.2 – Geometry for building the initial condition.

The plane perpendicular to this helical line at point $\mathrm{A}^\star$ is called the plane $\Pi_\perp^\star$. The unit vector $\boldsymbol{e}_{B_{\mathrm{A}^\star}}$ defines the upward normal vector to plane $\Pi_\perp^\star$:

$$\boldsymbol{e}_{B_{\mathrm{A}^\star}} = \alpha(r_{\mathrm{A}^\star})\left[\boldsymbol{e}_z + \frac{r_{\mathrm{A}^\star}}{L}\boldsymbol{e}_\theta(0)\right].$$

In the plane $\Pi_\perp^\star$, a *Cartesian* basis $\left(\boldsymbol{e}_{r_{\mathrm{A}^\star}}, \boldsymbol{e}_{\varphi_{\mathrm{A}^\star}}\right)$ is defined as well

$$\boldsymbol{e}_{r_{\mathrm{A}^\star}} \equiv \boldsymbol{e}_r(0), \quad \boldsymbol{e}_{\varphi_{\mathrm{A}^\star}} \equiv \alpha(r_{\mathrm{A}^\star})\left[\boldsymbol{e}_\theta(0) - \frac{r_{\mathrm{A}^\star}}{L}\boldsymbol{e}_z\right],$$

associated with local polar coordinates (ρ, ψ) centered at point $A^\star$ with local basis $\left(\boldsymbol{e}_\rho, \boldsymbol{e}_\psi\right)$:

$$\boldsymbol{e}_\rho = \cos\psi\, \boldsymbol{e}_{r_{\mathrm{A}^\star}} + \sin\psi\, \boldsymbol{e}_{\varphi_{\mathrm{A}^\star}}, \quad \boldsymbol{e}_\psi = \cos\psi\, \boldsymbol{e}_{\varphi_{\mathrm{A}^\star}} - \sin\psi\, \boldsymbol{e}_{r_{\mathrm{A}^\star}}.$$

Since the initial condition is assumed to be a thin-core vortex along the helical line: one chooses a compact profile for $\omega_B(\rho, \psi)$ and for $u_H(\rho, \psi)$ around point $A^\star$. This ensures that ω_φ and ω_r are also compact. For instance, one assumes axisymmetric profiles similar to a local Batchelor vortex:

$$\omega_B(\rho) = \omega_B^\star \exp(-\frac{\rho^2}{a^{\star 2}}), \quad u_H(\rho) = u_H^\star \exp(-\frac{\rho^2}{a^{\star 2}}), \tag{4.19}$$

From these analytical profiles in the plane $\Pi_\perp^\star$ as well as the values of the helical radius $r_{\mathrm{A}^\star}$ and pitch L, it is possible to compute the initial fields $\omega_B(r, \varphi)$ and $u_H(r, \varphi)$ on the Π_0 plane used in simulations. To do so, we establish the connections between (r, φ) given by a point in Π_0 and the polar radius ρ of the corresponding point in $\Pi_\perp^\star$, using invariances along the lines $\varphi = \theta - z/L = \mathrm{cst}$ (details on such procedure can be found in [Selçuk et al., 2017b], appendix A).

We simulate two initial conditions called case A and B. Case A is characterized by a circulation $\Gamma = 1$, a helical radius $r_{\mathrm{A}^\star} = 1$, a reduced helical pitch $L = 0.3$, an initial core size $a^\star = 0.1$, an initial axial flow intensity $u_H^\star r_{\mathrm{A}^\star}/\Gamma = 1$. Using some conservation relations (see section 4.3.3), this yields (using equation (4.44)) $\omega_B^\star r_{\mathrm{A}^\star}^2/\Gamma = 32.68$. On the $\Pi_\perp^\star$ plane, the fields are axisymmetric and Gaussian (figure 4.3a) whereas in the Π_0 plane, they take a bean-like shape (figure 4.3b).

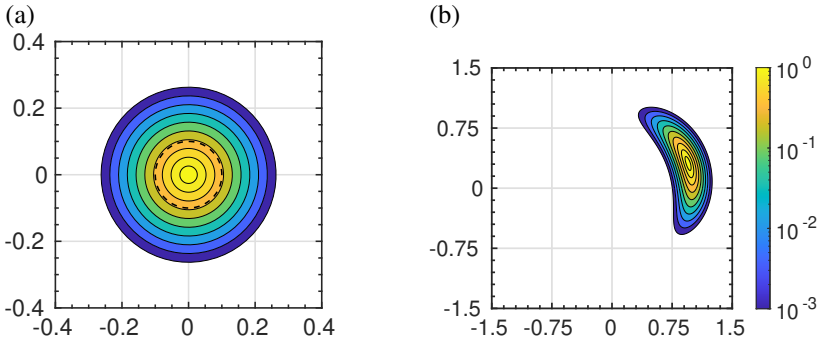

Figure 4.3 – Contours of $\omega_B/\omega_{B\max}$ for case A (see text) (a) in plane $\Pi_\perp^\star$ and (b) in plane Π_0. The dashed circle in graph (a) represents the initial vortex core size $\rho = a^\star$. Contour levels $C_p = \omega_B/\omega_{B\max}$ with $\sqrt{-\log(C_p)} = \frac{1}{10} p \sqrt{\log(10^3)}$ and $p = 1, \cdots, 10$.

For the second simulation (case B), the jet component is initially more intense: as before $\Gamma = 1$, $r_{A^\star} = 1$ but the initial axial flow intensity is larger $u_H^\star r_{A^\star}/\Gamma = 2$. In addition, the reduced helical pitch is set to $L = 1.5$ and the initial core size to $a^\star = 0.2$. This yields $\omega_B^\star r_{A^\star}^2/\Gamma = 9.52$.

4.2.2 Reaching a viscous helical quasi-equilibrium state

Starting from the previous initial condition, the Navier–Stokes equations with helical symmetry are integrated over time. This is performed by the numerical code Helix using a polar grid in a circular sub-domain of plane Π_0 (see the generalized Ψ–ω_B–u_H formulation described in section 3.2). In the code HELIX, we define dimensionless units, based on the characteristic length $[L] = r_{A^\star}$ and the characteristic time $[T] = r_{A^\star}^2/\Gamma$ leading to the Reynolds number

$$Re_{\rm DNS} = \frac{\Gamma}{\nu} \tag{4.20}$$

and the dimensionless equations

$$\partial_t \omega_B + \mathrm{NL}_\omega = \frac{1}{Re_{\rm DNS}} \mathrm{VT}_\omega\,, \tag{4.21}$$

$$\partial_t u_H + \mathrm{NL}_{u_H} = \frac{1}{Re_{\rm DNS}} \mathrm{VT}_{u_H}\,, \tag{4.22}$$

$$\omega_B = -\mathbb{L}\Psi + \frac{2\alpha^3}{L}(u_H + C_\infty). \tag{4.23}$$

For case A, the DNS Reynolds number is set to $Re_{\rm DNS} \equiv \Gamma/\nu = 2\pi 10^4$. It is observed that filaments are emitted during the early relaxation stage (see $t = 4$ at figures 4.4–4.5), and then quickly dissipate ($t = 10$). After this stage the vortex becomes quasi-steady for instance at $t = 20$. Note that the core of the helical vortex tends to an elliptical shape. This is due to the strain field induced by the helical geometry, through vortex curvature and interaction with the other turns of the helical vortex. Such a deformation is the cause of instabilities (see following chapters concerning instability).

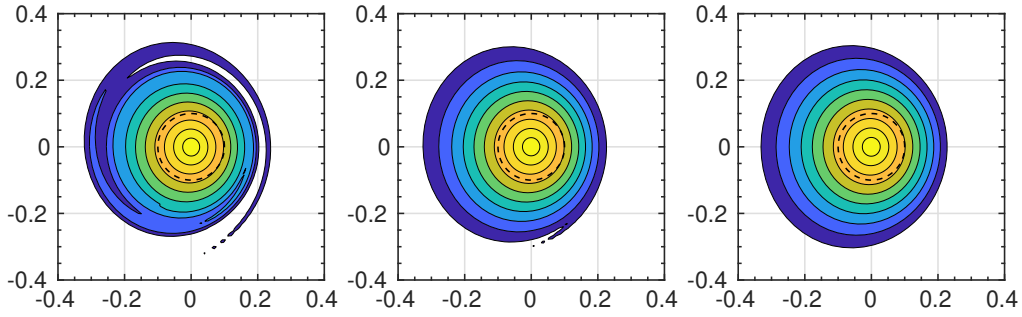

Figure 4.4 – Case A at $t = 4$, 10 and 20: contours of $\omega_B/\omega_{B\max}(t)$ in plane $\Pi_\perp(t)$. Contours levels are as defined in figure 4.3.

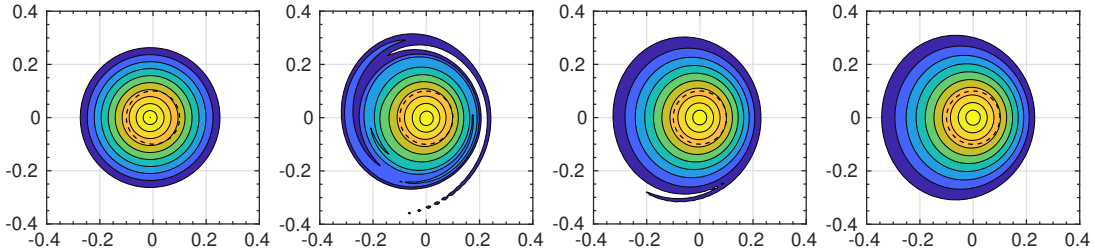

Figure 4.5 – Case A at $t = 0$, 4, 10 and 20: contours of $u_H/u_{H\max}$ in plane $\Pi_\perp(t)$. Contours levels are defined in the same way as in figure 4.3 for $\omega_B/\omega_{B\max}$.

We now check how the DNS solution approaches an Euler equilibrium using conditions (4.16). First, we determine the angular velocity $\Omega_0(t)$ along the z-axis by the best correlation of the vorticity field between successive time steps. This provides the translating reference frame : velocity $U_0(t) = -\Omega_0 L$. Second, the streamfunction $\Psi^{(\mathrm{T})}$ in the translating frame is computed using (4.10). From now on, we only consider streamfunction $\Psi^{(\mathrm{T})}$ which will be simply denoted Ψ. Figure 4.6a displays scatterplots of u_H versus Ψ at several times for case A. As time increases, it is observed that the points converge to a single continuous curve, supporting the existence of the function g such that $u_H + C = g(\Psi)$.

The second condition (4.16) requires the derivative $\mathrm{d}u_H/\mathrm{d}\Psi$. This quantity is *a priori* defined only if a steady state is reached. The following procedure however allows us to estimate this quantity during the whole time evolution, based on averages and least square interpolation. This quantity converges to the exact value when the quasi-steady state is reached. More specifically, we discretize the Ψ-axis in N_Ψ intervals of length $\Delta\Psi$ between the minimum and the maximum value of Ψ. In each interval $[\Psi_i - \frac{1}{2}\Delta\Psi, \Psi_i + \frac{1}{2}\Delta\Psi]$, there is a certain number K_i of points $(\Psi^{(k)}, u_H^{(k)})$ indexed by k. The mean value α_i of $u_H^{(k)}$ and the estimate β_i of $\mathrm{d}u_H/\mathrm{d}\Psi$ at point Ψ_i are such that

$$K_i\alpha_i + \beta_i \sum_k (\Psi^{(k)} - \Psi_i) = \sum_k u_H^{(k)} \tag{4.24}$$

$$\alpha_i \sum_k (\Psi^{(k)} - \Psi_i) + \beta_i \sum_k (\Psi^{(k)} - \Psi_i)^2 = \sum_k [u_H^{(k)}(\Psi^{(k)} - \Psi_i)] \tag{4.25}$$

where it has been assumed that $u_H^{(k)}$ can be estimated with the linear interpolation:

$$u_H^{(k)} = \alpha_i + \beta_i(\Psi^{(k)} - \Psi_i). \tag{4.26}$$

Quantities $\mathrm{d}u_H/\mathrm{d}\Psi$ are computed using a linear interpolation along the variable Ψ as follows:

$$\frac{\mathrm{d}u_H}{\mathrm{d}\Psi_T}(\Psi^{(k)}) = \beta_i + \left\{ \begin{array}{c} \beta_{i+1} - \beta_i \\ \beta_i - \beta_{i-1} \end{array} \right\} \frac{\Psi^{(k)} - \Psi_i}{\Delta\Psi} \quad \left\{ \begin{array}{l} \text{if } \Psi^{(k)} > \Psi_i \\ \text{if } \Psi^{(k)} < \Psi_i \end{array} \right. . \tag{4.27}$$

For the first and the last half-intervals, one uses an extrapolation from the neighbouring half-interval.

In figure 4.6b, scatterplots of quantity ϖ versus Ψ are found to support the existence of a function f such that $\varpi = f(\Psi)$. For case A, however, quantity $\alpha\omega_B$ dominates the value ϖ (see figure 4.6c) : when the jet

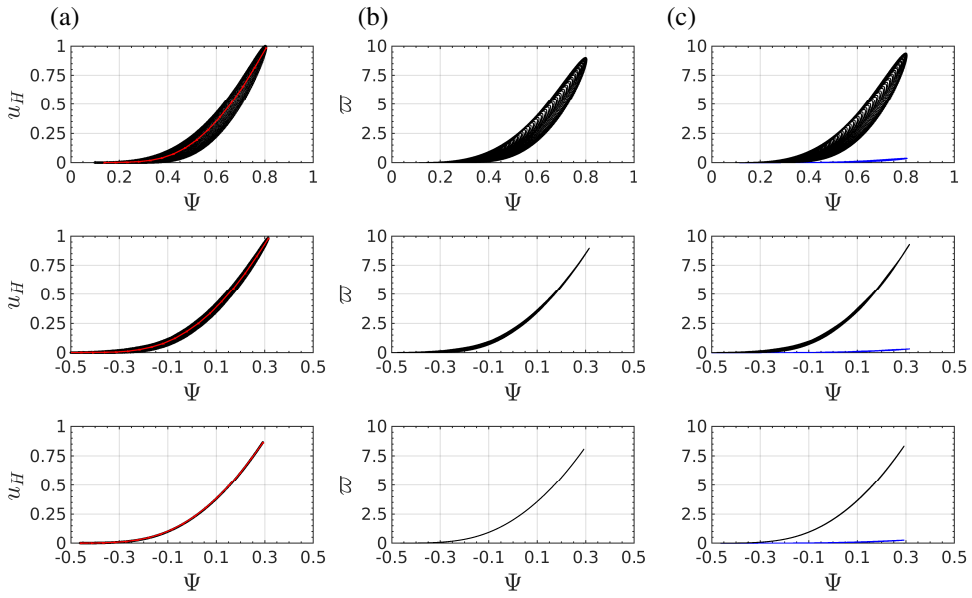

Figure 4.6 – Case A: scatterplots at times $t = 0$ (top), $t = 2$ (middle) and $t = 20$ (bottom): (a) u_H vs Ψ (the red curve is an estimate of $g(\Psi)$ obtained *via* formula (4.26)); (b) ϖ vs Ψ; (c) $\alpha\omega_B$ (black dots) and $\alpha^2\mathrm{d}(u_H + C)^2/\mathrm{d}\Psi$ (blue dots) vs Ψ. Note that only grid points such that $\omega_B/\omega_{B\max} > 10^{-3}$ have been represented.

component is weak, quantity ϖ almost equals $\alpha\omega_B$, which visually becomes a function of Ψ.

We present a second simulation (case B) where the jet component is initially more intense. The Reynolds number is set to $Re_{\mathrm{DNS}} = 2\pi 10^3$. As time evolves, velocity u_H converges to a function of Ψ (see figures 4.7a and b). For case B, partial quantities $\alpha\omega_B$ and $\alpha^2\mathrm{d}(u_H + C)^2/\mathrm{d}\Psi$ have same orders of magnitude (see figure 4.7c) so that the corresponding points remain scattered even at late times. Quantity $\varpi = \alpha\omega_B - \alpha^2\mathrm{d}(u_H+C)^2/\mathrm{d}\Psi$ however clearly converges towards a function of Ψ (see figure 4.7b). This fully confirms the new finding expressed by relations (4.16).

Figure 4.8 represents the relation reached in the quasi-equilibrium state between ϖ and u_H. When axial vorticity dominates over axial velocity (figure 4.8a) there is a linear relationship between $\varpi \approx \alpha\omega_B$ and

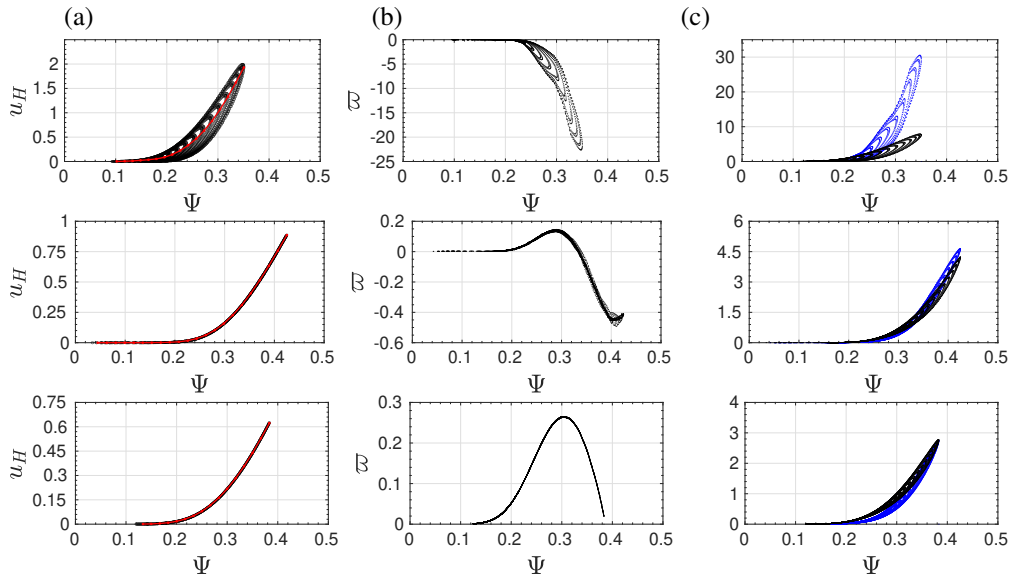

Figure 4.7 – Same as figure 4.6 but for case B (see text) plotted at times $t = 0$ (top), $t = 50$ (middle) and $t = 100$ (bottom).

u_H [Selçuk et al., 2017a]. When both effects have comparable orders of magnitude, this relation becomes highly nonlinear (figure 4.8b). Finding an analytical expression for such relations remains an open issue.

4.3 Generating a quasi-equilibrium helical vortex with prescribed parameter values

In this section, a procedure is introduced to generate by DNS a flow with prescribed parameter values. This is an alternative to the method employed by [Brynjell-Rahkola and Henningson, 2020]. The goal is to generate a quasi-equilibrium to be used as a base flow in an instability study. Hence we would like to prescribe the *final* state obtained through the DNS rather than the initial state (4.19) which is not a quasi-equilibrium. In section 4.2.1, however, the viscous quasi-equilibrium reached after certain relaxation time depends on five dimensional parameters used to initiate the simulation namely circulation Γ, helical radius $r_{A^\star}$, helical pitch $2\pi L$, vortex core size $a^\star$, axial flow intensity $u_H^\star$. The vorticity amplitude $\omega_B^\star$ is a function of circulation Γ and velocity $u_H^\star$. To implement this procedure, we first need to characterize the final state, that is to define five parameters based on the final state. These are defined in section 4.3.1.

4.3.1 Determination of the parameters characterizing the final helical vortex

The first parameter is the helical radius r_A of centre A of the vortex. In order to characterize the centre of the vortex, the most convenient way is to look for the point A where Ψ reaches a maximum in the plane Π_0 (for most single helical vortices, this point is unique). One then defines the associated plane $\Pi_\perp$ in a similar way as $\Pi_\perp^\star$ was defined from $A^\star$ (see section 4.2.1 and figure 4.2). Since the field Ψ depends on (r, φ), there is a one-to-one relation between its values in the plane $\Pi_\perp$ and in the plane Π_0. Consequently, it also reaches a maximum in the $\Pi_\perp$ plane at point A. Other properties can be useful to locate this central

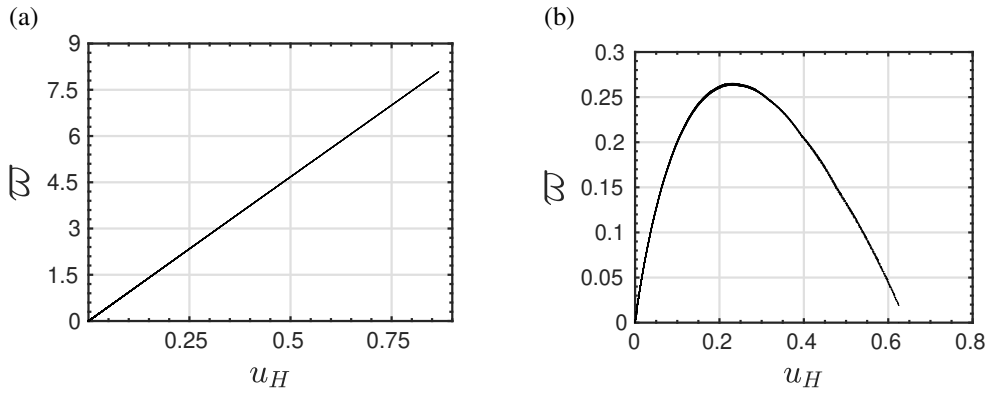

Figure 4.8 – Quantity ϖ as a function of u_H at quasi-equilibrium for (a) case A (see figure 4.6) and (b) case B (see figure 4.7).

	$\alpha\omega_B$	u_H	Ψ
case A	1.008	1.008	1.008
case B	0.983	1.015	1.015

Table 4.1 – Radial location of the maximum for different quantities, as measured in the DNS for cases A and B.

point. Since $ru_r = \partial_\varphi \Psi$ and $u_\varphi = -\alpha(r)\partial_r \Psi$, velocity at point A is such that $u_r = u_\varphi = 0$ and is thus tangent to a helical line, i.e. $\boldsymbol{u}(\mathrm{A}) = u_B \boldsymbol{e}_B$. Furthermore, if the solution is a quasi-steady equilibrium, then relation $u_H + C = g(\Psi)$ holds and necessarily, velocity u_H has an extremum at point A since at this point

$$\partial_\varphi u_H = \frac{\mathrm{d}u_H}{\mathrm{d}\Psi}\partial_\varphi \Psi = 0, \qquad \partial_r u_H = \frac{\mathrm{d}u_H}{\mathrm{d}\Psi}\partial_r \Psi = 0\,.$$

Since $\partial_\varphi u_H = r\omega_r$ and $\partial_r u_H = -\omega_\varphi/\alpha$, vorticity components ω_r and ω_φ hence vanishes at point A and the vorticity vector is thus tangent to a helical line, i.e. $\boldsymbol{\omega}(\mathrm{A}) = \omega_B \boldsymbol{e}_B$. Finally note that the points where u_H and $\alpha\omega_B$ reach an extremum generally do not coincide. Only in the particular case when $u_H = 0$, quantity $\alpha\omega_B$ is also a function of Ψ and thus reaches an extremum at point A. This is illustrated in table 4.1: for case A with relatively small axial flow, these radial locations differ by less than 0.1%, while they differ by 3% for case B because of the larger axial flow. The angle θ_A is not dynamically pertinent and is set to zero for the base state that is $\theta_\mathrm{A} = 0$. A local Cartesian basis $(\boldsymbol{e}_b, \boldsymbol{e}_r(\mathrm{A}), \boldsymbol{e}_\varphi(\mathrm{A}))$ is defined on $\Pi_\perp$ where the unit vector $\boldsymbol{e}_b \equiv \boldsymbol{e}_{B\mathrm{A}}$ is the upward normal vector to plane $\Pi_\perp$ and $\boldsymbol{e}_\varphi(\mathrm{A}) \equiv \boldsymbol{e}_{B\mathrm{A}} \times \boldsymbol{e}_r(\mathrm{A})$.

The four remaining parameters that define the final helical vortex, are the helical pitch $2\pi L$ and circulation Γ is given by

$$\Gamma \equiv \iint_{\Pi_0} \omega_z \, r\mathrm{d}r\mathrm{d}\theta\,. \tag{4.28}$$

Both parameters are constant during the simulations. The core size could be obtained through an integral in the plane $\Pi_\perp$ associated with point A:

$$a^2 \equiv \frac{1}{\Gamma} \iint_{\Pi_\perp} \boldsymbol{\omega} \cdot \boldsymbol{e}_{B_\mathrm{A}} \, (\boldsymbol{x} - \boldsymbol{x}_\mathrm{A})^2 \, dS_\perp \tag{4.29}$$

where $\boldsymbol{e}_{B_\mathrm{A}} \equiv \boldsymbol{e}_B(\mathrm{A})$ and $\boldsymbol{x}_\mathrm{A} \equiv \boldsymbol{x}(\mathrm{A})$. But in practice, the core size is obtained by fitting $\boldsymbol{\omega}\cdot\boldsymbol{e}_{B_\mathrm{A}}$ on $\Pi_\perp$ plane by:

$$\boldsymbol{\omega}\cdot\boldsymbol{e}_{B_\mathrm{A}} = \frac{\Gamma}{\pi a^2}\exp(-\frac{\rho^2}{a^2}). \tag{4.30}$$

The last parameter is the axial velocity parameter

$$W_B \equiv \frac{\alpha_\mathrm{A}^2}{\pi a^2}\iint_{\Pi_0} u_H \mathrm{d}S \quad \text{with} \quad \alpha_\mathrm{A} \equiv \alpha(r_\mathrm{A}). \tag{4.31}$$

Note that from the reduced pitch L and helical radius r_A, the curvature κ of the helix at $r = r_\mathrm{A}$ is given by

$$\kappa \equiv \frac{r_\mathrm{A}}{r_\mathrm{A}^2+L^2} = \alpha_\mathrm{A}^2\frac{r_\mathrm{A}}{L^2}, \ \text{with} \quad \alpha_\mathrm{A}^2 \equiv \alpha^2(r_\mathrm{A}) = \frac{L^2}{r_\mathrm{A}^2+L^2}, \tag{4.32}$$

and its torsion τ by

$$\tau \equiv \frac{L}{r_\mathrm{A}^2+L^2}. \tag{4.33}$$

If profiles are those of a thin curved Batchelor vortex (4.19), the core size a is almost equal to $a^\star$ and the quantity W_B is close to the amplitude of helical velocity $\alpha_\mathrm{A}u_H^\star$. Indeed, for a thin core, $\mathrm{d}S_\perp \approx \alpha\mathrm{d}S \approx \alpha_\mathrm{A}\mathrm{d}S$ and

$$W_B \approx \frac{\alpha_\mathrm{A}}{\pi a^2}\iint_{\Pi_\perp} u_H \mathrm{d}S_\perp = \frac{\alpha_\mathrm{A}}{\pi a^2}u_H^\star 2\pi\int_0^\infty \mathrm{e}^{-(\rho/a^\star)^2}\rho\mathrm{d}\rho = \frac{\alpha_\mathrm{A}}{\pi a^2}u_H^\star\pi a^{\star 2} \approx \alpha_\mathrm{A}u_H^\star. \tag{4.34}$$

4.3.2 Relations for some global quantities in viscous helical flows

For a viscous flow periodic along z of period $2\pi L$ and characterized by a compact vorticity field, the circulation Γ and the axial momentum per unit length $\mathcal{P}_z$ given by

$$\Gamma = \iint_{\Pi_0}\omega_z r\mathrm{d}r\mathrm{d}\theta\,, \quad \mathcal{P}_z = \frac{1}{2\pi|L|}\left(\frac{\rho}{2}\iiint_V \boldsymbol{x}\times\boldsymbol{\omega}\,\mathrm{d}V\right)\cdot\boldsymbol{e}_z = \frac{\rho}{4\pi|L|}\iiint_V r\omega_\theta\,\mathrm{d}V, \tag{4.35}$$

are two global viscous invariants. In (4.35), Π_0 denotes the plane $z = 0$ and V the volume defined by $z \in [-\pi|L|, \pi|L|]$. For such periodic flows, the axial angular momentum per unit length

$$\mathcal{L}_z = -\frac{\rho}{4\pi|L|}\iiint_V \boldsymbol{x}^2\omega_z\,\mathrm{d}V$$

is not an invariant but evolves according to

$$\frac{\mathrm{d}\mathcal{L}_z}{\mathrm{d}t} = -2\rho\Gamma\nu. \tag{4.36}$$

These conservation laws applied to viscous helical flows [Selçuk et al., 2017a] provide relations between

the following unsteady quantities

$$\mathcal{H}_1 \equiv \iint_{\Pi_0} \alpha\omega_B \,\mathrm{d}S\,, \quad \mathcal{H}_2 \equiv \iint_{\Pi_0} \alpha^4 u_H \,\mathrm{d}S\,, \quad \mathcal{H}_3 \equiv \iint_{\Pi_0} r^2\alpha\omega_B \,\mathrm{d}S\,, \quad \mathcal{H}_4 \equiv \iint_{\Pi_0} u_H \,\mathrm{d}S\,.$$

Since $\omega_z = \alpha(\omega_B - r\omega_\varphi/L)$ for helical flows, the conservation circulation Γ yields

$$\Gamma = \iint_{\Pi_0} \alpha\omega_B \,\mathrm{d}S + \iint_{\Pi_0} \frac{\alpha^2 r}{L}\frac{\partial u_H}{\partial r}\,\mathrm{d}S\,.$$

Integrating by parts the last integral leads to

$$\Gamma = \mathcal{H}_1(t) - \frac{2}{L}\mathcal{H}_2(t). \tag{4.37}$$

Similarly the conservation of axial momentum per unit length $\mathcal{P}_z$, implies for helical flows that

$$\mathcal{P}_z = \frac{\rho}{4\pi|L|}\int_{-\pi|L|}^{\pi|L|}\left[\iint_{\Pi_0} r\omega_\theta \, r\mathrm{d}r\mathrm{d}\theta\right]\mathrm{d}z = \frac{\rho}{2}\iint_{\Pi_0} r^2\omega_\theta \,\mathrm{d}r\mathrm{d}\theta\,.$$

Introducing $\omega_\theta = \alpha(\omega_\varphi + \frac{r}{L}\omega_B)$ and integrating by parts, yields

$$\frac{\mathcal{P}_z}{\rho} = \frac{1}{2L}\mathcal{H}_3(t) + \mathcal{H}_2(t). \tag{4.38}$$

Finally, helical symmetry imposes

$$\iiint_V \boldsymbol{x}^2\omega_z \,\mathrm{d}V = \iiint_V (z^2+r^2)\omega_z \,\mathrm{d}V = \frac{2\Gamma(\pi|L|)^3}{3} + 2\pi|L|\iint_{\Pi_0} r^2\omega_z \,\mathrm{d}S\,.$$

Upon introducing $\omega_z = \alpha(\omega_B - r\omega_\varphi/L)$, one gets

$$\begin{aligned}\iint_{\Pi_0} r^2\omega_z \,\mathrm{d}S \;&= \iint_{\Pi_0} \alpha r^2\omega_B \,\mathrm{d}S + \iint_{\Pi_0}\frac{\alpha^2 r^3}{L}\frac{\partial u_H}{\partial r}\,\mathrm{d}S \\ &= \mathcal{H}_3(t) + \iint_{\Pi_0} rL(1-\alpha^2)\frac{\partial u_H}{\partial r}\,\mathrm{d}S\,.\end{aligned}$$

Integrating by parts the last integral yields

$$\mathcal{L}_z(t) = -\frac{\rho}{4\pi|L|}\iiint_V \boldsymbol{x}^2\omega_z \,\mathrm{d}V = -\frac{\rho\Gamma(\pi L)^2}{6} - L\mathcal{P}_z + \rho L\mathcal{H}_4(t).$$

Since circulation Γ and axial momentum per unit length $\mathcal{P}_z$ are global viscous invariants for a compact vorticity field and that the axial angular momentum per unit length $\mathcal{L}_z(t)$ evolves according to equation (4.36), one gets

$$\frac{\mathrm{d}\mathcal{H}_4}{\mathrm{d}t} = -\frac{2\Gamma}{L}\nu \quad \text{or equivalently} \quad \mathcal{H}_4(t) = \mathcal{H}_4(0) - \frac{2\Gamma}{L}\nu t\,. \tag{4.39}$$

4.3.3 Iterative algorithm to obtain the prescribed base states

All variables are put in dimensionless form using as characteristic dimensional length scale $[L] = r_{\rm A}$ and time scale $[T] = r_{\rm A}^2/\Gamma$ of the ***final* state**. Since the dimensionless radius at point A and dimensionless circulation are equal to one, the quasi-equilibrium state depends only on two dimensionless lengths $L/r_{\rm A}$ and $a/r_{\rm A}$, and a third dimensionless number

$$\bar{W}_B \equiv \frac{2\pi a\, W_B}{\Gamma}. \tag{4.40}$$

This inverse swirl number $\bar{W}_B$ is the ratio of the axial velocity parameter W_B and the typical azimuthal velocity in the core $\Gamma/(2\pi a)$. In addition the dimensionless curvature can be helpful in comparing the DNS results with the theory

$$\varepsilon = \kappa a = \alpha_{\rm A}^2 \frac{r_{\rm A}}{L}\frac{a}{L}. \tag{4.41}$$

From now on in this section, all variables are assumed dimensionless. The algorithm presented below converges towards a base flow configuration denoted by $[L;\ a;\ \bar{W}^B]$ when the prescribed dimensionless parameters are L, a, $\bar{W}_B$, with $\Gamma = 1$ and $r_{\rm A} = 1$. The main building block of this procedure is based on a viscous simulation towards the quasi-equilibrium. To do so we select two values: the Reynolds number $Re_{\rm DNS} \equiv \Gamma/\nu$ and a dimensionless simulation time denoted as $T_{\rm sim}$. In the pure two-dimensional framework $L = \infty$, it is known that the characteristic time necessary for the vortex with a Lamb-Oseen type profile to reach a quasi-equilibrium is of order $a^2 Re_{\rm DNS}^{1/3}$ with a pre-factor of order 40 [Bernoff and Lingevitch, 1994]. This pre-factor changes with the vortex profile considered. We here select the final simulation time $T_{\rm sim} \sim 60 a^2 Re_{\rm DNS}^{1/3}$ and, in practice, check *a posteriori* that it is large enough to reach a quasi-equilibrium. For $Re_{\rm DNS} = 2\pi 10^4$, for instance, we selected $T_{\rm sim} = 20, 40, 100$ for $a = 0.11, 0.174$ and 0.3 respectively.

The reduced pitch L and circulation Γ of the initial condition are identical to those of the quasi-equilibrium we are looking for, that is the prescribed final state values L and $\Gamma = 1$. By contrast, initial parameters $r_{\rm A^\star}$, $a^\star$ differ from quantities $r_{\rm A} = 1$ and a of the prescribed final state. Similarly $u_H^\star$ differs from $W_B/\alpha_{\rm A}$. This is why an iterative procedure determines these three unknown dimensionless initial parameters $r_{\rm A^\star}$, $a^\star$ and $u_H^\star$. First, we select guess values for $a^\star$ and $r_{\rm A^\star}$, so that we link the two initial parameters $u_H^\star$ and $\omega_B^\star$ to parameters a, L, and $\bar{W}_B$. This connection is obtained *via* the two "conservation" laws (4.37) and (4.39) obtained in section 4.3.2 written in dimensionless form

$$\mathcal{H}_1(t) - \frac{2}{L}\mathcal{H}_2(t) = 1\ , \quad \mathcal{H}_4(t) = \mathcal{H}_4(0) - \frac{2t}{L\,Re}, \tag{4.42}$$

where

$$\mathcal{H}_1 \equiv \iint_{\Pi_0} \alpha\,\omega_B\,{\rm d}S\ , \quad \mathcal{H}_2 \equiv \iint_{\Pi_0} \alpha^4 u_H\,{\rm d}S \quad \text{and} \quad \mathcal{H}_4 \equiv \iint_{\Pi_0} u_H\,{\rm d}S. \tag{4.43}$$

Let us introduce the quantities

$$I_p^\star(a^\star, r_{\rm A^\star}, L) \equiv \iint_{\Pi_0} \alpha^p \exp(-(\rho/a^\star)^2)\, r{\rm d}r{\rm d}\theta$$

with p positive integers. Such quantities depend on L via the quantity ρ, itself depending on r, θ, $r_{\rm A^\star}$ and

L (see figure 4.2). Inserting the initial condition (4.19) into (4.42) allows one to write

$$\omega_B^\star I_1^\star - \frac{2}{\bar{L}} u_H^\star I_4^\star = 1\,, \quad u_H^\star I_0^\star = \mathcal{H}_4(T_{\rm sim}) + \frac{2T_{\rm sim}}{\bar{L}Re}\,. \tag{4.44}$$

where the value of $\mathcal{H}_4(T_{sim})$ is evaluated from the prescribed parameters a, $\bar{W}_B$ and L with

$$\mathcal{H}_4(T_{sim}) = \frac{1}{2}\bar{W}_B\bar{a}(1+\bar{L}^{-2}). \tag{4.45}$$

Introducing relation (4.40) leads to determine $u_H^\star$ and $\omega_B^\star$:

$$u_H^\star = \frac{1}{I_0^\star}\left[\frac{\bar{W}_B\bar{a}}{2\alpha_{\rm A}^2} + \frac{2T_{\rm sim}}{\bar{L}Re}\right], \quad \omega_B^\star = \frac{1}{I_1^\star}\left(1 + \frac{2}{\bar{L}}u_H^\star I_4^\star\right). \tag{4.46}$$

After a simulation from $t = 0$ to T_{sim}, we obtain a quasi-equilibrium state with same circulation and same $\mathcal{H}_4$ as the reference state at T_{sim}. Of course, since $a^\star$ and $r_{\rm A}^\star$ have only been guessed at this stage, the DNS initiated by the above procedure does not lead at once to the prescribed values of a and $r_{\rm A} = 1$ at $t = T_{\rm sim}$. We have to use a standard iterative procedure to search for the proper pair $(a^\star, r_{\rm A^\star})$ leading, after a simulation time of duration $T_{\rm sim}$, to the prescribed values $(a, 1)$, with a typical tolerance of 10^{-4}.

4.3.4 Checking the effect of Reynolds number

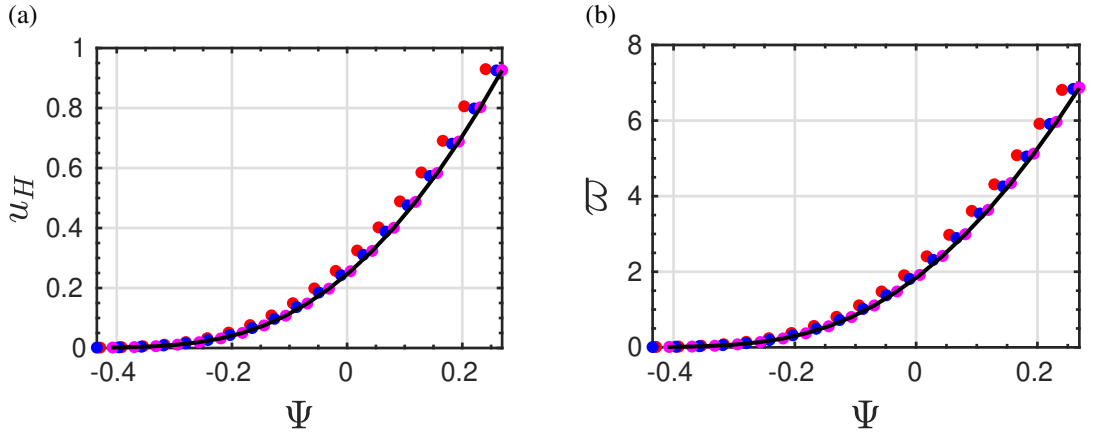

Figure 4.9 – Relations (a) $u_H = g(\Psi) - C$ and (b) $\varpi = f(\Psi)$ for quasi-equilibria obtained at different Reynolds numbers: $Re_{\rm DNS} = \pi 10^3$ (red dots, $T_{\rm sim} = 4$), $Re_{\rm DNS} = 2\pi 10^3$ (blue dots, $T_{\rm sim} = 4$), $Re_{\rm DNS} = \pi 10^4$ (magenta dots, $T_{\rm sim} = 10$) and $Re_{\rm DNS} = 2\pi 10^4$ (black solid line, $T_{\rm sim} = 20$). The dimensionless parameters of these states are $L = 0.3$, $a = 0.11$ and $\bar{W}_B = 0.2$.

The ability to prescribe the final state parameters presented in the previous section makes it possible to use several distinct Reynolds numbers to try to achieve the same quasi-equilibrium state. Figure 4.9 shows the influence of $Re = Re_{\rm DNS}/(2\pi)$ on the two curves $u_H = g(\Psi)$ and $\varpi = f(\Psi)$ obtained numerically. The cases $Re_{\rm DNS} = \pi 10^4$ and $2\pi 10^4$ cannot be visually distinguished, yet at lower Reynolds numbers (see $Re_{\rm DNS} = 2\pi 10^3$), the equilibrium curves shift more significantly as the value of $\Psi_{\rm max}$ also decreases. In the following, we always will adopt a sufficiently large Reynolds number (typically $Re_{\rm DNS} = 2\pi 10^4$) to

make sure that the quasi-equilibrium state obtained is *Re*-independent.

4.4 Asymptotic theory

This section discusses asymptotic theory [Moore and Saffman, 1972, Callegari and Ting, 1978] in the context of *helical vortices*. These techniques are valid when the core size is much smaller than the radius of curvature i.e. $a \ll r_{\mathrm{A}}$ or the pitch i.e. $a \ll L$. It is assumed that locally the profiles are close to an axisymmetric Batchelor vortex [Batchelor, 1964] of core size a_0 which must be very close to a. A dimensionless self-strain parameter $\varepsilon = \kappa a_0$ as defined in (4.41) is then small $\varepsilon \ll 1$ and can be used to expand velocity field components in power series of ε. In the matched asymptotic expansions [Blanco-Rodríguez et al., 2015], the vortex core structure is at leading order an axisymmetric Batchelor vortex [Batchelor, 1964] of core size a_0. Thereafter, small amplitude perturbations around this reference axisymmetric state introduce local effects due to curvature and torsion, and global ones due to the remote vorticity of nearby helix turns that modify this reference structure. It has been shown in [Callegari and Ting, 1978] and [Blanco-Rodríguez and Le Dizès, 2016, Blanco-Rodríguez and Le Dizès, 2017] that the dominant deformation stems from local curvature, and sets in as a dipolar first order term in ε. Local torsion and remote vorticity effects only appear at second order by a quadrupolar correction. We focus here on first order effects characterizing how local curvature deforms the vortex core.

We work in the translating reference frame (T) in which the vortex is steady. The internal structure, in particular the jet flow component within the vortex core, is described using local polar coordinates (ρ, ψ) centered at point A with local cylindrical basis $(\boldsymbol{e}_\rho, \boldsymbol{e}_\psi, \boldsymbol{e}_b)$. These variables and bases are defined from the local Cartesian basis $(\boldsymbol{e}_b, \boldsymbol{e}_r(\mathrm{A}), \boldsymbol{e}_\varphi(\mathrm{A}))$ (see section 4.3.1) :

$$\boldsymbol{e}_\rho = \cos\psi\, \boldsymbol{e}_r(\mathrm{A}) + \sin\psi\, \boldsymbol{e}_\varphi(\mathrm{A}), \quad \boldsymbol{e}_\psi = -\sin\psi\, \boldsymbol{e}_r(\mathrm{A}) + \cos\psi\, \boldsymbol{e}_\varphi(\mathrm{A}), \quad \boldsymbol{e}_b = \boldsymbol{e}_B(\mathrm{A}).$$

Since the reference state is a straight Batchelor vortex of core size a_0, we adopt in this section only, dimensionless quantities using as characteristic size the core size $[L] = a_0$ and as characteristic time $[T] = 2\pi a_0^2/\Gamma$, the Reynolds number for the asymptotic analysis being $Re = \Gamma/(2\pi\nu)$. To avoid ambiguity, we denote dimensionless quantities based on such characteristic size and time with a bar, for instance $\bar{\rho} = \rho/a_0$ stands for the non-dimensional radial distance to point A in the plane $\Pi_\perp$ and we use cylindrical coordinates $(\bar{\rho}, \psi, b)$, where b denotes the component parallel to the vortex axis. As mentioned above, the velocity field

$$\bar{\boldsymbol{u}} = \bar{u}_\rho\, \boldsymbol{e}_\rho + \bar{u}_\psi\, \boldsymbol{e}_\psi + \bar{u}_b\, \boldsymbol{e}_b\,,$$

can be expanded in power series in ε

$$\bar{u}_\rho = \varepsilon \bar{u}_\rho^{(1)} + \dots\,,$$
$$\bar{u}_\psi = \bar{u}_\psi^{(0)} + \varepsilon \bar{u}_\psi^{(1)} + \dots\,,$$
$$\bar{u}_b = \bar{u}_b^{(0)} + \varepsilon \bar{u}_b^{(1)} + \dots\,,$$

with similar expansions for vorticity.

Leading order term

The leading order term $\bar{\boldsymbol{u}}^{(0)}$ is assumed to be a Batchelor vortex. Indeed, this vortex model is known to be a self-similar attracting viscous solution for two-dimensional vortices with axial flow. This means that the

velocity distribution in the plane $\Pi_\perp$ is assumed to be equal to

$$\boxed{\bar{u}_\rho^{(0)} = 0\,, \quad \bar{u}_\psi^{(0)} = \frac{1-\exp(-\bar{\rho}^2)}{\bar{\rho}}\,, \quad \bar{u}_b^{(0)} = \bar{W}_0 \exp(-\bar{\rho}^2) + \bar{W}_{00}\,.} \tag{4.47}$$

The parameter $\bar{W}_0$ indicates the jet strength in the axial direction and the parameter $\bar{W}_{00}$ is a correction at leading order deduced from the background velocity outside the vortex. Based on these velocity fields, the vorticity field at zeroth order in ε is

$$\bar{\boldsymbol{\omega}}^{(0)} = \bar{\omega_{_B}}^{(0)} \boldsymbol{e}_b + \bar{\omega}_\psi^{(0)} \boldsymbol{e}_\psi\,,$$

with

$$\bar{\omega_{_B}}^{(0)} = 2\exp\left(-\bar{\rho}^2\right), \quad \bar{\omega}_\psi^{(0)} = 2\bar{W}_0\bar{\rho}\exp\left(-\bar{\rho}^2\right).$$

For any point M in plane $\Pi_\perp$(A) except A itself, the velocity component $u_{_B}$ along direction $\boldsymbol{e}_{_B}$(M) is different from the velocity component u_b along the direction $\boldsymbol{e}_b \equiv \boldsymbol{e}_{_B}$(A) orthogonal to the plane. Quantity $u_{_B}/\alpha$ is given by

$$\frac{u_{_B}}{\alpha} = \frac{u_\rho}{\alpha}\,\boldsymbol{e}_\rho \cdot \boldsymbol{e}_{_B} + \frac{u_\psi}{\alpha}\,\boldsymbol{e}_\psi \cdot \boldsymbol{e}_{_B} + \frac{u_b}{\alpha}\,\boldsymbol{e}_b \cdot \boldsymbol{e}_{_B}$$

where $\alpha \equiv \alpha$(M). Using relations

$$\boldsymbol{e}_\rho \cdot \boldsymbol{e}_{_B} = 0\,, \quad \boldsymbol{e}_\psi \cdot \boldsymbol{e}_{_B} = \alpha\alpha_{\mathrm{A}}\frac{\rho}{L}\,, \quad \boldsymbol{e}_b \cdot \boldsymbol{e}_{_B} = \alpha\alpha_{\mathrm{A}}\left(1 + \frac{r_{\mathrm{A}}^2}{L^2} - \frac{r_{\mathrm{A}}}{L}\frac{\rho}{L}\cos\psi\right),$$

one obtains, at zeroth order in ε:

$$\frac{\bar{u}_{_B}}{\alpha} = \frac{\bar{u}_b^{(0)}(\bar{\rho})}{\alpha_{\mathrm{A}}} + \bar{u}_\psi^{(0)}(\bar{\rho})\alpha_{\mathrm{A}}\frac{\bar{\rho}}{\bar{L}} = \frac{1}{\alpha_{\mathrm{A}}}[\bar{W}_0\exp\left(-\bar{\rho}^2\right) + \bar{W}_{00}] + \frac{\alpha_{\mathrm{A}}}{\bar{L}}[1-\exp\left(-\bar{\rho}^2\right)]. \tag{4.48}$$

or

$$\bar{u}_H = \left(\frac{1}{\alpha_{\mathrm{A}}}\bar{W}_0 - \frac{\alpha_{\mathrm{A}}}{\bar{L}}\right)\exp\left(-\bar{\rho}^2\right). \tag{4.49}$$

Using relation (4.49) at $\bar{\rho} = 0$, one gets at zeroth order in ε that quantity $\bar{W}_0$ is given by

$$\boxed{\bar{W}_0 = \alpha_{\mathrm{A}}\bar{u}_H^{(0)}(0) + \frac{\alpha_{\mathrm{A}}^2}{\bar{L}}.} \tag{4.50}$$

The latter term is originally presented at $O(\varepsilon)$ [Blanco-Rodríguez et al., 2015]. However it was found numerically, that taking this term into account at main order, a better fit of the numerical data is obtained,56 as shown in section 4.5 (see figure 4.12 as a example). For a thin core, the constant $\bar{W}_0$ can be related to the base state prescribed parameters

$$\bar{W}_B = \frac{\alpha_{\mathrm{A}}^2}{\pi}\iint_{\Pi_0}\bar{u}_H \mathrm{d}S \approx \frac{\alpha_{\mathrm{A}}}{\pi}\iint_{\Pi_\perp}\bar{u}_H \mathrm{d}S_\perp. \tag{4.51}$$

Performing the integration using the relation (4.49) yields

$$\boxed{\bar{W}_0 \approx \bar{W}_B + \frac{\alpha_\mathrm{A}^2}{\bar{L}}.} \tag{4.52}$$

The other velocity $\bar{W}_{00}$ is obtained by matching the constant introduced in (4.12):

$$\bar{C} = \frac{2\pi a C}{\Gamma} = \frac{1}{\bar{L}} + \bar{U}_z^{\infty(\mathrm{T})} \tag{4.53}$$

to the value reached by $\bar{u}_B/\alpha$ outside the vortex. Since for $\bar{\rho} \to \infty$, expression (4.48) tends to $\bar{W}_{00}/\alpha_\mathrm{A} + \alpha_\mathrm{A}/\bar{L}$, the matching yields

$$\boxed{\bar{W}_{00} = \alpha_\mathrm{A}\left(\bar{C} - \frac{\alpha_\mathrm{A}}{\bar{L}}\right) = \alpha_\mathrm{A}\bar{U}_z^{\infty(\mathrm{T})} + \frac{\alpha_\mathrm{A}(1-\alpha_\mathrm{A})}{\bar{L}}.} \tag{4.54}$$

In [Blanco-Rodríguez et al., 2015], the simplified expression $\bar{W}_{00} = \alpha_A U_z^{\infty(\mathrm{T})}$ was used. As above the latter term for W_0, the new expression (4.54) better agrees with the numerical results as shown in section 4.5. Since the base state is computed with $\bar{U}_z^{\infty} = 0$, one deduces $\bar{U}_z^{\infty(\mathrm{T})} = -\bar{U}_0 = \bar{\Omega}_0\bar{L}$. The constant $\bar{W}_{00}$ is expressed also as

$$\boxed{\bar{W}_{00} = \alpha_\mathrm{A}\bar{\Omega}_0\bar{L} + \frac{\alpha_\mathrm{A}(1-\alpha_\mathrm{A})}{\bar{L}}.} \tag{4.55}$$

The evaluation of $\bar{W}_{00}$ requires the knowledge of $\bar{\Omega}_0$. Here we deduce this quantity from the DNS results in a quite accurate way. We could have also used a theoretical evaluation [Okulov, 2004].

Order ε

Going now to order ε, the perturbation is purely dipolar [Blanco-Rodríguez et al., 2015]:

$$\bar{u}_\rho^{(1)} = -\frac{\bar{\Psi}^{(1)}}{\bar{\rho}}\sin\psi\,, \quad \bar{u}_\psi^{(1)} = \left[\bar{\rho}\bar{u}_\psi^{(0)} - \frac{\mathrm{d}\bar{\Psi}^{(1)}}{\mathrm{d}\bar{\rho}}\right]\cos\psi\,, \tag{4.56}$$

$$\bar{u}_b^{(1)} = \left[\bar{\rho}\bar{u}_b^{(0)} - \frac{1}{\bar{u}_\psi^{(0)}}\frac{\mathrm{d}\bar{u}_b^{(0)}}{\mathrm{d}\bar{\rho}}\bar{\Psi}^{(1)}\right]\cos\psi\,, \tag{4.57}$$

where the first order streamfunction perturbation $\bar{\Psi}^{(1)}(\bar{\rho})$ satisfies

$$\bar{\Psi}^{(1)} = \bar{\Psi}_0^{(1)} + \bar{W}_0^2\bar{\Psi}_1^{(1)} + \bar{W}_{00}\bar{W}_0\bar{\Psi}_2^{(1)}.$$

The three contributions $\bar{\Psi}_0^{(1)}$, $\bar{\Psi}_1^{(1)}$ and $\bar{\Psi}_2^{(1)}$ are solutions of

$$\mathcal{L}\bar{\Psi}_0^{(1)} = \bar{K}_0\,, \quad \mathcal{L}\bar{\Psi}_1^{(1)} = \bar{K}_1\,, \quad \mathcal{L}\bar{\Psi}_2^{(1)} = \bar{K}_2\,, \tag{4.58}$$

where the linear operator $\mathcal{L}(\bullet)$ is defined as:

$$\mathcal{L}(\bullet) \equiv \frac{\partial^2(\bullet)}{\partial\bar{\rho}^2} + \frac{1}{\bar{\rho}}\frac{\partial(\bullet)}{\partial\bar{\rho}} - \left(\frac{1}{\bar{\rho}^2} + H_0(\bar{\rho})\right)(\bullet) \tag{4.59}$$

and

$$\begin{aligned}
\bar{H}_0(\bar{\rho}) &\equiv \frac{1}{\bar{u}_\psi^{(0)}}\frac{\mathrm{d}\bar{\omega}_B{}^{(0)}}{\mathrm{d}\bar{\rho}} = \frac{-4\bar{\rho}^2}{\exp(\bar{\rho}^2)-1}, \\
\bar{K}_0(\bar{\rho}) &\equiv 2\bar{\rho}\bar{\omega}_b^{(0)} + \bar{u}_\psi^{(0)} = \frac{1-\exp(-\bar{\rho}^2)}{\bar{\rho}} + 4\bar{\rho}\exp(-\bar{\rho}^2), \\
\bar{K}_1(\bar{\rho}) &\equiv -\frac{4\bar{\rho}^3}{\exp(\bar{\rho}^2)-1}\exp(-\bar{\rho}^2), \quad \bar{K}_2(\bar{\rho}) \equiv -\frac{4\bar{\rho}^3}{\exp(\bar{\rho}^2)-1}.
\end{aligned} \tag{4.60}$$

The boundary conditions at $\bar{\rho} = 0$ are

$$\bar{\Psi}_i^{(1)}(0) = 0, \quad \frac{\partial\bar{\Psi}_i^{(1)}}{\partial\bar{\rho}}(0) = 0, \quad i = 0,1,2. \tag{4.61}$$

We hence compute the first order streamfunction perturbation $\bar{\Psi}^{(1)}$ numerically. For large $\bar{\rho}$, $\bar{\Psi}^{(1)}(\rho)$ expands as [Fukumoto and Miyazaki, 1991]:

$$\bar{\Psi}^{(1)}(\bar{\rho}) \sim \frac{1}{2}\bar{\rho}\log\bar{\rho} + \bar{\rho}\bar{A} + O(\frac{1}{\bar{\rho}}),$$

where

$$\bar{A} = \frac{1}{4}[1 - \bar{W}_0(\bar{W}_0 + 4\bar{W}_{00}) + \gamma - \log 2], \quad \gamma \approx 0.577.$$

This formula corrects the typo $2\bar{W}_{00}$ in equation (3.12) of [Blanco-Rodríguez et al., 2015].

4.5 Helical base states

All variables are again put in dimensionless form using as characteristic dimensional length scale $[L] = r_\mathrm{A}$ and time scale $[T] = r_\mathrm{A}^2/\Gamma$ of the ***final* state**. For a helical vortex of reduced pitch L, the dimensionless curvature $\kappa = 1/(1+L^2)$ decreases from 1 to 0 as L increases from 0, while dimensionless torsion τ first increases from 0 to 0.5 (reached for $L = 1$), and then slowly decreases to 0 (see figure 4.10). In the asymptotic theory presented in 4.4, we used parameter $\varepsilon \equiv a\kappa$ to quantify the curvature effects on a straight axisymmetric vortex. A given value of ε can be achieved from different pair values (L, a), thus corresponding to different curvature and torsion levels.

We choose five helical vortex states which are presented in table 4.2. The first three states correspond to the same value $\varepsilon = 0.1$. States BS1, BS2 are characterized by the same strain $\varepsilon = 0.1$ and inverse swirl parameter $\bar{W}_B$ but different pitch L and core size a: for BS1 relatively small values leading to high curvature and low torsion, for BS2 larger values leading to low curvature but near-maximum torsion. State BS3 is the same as BS1 except that the inverse swirl parameter $\bar{W}_B$ is twice as much that of BS1. State BS4 is identical to BS3 a state with a larger core size a hence a larger strain $\varepsilon = 0.16$. State BS5 is similar to BS4,

yet with reversed axial flow (hence negative inverse swirl). In the following, the base states are also named under the form $[L;\ a;\ \bar{W}^B]$ where L, a and $\bar{W}^B$ are the dimensionless prescribed parameters.

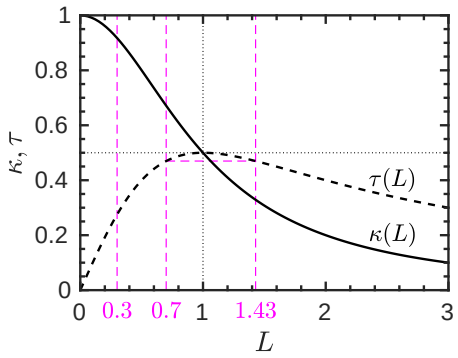

Figure 4.10 – Non-dimensional curvature κ (solid line) and torsion τ (black dashed line) as functions of the reduced pitch L. Pitches L and $1/L$ lead to the same value of the torsion but to different curvature levels, as illustrated for $L = 0.7$ and $1/0.7 \approx 1.43$.

case	ε	κ	τ
BS1 = [0.3 ; 0.11 ; 0.2]	0.1	0.92	0.28
BS2 = [1.43; 0.3 ; 0.2]	0.1	0.33	0.47
BS3 = [0.3 ; 0.11 ; 0.4]	0.1	0.92	0.28
BS4 = [0.3 ; 0.174; 0.4]	0.16	0.92	0.28
BS5 = [0.3 ; 0.174;-0.4]	0.16	0.92	0.28

Table 4.2 – Base states $[L;\ a;\ \bar{W}^B]$ with corresponding parameter ε, curvature κ and torsion τ.

Quasi-equilibrium states listed in table 4.2 are obtained as final states of simulations through the procedure explained in section 4.3. For each state, there exists an inertial frame of reference (T) in which the helical vortex is steady. In that frame, the helical vortex is located around a centre line $\boldsymbol{x}_0(\theta_s) = r_\mathrm{A}\boldsymbol{e}_r(\theta_s) + L\theta_s\boldsymbol{e}_z$ where θ_s is a continuous parameter, with associated tangent vector

$$\boldsymbol{e}_b \equiv \boldsymbol{e}_{B_\mathrm{A}} = \alpha_\mathrm{A}\left[\frac{r_\mathrm{A}}{L}\boldsymbol{e}_\theta(\theta_s) + \boldsymbol{e}_z\right]. \tag{4.62}$$

For a helical vortex filament, the velocity and vorticity fields are given by their distribution around the centerline in the plane $\Pi_\perp(\mathrm{A})$. Figure 4.11a (resp. figure 4.11b) shows the axial vorticity in the plane $\Pi_\perp$ for BS1 (resp. BS2).

The internal structure computed by Helix DNS code can be compared to the results obtained by the asymptotic theory presented in section 4.4. One needs to rewrite the Helix results by

1. Performing the transformation $u_B \longrightarrow u_B - \alpha U_0$ and $u_\varphi \longrightarrow u_\varphi + \alpha U_0 r/L$ to adopt the frame (T) translating at velocity $U_0\boldsymbol{e}_z$ with the vortex.
2. Computing the velocity field onto the plane $\Pi_\perp(\mathrm{A})$ and expressing its components (u_ρ, u_ψ, u_b) in the cylindrical basis used in the theory. The procedure is explained in Appendix A.1.

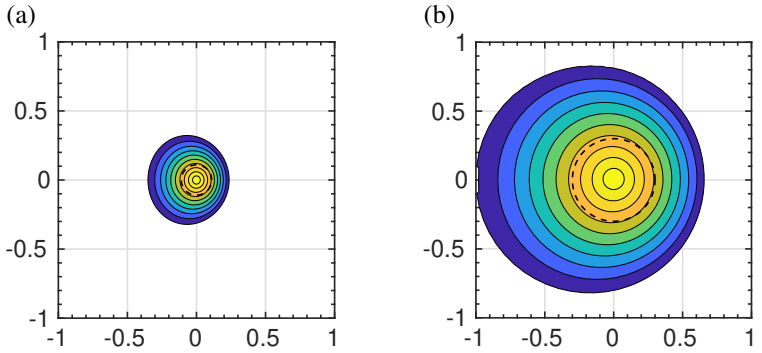

Figure 4.11 – (a) Contours of ω_B in plane $\Pi_\perp$ for the quasi-equilibrium state BS1. (b) Same for BS2, with the same spatial range represented. Contour levels are as in figure 4.3. The Reynolds number is $Re_{\rm DNS} = 2\pi 10^4$, and the simulation time $T_{\rm sim} = 20$ (resp. 100) for BS1 (resp. BS2).

	prescribed core size	Helix DNS results			Theory	
case	a	a_0	$\bar{W}_0$	$\bar{W}_{00}$	$\bar{W}_0$	$\bar{W}_{00}$
BS1	0.110	0.1108	0.2293	0.0057	0.230	0.0059
BS2	0.300	0.3001	0.3421	−0.1017	0.341	−0.1108
BS3	0.110	0.1109	0.4271	0.0071	0.430	0.0069
BS4	0.174	0.1767	0.4419	0.0289	0.448	0.0255
BS5	0.174	0.1730	−0.3524	0.0262	−0.352	0.0238

Table 4.3 – For helical vortex states BS1–BS5: prescribed parameter a ; effective core size a_0; $\bar{W}_0$ and $\bar{W}_{00}$ computed using Helix DNS results; theoretical values $\bar{W}_0$ and $\bar{W}_{00}$ obtained through (4.52) and (4.55).

3. Performing an azimuthal decomposition of such components

$$u^{(m)}_{\rho,\psi,b}(\rho_i) = \frac{1}{N_\psi}\sum_{j=1}^{N_\psi} u_{\rho,\psi,b}(\rho_i,\psi_j)\mathrm{e}^{-\mathrm{i}m\psi_j} \qquad (i = 1,\cdots,N_\rho) \tag{4.63}$$

   where (ρ_i,ψ_j) are the locations of $N_\rho \times N_\psi$ nodes of a polar mesh in plane $\Pi_\perp$;
4. Using the same nondimensionalization units as in the theory that is using the reference scales a_0 and $2\pi a_0^2/\Gamma$ where the value a_0 is obtained using a Gaussian fit of the axisymmetric component of fields u_H.

Based on the above procedure, the parameters presented in table 4.2 correspond to the values of effective core size a_0, inverse swirl $\bar{W}_0$ and constant $\bar{W}_{00}$ reported in table 4.3. Comparisons between asymptotic theory and internal structure of base states found by DNS of helical vortices are shown in figures 4.12–4.13. The adequacy of the asymptotic theory up to relatively large values of ε (for BS5 $\varepsilon = 0.16$) is shown : the contributions $m = 0$ to $(u^{(m)}_\rho, u^{(m)}_\psi, u^{(m)}_b)$ are plotted and excellent agreement is found for the axisymmetric part. A fairly small mismatch subsists for components $m = 1$.

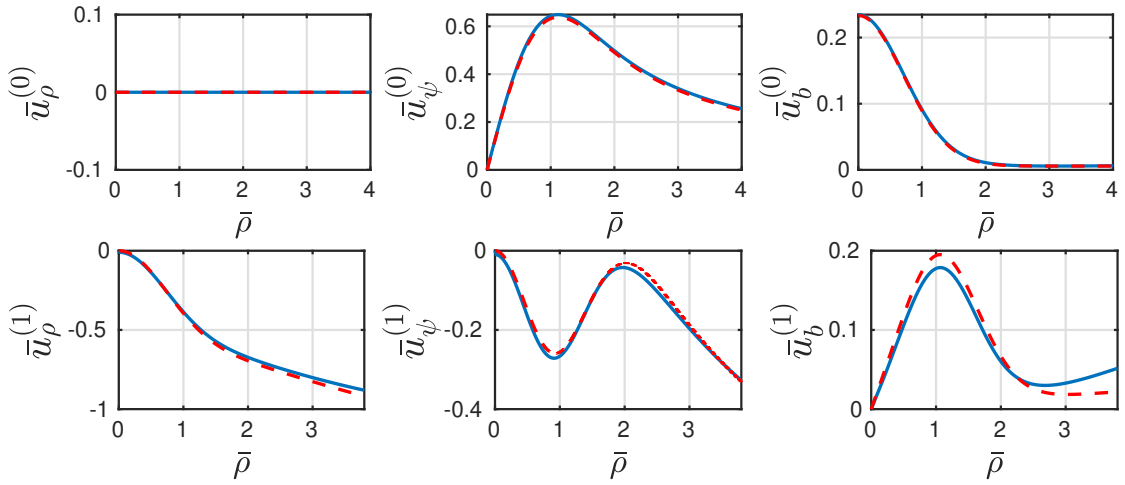

Figure 4.12 – Case BS1: radial distributions of velocity components $(\bar{u}_\rho^{(m)}, \bar{u}_\psi^{(m)}, \bar{u}_b^{(m)})$ for $m = 0$ (top) and $m = 1$ (bottom). Blue solid line: DNS results; red dashed line: theory.

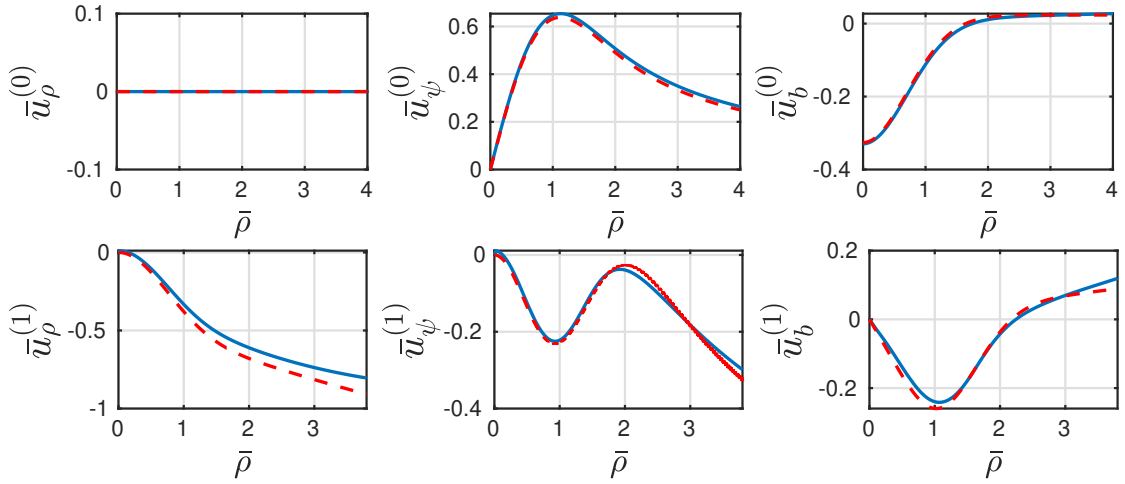

Figure 4.13 – Same as figure 4.12 for case BS5.

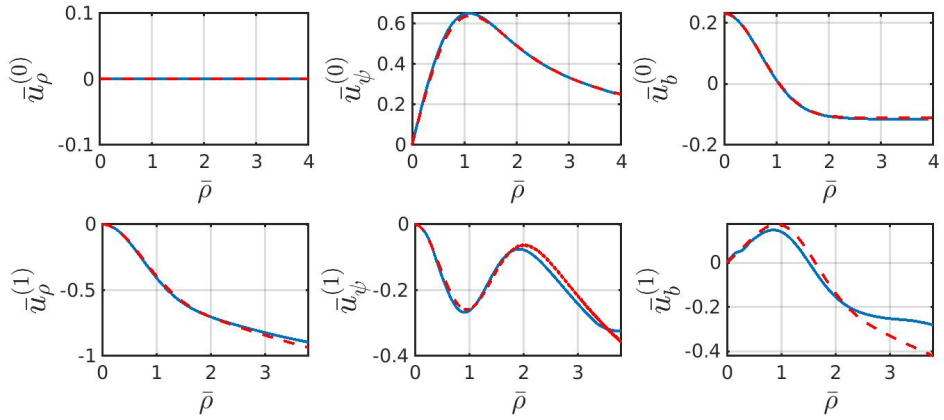

Figure 4.14 – Same as figure 4.12 for case BS2.

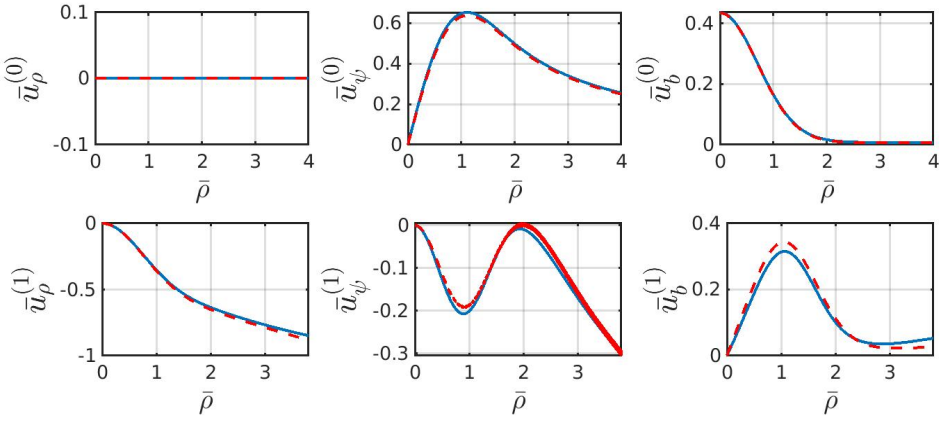

Figure 4.15 – Same as figure 4.12 for case BS3.

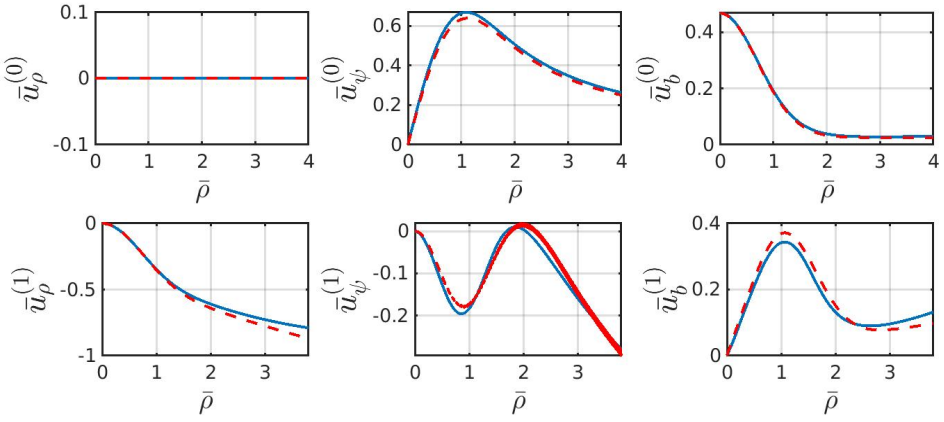

Figure 4.16 – Same as figure 4.12 for case BS4.

4.6 Effect of large axial flow

When a moderate axial flow is present in a helical vortex, a quasi-equilibrium can be reached, that can be linked to an equilibrium of a family of inviscid helical flows. We have exhibited the constraints of such equilibria: equations (4.16) extend formulae known for vortex rings. Such constraints are confirmed in the framework of quasi-equilibria of a single helical vortex with axial flow computed by DNS. When $\bar{W}_B$ is increased, the possibility of a quasi-equilibrium state disappears. There is a threshold above which centrifugal forces cannot be counter-balanced by swirl. This phenomenon has been studied in vortex rings by [Cheng et al., 2010].

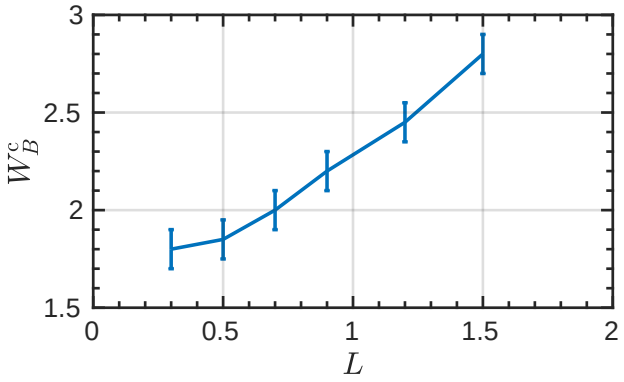

Figure 4.17 – Axial flow critical level $\bar{W}_B^c(L)$ above which the initial condition does not relax towards a quasi-steady equilibrium. Simulations with $a^\star = 0.11$, $Re_{\mathrm{DNS}} = 2\pi 10^3$ and $T_{\mathrm{sim}} = 4$.

The procedure to reach the quasi-equilibrium relies on the assumption that the initial condition rapidly relaxes towards a quasi-equilibrium. However, when the axial flow becomes large, such an equilibrium ceases to exist because the swirling motion can no more counter-balance the centrifugal forces generated by axial velocity in the curved vortex. In terms of vorticity, negative helical vorticity emerges and may persist over large evolution times. We can define a threshold value $\bar{W}_B^c$ above which negative vorticity is still present at $t = T_{\mathrm{sim}}$ (here $T_{\mathrm{sim}} = 4$ at $Re_{\mathrm{DNS}} = 2\pi 10^3$). In figure 4.17, we present the evolution of this threshold $\bar{W}_B^c$ as a function of the helical pitch starting the simulation with a fixed initial core size $a^\star = 0.11$. For given L and $\bar{W}_B < \bar{W}_B^c(L)$, the simulation converges towards a quasi-equilibrium state as shown in figure 4.18a. For $\bar{W}_B > \bar{W}_B^c(L)$, the system does not rapidly reach such an equilibrium (figure 4.18b). A dipolar structure can even emerge, as illustrated in figure 4.19. This phenomenon is similar to what is observed in vortex rings by [Cheng et al., 2010] when the axial flow becomes significant. Note also that the threshold value shown in figure 4.17 pinpoints the existence of an equilibrium up to relatively large values of $\bar{W}_B$. However, we suspect this helical equilibrium state to be itself unstable with respect to the swirling jet instability that occurs as soon as $\bar{W}_B > 0.7$ for a straight Batchelor vortex [Lessen et al., 1974, Mayer and Powell, 1992]. In our simulations, enforcing the helical symmetry filters out such instabilities.

In the present study, the method and the data are presented in the case of a single helical vortex. This could be easily extended to an arbitrary number of vortices with same pitch in quasi-equilibrium arrangement. These states are of great significance for helical vortex instability studies, e.g. in the wake of wind turbines, marine propellers, helicopter rotors... Let us stress the importance of monitoring the axial

(a)

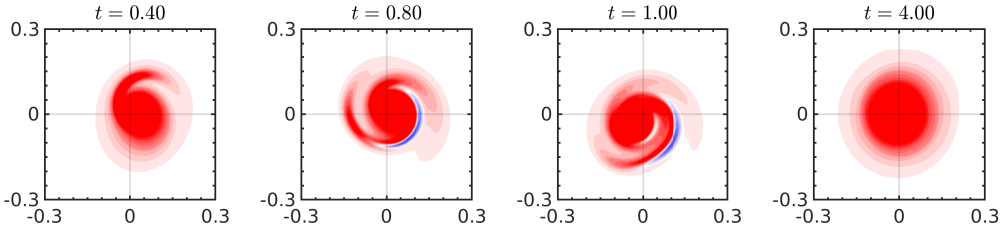

(b)

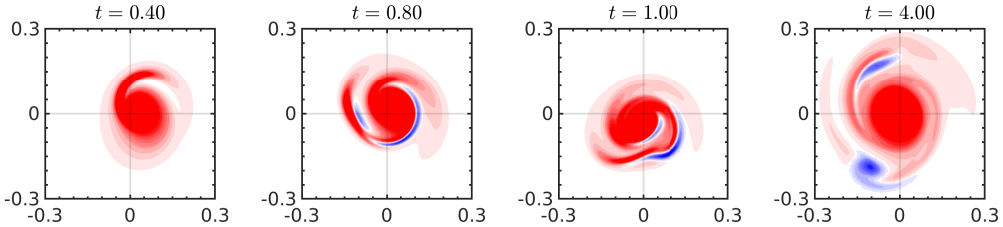

Figure 4.18 – Time evolution of a helical vortex at $L = 0.3$, $a^\star = 0.11$ and $Re_{\mathrm{DNS}} = 2\pi 10^3$ with axial flow (a) $\bar{W}_B = 1.8$ (below the critical threshold) and (b) $\bar{W}_B = 1.9$ (above it). Contours of $\omega_b/\omega_{b\max}$ in plane $\Pi_\perp(t)$. Contour levels are regularly spaced in the range $[-1/e, 1/e]$ (from blue to red).

velocity in such vortices, since curvature and elliptic short-wave instabilities crucially depend on the swirl parameter [Hattori and Fukumoto, 2014]. In this perspective, the present work provides a procedure to generate basic states with prescribed values of the numerous parameters characterizing the helical vortex, namely circulation, helix radius, helix pitch, vortex core size, swirl level.

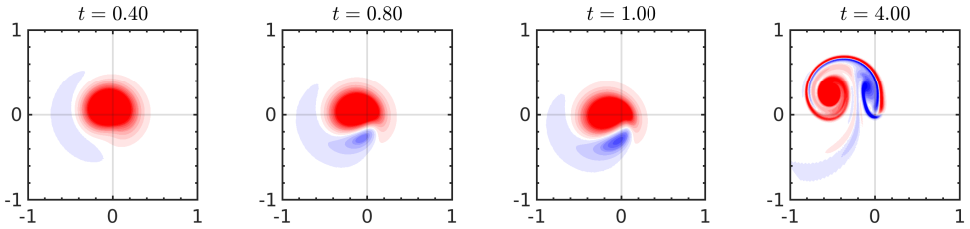

Figure 4.19 – Time evolution of a helical vortex at $L = 1.43$, $a^\star = 0.3$ and $Re_{\mathrm{DNS}} = 2\pi 10^3$ with axial flow $\bar{W}_B = 4.0$ (above the threshold) . Contours are as in figure 4.18.

Chapter 5

Stability equations

Contents

In the chapter 4, we obtained the helically symmetric quasi-equilibrium states with a jet inside the vortex core. From now, we study the stability properties of such flows by adding small amplitude perturbations, which depend on r, φ, and also on z. This topic has already been studied by [Selçuk, 2016] in the context of very weak jet component. In the present work, we study helical vortices with larger jet in the core.

5.1 Governing equation for infinitesimal perturbations

The base states found in chapter 4 represent helical vortices characterized by a circulation Γ and an external velocity U_z^∞ in the laboratory frame ($\mathrm{L_B}$). In the computations, we set the fluid velocity at infinity to be zero $U_z^\infty = 0$: the laboratory frame ($\mathrm{L_B}$) and the frame ($\mathrm{L_0}$) are thus identical. In such a reference frame, the base states are rotating with a constant angular velocity $\Omega_0 \boldsymbol{e}_z$ along the z axis. In the translating frame (T) or in the rotating frame (R), such base states become steady. We could write the stability equations in one of these two frames: here we choose the rotating frame (R) mainly for “historical" reasons.

The stability governing equations are put in dimensionless form using as characteristic scales and Reynolds

number

$$[\mathrm{L}] = r_A\,, \quad [\mathrm{T}] = \frac{r_A^2}{\Gamma}\,, \quad \text{and} \quad Re_{\mathrm{DNS}} = \frac{\Gamma}{\nu}. \tag{5.1}$$

In the rotating frame (R), velocity and vorticity fields of the base state are such that

$$\boldsymbol{u}^{\mathrm{BF}}(r,\varphi) \equiv \left(u_r^{\mathrm{BF}}(r,\varphi), u_\theta^{\mathrm{BF}}(r,\varphi), u_z^{\mathrm{BF}}(r,\varphi)\right), \quad \boldsymbol{\omega}^{\mathrm{BF}}(r,\varphi) \equiv \left(\omega_r^{\mathrm{BF}}(r,\varphi), \omega_\theta^{\mathrm{BF}}(r,\varphi), \omega_z^{\mathrm{BF}}(r,\varphi)\right), \tag{5.2}$$

and the Navier-Stokes equations become

$$\partial_t \boldsymbol{u} + \mathbf{NL} = -\boldsymbol{\nabla} G + \frac{1}{Re_{\mathrm{DNS}}}\mathbf{VT}, \quad \text{with} \quad \mathbf{NL} = \boldsymbol{\omega}\times\boldsymbol{u} + 2\Omega_0 \boldsymbol{e}_z \times \boldsymbol{u}\,, \quad \mathbf{VT} = \Delta \boldsymbol{u}\,, \tag{5.3}$$

$$\boldsymbol{\nabla}\cdot\boldsymbol{u} \equiv 0\,. \tag{5.4}$$

These fields are thereafter written as the sum of the base state and a perturbation of order ϵ with $\epsilon \ll 1$:

$$\boldsymbol{u}(r,\varphi,z,t) = \boldsymbol{u}^{\mathrm{BF}}(r,\varphi) + \epsilon \boldsymbol{u}'(r,\varphi,z,t), \tag{5.5}$$

$$\boldsymbol{\omega}(r,\varphi,z,t) = \boldsymbol{\omega}^{\mathrm{BF}}(r,\varphi) + \epsilon \boldsymbol{\omega}'(r,\varphi,z,t), \tag{5.6}$$

$$p(r,\varphi,z,t) = \Pi(r,\varphi) + \epsilon p'(r,\varphi,z,t), \tag{5.7}$$

Once the Navier-Stokes equations have been linearized, one obtains in the classical way the linear system governing perturbations that is incompressibility $\boldsymbol{\nabla}\cdot\boldsymbol{u}' = 0$ and momentum equation

$$\partial_t \boldsymbol{u}' + \underbrace{\boldsymbol{\omega}^{\mathrm{BF}}\times\boldsymbol{u}' + \boldsymbol{\omega}'\times\boldsymbol{u}^{\mathrm{BF}} + 2\Omega_0\boldsymbol{e}_z\times\boldsymbol{u}'}_{\mathbf{LNL}} = -\boldsymbol{\nabla}G' + \frac{1}{Re_{\mathrm{DNS}}}\underbrace{\Delta\boldsymbol{v}'}_{\mathbf{VT}} \quad \text{with} \quad \boxed{G' \equiv \frac{p'}{\rho} + \boldsymbol{u}^{\mathrm{BF}}\cdot\boldsymbol{u}'}\,. \tag{5.8}$$

Note that $\boldsymbol{\omega}^{\mathrm{BF}(L_0)} = \boldsymbol{\omega}^{\mathrm{BF}} + 2\Omega_0\boldsymbol{e}_z$, so that the term **LNL** can be written as

$$\boldsymbol{\omega}^{(L_0)}\times\boldsymbol{u}' + \boldsymbol{\omega}'\times\boldsymbol{u}^{\mathrm{BF}}.$$

Written in cylindrical basis $(\boldsymbol{e}_r, \boldsymbol{e}_\theta, \boldsymbol{e}_z)$ with helical coordinates, one gets the same linear operators as in section 3.1 for instance incompressibility reads:

$$\boldsymbol{\nabla}\cdot\boldsymbol{u}' = \frac{1}{r}\frac{\partial(ru_r')}{\partial r} + \frac{1}{r}\frac{\partial u_\theta'}{\partial\varphi} + \frac{\partial u_z'}{\partial z} - \frac{1}{L}\frac{\partial u_z'}{\partial\varphi} = 0\,. \tag{5.9}$$

The nonlinear terms **LNL** read

$$\mathrm{LNL}_r \equiv \omega_\theta' u_z^{\mathrm{BF}} + \omega_\theta^{\mathrm{BF}} u_z' - \omega_z' u_\theta^{\mathrm{BF}} - (\omega_z^{\mathrm{BF}} + 2\Omega_0)u_\theta'\,, \tag{5.10}$$

$$\mathrm{LNL}_\theta \equiv \omega_z' u_r^{\mathrm{BF}} + (\omega_z^{\mathrm{BF}} + 2\Omega_0)u_r' - \omega_r^{\mathrm{BF}} u_z' - \omega_r' u_z^{\mathrm{BF}}\,, \tag{5.11}$$

$$\mathrm{LNL}_z \equiv \omega_r' u_\theta^{\mathrm{BF}} + \omega_r^{\mathrm{BF}} u_\theta' - \omega_\theta' u_r^{\mathrm{BF}} - \omega_\theta^{\mathrm{BF}} u_r'. \tag{5.12}$$

Because the base state does not depend on z, t, the linear system (5.8) is not explicitly dependent on these two variables. Hence one may look for solutions under the form:

$$\begin{pmatrix} u_r' \\ u_\theta' \\ u_z' \\ G' \end{pmatrix} = \begin{pmatrix} \tilde{u}_r(r,\varphi) \\ \tilde{u}_\theta(r,\varphi) \\ \tilde{u}_z(r,\varphi) \\ \tilde{G}(r,\varphi) \end{pmatrix} \exp\left[\mathrm{i}(k_z z - \omega t)\right] \tag{5.13}$$

where the wavenumber k_z along the z-axis is real, and the complex frequency $\varpi = \omega + \mathrm{i}\sigma$ is based on the real frequency ω and growthrate σ. By introducing ansatz (5.13) into equation (5.8), we could transform these governing equations into an eigenvalue problem, providing the *complex* eigenfunctions $\tilde{u}_r$, $\tilde{u}_\theta$, $\tilde{u}_z$, $\tilde{p}$. However, the eigenvalue problem to be solved will be too large, this is why we use another procedure.

The alternative procedure consists in two steps. First, we restrict the study to a solution corresponding to given axial wavelength k_z,

$$\begin{pmatrix} u_r' \\ u_\theta' \\ u_z' \\ G' \end{pmatrix} = \begin{pmatrix} \tilde{u}_r(r,\varphi,t) \\ \tilde{u}_\theta(r,\varphi,t) \\ \tilde{u}_z(r,\varphi,t) \\ \tilde{G}(r,\varphi,t) \end{pmatrix} \exp(\mathrm{i}k_z z). \tag{5.14}$$

Second, we simulate equations (5.8) from a noisy perturbation using the code HELIKZ-LIN (see below). The idea is that the most unstable mode (that is the mode evolving with $\exp([\sigma_{\max} - \mathrm{i}\omega]t)$ where $\sigma_{\max}$ is the maximum growthrate) emerges once the system has evolved during a sufficient long time.

5.2 Simulating perturbation evolution: code HELIKZ-LIN

The assumed form (5.14) imposes the derivative $\partial/\partial z$ in the linearized Navier-Stokes equations (5.8)–(5.9) to reduce to a multiplication by $\mathrm{i}k_z$. Furthermore, quantities are 2π periodic in the φ direction and can be expanded using a Fourier decomposition along φ

$$\begin{pmatrix} \tilde{u}_r(r,\varphi,t) \\ \tilde{u}_\theta(r,\varphi,t) \\ \tilde{u}_z(r,\varphi,t) \end{pmatrix} = \sum_{m=-\infty}^{m=+\infty} \begin{pmatrix} \hat{u}_r^{(m)}(r,t) \\ \hat{u}_\theta^{(m)}(r,t) \\ \hat{u}_z^{(m)}(r,t) \end{pmatrix} \exp(\mathrm{i}m\varphi), \tag{5.15}$$

$$\tilde{G}(r,\varphi,t) = \sum_{m=-\infty}^{m=+\infty} \hat{G}^{(m)}(r,t) \exp(\mathrm{i}m\varphi). \tag{5.16}$$

Quantities $\hat{u}^{(m)}$ are complex and there is no relation between modes $\hat{u}^{(m)}$ and $\hat{u}^{(-m)}$. By introducing these relations into equations (5.8)–(5.9), one obtains for each mode m

$$\boldsymbol{\nabla} \cdot \hat{\boldsymbol{u}}^{(m)} = 0, \tag{5.17}$$

$$\frac{\partial \hat{\boldsymbol{u}}^{(m)}}{\partial t} + \mathbf{LNL}^{(m)} = -\boldsymbol{\nabla}\hat{G}^{(m)} + \frac{1}{Re_{\mathrm{DNS}}} \hat{\mathbf{V}}\mathbf{T}^{(m)}. \tag{5.18}$$

These equations are discretized in the code HELIKZ–LIN. Boundary conditions must be satisfied at $r = \infty$ (that is at some $r = R_{\mathrm{ext}}$ in practice) and $r = 0$. They are presented in Appendix B.1.

Most of the linear operators above take simpler expressions when the various fields are of the form

$$\boldsymbol{u} = \boldsymbol{u}^{(m)} \exp(\mathrm{i}(m\varphi + k_z z)) = \begin{pmatrix} \hat{u}_r^{(m)}(r,t) \\ \hat{u}_\theta^{(m)}(r,t) \\ \hat{u}_z^{(m)}(r,t) \end{pmatrix} \exp[\mathrm{i}(m\varphi + k_z z)], \quad G = \hat{G}^{(m)}(r,t) \exp[\mathrm{i}(m\varphi + k_z z)]. \tag{5.19}$$

Indeed the divergence operator becomes in modal form

$$\boldsymbol{\nabla}\cdot\boldsymbol{u} = (\boldsymbol{\nabla}\cdot\boldsymbol{u}^{(m)})\exp\left[\mathrm{i}(m\varphi + k_z z)\right], \quad \boldsymbol{\nabla}\cdot\boldsymbol{u}^{(m)} \equiv \frac{1}{r}\frac{\partial(r\hat{u}_r^{(m)})}{\partial r} - \mathrm{i}\,\frac{m}{r}\hat{u}_\theta^{(m)} + \mathrm{i}\,\beta\hat{u}_z^{(m)}, \tag{5.20}$$

with

$$\boxed{\beta(m,k_z) \equiv k_z - \frac{m}{L}.} \tag{5.21}$$

The gradient $\boldsymbol{\nabla}G$ of the scalar G becomes

$$\boldsymbol{\nabla}G = \boldsymbol{\nabla}\mathrm{G}^{(m)}\exp\left[\mathrm{i}(m\varphi + k_z z)\right], \quad \text{with} \quad \boldsymbol{\nabla}\mathrm{G}^{(m)} = \left(\frac{\partial\hat{G}^{(m)}}{\partial r},\ \frac{\mathrm{i}m}{r}\hat{G}^{(m)},\ \mathrm{i}\beta\hat{G}^{(m)}\right). \tag{5.22}$$

Similarly, the viscous operator

$$\mathrm{VT} = \mathrm{VT}^{(m)}\exp\left(\mathrm{i}(m\varphi + k_z z)\right) \tag{5.23}$$

possesses three components

$$\mathrm{VT}_r^{(m)} = \frac{\partial}{\partial r}\left(\frac{1}{r}\frac{\partial(r\hat{u}_r^{(m)})}{\partial r}\right) - \chi^2\hat{u}_r^{(m)} - \mathrm{i}\,\frac{2m}{r^2}\hat{u}_\theta^{(m)}, \tag{5.24}$$

$$\mathrm{VT}_\theta^{(m)} = \frac{\partial}{\partial r}\left(\frac{1}{r}\frac{\partial(r\hat{u}_\theta^{(m)})}{\partial r}\right) - \chi^2\hat{u}_\theta^{(m)} - \mathrm{i}\,\frac{2m}{r^2}\hat{u}_r^{(m)}, \tag{5.25}$$

$$\mathrm{VT}_z^{(m)} = \frac{1}{r}\frac{\partial}{\partial r}\left(r\frac{\partial\hat{u}_z^{(m)}}{\partial r}\right) - \chi^2\hat{u}_z^{(m)}, \tag{5.26}$$

with

$$\boxed{\chi^2(m,k_z) \equiv \frac{m^2}{r^2} + \beta^2.} \tag{5.27}$$

Finally the vorticity field is expressed as

$$\boldsymbol{\omega} = (\hat{\omega}_r^{(m)}, \hat{\omega}_\theta^{(m)}, \hat{\omega}_z^{(m)})\exp\left[\mathrm{i}(m\varphi + k_z z)\right], \tag{5.28}$$

with

$$\hat{\omega}_r^{(m)} = \frac{\mathrm{i}m}{r}\hat{u}_z^{(m)} - \mathrm{i}\,\beta\hat{u}_\theta^{(m)}, \tag{5.29}$$

$$\hat{\omega}_\theta^{(m)} = \mathrm{i}\,\beta\hat{u}_r^{(m)} - \frac{\partial\hat{u}_z}{\partial r}^{(m)}, \tag{5.30}$$

$$\hat{\omega}_z^{(m)} = \frac{1}{r}\frac{\partial}{\partial r}(r\,\hat{u}_\theta^{(m)}) - \frac{\mathrm{i}m}{r}\hat{u}_r^{(m)}. \tag{5.31}$$

In order to integrate equations (5.18), one needs to compute $\mathbf{LNL}^{(m)}$. This quantity is obtained using a pseudo-spectral method explained in Appendix B.1. In this approach, the three components (5.10)–(5.12) of **LNL** must be determined at specific locations on a grid in the physical space (r, φ). In turn, variables

(u_r, u_θ, u_z, p) of the base state and of perturbations should be evaluated at the same grid points.

5.2.1 Initial Perturbation for the code HELIKZ–LIN

Given an axial wavelength k_z, we run the code HELIKZ–LIN starting from a noisy perturbation. The initial velocity field is a complex quantity determined in several steps as follows:

1. In Fourier space, for each mode m, one computes real and imaginary radial components

$$v_r^{(m)R}(r), v_r^{(m)I}(r) = \frac{(\frac{r}{r_1})^p}{1+(\frac{r}{r_1})^p}\xi(r)M(r), \quad p = \|m|-1| \tag{5.32}$$

   real and imaginary azimuthal components

$$v_\theta^{(m)R}(r), v_\theta^{(m)I}(r) = \frac{(\frac{r}{r_1})^p}{1+(\frac{r}{r_1})^p}\xi(r)M(r), \quad p = \|m|-1| \tag{5.33}$$

   real and imaginary axial components

$$v_z^{(m)R}(r), v_z^{(m)I}(r) = \frac{(\frac{r}{r_1})^p}{1+(\frac{r}{r_1})^p}\xi(r)M(r), \quad p = |m| \tag{5.34}$$

   where function $\xi(x)$ denotes a noisy signal with a probability density function uniform on the interval $x \in [-\frac{1}{2}, \frac{1}{2}[$ and function $M(r) = \exp(-(\frac{r}{r_2})^6)$ is a mask function. Parameter r_1 (resp. r_2) is chosen as $r_1 = 0.5$ (resp. $r_2 > r_1$, is chosen to be smaller than radius of the outer boundary $r = R_{ext}$) to ensure the correct behavior near $r = 0$ (resp. to avoid noise near the outer boundary and to ensure zero circulation at "infinity").
2. One transforms these complex fields into the physical space, and multiplies them by a smooth function $g(x, y)$ which is non-zero in the rotational area of the base state $\boldsymbol{\omega}^{\mathrm{BF}(L_0)}$. More precisely this function is built so that it remains smooth and

$$g(x,y) \quad \text{is based on spline functions} \quad \text{when} \quad |\frac{\omega^{\mathrm{BF}(L_0)}(x,y)}{\omega_{\max}^{\mathrm{BF}(L_0)}}| \in [0.01, 0.1] \tag{5.35}$$

$$g(x,y) = 0 \quad \text{when} \quad |\frac{\omega^{\mathrm{BF}(L_0)}(x,y)}{\omega_{\max}^{\mathrm{BF}(L_0)}}| < 0.01\,, \quad g(x,y) = 1 \quad \text{when} \quad |\frac{\omega^{\mathrm{BF}(L_0)}}{\omega_{\max}^{\mathrm{BF}(L_0)}}| > 0.1\,. \tag{5.36}$$

3. One transforms back into spectral space. At this point the divergence is not zero.
4. One performs a standard projection step to enforce zero divergence and to satisfy boundary conditions at $r = \infty$ (that is $r = R_{ext}$ in practice) and $r = 0$. Note that this step uses a gradient field which is not singular. As a consequence, the circulation is not modified.

Figure 5.1 presents an example of initial condition in the Π_0 plane with $R_{\mathrm{ext}} = 2$, $N_r = 1024$ and $N_\theta = 256$. The perturbation outside the vortex region is principally in a corona. This is due to the numerical error generated by the back and forth transform from spectral space to physical space. The perturbation amplitude in the corona however is of order 10^{-3} compared to the one in the vortex region. The time evolution using the code HELIKZ–LIN is shown in figure 5.2 for a case of short wavelength instability mode of $k_z = 19.9$.

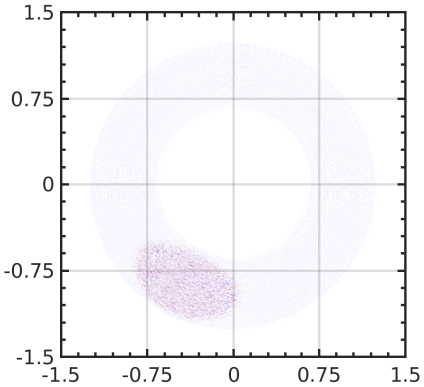

Figure 5.1 – An example of initial perturbation: the real part of axial vorticity ω'_B is displayed in the Π_0 plane for base state $[0.7; 0.15; 0.13]$.

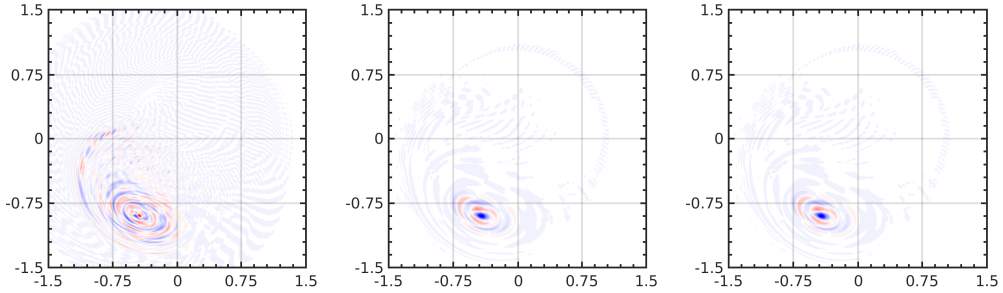

Figure 5.2 – The same perturbation as in figure 5.1, at (left) $t = 10$, (center) $t = 30$ and (right) $t = 100$.

5.3 Linear stability : the studied base states

Chapters 6-7 investigate the linear stability of several base states which are listed in table 5.1. This table presents the same quantities as tables 4.2–4.3, and cases BS1 and BS3 present in 4.2–4.3 are recalled.

In chapter 4, base states were computed with prescribed parameters, using an iterative process and the code HELIX. The stability study however is written in primitive variables, we hence need base states in primitive variables (u_r, u_θ, u_z, p). These quantities could be computed from the fields Ψ, u_H and ω_B obtained by HELIX for the final state BS_i. Because of truncation errors, however, this generates spurious effects. To avoid such problems, we proceed as follows : (1) we run the iterative loop with the code HELIX as previously and obtain the adequate set ($a^\star$, $r^\star$); (2) instead of running HELIX with the initial condition (named IC_i) corresponding to this set ($a^\star$, $r^\star$), we compute (u_r, u_θ, u_z, p) from IC_i and run another code in primitive variables (see below) for the identical simulation time T_{sim}. This procedure generates the final base state (5.2) in primitive variables without spurious effects.

L	a	$\breve{W}_B$	ε	κ	τ	$\breve{W}_0$	$\breve{W}_{00}$
0.3	0.110	−0.03	0.1	0.917	0.275	0.00	0.0054
		0.00				0.03	0.0055
		0.17				0.20	0.0058
		−0.26				−0.23	0.0058
		0.20				0.23	0.0059
		0.37				0.40	0.0067
0.4	0.116	−0.24	0.1	0.862	0.435	−0.20	−0.0112
		0.16				0.20	−0.0117
0.5	0.125	−0.25	0.1	0.800	0.400	−0.20	−0.0262
		0.15				0.20	−0.0117
0.6	0.136	−0.26	0.1	0.735	0.441	−0.20	−0.0396
		0.14				0.20	−0.0416
0.7	0.15	0.13	0.1	0.671	0.470	−0.20	−0.0523
		−0.27				0.20	−0.0545
		0.20				0.27	−0.0544
		0.25				0.32	−0.0541

Table 5.1 – In addition to $\Gamma = 1$ and $r_A = 1$, prescribed dimensionless parameters of the base states used for linear stability analysis. The two last columns provide the theoretical values given by equations (4.52) and (4.55).

5.3.1 Computing the base state in primitive variables: code HELIKZ–NL

For flows with strict *helical symmetry* of *helical pitch* $2\pi L$, the velocity components or the scalar field written in helical coordinates do not depend on z. As a consequence, the derivative of $\partial/\partial z$ in the Navier-Stokes equations written in helical coordinates disappears. These equations can be solved using the spectral representation in which quantities are Fourier decomposed along φ

$$\boldsymbol{u}(r,\varphi,t) = \begin{pmatrix} u_r(r,\varphi,t) \\ u_\theta(r,\varphi,t) \\ u_z(r,\varphi,t) \end{pmatrix} = \sum_{m=-\infty}^{m=+\infty} \boldsymbol{u}^{(m)}(r,t)\exp(\mathrm{i}m\varphi) = \sum_{m=-\infty}^{m=+\infty} \begin{pmatrix} \hat{u}_r^{(m)}(r,t) \\ \hat{u}_\theta^{(m)}(r,t) \\ \hat{u}_z^{(m)}(r,t) \end{pmatrix} \exp(\mathrm{i}m\varphi), \tag{5.37}$$

$$G(r,\varphi,t) = \sum_{m=-\infty}^{m=+\infty} G^{(m)}(r,t)\exp(\mathrm{i}m\varphi). \tag{5.38}$$

The base state field being real, it must satisfy

$$[\hat{u}_j^{(-m)}(r,t)]^* = \hat{u}_j^{(m)}(r,t) \quad j = r,\theta,z, \quad [\hat{G}^{(-m)}(r,t)]^* = \hat{G}^{(m)}(r,t), \tag{5.39}$$

where symbol $*$ means complex conjugate. By introducing relations (5.37)–(5.38) into equations (3.4)–(3.5) one obtains for each mode m

$$\boldsymbol{\nabla}\cdot\boldsymbol{u}^{(m)} = 0, \tag{5.40}$$

$$\frac{\partial \boldsymbol{u}^{(m)}}{\partial t} + \mathbf{NL}^{(m)} = -\boldsymbol{\nabla}G^{(m)} + \frac{1}{Re_{\mathrm{DNS}}}\mathbf{VT}^{(m)}, \tag{5.41}$$

where the linear operators are those defined as in section 5.2 but with $k_z = 0$, that is

$$\boxed{\beta(m) \equiv -\frac{m}{L}, \quad \chi^2(m) \equiv \frac{m^2}{r^2} + \beta^2.} \tag{5.42}$$

In addition, one computes $\mathbf{NL}^{(m)}$ by a pseudo-spectral method: the nonlinear term $\boldsymbol{\omega} \times \boldsymbol{u}$ is determined in the physical space and then projected on mode m. This procedure is discussed in Appendix B.1. The projection $\mathrm{PSM}^{(m)}$ on the mode m yields

$$\mathrm{NL}_r^{(m)} = \mathrm{PSM}^{(m)}\left(\omega_\theta u_z - \omega_z u_\theta\right), \tag{5.43}$$

$$\mathrm{NL}_\theta^{(m)} = \mathrm{PSM}^{(m)}\left(\omega_z u_r - \omega_r u_z\right), \tag{5.44}$$

$$\mathrm{NL}_z^{(m)} = \mathrm{PSM}^{(m)}\left(\omega_r u_\theta - \omega_\theta u_r\right). \tag{5.45}$$

These equations are discretized and forms the code HELIKZ–NL. The base state is computed in the frame $(\mathrm{L}_0) = (\mathrm{L}_\mathrm{B})$ using HELIKZ, which gives $\boldsymbol{u}^{(L_0)}$. It is then expressed in the rotating frame (R) inside HELIKZ–LIN by equation:

$$\boldsymbol{u}^{\mathrm{BF}} = \boldsymbol{u}^{(L_0)} - \Omega_0 r \boldsymbol{e}_\theta. \tag{5.46}$$

5.3.2 Checking the base states: comparison between HELIX and HELIKZ–NL

prescribed parameters			HELIX DNS results			
L	a	$\bar{W}^B$	Γ	Ω_0	a_0	$\bar{W}_0$
0.3	0.110	−0.03	1.0245	−0.0892	0.1102	0.0006
		0.00	1.0234	−0.0893	0.1103	0.0274
		0.17	1.0231	−0.0896	0.1107	0.1996
		−0.26	1.0062	−0.0879	0.1097	−0.2304
		0.20	1.0231	−0.0896	0.1108	0.2293
		0.37	1.0230	−0.0892	0.1112	0.3967
0.4	0.116	−0.24	1.0131	−0.0607	0.1151	−0.2019
		0.16	1.0143	−0.0117	0.1160	0.2004
0.5	0.125	−0.25	1.0086	−0.0492	0.1249	−0.1999
		0.15	1.0078	−0.0508	0.1264	0.1992
0.6	0.136	−0.26	1.0059	−0.0423	0.1358	−0.2004
		0.14	1.0056	−0.0439	0.1373	0.2000
0.7	0.15	−0.27	1.0046	−0.0385	0.1493	−0.2010
		0.13	1.0043	−0.0406	0.1517	0.2006
		0.20	1.0042	−0.0407	0.1521	0.2698
		0.25	1.0041	−0.0406	0.1524	0.3179

Table 5.2 – HELIX DNS results of base states $[L; a; \hat{W}^B]$ (prescribed parameters in table 5.1).

In chapter 4, for a given set of prescribed parameter $[L; a; \hat{W}^B]$, we get a set of $(a^\star, r^\star)$ for initial conditions (4.19). The simulation is then performed over a time T_{sim} using both codes HELIX or HELIKZ–NL. In table 5.2 (resp. table 5.3), we give the total circulation Γ, that is the integral of ω_z over the plane Π_0, the angular velocity Ω_0 in each simulation. We provide also other characteristic values of the quasi-equilibrium states obtained by HELIX (resp. HELIKZ-NL). Namely we compute the location where vorticity field

prescribed parameters			HELIKZ–NL DNS results			
L	a	$\bar{W}^B$	Γ	Ω_0	a_0	$\bar{W}_0$
0.3	0.110	−0.03	1.0240	−0.0893	0.1102	−0.005
		0.00	1.0095	−0.0887	0.1108	0.0294
		0.17	1.0228	−0.0898	0.1108	0.1997
		−0.26	1.0232	−0.0881	0.1098	−0.2308
		0.20	1.0232	−0.0887	0.1108	0.2294
		0.37	1.0226	−0.0893	0.1112	0.3969
0.4	0.116	−0.24	1.0132	−0.0635	0.1153	−0.2023
		0.16	1.0127	−0.0623	0.1161	0.2007
0.5	0.125	−0.25	1.0085	−0.0495	0.1250	−0.2003
		0.15	1.0072	−0.0511	0.1265	0.1993
0.6	0.136	−0.26	1.0058	−0.0427	0.1358	−0.2004
		0.14	1.0055	−0.0443	0.1372	0.1997
0.7	0.15	−0.27	1.0041	−0.0392	0.1493	−0.2010
		0.13	1.0039	−0.0414	0.1518	0.2010
		0.20	1.0038	−0.0414	0.1520	0.2687
		0.25	1.0032	−0.0414	0.1522	0.3156

Table 5.3 – HELIKZ–NL base flows $[L; a; \hat{W}^B]$ with prescribed parameters.

$\omega_{B\max}$ reaches its maximum. This point is chosen as the point that defines a plane $\Pi_\perp$ orthogonal to the helix located at this point. We then calculate on $\Pi_\perp$ a core size a_0 and an axial flow parameter $\bar{W}_0$ of the axisymmetric part of u_H. The comparison between both simulations indicates that the base state at T_{sim} is very similar as shown by comparing table 5.2 obtained via the code HELIX and table 5.3 obtained via HELIKZ-NL, and hence fits our requirements.

5.3.3 Comparison of base states in spectral space

In the previous section 5.3.2, we compared the base states obtained by HELIX and HELIKZ-NL in physical space with the core size of vortex, the position of maximum vorticity and some other parameters. In this section, we redid the comparison of two basic states in the spectral space, with methods described in appendix B, which allow to compare the basic states mode by mode.

The dependence of the convergence of the base state on the azimuthal discretization number N_θ was first studied with the base flow $[0.13, 0.7, 0.15]$ in HELIX. Two numbers $N_\theta = 256$ and $N_\theta = 512$ are used, with a fixed initial condition $a^\star = 0.1460403064$ and $r_A^\star = 0.9793868424468$ with initial angle of vortex center at $\theta_0 = 0.1$. The inverse of time step is chosen as $1/\delta t = 5000$, with Reynolds number $Re_{\mathrm{DNS}} = 2\pi 10^4$. The results of mode $m \in [-3, 3]$ are plotted in figure 5.3, excellent agreements are found for all the modes.

In the same way, the results obtained by HELIKZ with initial condition duplicated from HELIX is plotted in in figure 5.4, excellent agreements are also found for all the modes. That is to say the requirement on $N_\theta = 256$ are both satisfied for HELIX and HELIKZ–NL.

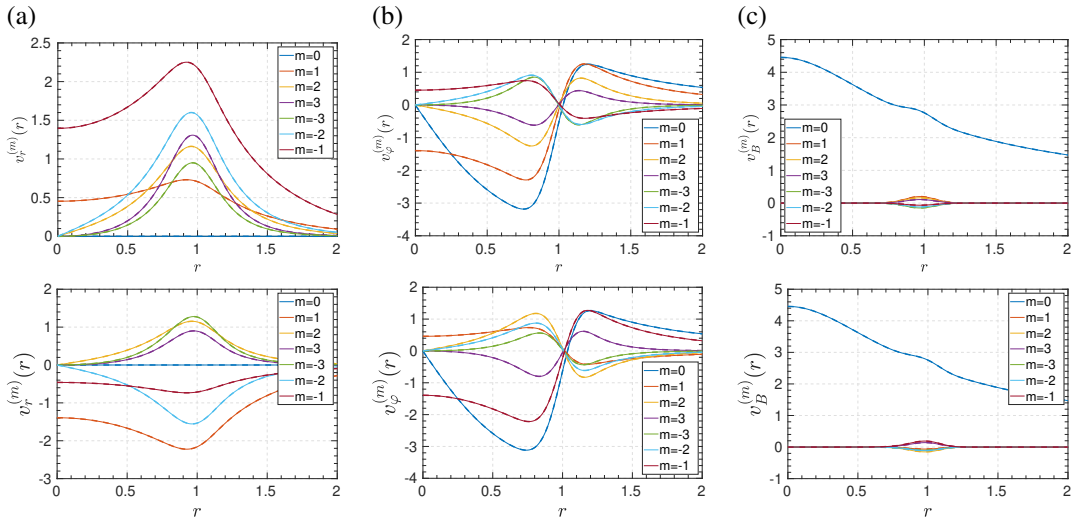

Figure 5.3 – Spectral function (a) $v_r^{(m)}$, (b) $v_\varphi^{(m)}$ and (c) $v_B^{(m)}$ at plane Π_0 of base state $[0.13; 0.7; 0.15]$ obtained by HELIX for (top) initial condition at $t = 0$ and (bottom) final state at $t = 30$. line: $N_\theta = 512$; dashed line: $N_\theta = 256$.

The states obtained by HELIX and HELIKZ are then compared, one obtains a good fit between the spectral functions from the two simulation results, as shown in figure 5.5. Here to eliminate the difference in azimuthal position of the vortex in the two codes, one shall take the modulus of the spectral function $f^{(|m|)} = \sqrt{(f^{(m)})^2 + (f^{(-m)})^2}$.

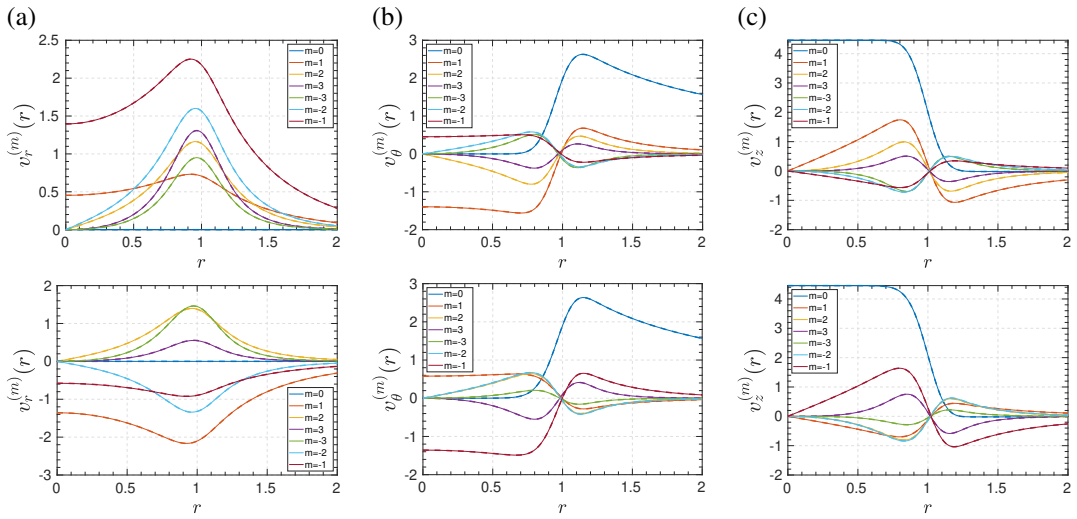

Figure 5.4 – Spectral function (a) $v_r^{(m)}$, (b) $v_\theta^{(m)}$ and (c) $v_z^{(m)}$ obtained by HELIKZ–NL. Others are idem to figure 5.3.

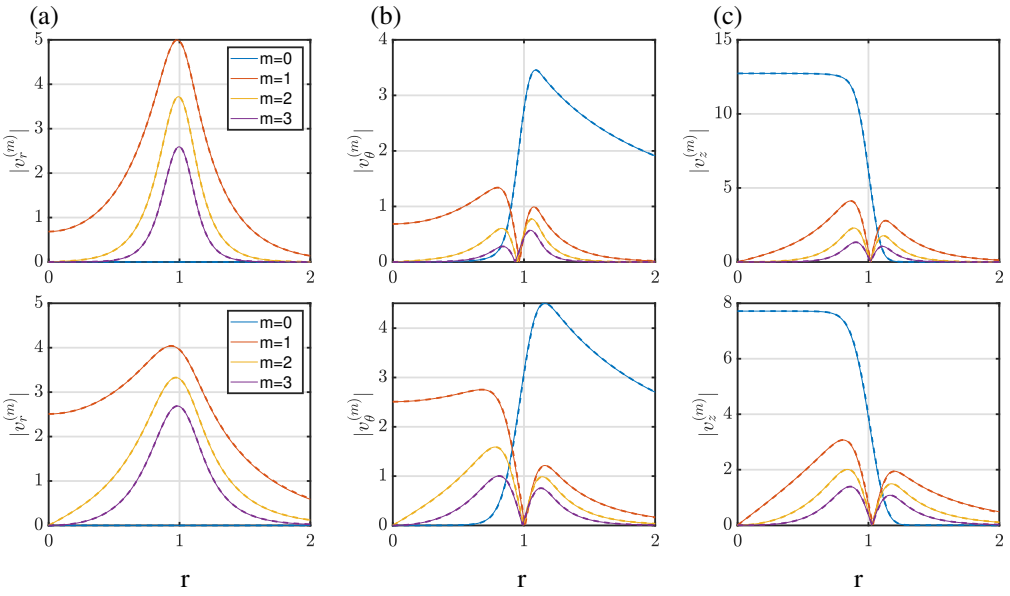

Figure 5.5 – Spectral function (a)$|v_r^{(m)}|$, (b) $|v_\theta^{(m)}|$ and (c) $|v_z^{(m)}|$ at plane Π_0 of base states (top) $[0.13; 0.7; 0.15]$ and (bottom) $[0.2; 0.3; 0.11]$. line: HELIKZ–NL; dashed line: HELIX.

5.3.4 Characterisation of the base states

To characterise the base state, we follow the prescription described in section 4.4 which was based on the stagnation point called point A. To locate this point, we iterate on the position where velocity u_H or stream function Ψ reaches its maximum. *A priori* the local azimuthal velocity $u_\psi^{(1)}$ must be zero at this point since $\rho = 0$. However it was found because of numerical truncation errors this is not the case but the two locations are near $r = 1$ with differences of order 10^{-4}. As a consequence, we slightly shift point A so that $u_\psi^{(1)}$ be zero at this point. The characteristic values, namely a_0, $\bar{W}_0$ and $\bar{W}_{00}$, are then estimated using an optimal fit of the axisymmetric part of the local axial velocity in the translating frame $u_b^{(T)}$ on the $\Pi_\perp$ plane by the following relation:

$$u_b^{(T,m=0)} = \frac{\Gamma}{2\pi a_0}\left[\bar{W}_0 \exp(-(\frac{\rho}{a_0})^2) + \bar{W}_{00}\right]. \tag{5.47}$$

In table 5.4, we present the characteristic values of the base states measured in table 5.1, these values will be used for instability studies.

When the core size is reasonably small with respect to the pitch and the curvature radius, the asymptotic theory adequately describes the structure of the numerical velocity field up to relatively large values of ε. Comparisons between asymptotic theory and DNS are not presented here but are similar to results of section 4.4.

prescribed parameters			HELIKZ–NL DNS results with fitting on $u_b^{(0)}$						
L	a	$\bar{W}^B$	r_A	L/r_A	Γ	Ω_0	a_0/r_A	$\bar{W}_0$	$\bar{W}_{00}$
0.3	0.110	−0.03	0.9933	0.3019	1.0240	−0.0893	0.1112	−0.0008	0.0042
		0.00	0.9932	0.3025	1.0095	−0.0887	0.1109	0.0226	0.0052
		0.17	0.9936	0.3019	1.0228	−0.0868	0.1116	0.1953	0.0061
		−0.26	0.9940	0.3018	1.0232	−0.0852	0.1106	−0.2236	0.0039
		0.20	0.9936	0.3019	1.0232	−0.0869	0.1110	0.2245	0.0060
		0.37	0.9944	0.3016	1.0226	−0.0870	0.1122	0.3874	0.0072
0.4	0.116	−0.24	0.9936	0.4025	1.0132	−0.0596	0.1159	−0.1977	−0.0132
		0.16	0.9931	0.4027	1.0127	−0.0623	0.1176	0.1986	−0.0124
0.5	0.125	−0.25	0.9931	0.5034	1.0085	−0.0481	0.1255	−0.1952	−0.0287
		0.15	0.9928	0.5035	1.0072	−0.0512	0.1289	0.1997	−0.0292
0.6	0.136	−0.26	0.9930	0.6042	1.0058	−0.0415	0.1361	−0.1954	−0.0426
		0.14	0.9935	0.6039	1.0055	−0.0446	0.1399	0.2014	−0.0446
0.7	0.15	−0.27	0.9926	0.7052	1.0041	−0.0379	0.1493	−0.1953	−0.0555
		0.13	0.9918	0.7057	1.0039	−0.0416	0.1551	0.2027	−0.0590
		0.20	0.9931	0.7048	1.0038	−0.0414	0.1530	0.2687	−0.0562
		0.25	0.9932	0.7047	1.0032	−0.0415	0.1522	0.3156	−0.0560

Table 5.4 – The characteristic values of base flows $[L; a; \hat{W}^B]$ in table 5.1. Quantity r_A is the radial position of point based on $u_\psi^{(1)} = 0$ and the values are obtained *via* a fitting on $u_b^{(0)}$.

5.4 Characterizations of most unstable perturbations

5.4.1 Procedure to compute the growth rate and frequency of a mode

The value of growth rate σ is obtained from the temporal evolution of the norm E_c based on kinetic energy

$$E_c \equiv \int_{\Pi_0} (u_r u_r^* + u_\theta u_\theta^* + u_z u_z^*) \mathrm{d}S \tag{5.48}$$

where $*$ stands for complex conjugate. Indeed for the most unstable mode which grows exponentially as $\exp[(\sigma - \mathrm{i}\omega)t]$, this norm varies as

$$E_c = E_0 \exp(2\sigma t), \quad \text{hence} \quad \sigma = \frac{1}{2}\frac{\mathrm{d}\ln E_c}{\mathrm{d}t}. \tag{5.49}$$

In figure 5.6 (a), one displays the norm E_c at different times t (black dots), the energy first decreases with time as the initial perturbation contains also damped modes, then the most unstable mode emerges and dominates the evolution. The growthrate of this unstable mode is calculated in the linear regime with equation (5.49) (red curve with value).

For the frequency in the rotating frame $\omega^{(\mathrm{R})}$, one can use any arbitrary field at two different times: take vorticity field ω_B' for example, one uses the "ancient" field $\omega_B'(t_1)$ and the new field $\omega_B'(t_2)$ with $t_2 = t_1 + \delta t$. Theoretically the two fields satisfy the relation:

$$\omega_B'(t_2) = \omega_B'(t_1) \exp[(\sigma - \mathrm{i}\omega^{(\mathrm{R})})\delta t]. \tag{5.50}$$

One defines a new variable f at t_1 (resp. g at t_2), which is a normalization of ω_B':

$$f = \frac{\omega_B'(t_1)}{\sqrt{\iint_{\Pi_0} \omega_B'(t_1)\omega_B'^*(t_1)\mathrm{d}S}}, \quad g = \frac{\omega_B'(t_2)}{\sqrt{\iint_{\Pi_0} \omega_B'(t_2)\omega_B'^*(t_2)\mathrm{d}S}}. \tag{5.51}$$

One then introduces the correlation coefficient I:

$$I(\omega) = \iint_{\Pi_0} f e^{-\mathrm{i}\omega\delta t} g^* \mathrm{d}S, \tag{5.52}$$

which equals 1 at the exact value of frequency $\omega = \omega^{(\mathrm{R})}$. In practice, one starts with the guess value $\omega^{(\mathrm{R})} = 0$ and one increases $\omega^{(\mathrm{R})}$ until $I = 1$ is reached, the time interval δt having to be sufficiently small to avoid the periodicity. In figure 5.6 (b), an example corresponding to the unstable mode found in figure 5.6 (a) is presented. One uses the vorticity perturbation ω_B' at times $t_1 = 129$ and $t_2 = 130$, the frequency obtained is $\omega^{(R)} = 2.52$.

Another method could be employed to obtain growthrate and frequency. It is based on the complex perturbation v_z' at the stagnation point A. The real part of this quantity reaches its maximum at time $t_3 \sim 0.53$ and $t_4 \sim 3.12$ (see figure 5.6 (c), solid line). It is possible to shift in time the companion imaginary part, so that they both reach their maximum at the same time (see figure 5.6 (c), black dashed line). We can check that this quantity indeed evolves with frequency $\omega^{(R)}$ and grows according to $\exp(\sigma\Delta t)$: the relation $v'(A, t_4) = v'(A, t_3)\exp([\sigma - \mathrm{i}\omega](t_4 - t_3))$ should be verified. Based on this rough estimate,

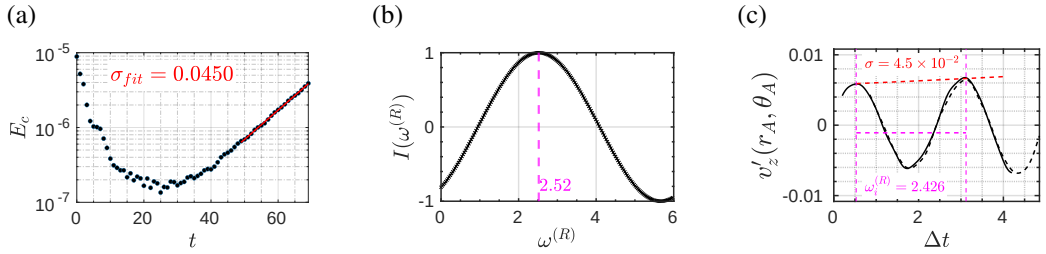

Figure 5.6 – An example of computation from numerical results of dimensionless growthrate σ_{DNS} and frequency ω_{DNS}. (a) Temporal evolution of energy E_c (black dots) and corresponding growthrate (red curve) obtained by eq. (5.49). (b) Correlation coefficient $I(\omega)$ given by eq. (5.52). (c) Superimposed temporal evolution of the real (solid) and imaginary (dashed) part of perturbation v_z' at a fixed point P_A in plane Π_0 in the linear regime as a final check for assessing the values σ and $\omega^{(R)}$ obtained in (a)–(b), represented by the colored dashed line.

one gets $\sigma = 0.045$ (resp.$\omega^{(R)} = 2.43$), which is close to the value 0.045 obtained in figure 5.6 (a) (resp. 2.52 in (b)).

5.4.2 Helical projection of perturbations

Consider the complex instability mode obtained through the linear simulation. It is characterized by vorticity components ω_r, ω_φ, ω_B or velocity components u_r, u_φ, u_B, obtained by the code HELIKZ–LIN in the plane Π_0. In order to have a clear picture of the mode structure (and compare with asymptotic theory), it is convenient to display these fields in the plane $\Pi_\perp$. When computing the values in $\Pi_\perp$ from those in Π_0, a phase shift should be taken into account:

$$f_{\Pi_\perp}(M_1(\rho,\psi)) = f_{\Pi_0}(M(r,\varphi)) \cdot \exp(\mathrm{i}k_z\Delta z). \tag{5.53}$$

where $M \in \Pi_0$, $M_1 \in \Pi_\perp$ are two points on the same helical line and $\Delta z = z_{M_1} - z_M$. This is similar to the method applied for base flows (yet without phase shift) as introduced in appendix A.2. Field f can then be normalized to yield f':

$$f'(\rho,\psi) = \frac{f_{\Pi_\perp}(\rho,\psi)}{f_{\Pi_\perp}(\rho_m,\psi_m)} \tag{5.54}$$

where (ρ_m, ψ_m) is the field component at the location of maximum $|f_{\Pi_\perp}|$. An example on the perturbation velocity component u_B' is given in figure 5.7.

In figure 5.7 left, the contours of $f_{\Pi_0}(r,\varphi)$ for real part (top) and imaginary part (bottom) of $u_B'(r,\varphi)$ at plane Π_0 is presented, with its zoom-view at the bottom right corner. The field is then projected onto plane $\Pi_\perp$ with equation (5.53), In figure 5.7 (right), one presents the normalized perturbation mode $u_B'(\rho,\psi)$ obtained with equation (5.54) . The shape of the perturbation at right-top is clearly one of the helical unstable modes we are looking for.

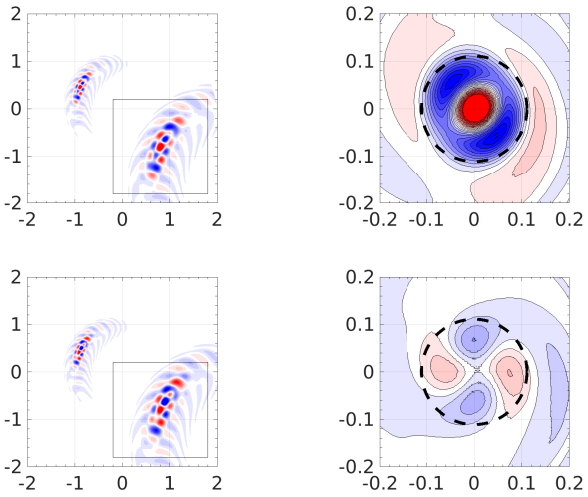

Figure 5.7 – Examples of helical projection from plane Π_0 to $\Pi_\perp$ and normalization for axial velocity perturbation u'_B showing real parts (top raw) and imaginary parts (bottom raw). [left] Contours for $f_{\Pi_0}(r,\varphi)$ in plane Π_0. The inset in the bottom-right corner is a zoom on the vortex location; blue (resp. red) represents negative (resp. positive) values. [right] Contours of normalized field $f'(\rho,\psi)$ in plane $\Pi_\perp$.

Mode decomposition

One reveals the spatial structure of this mode in the plane $\Pi_\perp$ by applying Fourier decomposition:

$$f'^{(m)}(\rho) = \frac{1}{2\pi}\int f'(\rho,\psi)\exp(-\mathrm{i}m\psi)\mathrm{d}\psi, \tag{5.55}$$

or in a discrete form:

$$f'^{(m)}(\rho_i) = \frac{1}{N_\psi}\sum_{j=1}^{N_\psi} f'(\rho_i,\psi_j)\mathrm{e}^{-\mathrm{i}m\psi_j} \quad (i=1,\cdots,N_\rho). \tag{5.56}$$

In practice, we analyse the axial velocity perturbation component $\boldsymbol{u}'\cdot\boldsymbol{e}_B(A)$ in plane $\Pi_\perp$. The energy of mode m for this field f' can be obtained by taking the integral in the radial direction:

$$E_f^{(m)} = \frac{1}{4}\int_\rho \|f'^{(m)}\|^2 \rho\,\mathrm{d}\rho. \tag{5.57}$$

For the total kinetic energy mode distribution $E_c^{(m)}$, the three components of velocity perturbation (u'_ρ, u'_ψ, u'_b) are taken into account using

$$E^{(m)} = E_{u\rho}^{(m)} + E_{u\psi}^{(m)} + E_{ub}^{(m)} \tag{5.58}$$

as well as the sum of all energy modes with $E = \sum E^{(m)}$. An example of energy ratios $E^{(m)}/E$ is plotted in figure 5.8 (c, top).

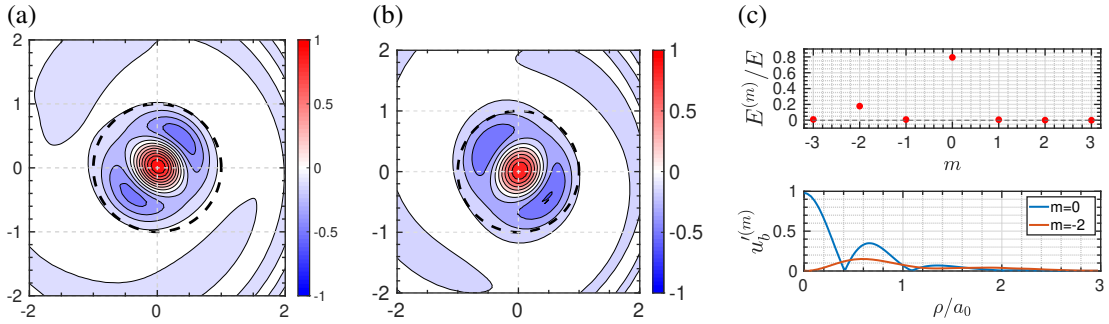

Figure 5.8 – Example of instability mode structure. (a) Contours of vorticity component ω'_B in plane $\Pi_\perp(\bar{\rho},\psi)$. (b) Contours of velocity component u'_b in plane $\Pi_\perp(\bar{\rho},\psi)$. (c) Top: ratio of total energy per mode on velocity field $\boldsymbol{u}'$. Bottom: radial distribution of $|u_b^{\prime(m)}|$ for $m = 0$ and $m = -2$.

5.5 Convergence study on the linear stability analysis

The dependence on mesh refinement varies according to several parameters

- a larger vortex pitch L usually requires a more refined mesh in azimuthal direction;
- a smaller vortex core a usually requires a more refined mesh in both directions;
- a base states with stronger jet component usually requires a more refined mesh in both directions.

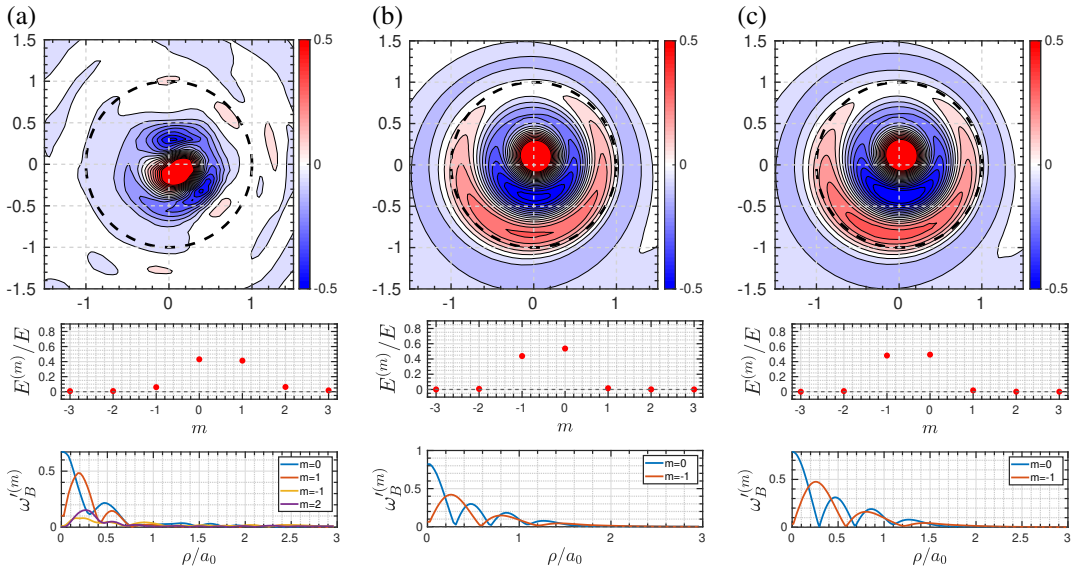

Figure 5.9 – Contours of unstable mode (top) and the mode decomposition of ω'_B for base state $[0.7; 0.15; 0.13]$ with $Re = 10^4, k_s a = 1.75$. Different mesh configuration $(N_r \times N_\theta, R_{ext})$ are used: (a) $(512 \times 128, 2)$, (b) $(512 \times 256, 2)$, (c)$(1024 \times 256, 2)$.

In figure 5.9, one presents the short wavelength instability mode for the base state $[L = 0.7; a = 0.15; \bar{W}^B = 0.13]$ obtained with three different mesh configurations $(N_r \times N_\theta, R_{ext})$. Clearly, the configuration $(512 \times$

$128, 2)$ is not sufficient. When the mesh configuration $(512 \times 256, 2)$ is used, we observe the expected instability structure. This is confirmed by the refined mesh configuration $(1024 \times 256, 2)$ yielding close results. For the same value $L = 0.7$, the long wavelength mode is more difficult to obtain numerically (figure 5.10): the modes $m = \pm 1$ become dominant with equal energy and radial distribution (that is the classic structure of long wavelength mode) only after a much longer time evolution ($t = 50$ is not enough, because of the slow decay of an axisymmetric component, almost disappeared at $t = 120$).

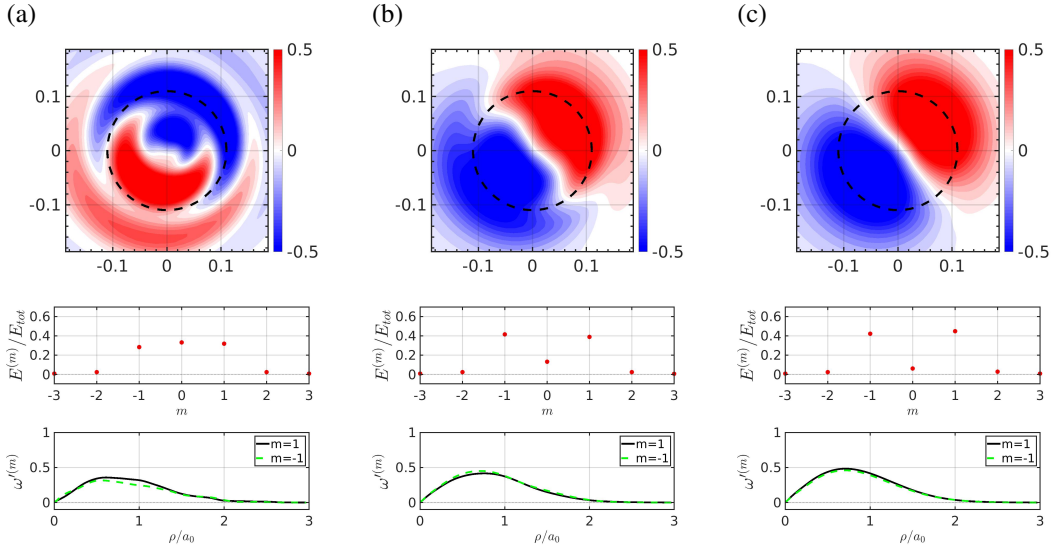

Figure 5.10 – Temporal evolution of long wavelength perturbation $k_z L = 0.5$ (ω'_B at plane $\Pi_\perp$ is displayed) for base state $L/R = 0.7$, $a_0/R = 0.11$, $W_0 = 0$, and $Re = 10^4$ (a) $t = 20$, (b) $t = 50$, (c) $t = 120$.

It should be mentioned when the reduced pitch L decreases at fixed core size a the computation needs less points N_θ. This is because in the Π_0 plane in which the simulation is performed, the vortex covers along the radial direction a region of size $2a$ but along the angular direction a region of size $2a\sqrt{1 + r_A^2/L^2} = 2a\sqrt{1 + 1/L^2}$. For a given N_θ, one obtains a cell along the radius at $r_A = 1$ of size $2\pi/N_\theta$. For a vortex of core size a, this means it is covered by

$$\frac{2a\sqrt{1 + 1/L^2}N_\theta}{2\pi}$$

points along the azimuthal direction in the Π_0 plane. To be coherent we need the same number of points in the radial direction so that

$$\frac{2a}{\delta_r} = \frac{2a\sqrt{1 + 1/L^2}N_\theta}{2\pi} \quad \text{with} \quad \delta_r = R_{ext}/(N_r - 1),$$

or

$$N_r = 1 + \frac{R_{ext}\sqrt{1 + 1/L^2}N_\theta}{2\pi}.$$

For a vortex of reduced pitch $L = 0.3$, core size $a = 0.11$ and $N_\theta = 256$, this means 30 points along the azimuthal direction. For a domain size $R_{ext} = 3$, this yields $N_r = 426$, thus the choice $N_r = 512$ is enough along the radial direction. For larger $L = 0.7$, core size $a = 0.11$ and $N_\theta = 512$, this means also 30 points along the azimuthal direction and yields $N_r = 427$. For some special cases, a vortex with extremely

small core size a/r_A less than $O(10^{-2})$, strong axial components $W_0 > 0.5$ more refined meshes in both directions are required, resulting in a very long simulation times to get the growth rate and frequency.

Chapter 6

Linear helical stability: Long wavelength modes

Contents

Theoretical studies of helical vortices with finite core size a indicate the existence of two types of instability modes: short-wave mode and long-wave mode. The present chapter focuses on the second kind of perturbations: modes the wavelength of which is much larger than a. Our normal modes are of the form $\exp(\mathrm{i}k_z z)$ or using the curvilinear abscissa $s = z\sqrt{1+\frac{R^2}{L^2}}$ of the form

$$\exp(\mathrm{i}k_s s) = \exp(\mathrm{i}k_z z) \quad \text{with} \quad k_z = \sqrt{1+\frac{R^2}{L^2}}\, k_s = \frac{k_s}{\alpha_A}\,. \tag{6.1}$$

For $R/L \ll 1$, the long-wave limit means

$$k_s\, a = \frac{1}{\sqrt{1+\frac{R^2}{L^2}}} k_z a \sim k_z a \ll 1\,.$$

For $L/R \ll 1$, the long-wave limit means

$$k_s\, a = \frac{1}{\sqrt{1+\frac{L^2}{R^2}}} (\frac{a}{R})(k_z L) \sim (\frac{a}{R})(k_z L) \ll 1\,,$$

which is valid as soon as $k_z L \sim O(1)$.

6.1 Theoretical elements for long wavelength instability modes

For such modes, the unstable mode is only a displacement mode: as its amplitude grows, the internal structure of the vortex core remains invariant but the vortex is locally displaced as a whole. In figure 6.1 from [Leweke et al., 2016], the experimental vortex indicates a clear displacement occurring near the 4th helical turn (position of white triangle). The shape of the perturbed filament is similar to the theoretical studies by [Widnall, 1972] (illustration on left). In this seminal work the stability of helical vortices with finite core size a has been studied in the context of filament theory taking into account the self-induced velocity through the Biot-Savart line integral, associated with the cut-off method. Theoretically a long-wave instability mode was found that is the filament was displaced by a mode of the form of wavelength k_s where k_s is measured along the vortex central line (if s denotes the curvilinear abscissa). This means that unstable modes dependence is of the form $\exp(\mathrm{i}k_s s)$ with $k_s a \ll 1$. The stability of long-wave modes has also been considered by [Gupta and Loewy, 1974], [Okulov, 2004], [Okulov and Sørensen, 2007]. In a recent study, the long-wave modes have been numerically investigated [Selçuk, 2016, Selçuk et al., 2017a] for single or multiple helical vortices with weak internal jet velocity. A good agreement on the growth rates was found for different reduced pitches L/R and perturbation wavenumbers.

In the thesis of [Selçuk, 2016], the long-wave instability had been numerically studied in the limit of zero axial jet component. We extended the study to the case of axial jet components, with the base states listed in previous chapter. These states are closer to the realistic model as the axial velocity of the helical vortices are usually non-zero [Quaranta et al., 2015].

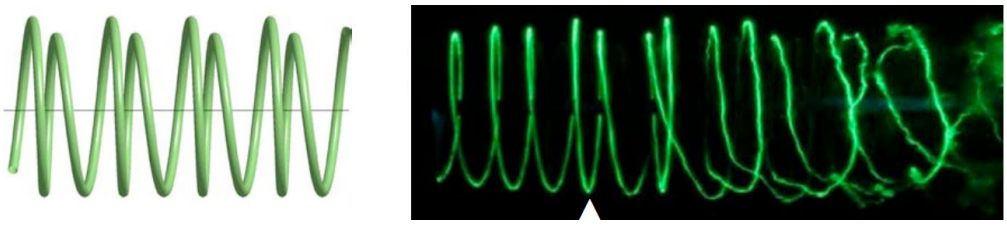

Figure 6.1 – Examples of long-wave instabilities cited from [Leweke et al., 2016]. Left: theoretical predictions by [Widnall, 1972], Right: experimental visualisations of one-bladed rotor wakes in a water channel.

For low pitch L/R, when visualized in the meridian plane, the situation is very similar to an infinite row of point vortices. Consider an infinite array of two-dimensional point vortices of circulation Γ situated at points $(mb, 0)$ with $m \in \mathbb{Z}$. Its stability is known [Lamb, 1932]: the vortex m subjected to a perturbation $(mb + x_m(0), y_m(0))$ with $x_m(0) = A_0 e^{\mathrm{i}m\phi}$ and $y_m(t) = -A_0 e^{\mathrm{i}m\phi}$ evolves as $x_m(t) = A_0 e^{\sigma t + \mathrm{i}m\phi}$ and $y_m(t) = -A_0 e^{\sigma t + \mathrm{i}m\phi}$ with growth rate given by

$$\sigma(\phi) = \frac{\Gamma}{4\pi b^2}\phi(2\pi - \phi). \tag{6.2}$$

The maximum occurs for $\phi = \pi$ corresponding to an out-of-phase displacement of the neighbouring vortices. Following [Bolnot, 2012], one may tentatively compare growth rates obtained for a helical vortex to those obtained for an array of point vortices. For a helical vortex, the shortest length between two successive coils is not the helical pitch $h = 2\pi L$ [Quaranta et al., 2015] but $b = h\cos\alpha$ with $\cos\alpha = R/(L^2 + R^2)^{1/2}$. The phase between two points in a period h is equal to $k_z h = 2\pi k_z L$. The phase between two points

corresponding to the shortest length becomes

$$\phi = k_z h \cos^2\alpha = 2\pi k_z L \cos^2\alpha,$$

and the expected growth rate (see [Quaranta et al., 2015]) can be replaced by

$$\sigma = \frac{\Gamma}{2h^2} 2\pi k_z L\left(1 - k_z L\cos^2\alpha\right) = \frac{\Gamma}{2h^2} 2\pi k_z L\left(1 - k_z L \frac{R^2}{R^2+L^2}\right).$$

This can be rewritten as

$$\boxed{\sigma = \sigma_0\left[2\pi\hat{k}\left(1-\hat{k}\right)\right], \quad \hat{k} \equiv \beta_0\, k_z L} \tag{6.3}$$

with

$$\boxed{\sigma_0 \equiv \frac{\Gamma}{8\pi^2}\left(\frac{1}{R^2}+\frac{1}{L^2}\right), \quad \beta_0 \equiv \frac{1}{1+\frac{L^2}{R^2}}.} \tag{6.4}$$

The maximum is equal to $\sigma_0\pi/2$ and is attained at $\hat{k} = 1/2$. As mentioned in the article [Quaranta et al., 2015], such an expression is only valid for small helix pitches, and for a helical vortex with large pitch, the interaction between neighbouring filaments becomes weaker, the dynamics are rather dominated by the vortex curvature and torsion.

In the following, the growth rate obtained by DNS σ_{DNS} is compared to the value obtained by the point-vortex theory, by evaluating

$$\sigma^d = \frac{\sigma_{\mathrm{DNS}}}{\sigma_0} \tag{6.5}$$

as a function to $\hat{k} \equiv \beta_0 k_z L$. The largest value of σ^d is expected to be $\pi/2$ as for the case of point vortices (see also [Selçuk et al., 2017a]). As mentioned in [Widnall, 1972], the stability property may change for other parameters.

- For a helical filaments with $L \leq 0.3$ ($\arctan(L/r_A) < 0.3$ in [Widnall, 1972]), in which neighbouring turns are within a distance of one radius, a third instability may occur at $\hat{k} = \frac{3}{2}$ and $\hat{k} = \frac{5}{2}$.
- Growth rates become smaller if the core size becomes larger.

[Fukumoto and Miyazaki, 1991] considered an axial flow along the vortex core, which was found to suppress the instability for certain configurations with large pitch.

6.2 Numerical results of long wavelength instability

In this section long wavelength ($k_s a \ll 1$) instability results are presented for a helical vortex with Gaussian core structure, reduced pitch $L = 0.3$ and axial jet velocity $W_0 = 0, 0.2, 0.4$.

In figure 6.2(a), contours of ω'_B in plane $\Pi_\perp$ are shown, where red (resp. blue) zones are for positive (resp. negative) values. The structure of displacement mode, typical for the long-wave instability, is found. In addition, an even distribution of mode $m = 1$ (black line) and $m = -1$ (green dashed line) (see mode

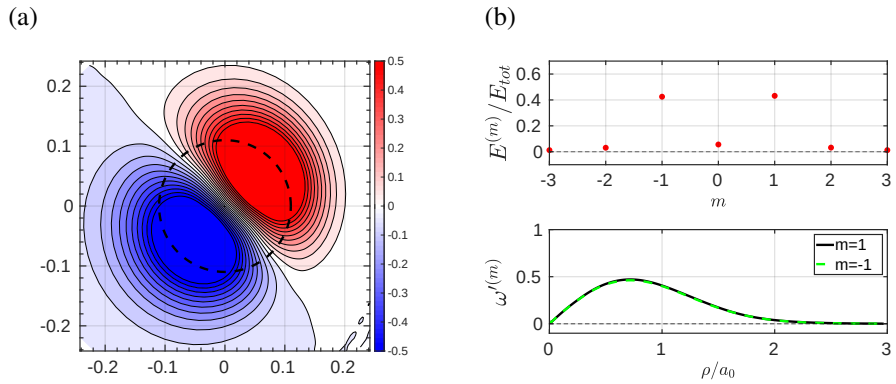

Figure 6.2 – Mode structure of long wave-length instability for $\hat{k} = 0.5$, $W_0 \sim 0$, $r_A = 0.994$, $a_0 = 0.1118$, $L = 0.3$ and $Re = 10^4$. [a] Contours of azimuthal vorticity ω'_B (blue: $\omega'_B < 0$, red: $\omega'_B > 0$) [b] Fourier decomposition of ω'_B: (top) ratio of energy per mode, (bottom) radial distribution of $\omega'^{(m)}_B$.

decomposition in figure 6.2(b)), indicates the resonance of Kelvin modes $m = -1$ and $m = 1$ with same energy and radial distributions, as predicted by theory.

In figure 6.3, the scaled growth rates σ^d are plotted for various dimensionless wavenumbers $\hat{k} \equiv \beta_0 k_z L$ for different core sizes a, for axial velocity $W_0 \approx 0$ and fixed reduced pitch $L = 0.3$. An overall good agreement is found with respect to the theoretical curve (equations (6.3)–(6.5)): the dispersion relations take identical forms with maxima located near $\hat{k} = 1/2$. A non-negligible shift is observed for larger core sizes a, which is not surprising since the theory is based on the assumption of small core sizes $a \ll 1$.

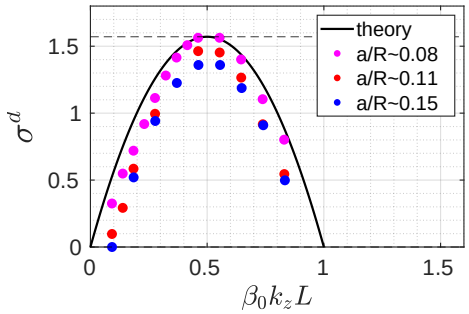

Figure 6.3 – The comparison of scaled growthrate σ_d from DNS (dots) and theory (line, equation (6.5)), for $L = 0.3$, $W_0 \approx 0$ with various core sizes: $a = 0.08$ (magenta), 0.11 (red), 0.15 (blue).

In figure 6.4, different axial velocities W_0 are presented, with fixed reduced pitch $L = 0.3$ and core size $a/R = 0.11$. Only slight differences are observed for different axial velocities. The work [Fukumoto and Miyazaki, 1991] introduced an axial jet velocity inside the vortex core with the cutoff method valid to the second order, extending the first-order scheme developed by [Widnall, 1972]. The axial velocity was found to discriminate between right- and left-handed helices and the dispersion relation to be modified by the axial velocity W_0, for certain configurations ($L = 1, 0.3, 0.2$ with $a = 0.33$). When W_0 is increased from 0, the flow is first destabilized by the weak jet component (with $W_0 < 0.3$), and then

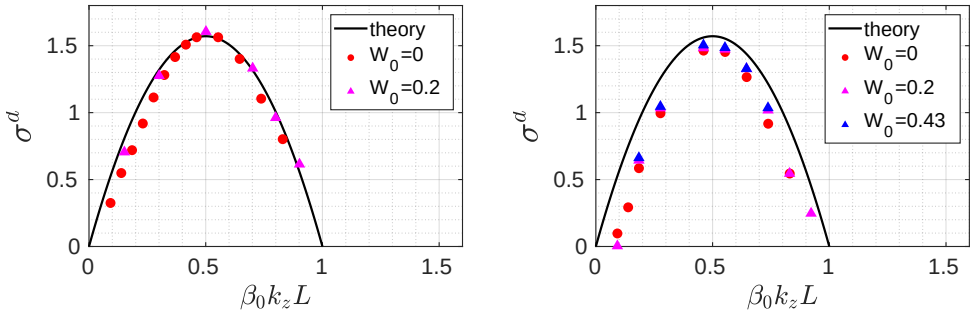

Figure 6.4 – The comparison of scaled growthrate σ_d from DNS (dots) and theory (line, equation (6.5)), for $L = 0.3$, (left)$a = 0.08$, (right)$a = 0.11$ with different axial velocity $W_0 \approx 0$ (red), 0.2 (yellow), 0.43 (purple).

stabilized by the strong jet component. We could not find such a behavior because of numerical problems.

Chapter 7

Linear helical stability: short wavelength

Contents

This chapter presents linear stability for modes of wavelength comparable to the core size a, that is such that $k_s a \equiv \alpha_A k_z a \sim O(1)$. Contrary to long-wavelength modes, these instability modes modify the vortex core structure. Physically, they originate from the resonance or near resonance between two Kelvin waves propagating along the steady base vortex flow. These two waves couple *via* the base flow deformation due to the action of a strain field. For a single vortex, this strain is induced by the curvature and torsion of the vortex nearby and from region far apart. This constitutes the so-called elliptic instability ([Kerswell, 2002, Meunier et al., 2005]) or curvature instability ([Fukumoto and Hattori, 2005, Hattori and Fukumoto, 2009]). For vortex rings, the theoretical predictions have already been well verified by [Bolnot, 2012, Hattori et al., 2019].

The elliptic instability is discussed in section 7.2, and the curvature instability in section 7.3. In particular, results of the procedure based on the code HELIKZ-LIN are compared to theoretical values given in [Blanco-Rodríguez et al., 2015].

7.1 Comparing numerical eigenvalues to theoretical predictions

In this section, let us use dimensional variables (denoted by $*$). Stability computations are performed in the rotating reference frame (R) in which the basic flow is steady, and provide the frequency $\omega^{(\mathrm{R})*}$ and growth rate $\sigma^{(R)*}$. In the translating frame (T) in which the basic flow is also steady, frequency and growth rate become

$$\omega^{(\mathrm{T})*} = \omega^{(\mathrm{R})*} - U_0^* k_z^*; \quad \sigma^{(T)*} = \sigma^{(R)*} \tag{7.1}$$

where U_0^* is the translation velocity of the frame along the z axis and k_z^* the dimensional wavenumber along the z axis.

The theoretical dimensional growth rate σ_{th}^* and frequency ω_{th}^* for the instability of a straight Batchelor vortex are given in a reference frame with zero axial velocity outside the vortex; the unstable modes read:

$$v' = \hat{v}(r)\exp(\mathrm{i}k_s^* s^* + \mathrm{i}m\psi - \mathrm{i}\omega_{\mathrm{th}}^* t^*)\ \exp(\sigma_{\mathrm{th}}^* t^*), \tag{7.2}$$

where the wavenumber k_s^* is along the filament direction $\boldsymbol{e}_s$. In order to match the numerical results to theory, one adds an axial flow W_{00}^* to the Batchelor vortex. This leaves the growth rate unchanged, but modifies the frequency into $\omega_{\mathrm{th}}^* + W_{00}^* k_s^*$, where k_s^* is the local wavenumber along the vortex axis. In the code HELIKZ-LIN, the solution is searched in the $\boldsymbol{e}_z$ direction. The relation (6.1) in dimensional units yields

$$k_s^* = \alpha_A k_z^*. \tag{7.3}$$

Matching the two computations imposes

$$\omega^{(\mathrm{T})*} = \omega_{\mathrm{th}}^* + W_{00}^* k_s^*; \quad \sigma^{(T)*} = \sigma_{\mathrm{th}}^* \tag{7.4}$$

or equivalently

$$\omega^{(\mathrm{R})*} = \omega_{\mathrm{th}}^* + \left(W_{00}^* \alpha_A + U_0^*\right) k_z^*; \quad \sigma^{(R)*} = \sigma_{\mathrm{th}}^*. \tag{7.5}$$

In the code HELIKZ-LIN, one uses the characteristic scales and Reynolds number

$$[\mathrm{L}] = r_A, \quad [\mathrm{T}] = \frac{r_A^2}{\Gamma}, \quad \text{and} \quad Re_{\mathrm{DNS}} = \frac{\Gamma}{\nu}. \tag{7.6}$$

One computes for the dimensionless wavenumber k_{DNS} the dimensionless growth rate σ_{DNS} and frequency ω_{DNS}

$$\boxed{\sigma_{\mathrm{DNS}}(k_{\mathrm{DNS}}) = \frac{r_A^2}{\Gamma}\sigma^{(R)*}, \quad \omega_{\mathrm{DNS}}(k_{\mathrm{DNS}}) = \frac{r_A^2}{\Gamma}\omega^{(\mathrm{R})*} \quad \text{with} \quad k_{\mathrm{DNS}} \equiv r_A k_z^*}. \tag{7.7}$$

For the asymptotic analysis in Ch 4, the scales and Reynolds number are chosen as follows

$$[\mathrm{L}] = a, \quad [\mathrm{T}] = \frac{2\pi a^2}{\Gamma}, \quad \text{and} \quad Re = \frac{\Gamma}{2\pi\nu} = \frac{1}{2\pi} Re_{\mathrm{DNS}}. \tag{7.8}$$

In these scales, one gets the dimensionless quantities

$$\bar{k}_z = \frac{k_{\mathrm{DNS}}}{\bar{r}_A}, \quad \bar{k}_s = \alpha_A \bar{k}_z, \quad \text{with} \quad \bar{r}_A \equiv \frac{r_A}{a}, \tag{7.9}$$

$$\boxed{\bar{\sigma}^{(\mathrm{R})} = \frac{2\pi}{\bar{r}_A^2}\sigma_{\mathrm{DNS}}(k_{\mathrm{DNS}}, Re_{\mathrm{DNS}}), \quad \bar{\omega}^{(\mathrm{R})} = \frac{2\pi}{\bar{r}_A^2}\omega_{\mathrm{DNS}}(k_{\mathrm{DNS}}, Re_{\mathrm{DNS}}).} \tag{7.10}$$

In dimensionless form, equation (7.5) becomes

$$\boxed{\bar{\sigma}^{(\mathrm{R})} = \bar{\sigma}_{\mathrm{th}}(\bar{k}_s; Re)\,, \quad \bar{\omega}^{(\mathrm{R})} = \bar{\omega}_{\mathrm{th}}(\bar{k}_s; Re) + \left(\bar{W}_{00} + \frac{\bar{U}_0}{\alpha_A}\right)\bar{k}_s\,, \quad \bar{U}_0 = -\bar{\Omega}_0 \bar{L}.} \tag{7.11}$$

If we use the asymptotic form, this can be written as

$$\bar{\omega}^{(\mathrm{R})} = \bar{\omega}_{\mathrm{th}}(\bar{k}_s; Re) + \left(\frac{\alpha_A(1-\alpha_A)}{\bar{L}} - \frac{\alpha_A \bar{\Omega}_0 \bar{r}_A^2}{\bar{L}}\right)\bar{k}_s\,, \tag{7.12}$$

where, from equation (4.55),

$$\bar{W}_{00} = \alpha_{\mathrm{A}}\bar{\Omega}_0\bar{L} + \frac{\alpha_{\mathrm{A}}(1-\alpha_{\mathrm{A}})}{\bar{L}}. \tag{7.13}$$

7.2 Elliptical instability

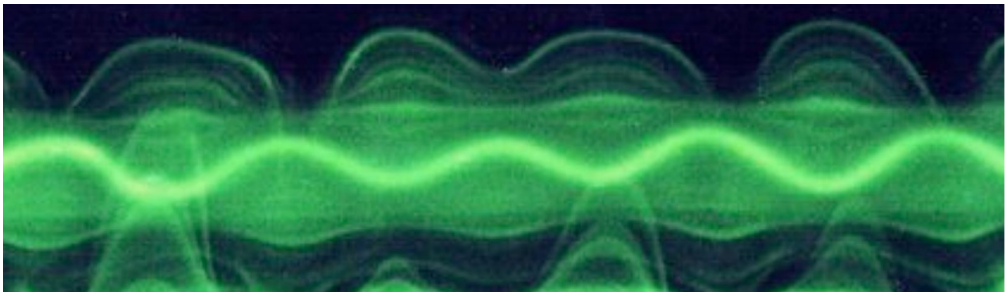

Figure 7.1 – Cited from [Leweke et al., 2016]: Experimental dye visualizations (side views) of the elliptic instability of strained vortices without axial flow, .

A number of experimental and numerical investigations are devoted to instability mechanisms for helical vortices. For instance, short-waves and filament twisting were observed in two-phase flows experiments by [Felli et al., 2011]. In [Quaranta et al., 2015, Leweke et al., 2016], the existence of short-wave elliptical deformation for monophasic flows were found in experiments and their growth rates were quantitatively compared with theoretical estimates. In figure 7.1, an experimental result is presented with a zoom-view inside the helical vortex core [Leweke et al., 2016] in which green color dye has been introduced. The elliptical instability is visualized by the light-green part indicating the deformation inside the vortex core. In Large Eddy Simulations, these instability patterns were also recovered [Ahmed et al., 2020].

The seminal works [Moore and Saffman, 1971] and [Widnall and Tsai, 1977] that understood elliptical instability modes, concerned a straight vortex subjected to an exterior strain. This base flow is not axisymmetric. Indeed, an elliptic deformation of the base state in $\cos(2\theta)$ is observed and explains the origin of a resonance or a near-resonance between two neutral Kelvin modes of characteristics (ω_A, k_A, m_A) and (ω_B, k_B, m_B) when $k_c = k_A = k_B$, $\omega_c = \omega_A \sim \omega_B$ and $m_A = m_B - 2$. More precisely it was shown that a perturbation $\boldsymbol{u}'$ of the form

$$\boldsymbol{u}' = \left(\mathrm{A}\tilde{\boldsymbol{u}}_A(r)e^{\mathrm{i}m_A\varphi} + \mathrm{B}\tilde{\boldsymbol{u}}_B(r)e^{\mathrm{i}m_B\varphi}\right)\mathrm{e}^{\mathrm{i}k_c z - \mathrm{i}\omega t} \tag{7.14}$$

exists when amplitudes A and B are such that

$$[\omega - \omega_c]A = \varepsilon C_{AB}B, \quad [\omega - \omega_c]B = \varepsilon C_{BA}A \quad \text{hence} \quad [\omega - \omega_c]^2 = \varepsilon^2 C_{AB}C_{BA}$$

where C_{AB} and C_{BA} are two coefficients due to the coupling through the base state deformation. When $C_{AB}C_{BA}$ is negative, this leads to an instability. The work [Robinson and Saffman, 1984] validated the above predictions with numerical simulations. Later, [Pierrehumbert, 1986], [Bayly, 1986] and [Waleffe, 1990] studied the local stability properties of an unbounded elliptical flow for short-wave and explained the physical mechanism. These results were obtained for a Rankine vortex for which the vorticity is constant inside the core. A more realistic model is a Batchelor profile with Gaussian profiles for the axial vorticity and the axial velocity. The work [Lacaze et al., 2007] determines the elliptic instability of this vortex and analyses the effect of an axial flow. In figure 7.2, the instability diagram of elliptic instability is presented for Reynolds number $Re = 2 \cdot 10^4$ and $\varepsilon = 0.01$: in the plane (W_0, k) with W_0 the axial jet parameter and k the wavenumber, grey levels correspond to the intensity of growth rate σ. Each resonance involves an azimuthal mode m_A and branch l_A and a mode m_B and a branch l_B and only exists in a certain interval of W_0 values. Note the presence of three main modes:

- mode $(-1, 1, [1, 1])$ for $0 \leq W_0 \leq 0.3$;
- mode $(-2, 0, [2, 2])$ for $0.15 \leq W_0 \leq 0.35$;
- mode $(-2, 0, [1, 1])$ for $0.3 \leq W_0 \leq 0.5$,

where notations (m_A, m_B, $[l_A, l_B]$) are sometimes simplified into (m_A, m_B, $l_A = l_B$) as in figure 7.2. l_A is related to the number of radial oscillations of mode m_A.

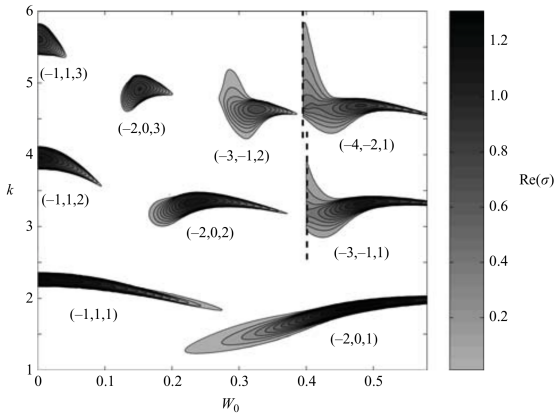

Figure 7.2 – Instability area and growth rates of the principal coupling modes (m_A, m_B, $l_A = l_B$) in plane (W_0, k) for $Re = 2 \times 10^4$ and $\varepsilon = 0.01$from [Lacaze et al., 2007].

7.2.1 Asymptotic theory

A recent theoretical study by Blanco-Rodríguez [Blanco-Rodríguez and Le Dizès, 2016] analysed the elliptic instability for vortex rings and helical vortices with a Batchelor profile. It was shown that at leading order, the curvature of the helical vortex does not change the Kelvin mode structure but modifies the local strain field hence changing the elliptic instability growth rate. More quantitatively, if (ω_c, k_c), is a resonant set i.e. an intersection of Kelvin waves branches, the complex frequency $\varpi = \omega - \mathrm{i}\sigma$ of the elliptic instability mode depends on the axial wavenumber $\bar{k} = \bar{k}_s$ close to k_c so that

$$\begin{aligned}&\left(\varpi-\omega_c-\mathrm{i}\,\mathrm{Im}\left(\omega_A\right)-Q_A\left(\bar{k}-k_c\right)-\mathrm{i}\frac{V_A}{Re}-\varepsilon^2 D_A^{(\varepsilon)}\right)\\&\times\left(\varpi-\omega_c-\mathrm{i}\,\mathrm{Im}\left(\omega_B\right)-Q_B\left(\bar{k}-k_c\right)-\mathrm{i}\frac{V_B}{Re}-\varepsilon^2 D_B^{(\varepsilon)}\right)\\=&\varepsilon^4\left(R_{AB}S+R_{AB}^{(\varepsilon)}\right)\left(R_{BA}S+R_{BA}^{(\varepsilon)}\right)\end{aligned}\tag{7.15}$$

The r.h.s. terms are the coupling terms due to the base state deformation that couples Kelvin waves. All coefficients $(Q_A, Q_B, V_A, V_B, D_A, D_B, R_{AB}, R_{BA}, R_{AB}^{(\varepsilon)}, R_{BA}^{(\varepsilon)})$ depend on parameter W_0. The strain parameter S only depends on $\tilde{L} = L/r_A$. For a single helical vortex with a Batchelor profile,

$$S=-\frac{3}{16}\log\left(\frac{\tilde{L}}{\left(\tilde{L}^2+1\right)^{3/2}\varepsilon}\right)-\frac{\left(\tilde{L}^2+1\right)^2}{24\tilde{L}^2}-\frac{1}{4}\left(\tilde{L}^2+1\right)^2+\frac{1}{4}\tilde{L}\left(\tilde{L}^2+1\right)^{3/2}\tag{7.16}$$

$$+\frac{1}{96}\left(28\tilde{L}^2+11\right)+\sum_{m=1}^{\infty}R_m(\tilde{L}),\tag{7.17}$$

with the polynomial R_m

$$R_m(\tilde{L})\equiv\frac{\tilde{L}\left(\tilde{L}^2+1\right)^{3/2}}{2}+\frac{3}{16m}-\frac{\left(1+\tilde{L}^2\right)^3 m}{2\tilde{L}^2}\tag{7.18}$$

$$+\frac{m^2\left(\tilde{L}^2+1\right)^{5/2}}{\tilde{L}^3}\left(-I_{m-1}\left(\frac{m}{\tilde{L}}\right)+\tilde{L}I_m\left(\frac{m}{\tilde{L}}\right)\right)\left(K_{m-1}\left(\frac{m}{\tilde{L}}\right)+\tilde{L}K_m\left(\frac{m}{\tilde{L}}\right)\right)\tag{7.19}$$

$$+m\left(\tilde{L}^2+1\right)^{3/2}I_m\left(\frac{m}{\tilde{L}}\right)\left(K_{m-1}\left(\frac{m}{\tilde{L}}\right)+\tilde{L}K_m\left(\frac{m}{\tilde{L}}\right)\right).\tag{7.20}$$

Explicit expressions for coefficients $(Q_A, Q_B, V_A, V_B, D_A, D_B, R_{AB}, R_{BA}, R_{AB}^{(\varepsilon)}, R_{BA}^{(\varepsilon)})$ are given in table 2 in [Blanco-Rodríguez and Le Dizès, 2016] (corrected in [Blanco-Rodríguez and Le Dizès, 2017] by a factor 2 affecting R_{AB} and R_{BA}) for the three main unstable modes mentioned above and some specific velocity W_0 namely

- Case a: mode $(-1, 1, [1, 1])$ for $W_0 = 0.$;
- Case b: mode $(-2, 0, [2, 2])$ for $W_0 = 0.2$;
- Case c: mode $(-2, 0, [1, 1])$ for $W_0 = 0.4$;

Furthermore, an approximation provides the dependency of these coefficients with respect to W_0. It is given in the Appendix C in [Blanco-Rodríguez and Le Dizès, 2016] with corrections mentioned

in [Blanco-Rodríguez and Le Dizès, 2017]. We noticed that a minus sign is also missing for term Real(R_{BA}). This approximation differs with the specific values : for the elliptical mode $(-2, 0, [2, 2])$ on a helical vortex with $W_0 = 0.2$, $L = 0.3$ ($S = -0.7427$), $\varepsilon = 0.1$ and $Re = 10^4$, the approximate and exact coefficients are given in table 7.1. The two sets yield two theoretical growth rates (figure 7.3 left) and frequencies (figure 7.3 right): red lines are results based on exact coefficients, blue lines are based on the approximation of Appendix C. There exist differences of order 15%.

Coef.	Approximation	Exact
Q_A	$0.1250 + 0.0390\mathrm{i}$	$0.116 + 0.042\mathrm{i}$
Q_B	-0.0260	-0.027
V_A	$-16.7860 - 4.3200\mathrm{i}$	$-16.406 - 4.324\mathrm{i}$
V_B	-26.4360	-26.419
$D_A^{(\varepsilon)}$	$-0.3660 - 0.2460\mathrm{i}$	$-0.340 - 0.258\mathrm{i}$
$D_B^{(\varepsilon)}$	$-0.2692 + 0.0192\mathrm{i}$	$-0.283 + 0.019\mathrm{i}$
R_{AB}	$\mathbf{6.8000} + \mathbf{2.3800}\mathrm{i}$	$\mathbf{6.928} + \mathbf{2.424}\mathrm{i}$
R_{BA}	$\mathbf{-0.7420}$	$\mathbf{-0.824} + \mathbf{0.040}\mathrm{i}$
$R_{AB}^{(\varepsilon)}$	$0.6400 - 0.0220\mathrm{i}$	$0.542 - 0.027\mathrm{i}$
$R_{BA}^{(\varepsilon)}$	$-0.0466 + 0.0168\mathrm{i}$	$-0.057 + 0.025\mathrm{i}$

Table 7.1 – Coefficients in equation (7.21) cited from [Blanco-Rodríguez and Le Dizès, 2016] for elliptical mode (case b), The column "approximation" are values obtained with the expressions given in Appendix C, and column "exact" are given in Table 2. Numbers in bold are the corrected values as indicated in [Blanco-Rodríguez and Le Dizès, 2017].

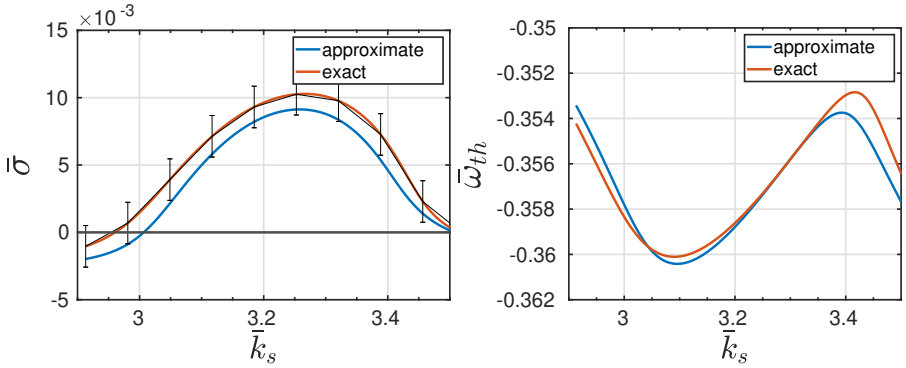

Figure 7.3 – Theoretical growth rate (left) and frequency (right) of elliptical mode $(-2, 0, [2, 2])$ obtained from equation (7.15) for a helical vortex with $L = 0.3$ ($S = -0.7427$), $W_0 \sim 0.2$, $Re = 10^4$ and $\varepsilon = 0.1$. The two sets of coefficients given in table 7.1 are used : red (resp. blue) line corresponds to exact (resp. approximated) coefficients. An error-bar with $15\%\sigma_{max}$ is added.

For zero torsion i.e. for a vortex ring, the theoretical growth rates computed using equation (7.15) have been validated by DNS results (see for instance the figures 9-12 showing different modes in [Hattori et al., 2019]). For non zero-torsion, unfortunately this equation (7.15) is not valid: some terms in the expansion that yields this equation, have been forgotten. To be more precise, the authors

in [Blanco-Rodríguez and Le Dizès, 2016] work in the non-orthogonal basis (r,φ,s). They forgot to introduce the dependency with respect to torsion of operators defined in their appendix B. For the elliptical resonance, this affects the values of coefficients in (7.15) originating from a modification of the linear operator of each Kelvin wave as well as the coupling coefficient due to the base state deformation in the r.h.s. of equation (7.15). In such a case, one needs to redo the computations. In the present thesis, we assume the dependency on torsion of the r.h.s. coefficient to be negligible and we simply use a trick to get free of charge, the correct coefficients due to the modification of l.h.s. terms! To do so, we use another viewpoint: if one works in the associated orthogonal basis (r,θ,s), the normal perturbations $\exp(\mathrm{i}ks+\mathrm{i}m\varphi)$ in the non-orthogonal basis (r,φ,s) reads with a shift of wavenumber along s due to torsion since

$$\mathrm{i}ks+\mathrm{i}m\varphi=\mathrm{i}(k-m\epsilon\frac{L}{r_A})s+\mathrm{i}m\theta\,.$$

This supplementary term precisely contains the dependency with respect to torsion τ. Because of a shift of wavenumber due to torsion [Hattori and Fukumoto, 2014], two terms in red should be added in equation (7.15):

$$\begin{aligned}&\left(\omega-\omega_c-\mathrm{i}\,\mathrm{Im}\,(\omega_A)-Q_A\left(\bar{k}-m_A\epsilon\frac{L}{r_A}-k_c\right)-\mathrm{i}\frac{V_A}{Re}-\varepsilon^2D_A^{(\varepsilon)}\right)\\&\times\left(\omega-\omega_c-\mathrm{i}\,\mathrm{Im}\,(\omega_B)-Q_B\left(\bar{k}-m_B\epsilon\frac{L}{r_A}-k_c\right)-\mathrm{i}\frac{V_B}{Re}-\varepsilon^2D_B^{(\varepsilon)}\right)\\=&\varepsilon^4\left(R_{AB}S+R_{AB}^{(\varepsilon)}\right)\left(R_{BA}S+R_{BA}^{(\varepsilon)}\right)\end{aligned}\tag{7.21}$$

One solves the problem anew: growth rates and frequencies are plotted in figure 7.4 for the elliptical mode $(-2,0,[2,2])$ with $L/R=0.3$, $|W_0|=0.2$ and $Re=10^4$. If one compares the growth rate and frequency with correction terms (equation (7.21) and red line) or without correction terms (equation (7.15) and black line), obvious differences are found : a shift in $\bar{k}$, but the maximum growth rate changes only slightly. Finally, note that equation (7.21) is valid for positive W_0 with $\bar{k}W_0>0$ or for negative W_0 with $\bar{k}<0$. For cases with $\bar{k}W_0<0$, if one changes the sign of ω and m, with the coefficient remains the same, the stability equation should also works.

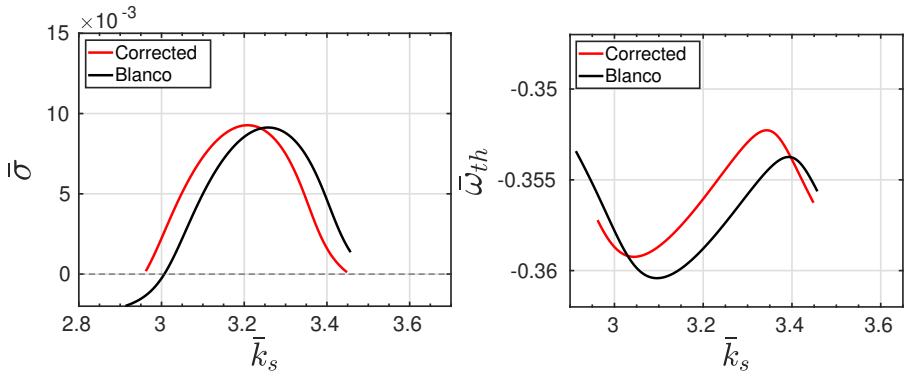

Figure 7.4 – Comparison of growth rate (left) and frequency (right) for elliptical mode $(-2,0,[2,2])$ given by equation (7.21) with $L/R=0.3$, $\epsilon=0.1$, $W_0=0.2$, $Re=10^4$ and approximate values of the coefficients. Black : original expression without terms $m\varepsilon L/R$. Red: new expression with two correction terms.

The asymptotic equation (7.21) provides an estimate for the interval of unstable wavenumbers worth

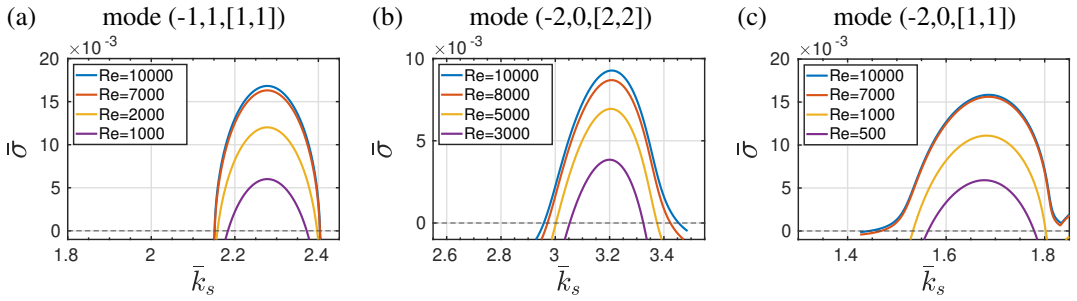

Figure 7.5 – Theoretical growth rates $\bar{\sigma}(\bar{k}_s)$ of elliptical modes given by equation (7.21) for helical vortex $\varepsilon = 0.1$, $L = 0.3$ and different Reynolds numbers Re.

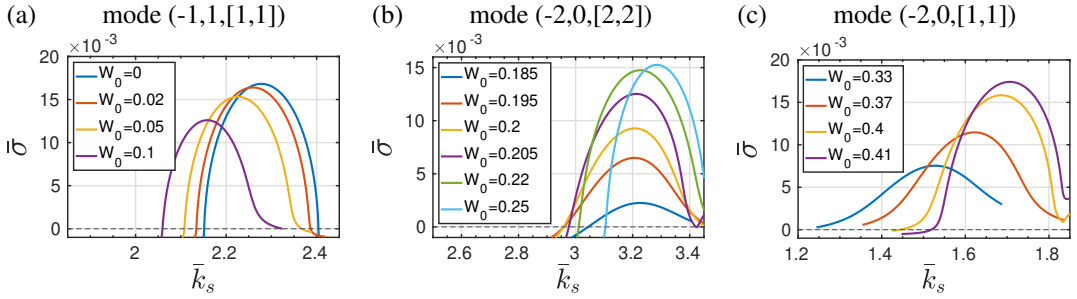

Figure 7.6 – Theoretical growth rate $\bar{\sigma}(\bar{k}_s)$ of elliptical modes given by equation (7.21) but with $\varepsilon = 0.1$, $L = 0.3$, $Re = 10^4$ and different W_0.

studying numerically in $\bar{k}_s$ space. For cases (a) , (b) and (c), figure 7.5 displays the dependency on Reynolds number of theoretical growth rates (helical vortex with $L = 0.3$ and $\varepsilon = 0.1$). It seems that above $Re = 10^4$, the growth rate does not change much. By contrast, growth rates are very sensitive to the jet value W_0 (figure 7.6). This is due to the presence of a critical layer damping.

7.2.2 Structure of the elliptical modes found by direct numerical simulation

We present numerical results of elliptical instability modes for different base states corresponding to a fixed Reynolds number $Re = 10^4$, $a_0 = 0.11$, $L = 0.3$ ($\varepsilon = 0.1$ from relation (4.41)) but different $\bar{W}_B$:

- mode A : branch (-1,1,[1,1]) for base state $[0.3; 0.11; 0]$ corresponding to $W_0 \approx 0.027$.
- mode B : branch (-2,0,[2,2]) for base state $[0.3; 0.11; 0.2]$ corresponding to $W_0 \approx 0.224$
- mode C : branch (2,0,[2,2]) for base state $[0.3; 0.11; -0.26]$ corresponding to $W_0 \approx -0.23$
- mode D : branch (-2,0,[1,1]) for base state $[0.3; 0.11; 0.4]$ corresponding to $W_0 \approx 0.427$.

More details on these base states can be found in table 5.4. The structures of these unstable modes are now presented, based on a Fourier decomposition revealing the azimuthal contributions m. The growth rates and frequencies are presented in the next section.

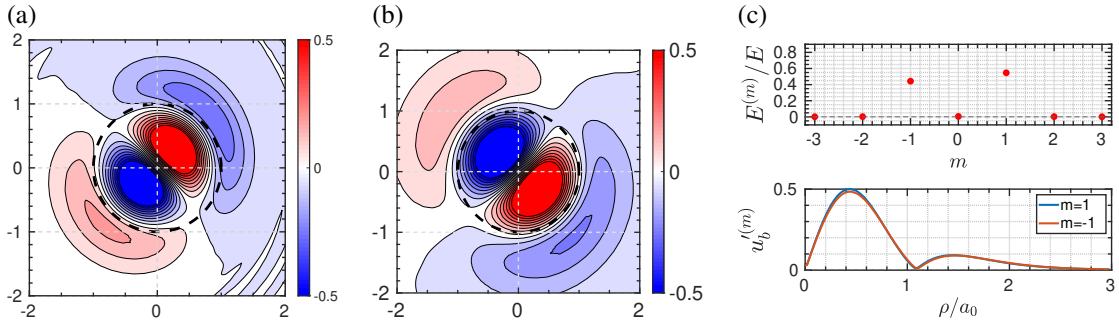

Figure 7.7 – The elliptical instability mode A with $Re = 10^4$ at $\bar{k}_s = 2.24$. (a) Contours of normalized azimuthal vorticity ω_B' in plane $\Pi_\perp$: $\omega_B' > 0$ (red), $\omega_B' < 0$ (blue), with extreme values ± 0.5. (b) Idem to (a) but for the normalized u_b'. (c) Fourier decomposition: (top) distribution of energy over modes m, (bottom) radial distribution of $u_b'^{(m)}$.

Elliptical mode A

The first unstable mode $(-1, 1, [1, 1])$ is studied with base state $[0.3; 0.11; 0]$, which contains a negligible axial jet component $W_0 = 0.027$. Figure 7.7 contains the main elements that identify the mode obtained at $\bar{k}_s = 2.24$. Graph 7.7(a) [resp. (b)] displays contours of the normalized vorticity component ω_B' (resp. normalized velocity component u_b') in plane $\Pi_\perp$; graph 7.7(c) displays the relative contribution of each mode (m) to the total energy, and graph 7.7(d) gives the radial distributions $u_b'^{(m)}(r)$ for the dominant azimuthal contributions, here $m = \pm 1$. On this latter graph, the radial structure of each wave reveals a single node typical for the branch labels $[1, 1]$. This node is also seen on the contours of ω_B' and u_b': the circle $\rho \approx a_0$ is undisturbed, while the interior is shifted in one direction and the external region in the opposite one. It shows the core structure deformation in the stretching direction due to the strain field from base state. Due to the fact that $W_0 \approx 0$, the two inertial waves are almost symmetric and each contains half of the energy.

Elliptical mode B

At larger axial flow ($W_0 = 0.224$), an elliptic mode B is found for base state $[0.3; 0.11; 0.2]$, represented for $\bar{k}_s = 3.25$ in figure 7.8. It is a branch $(-2, 0, [2, 2])$: the resonance now involves $m_A = -2$ and $m_B = 0$, and the radial structure reveals two nodes characteristic of branch labels $[2, 2]$. Again, the perturbation vanishes near the circle $\rho = a$.

Elliptical mode D

When $0.3 \leq W_0 \leq 0.5$, mode D become dominant. This is a branch $(-2, 0, [1, 1])$ obtained with base state $[0.3; 0.11; 0.4]$ ($W_0 = 0.427$).

Figure 7.9 displays the characteristics of this mode at $\bar{k}_s = 1.73$. The resonance involves $m_A = -2$ and $m_B = 0$, with a single node radially, which corresponds to branch labels $[1, 1]$. The radial structure shows that the perturbation does not vanish near $\rho = a$, contrarily to the two previous modes, and has a maximum at $\rho \approx 1.5a$. These three elliptical instability modes (A,B,D) are almost identical to the ones obtained by [Hattori et al., 2019] for vortex rings, however different energy distributions and radial functions are

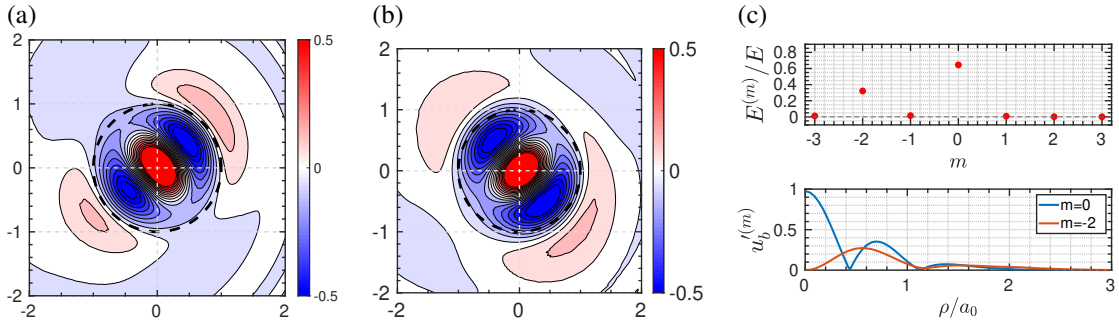

Figure 7.8 – The elliptic mode B with $Re = 10^4$ and $\bar{k}_s = 3.25$. Graphs are similar to those in figure 7.7.

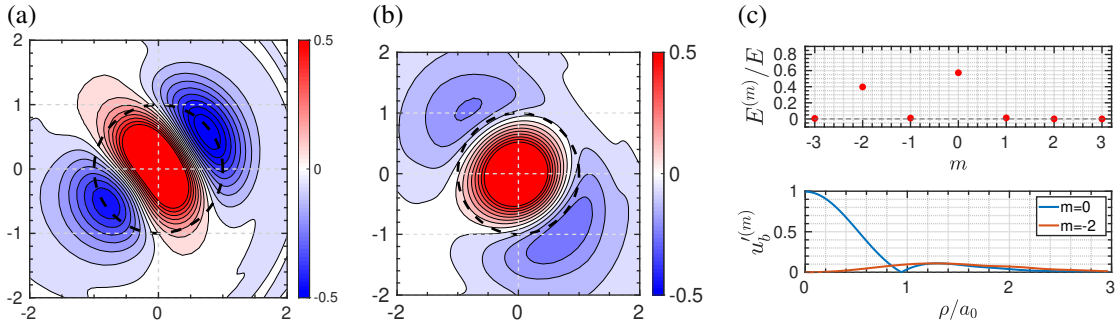

Figure 7.9 – The elliptical mode D with $Re = 10^4$ and $\bar{k}_s = 1.73$. Graphs are similar to those in figure 7.7.

found in all cases. Figure 7.10 displays a 3D visualization.

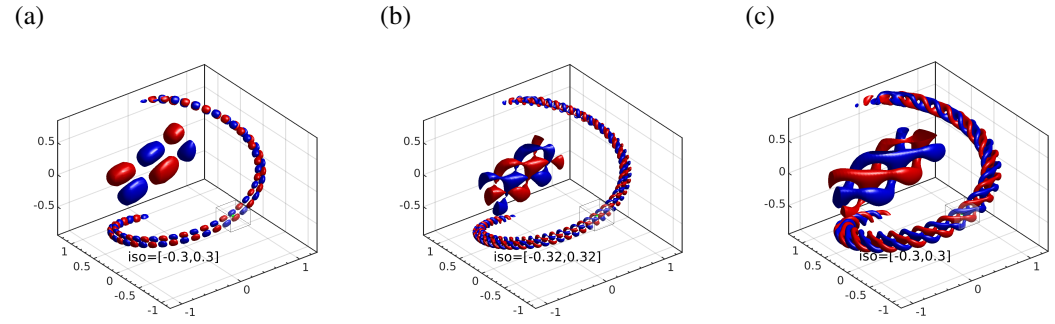

Figure 7.10 – 3D iso-surfaces of perturbation ω_B' for elliptical instability modes $(-1, 1, [1, 1])$, $(-2, 0, [2, 2])$ and $(-2, 0, [1, 1])$ corresponding to three different base states. Red and blue iso-surfaces correspond to ± 0.3 of the maximum. A close-up is presented in the central part of the plots.

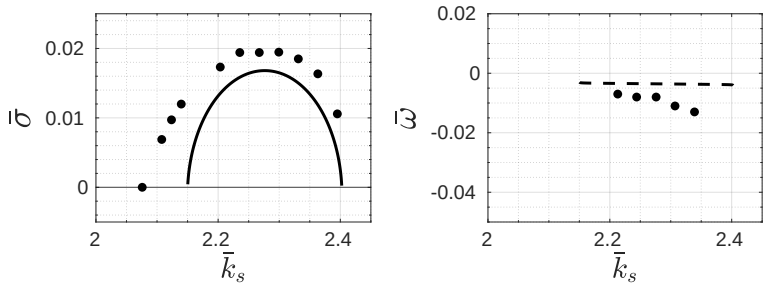

Figure 7.11 – Growth rate $\bar{\sigma}$ (left, solid line) and frequency $\bar{\omega}$ (right, dashed line) obtained by theory equation 7.21 and DNS results (dots) for elliptical mode A with $Re = 10^4$ and base state $[0.3; 0.11; 0.]$ ($W_0 \sim 0.03$).

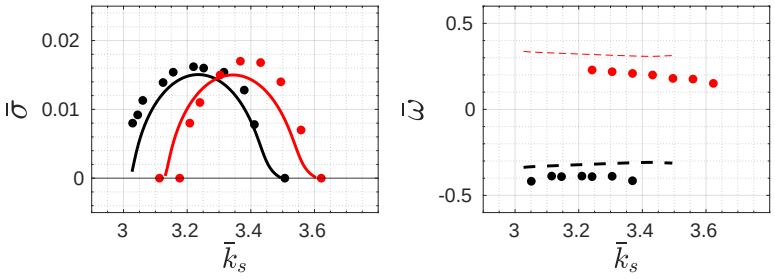

Figure 7.12 – Growth rate $\bar{\sigma}$ and frequency $\bar{\omega}$ for mode B (black line or black dots) or mode C (red dots). The branch is in both cases a branch $(-2, 0, [2, 2])$ but for mode B with $W_0 \sim 0.23$ and mode C with $W_0 \sim -0.23$. Lines and symbols similar to those in figure 7.11.

7.2.3 Growth rates and frequencies for elliptical modes

We present growth rates and frequencies of the three main elliptical modes. All base states have same core size $a = 0.11$ and reduced pitch $L = 0.3$, but different axial jet parameter W_0. In figure 7.11, values found for the elliptical mode A are plotted. The theoretical growth rate $\bar{\sigma}$ (left) or frequency (right) are displayed : dots are DNS results and solid or dashed lines are obtained from equation (7.21). A fair agreement between numerical results and theory (7.21) is found (theoretical values however are obtained from estimated coefficients, which are uncertained of 15%).

Figure 7.12 gives a similar representation for base states $[0.3; 0.11; -0.26]$ ($W_0 = -0.2236$, red) and $[0.3; 0.11; 0.2245]$ ($W_0 = 0.2301$, black). This agreement between DNS results and theory 7.21 is rather satisfactory (note that only $W_0 \approx 0.23$ could be compared). The effect of torsion, proves here to be important for both the wavenumber of maximum amplification and the value of the maximum growth rate. Unfortunately, we could not compare with the theory for mode C since $W_0 \approx -0.23$.

A similar agreement is found for mode D (see figure 7.13), however with a small shift between theoretical and DNS results.

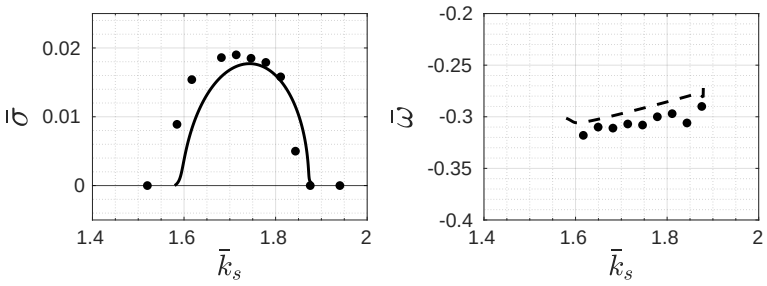

Figure 7.13 – Growth rate $\bar{\sigma}$ and frequency $\bar{\omega}$ for elliptical mode D. Lines and symbols are similar to those in figure 7.11.

7.3 Curvature instability

Curvature deforms the core structure of a vortex ring and yields short-wave instability modes [Fukumoto and Hattori, 2005, Hattori and Fukumoto, 2003]. In such a case, a resonance or a near-resonance occurs between two Kelvin modes of characteristics (ω_A, k_A, m_A) and (ω_B, k_B, m_B) *via* the dipolar deformation of the core in $\cos(\theta)$. This implies that, as for the elliptic instability, $k_A = k_B$, $\omega_A \sim \omega_B$ but now the azimuthal wave numbers are such that $m_A = m_B - 1$ which differs from the elliptic instability resonance.

7.3.1 Asymptotic theory

The curvature instability mode theoretically exists for helical vortices, as shown on a helical Rankine vortex tube by [Hattori and Fukumoto, 2014]. Recently, [Blanco-Rodríguez and Le Dizès, 2017] analysed the curvature instability of a curved Batchelor vortex. The theoretical stability analysis provided the formulae for the complex frequency ϖ

$$\left[\varpi - \omega_c - Q_A\left(\bar{k} - k_c\right) - \mathrm{i}\frac{V_A}{Re}\right]\left[\varpi - \omega_c - \mathrm{i}\,\mathrm{Im}\left(\omega_B\right) - Q_B\left(\bar{k} - k_c\right) - \mathrm{i}\frac{V_B}{\mathrm{Re}}\right] = \varepsilon^2 C_{AB} C_{BA} \tag{7.22}$$

with constants $(Q_A, Q_B, V_A, V_B, C_{AB}, C_{BA}, R_{AB}, R_{BA})$ depending only on the axial jet amplitude W_0. They showed that the combination of modes $m_A = 0$ and $m_B = 1$ becomes the most unstable for moderate viscosity, and that without axial flow, the elliptic instability is always dominant. The situation is different in the presence of an axial flow W_0: the region of the (ε,Re) plane where the curvature instability dominates over the elliptical instability (see figure 9 of [Blanco-Rodríguez and Le Dizès, 2017]) changes for different axial flow intensity.

For zero torsion i.e. for vortex rings, this theoretical evaluation has been validated, both the structure and the growth rate of the unstable modes are found to be in good agreement [Hattori et al., 2019]. When torsion is present as in helical vortices, for the same reasons which imposed to modify the elliptical instability, correction terms (in red) should be added to the original expression (7.22) estimating the complex frequency $\varpi = \omega - \mathrm{i}\sigma$ as a function of the axial wavenumber $\bar{k} = \bar{k}_s$:

$$\left(\varpi - \omega_c - Q_A\left(\bar{k} - m_A\epsilon\frac{L}{R} - k_c\right) - \mathrm{i}\frac{V_A}{Re}\right)\left(\varpi - \omega_c - \mathrm{i}\,\mathrm{Im}\left(\omega_B\right) - Q_B\left(\bar{k} - m_B\epsilon\frac{L}{R} - k_c\right) - \mathrm{i}\frac{V_B}{\mathrm{Re}}\right) = \varepsilon^2 C_{AB} C_{BA}\,. \tag{7.23}$$

For the curvature instability, the equation is obtained at first order instead of at second order. In that case the r.h.s. terms represents the coupling terms with the base state deformation while the l.h.s. is the product of two terms each one representing the dispersion curve for each one of the two Kelvin waves. Only the latter product is thus affected inside the corrected version which estimates the complex frequency ϖ as a function of the axial wavenumber $\bar{k} = \bar{k}_s$. As a consequence, by contrast with the elliptical instability, the above modification is sufficient to take into account the effects of torsion.

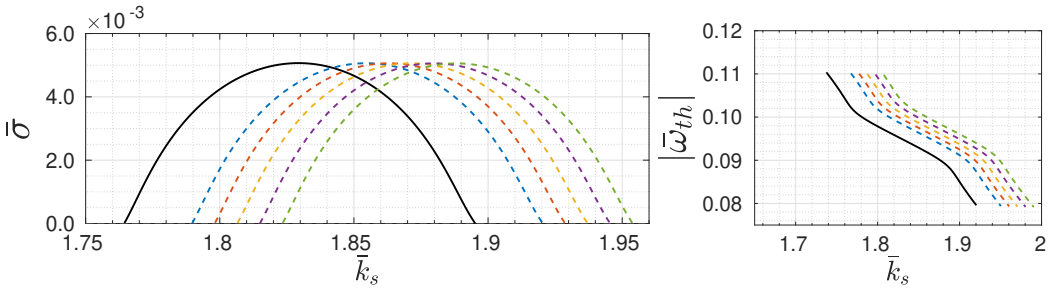

Figure 7.14 – Theoretical growth rate $\bar{\sigma}$ (left) and absolute frequency $|\bar{\omega}_{th}|$ (right) of the curvature mode $(-1, 0, [2, 4])$ for base state with $\varepsilon = 0.1$, $Re = 10^4$ and $W_0 = -0.2$ (solid line given by equation 7.22). Corrected curves (dashed lines given by equation 7.23) with $L = 0.3$ (blue); $L = 0.4$ (red); $L = 0.5$ (yellow); $L = 0.6$ (purple); $L = 0.7$ (green).

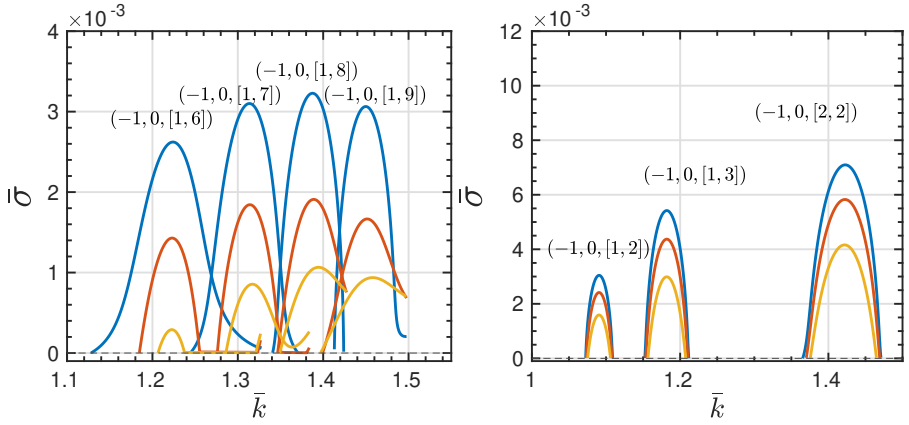

Figure 7.15 – Theoretical growth rate $\bar{\sigma}$ of curvature modes $(-1, 0, [l_A, l_B])$ given by equation (7.23) for a base helical vortex with $\varepsilon = 0.1$, $L = 0.7$ and (Left) $W_0 = 0$ the blue line corresponds to Reynolds $Re = 10^6$ and red to $5 \cdot 10^5$, yellow to $3 \cdot 10^5$. (Right) $W_0 = -0.4$ the blue line corresponds to Reynolds $Re = 10^4$ and red to $5 \cdot 10^3$, yellow to 10^3.

Note that equation (7.23) is valid for positive W_0 with $\bar{k} W_0 < 0$ or for negative W_0 with $\bar{k} > 0$, but not cases where $\bar{k} W_0 > 0$. For example, case A and B in table 7.2 are equivalent. One example case is plotted in figure 7.14. Based on equation (7.23), the growth rate of dominant modes has been plotted for various Re values and axial flows $W_0 = 0$ and -0.4 (figure 7.15). Compared to the elliptical instability, the growth rate of curvature instability is much weaker in a vast majority of cases. Only in specific circumstances (small ε and high Re), curvature instability is found to dominate the flow evolution, which makes it difficult to implement in the real situation. To the best of our knowledge, no experimental study has succeeded yet in evidencing curvature instability.

Case	Mode	W_0	k_c	ω_c
A	$(0,1,[3,1])$	0.2	−1.14	0.11
B	$(-1,0,[1,3])$	−0.2	1.14	−0.11

Table 7.2 – Symmetrical cases A and B, involving similar modes for opposite axial jet directions.

7.3.2 Curvature modes for the base state $[0.7;0.15;0.13]$ ($W_0 = 0.2$).

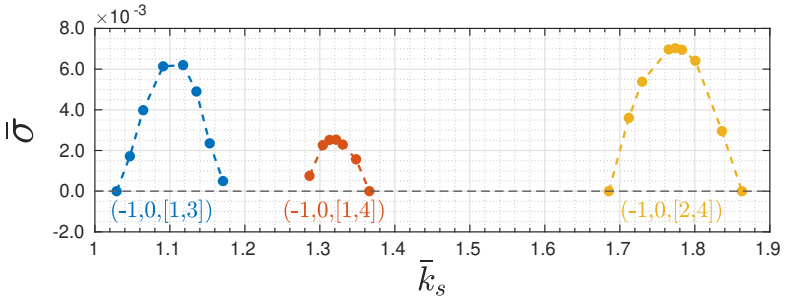

Figure 7.16 – Growth rate $\bar{\sigma}$ obtained by DNS as a function of wavenumber $\bar{k}_s$ (dashed-dot lines) for base state $[0.7;0.150;0.13]$ ($W_0 \approx 0.2$) with $Re = 10^4$. Different colors correspond to different modes: $(-1,0,[1,3])$ (blue) ; $(-1,0,[1,4])$ (red); $(-1,0,[2,4])$ (yellow).

The stability properties of base state $[0.7;0.150;0.13]$ ($W_0 \approx 0.2$) are here studied. Figure 7.16 displays the growth rates obtained numerically versus the wavenumber $\bar{k}_s$. Three dominant branches are found for wavelengths $\bar{k}_s \leq 4$ and $Re = 10^4$, namely near $\bar{k}_s = 1.1$ for mode $(-1,0,[1,3])$ (blue), near $\bar{k}_s = 1.3$ for mode $(-1,0,[1,4])$ (red) and near $\bar{k}_s = 1.8$ for mode $(-1,0,[2,4])$ (yellow). The asymptotic theory for $W_0 = -0.2$ (see figure 7.17) predicts the same three dominant modes but for slightly shifted wavenumbers (see below figure 7.25).

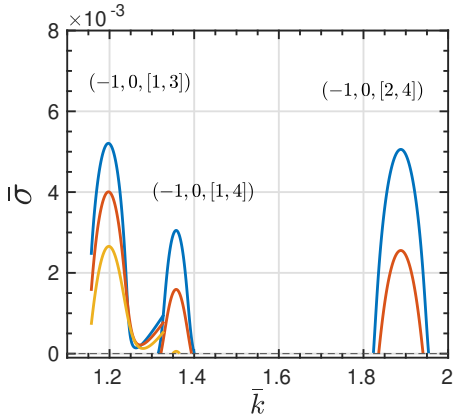

Figure 7.17 – Theoretical growth rate $\bar{\sigma}$ of curvature modes $(-1,0,[l_A,l_B])$ given by equation (7.23) for a base helical vortex with $\varepsilon = 0.1$, $L = 0.7$ and $W_0 = -0.2$. Blue line corresponds to Reynolds $Re = 10^4$, red to $5 \cdot 10^3$ and yellow to 10^3.

Figure 7.18(a) (resp. figure 7.18 b) reveals the structure in plane $\Pi_\perp$ of the perturbation vorticity component ω'_B (resp. u'_b) corresponding to a curvature mode $(-1,0,[1,3])$ with $\bar{k}_s = 1.1$. Since the resonance involves

two modes with very different radial structures (figure 7.18 (c) bottom graph), the the obtained perturbation has itself a quite complex structure. The energy distribution confirms the dominant contributions $m = -1$ and $m = 0$. Compared to the results for a ring vortex [Hattori et al., 2019], a good agreement is found.

Figure 7.19 shows the structure of a third mode $(-1, 0, [2, 4])$. When comparing to the case of vortex rings [Hattori et al., 2019], the agreement is fair, but slight differences are observed: the amplitude of the first peak in the radial structure of u_b' for mode $(m = -1)$ (orange line) is close to 0.4 (at $\bar{\rho} \approx 0.3$) while it is 0.7 for vortex rings. This also implies differences in the energy distribution. This may be a torsion effect affecting slightly the structure of this unstable mode.

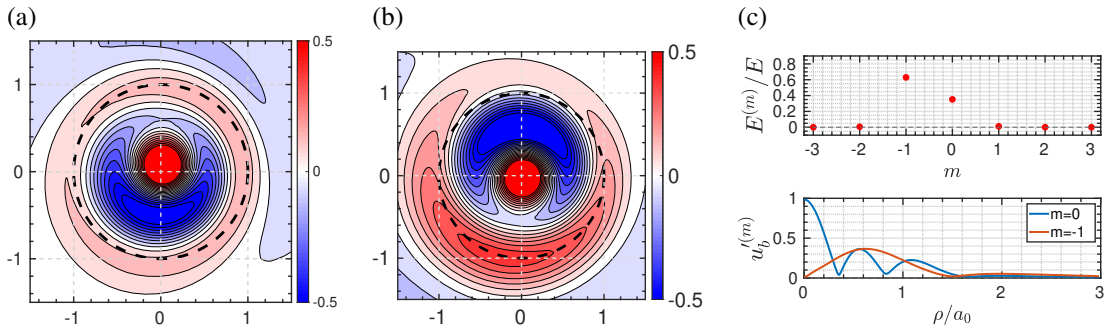

Figure 7.18 – The contours of curvature instability mode $(-1, 0, [1, 3])$ with $\bar{k}_s = 1.1$ of the base state $[0.7; 0.150; 0.13]$ ($W_0 \approx 0.2$). Visualization is similar to figure 7.7.

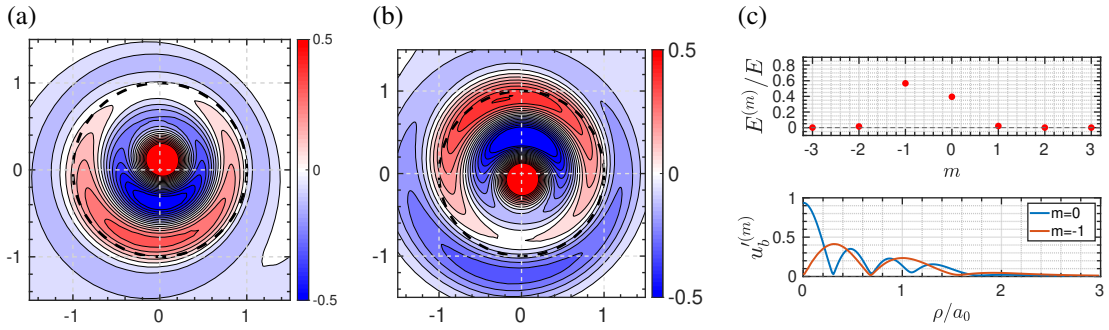

Figure 7.19 – Same as figure 7.18 ($W_0 \approx 0.2$) but for curvature instability mode (-1,0,[2,4]) with $\bar{k}_s = 1.7$.

The 3D structures of these two curvature modes are plotted in figure 7.20.

Growth rates obtained for larger wavenumbers $\bar{k}_s \in (2, 3.1)$ are presented in figure 7.21 (top graph). Based on the structure of these modes (bottom graphs) and their theoretical unstable region (predicted by [Blanco-Rodríguez and Le Dizès, 2017]), one concludes that these modes are identified. However, they are not our main focus and are actually difficult to capture due to weak growth rates and complex structures: well-converged results would require a much more refined mesh and a longer simulation times. These modes are not investigated further in the following.

In addition, we studied a larger axial velocity $W_0 \approx 0.32$ and $W_0 \approx 0.27$. The value $W_0 \approx 0.32$ corresponds to the base state $[0.7; 0.15; 0.25]$, the value $W_0 \approx 0.32$ to the base state $[0.7; 0.150; 0.2]$.

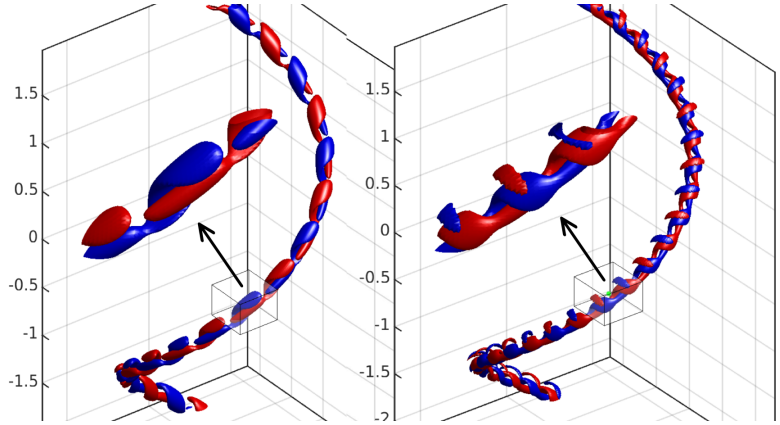

Figure 7.20 – 3D iso-contours of perturbation ω'_B for curvature instability modes $(-1, 0, [1, 3])$, and $(-1, 0, [2, 4])$ for base state $[0.7; 0.150; 0.13]$ ($W_0 \approx 0.2$). Red and blue iso-surfaces correspond to ± 0.3 of the maximum.

For $W_0 \approx 0.32$ and $Re = 10^4$, the unstable wavenumbers are such that $\bar{k}_s \leq 2.5$. Near the first mode $(-1, 0, [1, 3])$, another mode $(-1, 0, [1, 2])$ is found with $\bar{k}_s = 0.95$, which is also predicted by the theory. The structure of this mode is much simpler, as shown in figure 7.22: a slightly off-centered vorticity region (positive) is surrounded by a region of opposite values (negative), the radial extent of the mode being comparable to the size of the vortex core a.

In addition, we studied the base state $[0.7; 0.15; 0.2]$ ($W_0 \approx 0.27$) for wavenumbers $\bar{k}_s \leq 2.5$ and $Re = 10^4$. Figure 7.23 show 4 unstable modes found, plotted in blue for mode $(-1, 0, [1, 3])$, orange for mode $(-1, 0, [1, 2])$, yellow for mode $(-1, 0, [2, 3])$ and purple for mode $(-1, 0, [3, 4])$. The mode $(-1, 0, [2, 4])$ is not found for the numerical simulation, and is replaced by the modes $(-1, 0, [2, 3])$ and $(-1, 0, [3, 4])$.

7.3.3 The effect of jet strength

We investigated the effect of the jet strength for a range of wavenumbers $\bar{k}_s \in (0.9, 1.4)$. Three base states

- $[0.7; 0.15; 0.13]$ for $W_0 \approx 0.2$
- $[0.7; 0.15; 0.20]$ for $W_0 \approx 0.27$
- $[0.7; 0.15; 0.25]$ for $W_0 \approx 0.32$.

are used, leading to $W_0 \approx 0.2$, 0.27 and 0.32. Growth rates obtained by DNS are plotted in figure 7.24. One observes that, as W_0 increases, the mode $(-1, 0, [1, 4])$ becomes stable and the mode $(-1, 0, [1, 2])$ becomes unstable, which is in a good agreement with theoretical predictions as shown from figure 7.15 (right, $W_0 = 0.4$ at $\bar{k} \sim 1.4$) to figure 7.17 ($W_0 = 0.2$).

7.3.4 The effect of torsion by varying the pitch

The effect of torsion was investigated on mode $(-1, 0, [2, 4])$ by varying the reduced pitch of the base state:

$$L \in \{0.7, 0.6, 0.5, 0.4, 0.3\},$$

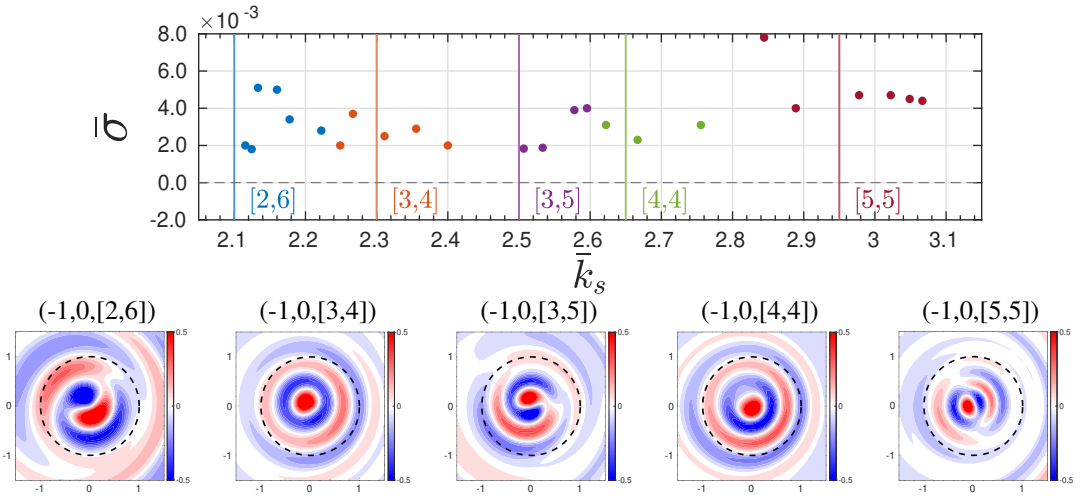

Figure 7.21 – Top: growth rates obtained by DNS for "weaker" curvature modes (dots) of base state $[0.7; 0.150; 0.13]$ ($W_0 \sim 0.2$) with $Re = 10^4$. Different colors correspond to different modes, and vertical lines indicate the theoretical resonant wavenumber $\bar{k}_c$ of each modes. Bottom: contours of ω'_B for each mode, visualizations are similar to those of figure 7.7.

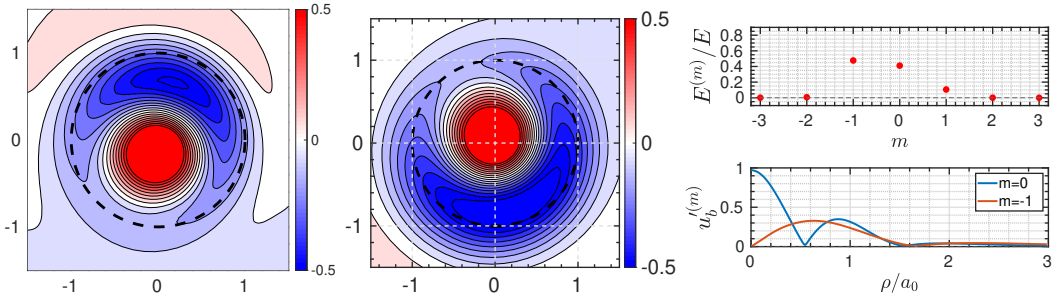

Figure 7.22 – Same as figure 7.18 but for curvature instability mode $(-1, 0, [1, 2])$ with base state $[0.7; 0.15; 0.25]$ ($W_0 \approx 0.32$) and $\bar{k}_s = 0.95$.

fixing the jet strength to be $W_0 = \pm 0.2$ and fixing $\varepsilon = 0.1$ (the core size a is adapted to satisfy this value) One uses the following base states to investigate the role of the axial flow direction, these base states have same pitches and core sizes but $W_0 \approx -0.2$ or $W_0 \approx 0.2$:

- $[0.7; 0.15; 0.13]$ and for negative W_0 $[0.7; 0.150; -0.27]$
- $[0.6; 0.136; 0.14]$ and for negative W_0 $[0.6; 0.136; -0.26]$
- $[0.5; 0.125; 0.15]$ and for negative W_0 $[0.5; 0.125; -0.25]$
- $[0.4; 0.116; 0.16]$ and for negative W_0 $[0.4; 0.116; -0.24]$

These states are already listed in table 5.4. In addition the Reynolds number $Re = 10^4$ is adopted for the dynamics of the perturbations.

In figure 7.25, the growth rates for base states $[0.7; 0.15; 0.13]$ and $[0.7; 0.15; -0.26]$ are plotted. Since

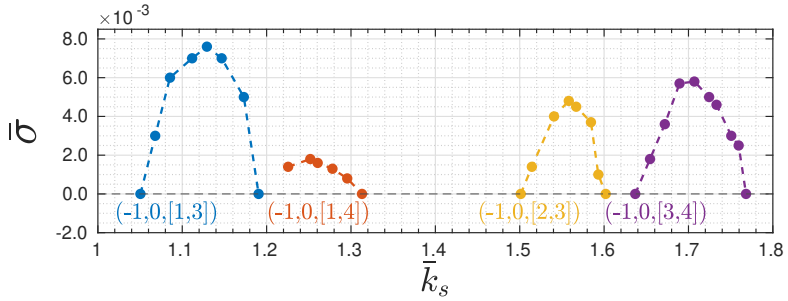

Figure 7.23 – Growth rate $\bar{\sigma}$ obtained by DNS as a function of wavenumber $\bar{k}_s$ for state $[0.7; 0.150; 0.2]$ ($W_0 \approx 0.27$) at $Re = 10^4$.

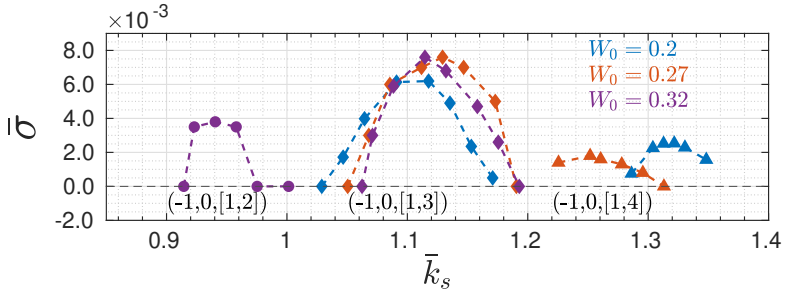

Figure 7.24 – Growth rates of curvature instability modes obtained by DNS for base states $[0.7; 0.150; W^B]$ with $\bar{k}_s \in (0.9, 1.4)$ and $Re = 10^4$. Different colors correspond to different axial velocity parameter values W_0: $W_0 \approx 0.2$ (blue); $W_0 \approx 0.27$ (orange); $W_0 \sim 0.32$ (purple). Dots: mode $(-1, 0, [1, 2])$; diamonds: mode $(-1, 0, [1, 3])$; triangles: mode $(-1, 0, [1, 4])$.

both states have identical parameters $\varepsilon = 0.1$, $L = 0.7$, $Re = 10^4$, similar core sizes, the two opposite axial velocities (see exact values in Table 5.4) lead to two opposite values of torsion. Two effects are seen when going from $W_0 = 0.2$ to -0.2: the increase of the most unstable wavenumber by 10%, and the decrease of the maximum growth rate by a factor of 2. The shift of the most unstable wavenumber is also observed for the cases at $L = 0.6$, 0.5 and 0.4, as shown in figures 7.25–7.25. The variations of the growth rate seem however different.

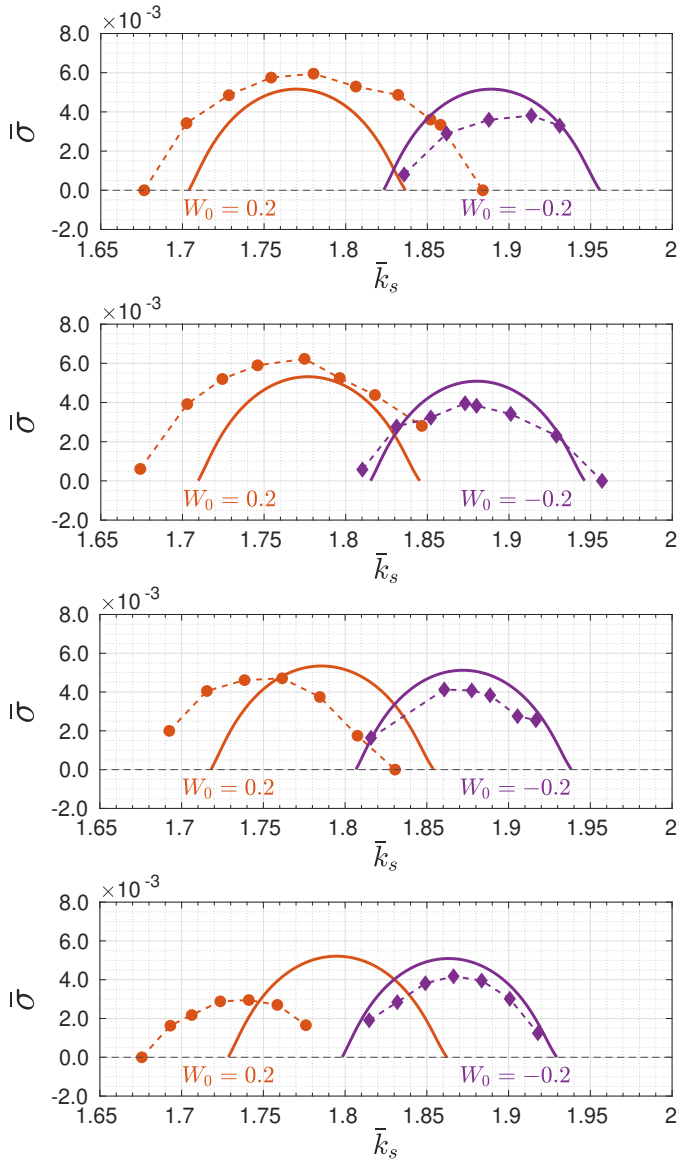

Figure 7.25 – Growth rate $\bar{\sigma}$ obtained by DNS for base state $[0.7; 0.15; 0.13]$ (circles) of curvature mode $(-1, 0, [2, 4])$ and for $[0.7; 0.15; -0.26]$ (diamonds) of curvature mode $(1, 0, [4, 2])$. From top to bottom $L = 0.7$, $L = 0.6$, $L = 0.5$, $L = 0.4$. The (purple) solid line is the theoretical estimation from equation 7.23 only available for $W_0 \approx -0.2$.

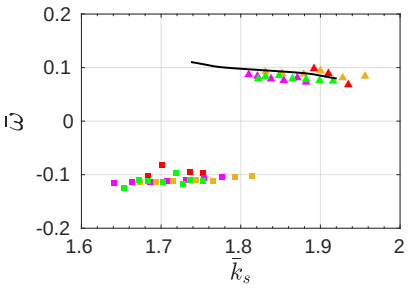

Figure 7.26 – Frequencies $\bar{\omega}$ for the instability modes of base states $W_0 \approx \pm 0.2$, $\varepsilon = 0.1$, $Re = 10^4$. Different colors correspond to different pitch values: $L = 0.4$ (green), 0.5 (magenta), 0.6 (yellow), 0.7 (red). The colored squares (resp. triangles) correspond to DNS results with $W_0 \approx 0.2$ (resp. -0.2). The black curve corresponds to theoretical frequency given by [Blanco-Rodríguez and Le Dizès, 2017] where L is not taken into account ($L = 0$).

Part II

Instabilities of two-phase vortices

Chapter 8

Introduction of two-phase flows vortex dynamics

In the first part of the thesis, we studied the stability of monophasic vortices but in a complex geometrical configuration. In the second part, we consider vortices in two-phase flows but in simpler configurations: a two-phase straight or toroidal vortex. Such a situation is found for a liquid jet subjected to rotation. The stability of such a flow is important for industrial design or safety analysis, including liquid atomization, nozzle type spray, and combustion processes, jet imprint technology, among others.

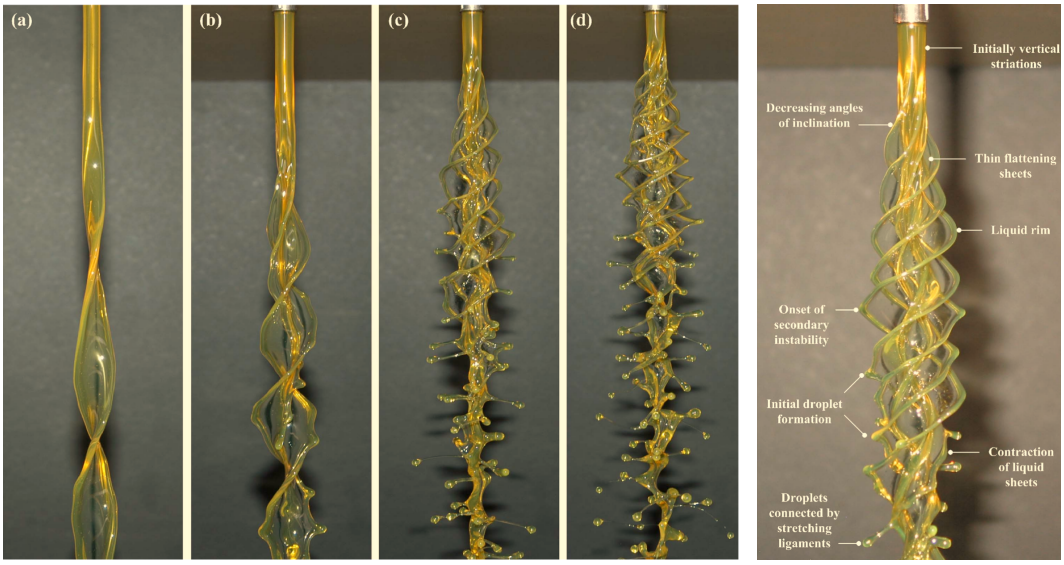

Figure 8.1 – Experimental images of a rotating jet instabilities for azimuthal wavenumber varying from $m = 2$ to $m = 5$, cited from [Kubitschek and Weidman, 2007b] (left) figure 4 and (right) figure 12.

An appropriate azimuthal velocity profile may modify the stability propriety of a liquid or gas jet, since a

centrifugal force is added to the surface tension. This stability problem has been studied for the last seventy years. [Hocking and Michael, 1959] considered an inviscid liquid jet with surface tension coefficient γ, density ρ, initial radius R_0. destabilized by a perturbation of azimuthal mode numbers m and axial mode $k = 0$, when the liquid jet was rotated at a large enough angular rotation rate Ω. Specifically the stability criterion was

$$\frac{1}{L} \leqslant m(m+1), \quad \text{with} \quad L \equiv \frac{\gamma}{\rho R_0^3 \Omega^2} \tag{8.1}$$

In subsequent studies, Hocking showed that the stability criterion of an inviscid or a highly viscous liquid jet to axisymmetric $m = 0$ perturbations can be expressed by:

$$\frac{1}{L} \leqslant \bar{k}^2 - 1 \quad \text{with} \quad \bar{k} = kR_0 \tag{8.2}$$

[Gillis and Kaufman, 1962] gives the general stability criterion for three dimension disturbances on a highly viscous jet:

$$\frac{1}{L} \leqslant \bar{k}^2 + m^2 - 1 \tag{8.3}$$

Thirty years later, [Weidman et al., 1997] quantified the dependency of the dominant azimuthal mode for a two-phase axisymmetric rotating system with respect to the Reynolds number Re. An investigation of the linear stability of a uniform rotating viscous liquid jet has been done by Kubitschek and Weideman later, they validated their theoretical prediction [Kubitschek and Weidman, 2007a] from an experimental perspective [Kubitschek and Weidman, 2007b](results shown in Figure 8.1). In more general cases, helical instability will dominate the flow and the surface disturbance is usually not axisymmetric. The dominating mode of helical instability depends on Re number and the rotation speed [Kubitschek and Weidman, 2007a].

In this second part, the linear and non-linear instability of a liquid jet in the presence of an azimuthal velocity profile are investigated with two numerical tools: a house-made linear stability code extended for two-phase flows during this thesis and the Basilisk solver [Popinet, 2015] to study the non-linear behavior of the instability. In Chapter 9, the governing equations of two-phase fluids and several different stable states are introduced. In Chapter 10, the governing equations are linearized and changed into an eigenvalue problem with normal modes analysis. It is then discretized using a spectral decomposition in both phases separately, and yields a general eigenvalue problem. In Chapter 11, the code is validated with some known solutions. The dispersion relations for the axisymmetric case in the presence of azimuthal velocity is then investigated. Later results are compared with the DNS method in chapter 12, where also non-axisymmetric non-linear evolution are discussed for the liquid jet.

In chapter 13, one also presents the formation and evolution of a toroidal bubble. We simply reproduce the article "Instability of a swirling bubble ring".

Chapter 9

Equations for a two-phase columnar flow

Contents

9.1 Governing equations

9.1.1 Dimensional equations

In this section we present the governing equations for a two-phase columnar flow. This flow is composed of a fluid core denoted as fluid $k = 1$, surrounded by a fluid of different nature denoted as fluid $k = 2$. Both fluids are incompressible, with uniform and constant densities $\rho^{(k)}$ and viscosities $\mu^{(k)}$. We write the Navier–Stokes equation within each fluid ($k = 1$ or 2):

$$\nabla \cdot \boldsymbol{u}^{(k)} = 0 \tag{9.1}$$

$$\rho^{(k)} \left[\frac{\partial \boldsymbol{u}^{(k)}}{\partial t} + (\boldsymbol{u}^{(k)} \cdot \nabla)\boldsymbol{u}^{(k)} \right] = -\nabla p^{(k)} + \mu^{(k)} \nabla^2 \boldsymbol{u}^{(k)} \tag{9.2}$$

where $p^{(k)}$ stands for the pressure, that may include gravity effects. In the following, whenever there is no ambiguity, we remove the reference (k) to the fluid.

It is convenient to write the equation system using cylindrical coordinates, with unit vectors $\boldsymbol{e}_x$ along the jet axis i.e. , $\boldsymbol{e}_r$ along the radial direction and $\boldsymbol{e}_\theta$ along the azimuth. Both fluids extend to infinity along the

axial direction, and fluid 2 extends to infinity along the radial direction. The momentum equations read:

$$\rho \frac{\mathrm{D}u_x}{\mathrm{D}t} = -\frac{\partial p}{\partial x} + \mu \nabla^2 u_x \tag{9.3}$$

$$\rho\left(\frac{\mathrm{D}v_r}{\mathrm{D}t} - \frac{w_\theta^2}{r}\right) = -\frac{\partial p}{\partial r} + \mu\left(\nabla^2 v_r - \frac{v_r}{r^2} - \frac{2}{r^2}\frac{\partial w_\theta}{\partial \theta}\right) \tag{9.4}$$

$$\rho\left(\frac{\mathrm{D}w_\theta}{\mathrm{D}t} + \frac{v_r w_\theta}{r}\right) = -\frac{1}{r}\frac{\partial p}{\partial \theta} + \mu\left(\nabla^2 w_\theta - \frac{w_\theta}{r^2} + \frac{2}{r^2}\frac{\partial v_r}{\partial \theta}\right) \tag{9.5}$$

where (u_x, v_r, w_θ) are the axial, radial and azimuthal cylindrical components of the velocity field $\boldsymbol{u}$, where $\mathrm{D}/\mathrm{D}t$ stands for the convective derivative:

$$\frac{\mathrm{D}}{\mathrm{D}t} \equiv \frac{\partial}{\partial t} + u_x \frac{\partial}{\partial x} + v_r \frac{\partial}{\partial r} + \frac{w_\theta}{r}\frac{\partial}{\partial \theta} \tag{9.6}$$

and ∇^2 represent the scalar cylindrical Laplacian:

$$\nabla^2 \Phi \equiv \frac{\partial^2 \Phi}{\partial x^2} + \frac{\partial^2 \Phi}{\partial r^2} + \frac{1}{r}\frac{\partial \Phi}{\partial r} + \frac{1}{r^2}\frac{\partial^2 \Phi}{\partial \theta^2}\,. \tag{9.7}$$

Incompressibility in cylindrical coordinates is expressed as:

$$\frac{\partial u_x}{\partial x} + \frac{1}{r}\frac{\partial (r v_r)}{\partial r} + \frac{1}{r}\frac{\partial w_\theta}{\partial \theta} = 0\,. \tag{9.8}$$

In the present columnar configuration, the interface between the two fluids is a surface that we assume to be described by its radial location ζ:

$$r = \zeta(\theta, x, t)\,. \tag{9.9}$$

This interface is characterized by an outward normal $\boldsymbol{n}$ (pointing from fluid 1 to fluid 2):

$$\boldsymbol{n} = \frac{(1, -\frac{1}{\zeta}\frac{\partial \zeta}{\partial \theta}, -\frac{\partial \zeta}{\partial x})}{\sqrt{1 + (\frac{\partial \zeta}{\partial x})^2 + (\frac{1}{\zeta}\frac{\partial \zeta}{\partial \theta})^2}}\,. \tag{9.10}$$

and two tangential vectors:

$$\boldsymbol{t}_\theta = \frac{(\frac{1}{\zeta}\frac{\partial \zeta}{\partial \theta}, 1 + (\frac{\partial \zeta}{\partial x})^2, -\frac{1}{\zeta}\frac{\partial \zeta}{\partial x}\frac{\partial \zeta}{\partial \theta})}{\sqrt{(\frac{1}{\zeta}\frac{\partial \zeta}{\partial \theta})^2 + (1 + (\frac{\partial \zeta}{\partial x})^2)^2 + (\frac{1}{\zeta}\frac{\partial \zeta}{\partial \theta}\frac{\partial \zeta}{\partial x})^2}} \qquad \boldsymbol{t}_x = \frac{(\frac{\partial \zeta}{\partial x}, 0, 1)}{\sqrt{1 + (\frac{\partial \zeta}{\partial x})^2}} \tag{9.11}$$

such that $(\boldsymbol{n}, \boldsymbol{t}_\theta, \boldsymbol{t}_x)$ forms an orthonormal basis.

A kinematic boundary condition comes from the fact that the radial velocity of fluid particles at the interface must be compatible with the velocity of the interface itself. If we assume that the fluid particles which are located on the interface remain on it at subsequent times, mathematically we differentiate equation (9.9) with respect to time:

$$\frac{\mathrm{d}r}{\mathrm{d}t} = \frac{\mathrm{d}\zeta}{\mathrm{d}t} \equiv \frac{\partial \zeta}{\partial t} + \frac{\partial \zeta}{\partial x}\frac{\mathrm{d}x}{\mathrm{d}t} + \frac{\partial \zeta}{\partial \theta}\frac{\mathrm{d}\theta}{\mathrm{d}t} \tag{9.12}$$

where (x, r, θ) here denote the coordinates of a fluid particule at the interface. Since by definition:

$$\frac{\mathrm{d}\,x}{\mathrm{d}\,t} = u_x(\zeta,\theta,x,t), \quad \frac{\mathrm{d}\,r}{\mathrm{d}\,t} = v_r(\zeta,\theta,x,t), \quad \zeta\frac{\mathrm{d}\,\theta}{\mathrm{d}\,t} = w_\theta(\zeta,\theta,x,t), \tag{9.13}$$

equation (9.12) leads to the kinematic condition:

$$v_r(\zeta,\theta,x,t) = \frac{\partial\,\zeta}{\partial\,t} + u_x(\zeta,\theta,x,t)\frac{\partial\,\zeta}{\partial\,x} + \frac{w_\theta(\zeta,\theta,x,t)}{\zeta}\frac{\partial\,\zeta}{\partial\,\theta} \tag{9.14}$$

which can be written as well as :

$$\frac{\mathrm{d}\,\zeta}{\mathrm{d}\,t}(\theta,x,t) = v_r(\zeta,\theta,x,t). \tag{9.15}$$

Let us introduce a notation for the jump of any field $Q(r=\zeta,\theta,x,t)$ at the interface $r=\zeta$:

$$[\![Q]\!] = Q^{(1)}(\zeta,\theta,x,t) - Q^{(2)}(\zeta,\theta,x,t).$$

We impose the continuity of the velocity field across the interface:

$$[\![u_x]\!] = 0\,, \quad [\![v_r]\!] = 0\,, \qquad [\![w_\theta]\!] = 0\,. \tag{9.16}$$

Dynamic conditions come from the balance between capillary force, pressure force and viscous constraints on the interface [Batchelor, 2000]:

$$(\sigma_{ij}^{(1)} - \sigma_{ij}^{(2)})n_j = \gamma(\frac{1}{R_1} + \frac{1}{R_2})n_i \tag{9.17}$$

where $R_{1,2}$ are the local main curvature radii of the interface and $\sigma^{(k)}$ denotes the stress tensor given by

$$\sigma_{ij}^{(k)} = -p^{(k)}\delta_{ij} + 2\mu^{(k)}e_{ij}^{(k)}$$

and $e^{(k)}$ the symmetric rate of strain tensor defined by

$$e_{ij}^{(k)} \equiv \frac{1}{2}(\frac{\partial\,u_i^{(k)}}{\partial\,x_j} + \frac{\partial\,u_j^{(k)}}{\partial\,x_i}).$$

In particular, the normal stress is balanced by surface tension. In cylindrical coordinates, the stress tensor reads

$$2\boldsymbol{e} = \begin{bmatrix} 2\dfrac{\partial\,v_r}{\partial\,r} & \dfrac{1}{r}\dfrac{\partial\,v_r}{\partial\,\theta} + \dfrac{\partial\,w_\theta}{\partial\,r} - \dfrac{w_\theta}{r} & \dfrac{\partial\,v_r}{\partial\,x} + \dfrac{\partial\,u_x}{\partial\,r} \\ \dfrac{1}{r}\dfrac{\partial\,v_r}{\partial\,\theta} + \dfrac{\partial\,w_\theta}{\partial\,r} - \dfrac{w_\theta}{r} & 2(\dfrac{1}{r}\dfrac{\partial\,w_\theta}{\partial\,\theta} + \dfrac{v_r}{r}) & \dfrac{1}{r}\dfrac{\partial\,u_x}{\partial\,\theta} + \dfrac{\partial\,w_\theta}{\partial\,x} \\ \dfrac{\partial\,v_r}{\partial\,x} + \dfrac{\partial\,u_x}{\partial\,r} & \dfrac{1}{r}\dfrac{\partial\,u_x}{\partial\,\theta} + \dfrac{\partial\,w_\theta}{\partial\,x} & 2\dfrac{\partial\,u_x}{\partial\,x} \end{bmatrix}. \tag{9.18}$$

The dynamic condition (9.17) thus reads:

$$[\![\mu \boldsymbol{t}_x \cdot \boldsymbol{e} \cdot \boldsymbol{n}]\!] = 0 \tag{9.19}$$

$$[\![-p + 2\mu \boldsymbol{n} \cdot \boldsymbol{e} \cdot \boldsymbol{n}]\!] = \gamma(\frac{1}{R_1} + \frac{1}{R_2}) \tag{9.20}$$

$$[\![\mu \boldsymbol{t}_\theta \cdot \boldsymbol{e} \cdot \boldsymbol{n}]\!] = 0\,. \tag{9.21}$$

9.1.2 Dimensionless equations

In order to put the governing equations in dimensionless form, we choose three reference quantities containing length, mass and time in an independant manner. For a columnar flow involving air and water, we may select such quantities as the mean section radius R_0, the water density $\rho^{(w)}$ and surface tension γ. This yields the following reference scales :

$$\text{length: } L = R_0\ , \quad \text{mass: } M = \rho^{(w)} R_0^3\ , \quad \text{time: } T = \rho^{(w)1/2} R_0^{3/2} \gamma^{-1/2}\ .$$

Noting the dimensionless quantities with a bar, the Navier-Stokes equations now read

$$\bar{\nabla} \cdot \bar{\boldsymbol{u}}^{(k)} = 0 \tag{9.22}$$

$$\bar{\rho}^{(k)} \frac{\bar{\mathrm{D}}\, \bar{\boldsymbol{u}}^{(k)}}{\bar{\mathrm{D}}\, \bar{t}} = -\bar{\nabla} \bar{p}^{(k)} + \bar{\mu}^{(k)} \frac{1}{Re} \bar{\nabla}^2 \bar{\boldsymbol{u}}^{(k)}\,. \tag{9.23}$$

In the above equations, we have $\bar{\rho}^{(k)} \equiv \rho^{(k)}/\rho^{(w)}$ as expected, but we have defined $\bar{\mu}^{(k)}$ as $\bar{\mu}^{(k)} \equiv \mu^{(k)}/\mu^{(w)}$ for simplicity (using the above reference scales would have led to a different definition of $\bar{\mu}^{(k)}$). In water (w), the coefficient of the viscous term is the inverse of the Reynolds number

$$Re = \frac{\sqrt{\rho^{(w)} \gamma R_0}}{\mu^{(w)}}\,.$$

Sometimes, one uses the Ohnesorge number defined by $Oh = 1/Re$. Concerning the kinematic and dynamic conditions at the interface, one gets:

$$\frac{\bar{\mathrm{d}}\, \bar{\zeta}}{\bar{\mathrm{d}}\, \bar{t}} = \bar{v_r} \tag{9.24}$$

$$[\![\bar{\boldsymbol{u}}]\!] = \boldsymbol{0} \tag{9.25}$$

$$[\![\bar{\mu} \boldsymbol{t}_x \cdot \bar{\boldsymbol{e}} \cdot \boldsymbol{n}]\!] = 0 \tag{9.26}$$

$$[\![-\bar{p} + 2\,\bar{\mu} \frac{1}{Re} \boldsymbol{n} \cdot \bar{\boldsymbol{e}} \cdot \boldsymbol{n}]\!] = (\frac{1}{\bar{R}_1} + \frac{1}{\bar{R}_2}) \tag{9.27}$$

$$[\![\bar{\mu} \boldsymbol{t}_\theta \cdot \bar{\boldsymbol{e}} \cdot \boldsymbol{n}]\!] = 0\,. \tag{9.28}$$

In the following, whenever there is no ambiguity, we remove the reference (k) to the fluid and the overbar.

9.2 Two-phase columnar flow equilibria

In this section, we identify some equilibrium solutions for two-phase columnar flows, listed here in their dimensionless form. These solutions are used as base states for instability studies.

9.2.1 Two-phase rest state

In the first equilibrium, all we have is a still column of fluid (1) surrounded by fluid (2), also at rest:

$$U_x(r,\theta,x) = 0\,, \quad V_r(r,\theta,x) = 0\,, \quad W_\theta(r,\theta,x) = 0\,, \tag{9.29}$$

the interface is located at $\zeta(\theta,x) = 1$, and the base pressure P is given by

$$P^{(1)}(r,\theta,x) = 1 \quad \text{for} \quad r \leq 1 \tag{9.30}$$

$$P^{(2)}(r,\theta,x) = 0 \quad \text{for} \quad r > 1 \tag{9.31}$$

up to an additive arbitrary constant. Note that this base state can also be used for liquid jets with uniform axial velocity if the presence of the surrounding fluid is overlooked. In the Galilean reference frame translating with the liquid, the flow is at rest.

9.2.2 Two-phase columnar vortex

For this second class of base states, we assume a general form $(U_x(r,t), 0, W_\theta(r,t))$ for the base velocity components, and $P(r,t)$ for the base pressure. This can be written in terms of vorticity as

$$\boldsymbol{\omega}(x,r,\theta,t) = \left(\frac{W_\theta}{r} + \frac{\partial W_\theta}{\partial r}, 0, -\frac{\partial U_x}{\partial r}\right). \tag{9.32}$$

possess azimuthal velocity, hence axial vorticity. The Navier-Stokes equations in each domain:

$$\rho\frac{\partial U_x}{\partial t} = \frac{\mu}{Re}\left(\frac{\partial^2 U_x}{\partial r^2} + \frac{1}{r}\frac{\partial U_x}{\partial r}\right) \tag{9.33}$$

$$\rho\frac{W_\theta^2}{r} = \frac{\partial P}{\partial r} \tag{9.34}$$

$$\rho\frac{\partial W_\theta}{\partial t} = \frac{\mu}{Re}\left(\frac{\partial^2 W_\theta}{\partial r^2} + \frac{1}{r}\frac{\partial W_\theta}{\partial r} - \frac{W_\theta}{r^2}\right). \tag{9.35}$$

Because of the slow radial diffusion caused by viscosity, this base flow is actually unsteady. However, if we expect the instability to grow on much faster time scales, we neglect the diffusion of this base flow. Note that viscous diffusion still included in the equations governing perturbations.
If we remove all diffusion terms, we find that any velocity profile of the form

$$\boldsymbol{U} = (U_x(r), 0, W_\theta(r)) \tag{9.36}$$

is an equilibrium of the Euler equations for the base state.
The velocity field should satisfy continuity at the interface $r = \zeta = 1$:

$$U_x^{(1)}(1) = U_x^{(2)}(1), \tag{9.37}$$

$$W_\theta^{(1)}(1) = W_\theta^{(2)}(1), \tag{9.38}$$

but the continuity of tangential stresses:

$$\mu^{(1)}\left[\frac{\partial W_\theta^{(1)}(1)}{\partial r} - W_\theta^{(1)}(1)\right] = \mu^{(2)}\left[\frac{\partial W_\theta^{(2)}(1)}{\partial r} - W_\theta^{(2)}(1)\right] \tag{9.39}$$

$$\mu^{(1)}\frac{\partial U_x^{(1)}(1)}{\partial r} = \mu^{(2)}\frac{\partial U_x^{(2)}(1)}{\partial r}. \tag{9.40}$$

Introducing (9.32) into the above equations leads to:

$$\mu^{(1)}[\omega_x^{(1)}(1) - 2W_\theta^{(1)}(1)] = \mu^{(2)}[\omega_x^{(2)}(1) - 2W_\theta^{(2)}(1)] \tag{9.41}$$

$$\mu^{(1)}\omega_\theta^{(1)}(1) = \mu^{(2)}\omega_\theta^{(2)}(1). \tag{9.42}$$

The base pressure should satisfy (9.34) and the constraint $[\![P]\!] = 1$ at $r = 1$, this yields

$$P^{(1)}(r) = \rho^{(1)}\int_0^r \frac{[W_\theta^{(1)}]^2}{r}\,\mathrm{d}r \quad \text{for} \quad r \le 1 \tag{9.43}$$

$$P^{(2)}(r) = P^{(1)}(1) - 1 + \rho^{(2)}\int_1^r \frac{[W_\theta^{(2)}]^2}{r}\,\mathrm{d}r \quad \text{for} \quad r > 1\,. \tag{9.44}$$

Building a base state

To build a base state that satisfies the above constraints, we can assume an arbitrary vorticity profile $\omega^{(1)}(r)$ in phase 1 and an –almost – arbitrary vorticity profile $\omega^{(2)}(r)$ in phase 2. The velocity profiles can then be obtained by radially integrating the vorticity profiles.
a) azimuthal velocity W_θ
From equation (9.32), since

$$\omega_x = \frac{1}{r}\frac{\partial}{\partial r}(rW_\theta),$$

we can first compute $W_\theta^{(1)}(r)$ in the region $r \le 1$:

$$W_\theta^{(1)}(r) = \frac{1}{r}\int_0^r r\omega_x^{(1)}(r)\mathrm{d}r \quad \text{for } r \le 1\,.$$

We then deduce $W_\theta^{(2)}(r)$ in the region $r > 1$ as

$$W_\theta^{(2)}(r) = \frac{1}{r}\left(\int_0^1 r\omega_x^{(1)}(r) + \int_1^r r\omega_x^{(2)}(r)\right)\mathrm{d}r = \frac{1}{r}W_\theta^{(1)}(1) + \frac{\omega_x^{(2)}(1)}{r}\int_1^r rR_x^0(r)\mathrm{d}r$$

where function R_x^0 is defined as

$$R_x^0(r) \equiv \frac{\omega_x^{(2)}(r)}{\omega_x^{(2)}(1)}$$

and thus satisfies $R_x^0(1) = 1$. As the vorticity in phase 2 eventually decays to zero as $r \to \infty$, so does R_x^0. At the interface, the vorticity in fluid (2) is determined through relation (9.41):

$$\omega_x^{(2)}(1) = \frac{\mu^{(1)}}{\mu^{(2)}}\omega_x^{(1)}(1) - 2\frac{[\mu^{(1)} - \mu^{(2)}]}{\mu^{(2)}}W_\theta^{(1)}(1).$$

b) axial velocity U_x

From equation (9.32), we first compute $U_x^{(1)}(r)$ in the region $r \leq 1$:

$$U_x^{(1)}(r) = -\int_0^r \omega_\theta^{(1)}(r)\mathrm{d}r \quad \text{for} \quad r \leq 1\,.$$

We then deduce $U_x^{(2)}(r)$ in the region $r > 1$:

$$U_x^{(2)}(r) = -\int_0^1 \omega_\theta^{(1)}(r)\mathrm{d}r - \int_1^r \omega_\theta^{(2)}(r)\mathrm{d}r = U_x^{(1)}(1) - \omega_\theta^{(2)}(1)\int_{r=1}^r R_\theta^0(r)\mathrm{d}r$$

where function R_θ^0 is defined as

$$R_\theta^0(r) \equiv \frac{\omega_\theta^{(2)}(r)}{\omega_\theta^{(2)}(1)}$$

so that $R_\theta^0(1) = 1$. At the interface, the vorticity in fluid (2) is determined through relation (9.42):

$$\omega_\theta^{(2)}(1) = \frac{\mu^{(1)}}{\mu^{(2)}}\omega_\theta^{(1)}(1).$$

9.2.3 Example solutions for columnar vortex base states

In this study, we wish to evaluate the role of the azimuthal velocity on the stability of the system. We assume that the axial velocity is uniformly zero for the base state in both fluids ($U_x = 0$, $\omega_\theta = 0$). We now build two base states corresponding to a water column surrounded by air, and an air column surrounded by water. The vorticity profiles are chosen arbitrarily (they are not meant to reproduce the vorticity that could be measured in an experiment or obtained by a realistic three-dimensional DNS). However, we made the assumption that vorticity has been in major part introduced in the liquid, which explains the profiles selected below.

Base state A: water column surrounded by air

In the case of a liquid column surrounded by air, we assume that the vorticity in mainly present in the liquid. Hence we assume that fluid (1) is in solid-body rotation with angular velocity q, or equivalently that $\omega_x^{(1)} = 2q$. We get

$$W_\theta^{(1)}(r) = qr \quad \text{for} \quad r \leq 1\,.$$

In fluid (2), we assume that the vorticity has not penetrated much the region $r > 1$, and that it decays near the interface over a small length δ. We get:

$$W_\theta^{(2)}(r) = \frac{q}{r} + 2\frac{q}{r}\int_1^r rR_r^0(r)\mathrm{d}r \quad \text{for} \quad r > 1\,,$$

with

$$\omega_x^{(2)}(r) = 2qR_r^0(r)\,, \qquad R_r^0(r) = \exp\left(-\frac{(r-1)^2}{\delta^2}\right).$$

The azimuthal base velocity in the gas phase can be deduced:

$$W_\theta^{(2)}(r) = \frac{q}{r}\left[1 + \delta^2[1 - \exp\left(-\frac{(r-1)^2}{\delta^2}\right)] + \delta\sqrt{\pi}\,\mathrm{erf}\left(\frac{r-1}{\delta}\right)\right] \quad \text{for} \quad r > 1\,, \tag{9.45}$$

which involved the error function erf defined as:

$$\mathrm{erf}(x) \equiv \frac{2}{\sqrt{\pi}}\int_0^x \exp(-t^2)\mathrm{d}t\,.$$

We will need the first derivative:

$$W_\theta^{(2)\prime}(r) = \frac{q}{r^2}\left[-1 - \delta^2 + (\delta^2 + 2r^2)\exp\left(-\frac{(r-1)^2}{\delta^2}\right) - \delta\sqrt{\pi}\,\mathrm{erf}\left(\frac{r-1}{\delta}\right)\right]$$

and the second derivative:

$$W_\theta^{(2)\prime\prime}(r) = \frac{2q}{r^3}\left[1 + \delta^2 + \left(\frac{2r^3(1-r)}{\delta^2} - \delta^2 - r^2\right)\exp\left(-\frac{(r-1)^2}{\delta^2}\right) + \delta\sqrt{\pi}\,\mathrm{erf}\left(\frac{r-1}{\delta}\right)\right].$$

An example of such distribution is plotted in figure 9.1.

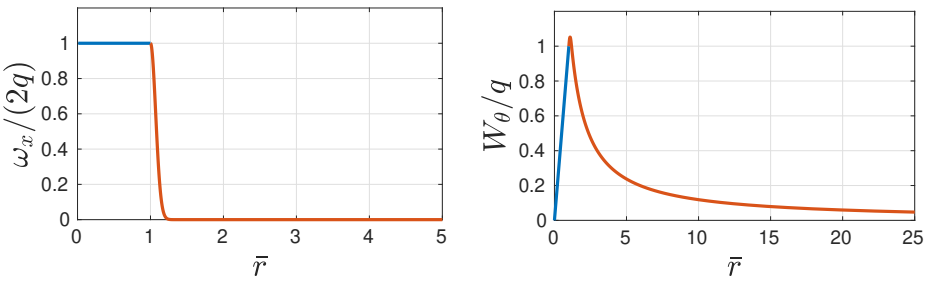

Figure 9.1 – Normalized axial vorticity (left) and azimuthal velocity (right) profiles in fluids (1) and (2) for base state A with $\delta = 0.1$, $\mu^{(1)} = 1$, $\mu^{(2)} = 0.02$.

Base state B: air column surrounded by water

In the case of an air column surrounded by water, we assume that the vorticity is present in the vicinity of the interface in the outer liquid over a small distance δ_2, and that it has also penetrated in the air column, again only near the interface over a small distance δ_1.
We propose $\omega_x^{(1)}(1) = q$ at the interface which is the maximum vorticity, together with Gaussian decays

from the interface location, described by

$$\frac{\omega_x^{(1)}(r)}{\omega_x^{(1)}(1)} = \exp(-\frac{(r-1)^2}{\delta_1^2}) \quad \text{for } r \leq 1, \quad \frac{\omega_x^{(2)}(r)}{\omega_x^{(2)}(1)} = \exp(-\frac{(r-1)^2}{\delta_2^2}) \quad \text{for } r > 1\,.$$

The azimuthal velocity in fluid (1) then reads as

$$W_\theta^{(1)}(r) = \frac{q}{r}\left[\frac{\delta_1^2}{2}(\exp\left(-\frac{1}{\delta_1^2}\right) - \exp\left(-\frac{(r-1)^2}{\delta_1^2}\right)) + \delta_1\frac{\sqrt{\pi}}{2}\left(\mathrm{erf}(\frac{r-1}{\delta_1}) - \mathrm{erf}(\frac{-1}{\delta_1})\right)\right]. \tag{9.46}$$

and its first and second derivatives as

$$W_\theta'^{(1)}(r) = q\left[(\frac{\delta_1^2}{2r^2}+1)\exp\left(-\frac{(r-1)^2}{\delta_1^2}\right) - \frac{\delta_1^2}{2r^2}\exp\left(-\frac{1}{\delta_1^2}\right) + \frac{\sqrt{\pi}\delta_1}{2r^2}\left(\mathrm{erf}(\frac{r-1}{\delta_1}) - \mathrm{erf}(\frac{-1}{\delta_1})\right)\right]$$

$$W_\theta''^{(1)}(r) = q\left[\exp\left(-\frac{(r-1)^2}{\delta_1^2}\right)\left(-\frac{\delta_1^2}{r^3} - \frac{1}{r} - \frac{2(r-1)}{\delta_1^2}\right) + \frac{\delta_1^2}{r^3}\exp\left(-\frac{1}{\delta_1^2}\right) + \frac{\sqrt{\pi}\delta_1}{r^3}\left(\mathrm{erf}(\frac{r-1}{\delta_1}) - \mathrm{erf}(\frac{-1}{\delta_1})\right)\right].$$

At the interface, the azimuthal velocity of fluid (1) is

$$W_\theta^{(1)}(1) = q\frac{\delta_1}{2}\left[\delta_1(\exp\left(-\frac{1}{\delta_1^2}\right) - 1) + \sqrt{\pi}\right].$$

The azimuthal velocity in phase (2) is under the form :

$$W_\theta^{(2)}(r) = \frac{W_\theta^{(1)}(1)}{r} + \frac{\omega_x^{(2)}(1)}{r}\left[\frac{\delta_2^2}{2}(1 - \exp\left(-\frac{(r-1)^2}{\delta_2^2}\right)) + \delta_2\frac{\sqrt{\pi}}{2}\,\mathrm{erf}\left(\frac{r-1}{\delta_2}\right)\right]$$

where

$$\omega_x^{(2)}(1) = \frac{\mu^{(1)}}{\mu^{(2)}}q - 2\frac{\left(\mu^{(1)} - \mu^{(2)}\right)}{\mu^{(2)}}W_\theta^{(1)}(1). \tag{9.47}$$

The derivatives are

$$W_\theta'^{(2)}(r) = -\frac{W_\theta^{(1)}(1)}{r^2} + \frac{\omega_x^{(2)}(1)}{2r^2}\left[\left(\delta_2^2 + 2r^2\right)\exp\left(-\frac{(r-1)^2}{\delta_2^2}\right) - \delta_2\sqrt{\pi}\,\mathrm{erf}\left(\frac{r-1}{\delta_2}\right) - \delta_2^2\right]$$

$$W_\theta''^{(2)}(r) = 2\frac{W_\theta^{(1)}(1)}{r^3} + \omega_x^{(2)}(1)\left[\frac{\delta_2^2}{r^3} - \left(\frac{\delta_2^2}{r^3} + \frac{1}{r} + \frac{2(r-1)}{\delta_2^2}\right)\exp\left(-\frac{(r-1)^2}{\delta_2^2}\right) + \frac{\delta_2\sqrt{\pi}}{r^3}\,\mathrm{erf}\left(\frac{r-1}{\delta_2}\right)\right].$$

An example of such distribution is plotted in figure 9.2.

Test base state: the Batchelor vortex

In the special case $\mu^{(1)} = \mu^{(2)}$, no special care is needed at the interface to fulfill the equality of shear stresses, and one may use whatever profile valid for a homogeneous flow. For instance, one may adopt the

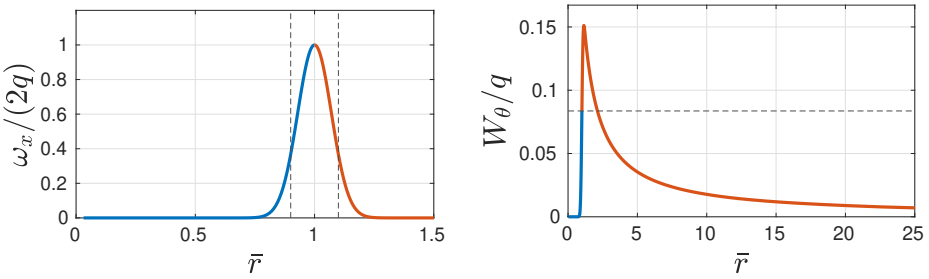

Figure 9.2 – Normalized axial vorticity (left) and azimuthal velocity (right) profiles in fluids (1) and (2) for base state B with $\delta_1 = \delta_2 = 0.1$, $\mu^{(1)} = 1$, $\mu^{(2)} = 1$.

Batchelor vortex profile [Batchelor, 1964] given by:

$$U_x(r,t) = \frac{\beta_0}{a^2}\exp\left(-\frac{r^2}{a^2}\right) \tag{9.48}$$

$$W_\theta(r,t) = \frac{\Gamma}{2\pi r}\left[1-\exp\left(-\frac{r^2}{a^2}\right)\right] \tag{9.49}$$

where $a(t)$ is the time-dependant core size and β_0/a^2 the centerline axial velocity. Again, if one assumes that diffusion acts slowly with respect to instabilities, one adopts a fixed core size $a = a_0$. This base state will be used as a test case for the numerical instability code.

Chapter 10

Linearization and discretization

Contents

In this chapter, we linearize the governing equations presented in Ch 9. After spatial discretization of the linear system, we obtain a generalized eigenvalue problem $\boldsymbol{AX} = \mathrm{i}\omega\boldsymbol{BX}$ that rules the linear instability of the two-phase columnar flow. The eigenvalues $\mathrm{i}\omega$ are complex: the imaginary part of ω is a growth rate and its real part the oscillation frequency. Complex eigenvectors $\boldsymbol{X}$ contain the discretized velocity and pressure eigenfunctions. The chapter contains the main results, more computation details and complements can be found in the appendix D.

10.1 Linearization approximation and eigenvalue problem

The velocity are written as the sum of the base state and small perturbations of order $\epsilon \ll 1$:

$$v_r = 0 + \epsilon v_r'(r,\theta,x,t) \tag{10.1}$$
$$w_\theta = W_\theta(r) + \epsilon w_\theta'(r,\theta,x,t) \tag{10.2}$$
$$u_x = U_x(r) + \epsilon u_x'(r,\theta,x,t) \tag{10.3}$$
$$p = \Pi(r) + \epsilon p'(r,\theta,x,t) \tag{10.4}$$
$$\zeta = 1 + \epsilon \zeta'(\theta,x,t) \tag{10.5}$$

where $(U_x(r), V_r = 0, W_\theta(r))$ and $\Pi(r)$ are the cylindrical components of the velocity and the pressure corresponding to one of the steady base flows listed in Sec 9.2.

10.1.1 Linearization of the governing equations

Introducing expression (10.1) to (10.5) into Eq.(9.22) and Eq.(9.23), we linearize these equations by keeping $O(\epsilon)$ terms and neglecting terms of higher order, and get the following system valid in each fluid region:

$$\frac{\partial u_x'}{\partial x} + \frac{v_r'}{r} + \frac{\partial v_r'}{\partial r} + \frac{1}{r}\frac{\partial w_\theta'}{\partial \theta} = 0 \tag{10.6}$$

$$\rho\left(\frac{\partial u_x'}{\partial t} + U_x\frac{\partial u_x'}{\partial x} + v_r'\frac{\partial U_x}{\partial r} + \frac{W_\theta}{r}\frac{\partial u_x'}{\partial \theta}\right) = -\frac{\partial p'}{\partial x} + \frac{\mu}{Re}\nabla^2 u_x' \tag{10.7}$$

$$\rho\left(\frac{\partial v_r'}{\partial t} + U_x\frac{\partial v_r'}{\partial x} + \frac{W_\theta}{r}\frac{\partial v_r'}{\partial \theta} - 2\frac{W_\theta w_\theta'}{r}\right) = -\frac{\partial p'}{\partial r} + \frac{\mu}{Re}\left[\nabla^2 v_r' - \frac{v_r'}{r^2} - \frac{2}{r^2}\frac{\partial w_\theta'}{\partial \theta}\right] \tag{10.8}$$

$$\rho\left(\frac{\partial w_\theta'}{\partial t} + U_x\frac{\partial w_\theta'}{\partial x} + \frac{\partial W_\theta}{\partial r}v_r' + \frac{W_\theta}{r}\frac{\partial w_\theta'}{\partial \theta} + \frac{W_\theta v_r'}{r}\right) = -\frac{1}{r}\frac{\partial p'}{\partial \theta} + \frac{\mu}{Re}\left[\nabla^2 w_\theta' - \frac{w_\theta'}{r^2} + \frac{2}{r^2}\frac{\partial v_r'}{\partial \theta}\right]. \tag{10.9}$$

When linearizing the conditions at the interface, it is convenient to introduce the following jump notation. For any field $Q(r,\theta,x,t)$, one introduces the jump $\langle\!|Q|\!\rangle$ at the location of the unperturbed interface $r = 1$:

$$\langle\!|Q|\!\rangle \equiv Q^{(1)}(1,\theta,x,t) - Q^{(2)}(1,\theta,x,t).$$

We linearize Eqs. (9.24)–(9.28) using the above notation. When there is no ambiguity, the velocity in capital letter refers to the base flow at $r = 1$ (for instance $U_x(r = 1)$ is simply denoted as U_x).
The kinematic condition (9.24) then reads

$$v_r' = \frac{\partial \zeta'}{\partial t} + U_x\frac{\partial \zeta'}{\partial x} + W_\theta\frac{\partial \zeta'}{\partial \theta} \quad \text{at } r = 1. \tag{10.10}$$

The continuity of the three velocity components (9.25) reads:

$$0 = \langle\!|u_x' + \zeta'\frac{\partial U_x}{\partial r}|\!\rangle \tag{10.11}$$

$$0 = \langle\!|v_r'|\!\rangle \tag{10.12}$$

$$0 = \langle\!|w_\theta' + \zeta'\frac{\partial W_\theta}{\partial r}|\!\rangle. \tag{10.13}$$

The dynamic condition along the axial direction (9.26) reads:

$$0 = \langle\!|\mu\left(\zeta'\frac{\partial^2 U_x}{\partial r^2} + \frac{\partial v_r'}{\partial x} + \frac{\partial u_x'}{\partial r}\right)|\!\rangle. \tag{10.14}$$

The dynamic condition along the normal direction (9.27) reads:

$$\langle\!|-p' - \rho\zeta' W_\theta^2 + 2\frac{\mu}{Re}\left[\frac{\partial v_r'}{\partial r} - \frac{\partial \zeta'}{\partial \theta}\left(\frac{\partial W_\theta}{\partial r} - W_\theta\right) - \frac{\partial \zeta'}{\partial x}\frac{\partial U_x}{\partial r}\right]|\!\rangle = \zeta' + \frac{\partial^2 \zeta'}{\partial x^2} + \frac{\partial^2 \zeta'}{\partial \theta^2}. \tag{10.15}$$

The dynamic condition along the azimuthal direction (9.28) reads:

$$0 = \langle\!|\mu\left[\zeta'\left(\frac{\partial^2 W_\theta}{\partial r^2} - \frac{\partial W_\theta}{\partial r} + W_\theta\right) + \frac{\partial v_r'}{\partial \theta} + \frac{\partial w_\theta'}{\partial r} - w_\theta'\right]|\!\rangle. \tag{10.16}$$

10.1.2 Normal mode decomposition

The set of linearized equations presented above contains no explicit reference to θ, to x nor to t. The solutions can thus be decomposed on an eigenmode basis of the form:

$$\begin{pmatrix} u_x' \\ v_r' \\ w_\theta' \\ p' \\ \zeta' \end{pmatrix} = \begin{pmatrix} F(r) \\ G(r) \\ H(r) \\ P(r) \\ \zeta_0 \end{pmatrix} e^{\mathrm{i}(kx+m\theta-\omega t)} \tag{10.17}$$

where m denotes the (integer) azimuthal wavenumber, k the axial wavenumber and ω the frequency.

In such problems, is it convenient, instead of v_r and w_θ, to use the two variables

$$v_+' = v_r' + \mathrm{i}w_\theta' \quad \text{and} \quad v_-' = v_r' - \mathrm{i}w_\theta'. \tag{10.18}$$

This makes the enforcement of boundary conditions at $r = 0$ easier and decouples the viscous terms in the equation system. One then uses a decomposition of the form

$$\begin{pmatrix} u_x' \\ v_+' \\ v_-' \\ p' \\ \zeta' \end{pmatrix} = \begin{pmatrix} F(r) \\ G_+(r) \\ G_-(r) \\ P(r) \\ \zeta_0 \end{pmatrix} e^{\mathrm{i}(kx+m\theta-\omega t)}. \tag{10.19}$$

For fluid 2 as example, the equation system valid for $r > 1$ reads:

$$\begin{aligned}
&\mathrm{i}kF + \frac{1}{2r}\left[(1+m)\,G_+ + (1-m)\,G_-\right] + \frac{1}{2}\left(G_+' + G_-'\right) = 0 \\
&\rho^{(2)}\left[(-\mathrm{i}\omega + \mathrm{i}X)F + \frac{1}{2}\left(G_+ + G_-\right)U_x'\right] + \mathrm{i}kP - \frac{\mu^{(2)}}{Re}\left[F'' + \frac{1}{r}F' - \left(k^2 + \frac{m^2}{r^2}\right)F\right] = 0 \\
&\rho^{(2)}\left[(-\mathrm{i}\omega + \mathrm{i}X)\,G_+ + \mathrm{i}\left(\frac{3}{2}\Omega + \frac{1}{2}W_\theta'\right)G_+ + \mathrm{i}\left(-\frac{1}{2}\Omega + \frac{1}{2}W_\theta'\right)G_-\right] \\
&\qquad + P' - \frac{n}{r}P - \frac{\mu^{(2)}}{Re}\left[G_+'' + \frac{1}{r}G_+' - \left(\frac{(m+1)^2}{r^2} + k^2\right)G_+\right] = 0 \\
&\rho^{(2)}\left[(-\mathrm{i}\omega + \mathrm{i}X)\,G_- + \mathrm{i}\left(\frac{1}{2}\Omega - \frac{1}{2}W_\theta'\right)G_+ + \mathrm{i}\left(-\frac{3}{2}\Omega - \frac{1}{2}W_\theta'\right)G_-\right] \\
&\qquad + P' + \frac{n}{r}P - \frac{\mu^{(2)}}{Re}\left[G_-'' + \frac{1}{r}G_-' - \left(\frac{(m-1)^2}{r^2} + k^2\right)G_-\right] = 0
\end{aligned} \tag{10.20}$$

where $'$ now indicates the derivative, and

$$\Omega \equiv \frac{W_\theta}{r}\,, \quad X \equiv kU_x + m\Omega\,. \tag{10.21}$$

For the inner fluid (1), a further change of variable is performed:

$$F(r) = r^{|m|} f(r), \quad G_{\pm}(r) = r^{|m\pm 1|} g_{\pm}(r), \quad P(r) = r^{|m|} p(r) \tag{10.22}$$

so that f, g_+,g_- and p can be considered as even functions of r, that will, in general, reach finite values at $r = 0$. Neumann boundary conditions will thus be naturally enforced on these functions at $r = 0$.

We give here the equations for the case $m \geq 1$. Introducing expression (10.22) into Eq.(10.20) leads to the system valid for $r < 1$:

$$\begin{aligned}
&\mathrm{i}kf + (m+1)g_+ + \frac{r^2}{2}\frac{g_+'}{r} + \frac{1}{2}\frac{g_-'}{r} = 0 \\
&\rho^{(1)}\left[(-\mathrm{i}\omega + \mathrm{i}X)f + \frac{r^2}{2}\frac{U_x'}{r}g_+ + \frac{1}{2}\frac{U_x'}{r}g_-\right] + \mathrm{i}kp - \frac{\mu^{(1)}}{Re}\left[f'' + (2m+1)\frac{f'}{r} - k^2 f\right] = 0 \\
&\rho^{(1)}\left[(-\mathrm{i}\omega + \mathrm{i}X)g_+ + \frac{\mathrm{i}}{2}\left(3\Omega + W_\theta'\right)g_+ - \frac{\mathrm{i}}{2}Y g_-\right] + \frac{p'}{r} - \frac{\mu^{(1)}}{Re}\left[g_+'' + (2m+3)\frac{g_+'}{r} - k^2 g_+\right] = 0 \\
&\rho^{(1)}\left[(-\mathrm{i}\omega + \mathrm{i}X)g_- - \frac{\mathrm{i}}{2}\left(3\Omega + W_\theta'\right)g_- + \frac{\mathrm{i}}{2}r^4 Y g_+\right] + 2mp + r^2\frac{p'}{r} - \frac{\mu^{(1)}}{Re}\left[g_-'' + (2m-1)\frac{g_-'}{r} - k^2 g_-\right] = 0
\end{aligned} \tag{10.23}$$

where

$$Y \equiv \frac{\Omega - W_\theta'}{r^2}. \tag{10.24}$$

The systems for the cases $m = 0$ and $m \leq -1$, as well as the details of the computations can be found in the appendix D.

We now write the conditions at the interface $r = 1$. The kinematic condition (10.10) at $r = 1$ reads as

$$\frac{1}{2}(G_+ + G_-) = \mathrm{i}(-\omega + kU_x^{(2)} + mW_\theta^{(2)})\zeta_0. \tag{10.25}$$

The continuity (10.11) of the axial velocity component reads as

$$f + \zeta_0 U_x^{(1)\prime} = F + \zeta_0 U_x^{(2)\prime}, \tag{10.26}$$

the continuity (10.12) of the radial velocity component as

$$g_+ + g_- = G_+ + G_-, \tag{10.27}$$

the continuity (10.13) of the azimuthal velocity component as

$$\mathrm{i}(g_- - g_+) + 2\zeta_0 W_\theta^{(1)\prime} = \mathrm{i}(G_- - G_+) + 2\zeta_0 W_\theta^{(2)\prime}, \tag{10.28}$$

the dynamic condition (10.14) along $\boldsymbol{e}_x$ reads as

$$\mu^{(1)}\left[2\zeta_0 U_x^{(1)\prime\prime} + \mathrm{i}k(g_+ + g_-) + 2(f' + |m|f)\right] = \mu^{(2)}\left[2\zeta_0 U_x^{(2)\prime\prime} + \mathrm{i}k(G_+ + G_-) + 2F'\right], \tag{10.29}$$

the dynamic condition (10.15) along $\boldsymbol{e}_r$ as

$$p+\rho^{(1)}\zeta_0 W_\theta^{(1)2}-\frac{\mu^{(1)}}{Re}\left[|m+1|g_+ + g_+' + |m-1|g_- + g_-' - 2\,\mathrm{i}\,\zeta_0[m(W_\theta^{(1)\prime}-W_\theta^{(1)})+kU_x^{(1)\prime}]\right]$$
$$+\,\zeta_0\left(1-k^2-n^2\right) = P+\rho^{(2)}\zeta_0 W_\theta^{(2)2}-\frac{\mu^{(2)}}{Re}\left[G_+' + G_-' - 2\,\mathrm{i}\,\zeta_0[m(W_\theta^{(2)\prime}-W_\theta^{(2)})+kU_x^{(2)\prime}]\right], \quad (10.30)$$

and the dynamic condition (10.16) along $\boldsymbol{e}_\theta$ as

$$\mu^{(1)}\left[2\zeta_0(W_\theta^{(1)\prime\prime}-W_\theta^{(1)\prime}+W_\theta^{(1)})+\mathrm{i}(m+1-|m+1|)g_+ + \mathrm{i}(m-1+|m-1|)g_- + \mathrm{i}(g_-'-g_+')\right]$$
$$=\mu^{(2)}\left[2\zeta_0(W_\theta^{(2)\prime\prime}-W_\theta^{(2)\prime}+W_\theta^{(2)})+\mathrm{i}(m+1)G_+ + \mathrm{i}(m-1)G_- + \mathrm{i}(G_-'-G_+')\right]. \quad (10.31)$$

10.2 Discrete eigenvalue problem

The continuous generalized eigenvalue problem obtained in previous section is discretized to yield a matrix/vector form $\boldsymbol{AX} = \mathrm{i}\omega\boldsymbol{BX}$, where matrices $\boldsymbol{A}$ and $\boldsymbol{B}$ come from the Navier–Stokes equations and boundary conditions, and the vector $\boldsymbol{X}$ contains the unknown velocity, pressure and interface deformation variables. We first discuss the choice of the collocation points in each fluid domain as well as the collocation method used and the tool used to solve the problem.

10.2.1 Collocation points and method

We present the discretization of the two fluid domains.

Fluid (1) : let

$$\xi_i^{(1)} \equiv \cos\left(\frac{\pi i}{2N_1}\right), \quad i=0,1,\cdots,N_1\,. \quad (10.32)$$

In the interval $[0,1]$, one uses N_1+1 collocation points situated at $r_i^{(1)} = \xi_i^{(1)}$ (no mapping). The points are thus more dense near the interface at $r=1$ ($i=0$) than at the axis $r=0$ ($i=N_1$).

Fluid (2) : let

$$\xi_i^{(2)} \equiv \cos\left(\frac{\pi i}{2N_2}\right), \quad i=0,1,...,2N_2\,. \quad (10.33)$$

In the interval $[1,R_{\mathrm{ext}}]$, one uses $2N_2+1$ collocation points situated at $r_i^{(2)} = R(\xi_i^{(2)})$ where the mapping function is defined by

$$R(\xi) \equiv 1+\frac{1-\xi}{\sqrt{1+\alpha-\beta(1-\xi)^2}}, \quad (10.34)$$

the reciprocal of which reads

$$\xi(r) = 1-\frac{\sqrt{1+\alpha}}{\sqrt{1+\beta r^2}}r\,. \quad (10.35)$$

The interface $r=1$ corresponds to $\xi=1$ ($i=0$), the outer boundary $r=R_{\mathrm{ext}}$ corresponds to $\xi=-1$ ($i=2N_2+1$). The point where $\xi=0$ ($i=N_2$) corresponds to a radial location $r=R_c$: by construction,

half of the collocation points in fluid (2) are between $r = 1$ and $r = R_c$, and the other half between $r = R_c$ and $r = R_{\text{ext}}$. If we prescribe the values of R_c and R_{ext} (typically, $R_c = 2$ and $R_{\text{ext}} = 30$), since

$$R_{\text{ext}} = \frac{2}{\sqrt{1+\alpha-4\beta}}\,, \quad R_c = \frac{1}{\sqrt{1+\alpha-\beta}}\,,$$

we can deduce the values of α and β of the mapping function as:

$$\alpha = \frac{4}{3}\left(\frac{1}{R_c^2} - \frac{1}{R_{\text{ext}}^2}\right) - 1\,, \quad \beta = \frac{1}{3}\left(\frac{1}{R_c^2} - \frac{4}{R_{\text{ext}}^2}\right).$$

The derivative of a function at the collocation points is expressed as a linear combination of the function values thanks to the Tchebychev-collocation method. In fluid (1) for $r \leq 1$, as only **even** functions q are dealt with, only half of the Gauss–Lobatto collocation points is used (the points for $i = N_1 + 1, \cdots, 2N_1$ are not used), leading to differentiation formulas

$$\frac{q'(r_i)}{r_i} = \sum_{j=0}^{N_1} \boldsymbol{A}^r_{ij} q_j\,, \quad q''(r_i) = \sum_{j=0}^{N_1} \boldsymbol{B}^r_{ij} q_j\,. \tag{10.36}$$

In fluid (2) for $r \geq 1$, the formulas are written for an arbitrary function Q and also involve factors due to the mapping (see Eq. 10.35). They read

$$Q'(r_i) = \xi'(r_i) \sum_{j=0}^{2N_2} \boldsymbol{A}^*_{ij} Q_j\,, \quad Q''(r_i) = \xi'^2(r_i) \sum_{j=0}^{2N_2} \boldsymbol{B}^*_{ij} Q_j + \xi''(r_i) \sum_{j=0}^{2N_2} \boldsymbol{A}^*_{ij} Q_j\,. \tag{10.37}$$

The matrices $\boldsymbol{A}^r$, $\boldsymbol{A}^*$, $\boldsymbol{B}^r$ and $\boldsymbol{B}^*$ are given in Appendix E.

10.2.2 Boundary conditions at R_{ext}

As the numerical domain has a finite extent, we select boundary conditions at the outer boundary $r = R_{\text{ext}}$. Such conditions are Robin conditions that mimick an outer potential flow of infinite extent:

$$\frac{dF}{dr} - C_r^{(m)} F = 0 \tag{10.38}$$

$$\frac{dG_+}{dr} - \frac{C_r^{(m)} + C_\theta^{(m)}}{2} G_+ - \frac{C_r^{(m)} - C_\theta^{(m)}}{2} G_- = 0 \tag{10.39}$$

$$\frac{dG_-}{dr} - \frac{C_r^{(m)} - C_\theta^{(m)}}{2} G_+ - \frac{C_r^{(m)} + C_\theta^{(m)}}{2} G_- = 0 \tag{10.40}$$

where the values of the coefficients in the asymptotic expressions (10.38)–(10.39) are explained in Appendix F.

10.2.3 Discrete generalized eigenvalue problem

If the unknown discrete variables relative to fluid (1) are gathered in vector

$$\boldsymbol{X}^{(1)} \equiv \left(\{f_i, g_{+,i}, g_{-,i}, p_i\}_{i=0,1,\cdots,N_1} \right) ,$$

the spatial discretization of system (10.20) leads to a problem of the form $\boldsymbol{A}^{(1)}\boldsymbol{X}^{(1)} = \mathrm{i}\omega\boldsymbol{B}^{(1)}\boldsymbol{X}^{(1)}$.

Similarly, the vector of unknown discrete variables relative to fluid (2) reads

$$\boldsymbol{X}^{(2)} \equiv \left(\{F_i, G_{+,i}, G_{-,i}, P_i\}_{i=0,1,\cdots,2N_2} \right) ,$$

and the discretization of system (10.23) leads to a problem of the form $\boldsymbol{A}^{(2)}\boldsymbol{X}^{(2)} = \mathrm{i}\omega\boldsymbol{B}^{(2)}\boldsymbol{X}^{(2)}$.

The final problem involves the coupling between the two fluids at the interface, which deforms with complex amplitude ζ_0. The total vector of unknowns then contains $(N_1 + 2N_2) \times 4 + 3$ complex elements :

$$\boldsymbol{X} \equiv \left(\{f_i, g_{+,i}, g_{-,i}, p_i\}_{i=0,1,\cdots,N_1}, \{F_i, G_{+,i}, G_{-,i}, P_i\}_{i=0,1,\cdots,2N_2}, \zeta_0 \right) .$$

This leads eventually to a problem of the form

$$\boldsymbol{A}\boldsymbol{X} = \mathrm{i}\omega\boldsymbol{B}\boldsymbol{X} \tag{10.41}$$

where the matrices $\boldsymbol{A}$ and $\boldsymbol{B}$ are built from blocks $\boldsymbol{A}^{(k)}$ and $\boldsymbol{B}^{(k)}$ for $k = 1, 2$, with some modifications and add-ons, as explained below :

1. the additional equation needed (the last line of $\boldsymbol{A}$ and $\boldsymbol{B}$, corresponding to the index of variable ζ_0 in the vector $\boldsymbol{X}$) is directly taken to be the kinematic condition (10.25) at $r = 1$:

$$-\frac{1}{2}(G_{+,0} + G_{-,0}) + \mathrm{i}(kU_x^{(2)} + mW_\theta^{(2)})\zeta_0 = \mathrm{i}\omega\zeta_0 \, ; \tag{10.42}$$

2. 6 conditions (10.26)–(10.31) at the interface $r = 1$ remain to be enforced: in the total equation system, these relations are plugged into the 6 lines corresponding to variables $f_0, g_{+,0}, g_{-,0}, F_0, G_{+,0}$ and $G_{-,0}$;
3. 3 conditions at the outer boundary $r = R_{\mathrm{ext}}$ given by (10.38) or (10.39) are plugged into the lines corresponding to variables $F_{2N_2+1}, G_{+,2N_2+1}$ and $G_{-,2N_2+1}$;
4. the equations corresponding to the zero-divergence equation, to the above-mentioned group of 6 conditions at the interface and 3 at the outer boundary a priori do not contain $\mathrm{i}\omega$, thus the corresponding lines in the $\boldsymbol{B}$ matrix contain only 0 values. This would yield to a group of unphysical zero eigenvalues associated to these conditions, that we prefer to monitor and displace far from the origin. To do so, instead of directly coding the equation (say, Eq = 0), we implement $(\alpha - \mathrm{i}\omega)\mathrm{Eq} = 0$, where α is an arbitrary large constant (30 for instance). This will lead to a purely imaginary frequency $\omega_i = -\alpha$, thus strongly damped, which can be discarded from the set of obtained eigenvalues.

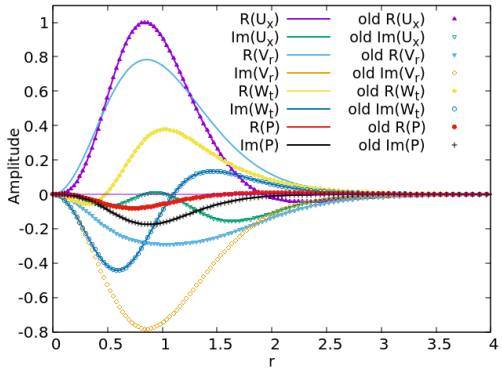

Figure 10.1 – Normalized velocity and pressure eigenfunctions for the most unstable mode of the homogeneous Batchelor vortex with swirl $q = 0.656$ at $Re = 100$. Axial and azimuthal wavenumbers are $k = 1.582$ and $m = -3$. Lines: two-phase code; dots: homogeneous code.

10.2.4 Extracting the most unstable mode in the linear regime

System (10.41) is solved using the subroutine F02GJF of the NAG library. The computation is done twice with different numbers of grid points, so as to eliminate spurious (non-physical) eigenvalues that depend on this numerical parameter. Physical eigenvalues are sorted from the most unstable to the most damped. Here, only the dominant instability mode, i.e. the one with the largest growth rate ω_i is considered. The associated eigenvector $\boldsymbol{X}$ provides the complex amplitude of the velocity and pressure eigenfunctions, once the backward change of variables

$$F(r_i) = r_i^{|m|} f_i \ , \quad G_\pm(r_i) = r_i^{|m\pm1|} g_{\pm,i} \ , \quad P(r_i) = r_i^{|m|} p_i$$

has been done in fluid (1), and the usual eigenfunctions G and H relative to radial and azimuthal velocity components have been restored for both fluids (1) and (2):

$$G(r_i) = \frac{1}{2}[G_+(r_i) + G_-(r_i)] \ , \quad H(r_i) = \frac{1}{2\mathrm{i}}[G_+(r_i) - G_-(r_i)] .$$

The eigenmode is then normalized: first the location r_m of maximum $|F(r_i)|$ over the whole domain is found. All the eigenfunctions Q are then divided by the complex value $F(r_m)$:

$$\bar{Q}(r_i) \equiv \frac{Q(r_i)}{F(r_m)} ,$$

or, using the real and imaginary parts:

$$\bar{Q}(r_i) = \frac{Q_r(r_i) + \mathrm{i}Q_i(r_i)}{F_r(r_m) + \mathrm{i}F_i(r_m)} = \frac{[Q_r(r_i) + \mathrm{i}Q_i(r_i)][F_r(r_m) - \mathrm{i}F_i(r_m)]}{F_r(r_m)^2 + F_i(r_m)^2} .$$

An example of normalized eigenfunctions is given in Fig. 10.1. For the interface deformation amplitude, on defines $\bar{\zeta}_0 \equiv \zeta_0 / F(r_m)$. In the following, whenever there is no ambiguity, we will remove the overbar.

Chapter 11

Linear instability : validation and results

Contents

First we validate the instability code presented in chapter 10 by comparing its growthrates with results known from the literature: the case of a homogeneous swirling jet flow, of the two-phase Rayleigh-Plateau instability. We then study the role of azimuthal velocity profiles.

11.1 Validation of viscous instability code

The instability code for two-phase columnar flows has been built from an existing instability code for homogeneous columnar flows [IQBAL, 2005]. A first test consists in running the two-phase instability code with two identical fluids, and setting surface tension to zero: the same instability modes as the homogeneous flow are to be found. The base profile used is that of the swirling jet:

$$U_x(r) = e^{-r^2}, \quad V_r = 0, \quad W_\theta(r) = q\frac{1-e^{-r^2}}{r}, \tag{11.1}$$

where the swirl number q characterizes the ratio between azimuthal and axial velocities.

Results obtained by our code are listed in table 11.1 (column Xu) and compared to those of Fabre & Jacquin [FABRE and JACQUIN, 2004] (column FJ04) and of Iqbal [IQBAL, 2005] (column I05). Different values of azimuthal number m, Reynolds number Re, swirl q and axial wave number k are tested: the code is shown to yield the same results up to 4 digits, which is fully satisfactory. Note that the two combinations (m, q) and $(-m, -q)$ give, as expected, the same results.

	q	k	FJ04	I05	Xu
$m=-1, Re=10^2$	0.406	0.769	0.1734	0.1734	0.1734
$m=-1, Re=10^3$	0.448	0.811	0.2339	0.2339	0.2339
$m=-1, Re=10^4$	0.457	0.812	0.2416	0.2416	0.2416
$m=-2, Re=10^2$	0.622	1.108	0.1812	0.1812	0.1812
$m=-2, Re=10^3$	0.680	1.174	0.2956	0.2956	0.2956
$m=-2, Re=10^4$	0.691	1.180	0.3119	0.3119	0.3119
$m=-3, Re=10^2$	0.656	1.582	0.1431	0.1431	0.1431
$m=-3, Re=10^3$	0.761	1.659	0.3245	0.3245	0.3245
$m=-3, Re=10^4$	0.776	1.664	0.3514	0.3514	0.3514
$m=+3, Re=10^4$	-0.776	1.664	0.3514	0.3514	0.3514

Table 11.1 – Comparison of growth rates ω_i for several maximum amplification cases: azimuhtal wavenumber m, Reynolds number Re, swirl number q, axial wavenumber k. FJ04 indicates results by Fabre and Jacquin [FABRE and JACQUIN, 2004], I05 by Iqbal [IQBAL, 2005], for comparing with those of the present code (Xu).

For a two phase flow, comparisons between analytical and numerical code results are presented for the Rayleigh–Plateau instability of inviscid and viscous case in Fig. 1.3 a for the dependency on density ration and b for the dependency on Re number. Excellent agreement is found.

11.2 Effect of azimuthal velocity profile

11.2.1 Liquid column in solid body rotation (viscous)

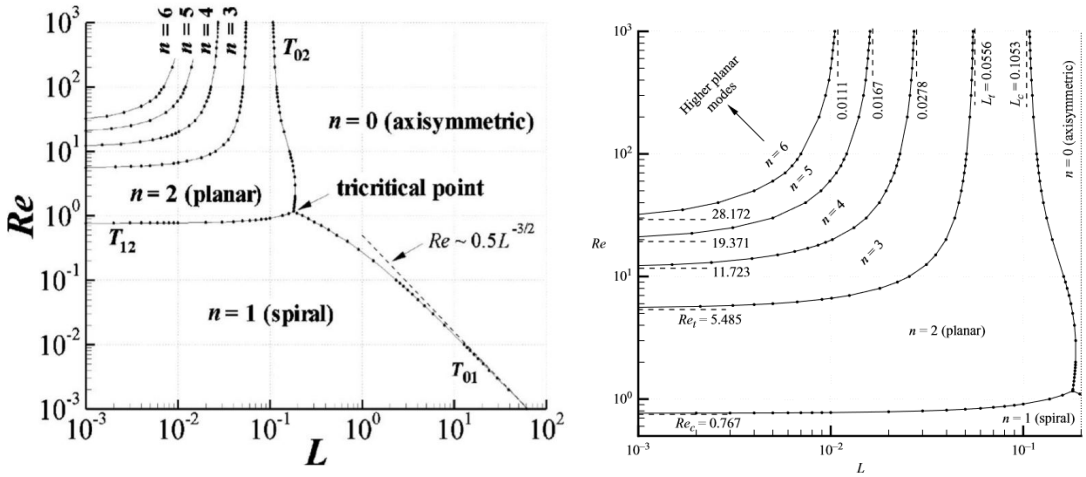

Figure 11.1 – Liquid column in solid body rotation: preferred mode in the $L - Re_q$ plane [Kubitschek and Weidman, 2007a].

Works by Gillis & Kaufman [Gillis and Kaufman, 1962] and Kubitschek & Weidman [Kubitschek and Weidman, 2007a] describe the instability of a liquid column of radius R_0

rotating as a solid body. In fluid (1), the dimensional base velocity reads:

$$U_x = 0, \quad V_r = 0, \quad W_\theta(r) = \Omega\, r, \tag{11.2}$$

and the motion of the outer flow is not taken into account (free-surface). The preferred instability mode is axisymmetric or spiral depending on the values of the parameters (see figure 11.1): these authors used the Hocking parameter comparing surface tension to centrifugal effects $L \equiv \gamma/(\rho R_0^3 \Omega^2) = 1/q^2$, and a Reynolds number based on the azimuthal motion $Re_q \equiv \rho R_0^2 \Omega/\mu$. As shown in figure 11.1, at large Re_q, the preferred mode is either axisymmetric ($m = 0$) at low rotation (high surface tension) or spiral ($m = 2, 3, \ldots$) at larger rotation (lower surface tension). Viscosity tends to dampen the spiral modes, and at low Re_q and low L, a $m = 1$ spiral mode dominates the instability (for instance, at $q = 10$ and $Re_q = 0.05$).

The present code is tested with a water/air interface (see model A in section 9.2.3), for the axisymmetric mode ($m = 0$) of instability. The comparison is given in figure 11.2, with fair agreement. The small shift may be due to the presence of air which affects the results.

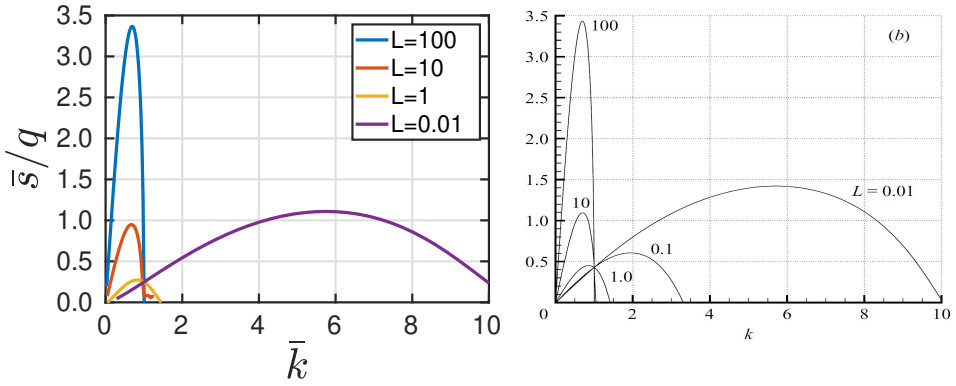

Figure 11.2 – Dimensionless growth rate of the axisymmetric instability mode in a liquid column in solid body rotation, as a function of dimensionless wavenumber kR_0 for different values of the Hocking parameter L, at $Re_q = 1000$. Left: present results with two fluids (water/air, model A); right: results from [Kubitschek and Weidman, 2007a] with free surface.

11.2.2 Hollow vortex

[Ponstein, 1959] gives the dispersion relation for an inviscid dense potential vortex of circulation Γ with a cylindrical hollow core (no motion) of radius R_0. The outer liquid rotates according to a potential vortex solution: $W_\theta(r) = \Gamma/(2\pi r)$ for $r \geq R_0$. The dimensional growth rate of axisymmetric waves reads

$$s^2 = \frac{\bar{k} K_1(\bar{k})}{K_0(\bar{k})} \left[\left(1 - \bar{k}^2\right) \frac{\gamma}{\rho R_0^3} - \frac{\Gamma^2}{4\pi^2 R_0^4} \right], \tag{11.3}$$

where $\rho = \rho_2$ (one has $\rho_1 = 0$). The critical wavenumber $\bar{k}_c$ below which axisymmetric waves are unstable can be deduced as

$$\bar{k}_c = \sqrt{1 - \frac{\bar{\Gamma}^2}{4\pi^2}}\,, \quad \bar{\Gamma} \equiv \sqrt{\frac{\rho}{\gamma R_0}}\,\Gamma\,. \tag{11.4}$$

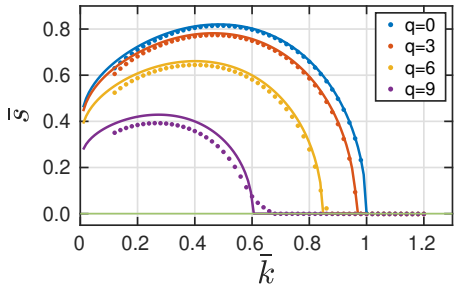

Figure 11.3 – Influence of the rotation parameter q (base state B) on the growth rate of mode $m = 0$ when $\delta_1 = \delta_2 = 0.1$, $\rho^{(1)} = 10^{-3}$, $\rho^{(2)} = 1$, $\mu^{(1)} = 10^{-3}$ and $\mu^{(2)} = 1$. Solid lines: theoretical inviscid dispersion relation ; symbols: results from the instability code at $Re_q = 10^3$.

If the base state B of section 9.2.3 is taken as base flow to describe such a case, then $\bar{\Gamma} \approx \pi^{3/2} q\delta$ and the nondimensional dispersion relation becomes

$$\bar{s}^2 \approx \bar{k}\frac{K_1(\bar{k})}{K_0(\bar{k})}(1 - \bar{k}^2 - \frac{1}{4}\pi\delta^2 q^2) \tag{11.5}$$

The unstable range of wavenumbers and the maximum growth rate both reduce as q is increased from 0, until the flow becomes totally stable with respect to axisymmetric perturbations. This behaviour can be explained by the centrifugal force which becomes dominant over the capillary force and kills the Rayleigh-Plateau instability. The way to the stabilisation due to rotation is seen in figure 11.3 at $Re_q = 10^3$. Stabilization occurs for $q_c \approx 11.28$. Excellent agreement is found on the critical wavenumber values at all the q levels investigated as well as a fair agreement between the growth rates from the inviscid theory with free surface and those from the viscous numerics with an external layer.

11.2.3 Air column in water : another profile

The base state B adopted in the previous subsection is pertinent to describe a hollow vortex. Yet, in some cases with air as inner fluid and water as ambient fluid, the azimuthal profile may be better described by base state A with solid-body rotation in air. Indeed, the kinematic viscosity of air is larger than that of water, which enhances the convergence to a solid-body in the gas. Other effects can accelerate the process, such as stretching. This is precisely what occurs in a toroidal bubble as formed by scuba divers, beluga whales or dolphins. After releasing a puff of gas into water, a small gaseous torus forms, that can then be stretched up to large radii. This is the topic of the publication in chapter 13, which focuses both on the formation of the toroidal bubble and on its stabilization due to rotation. The section 4.2.2 of this publication is presented below.

Symmetry ********** We study the linear stability for the air-water column of the base flow A. The Reynolds number used in article $Re_B = \sqrt{\gamma^{(air)}\sigma R_0/\mu^{(air)}}$. Figures 11.4–11.6 provide linear instability results for non axisymmetric modes $m \pm 1$, ± 2 and ± 3. The first observation is that, at given $\bar{k}$ and $|m|$ values, the growth rate is found almost the same for $m > 0$ and $m < 0$. The equality exactly holds when $q = 0$ for symmetry reasons, and the fact that it holds also roughly for $q \neq 0$ can be explained by the uniform vorticity inside the bubble. Interestingly, rotation does not influence mode $|m| = 1$, that remains stable. For sufficiently low Reynolds number and small δ, other azimuthal modes

$m \neq 0$ for small k can be destabilized. For instance, the mode $m = 2$ is found unstable for $Re_B = 10$ and $\delta = 0.3$ (figure 11.4b). The growth rate decreases as the Reynolds number increases (figure 11.6b). This is reminiscent of planar modes $k = 0$ in Ref. [Kubitschek and Weidman, 2007a]. Note that for larger values of δ, this mode is restabilized: for $\delta = 1$, all modes tested are stabilized by rotation, this conclusion holding irrespective of the Reynolds number as in figures 11.5.

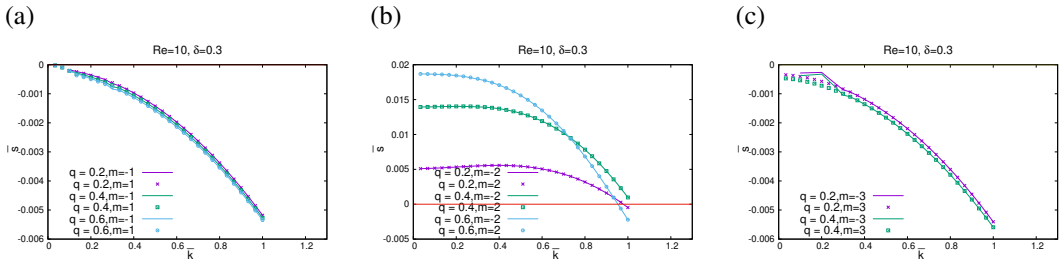

Figure 11.4 – Growth rate $\bar{s}$ as a function of wavenumber $\bar{k}$ for a viscous column of air surrounded by water at $\delta = 0.3$, $Re_B = 10$ and various swirl $q = 0.2, 0.4, 0.6$. (a) $m = \pm 1$; (b) $m = \pm 2$; (c) $m = \pm 3$. Positive m: symbols; negative m: bold line.

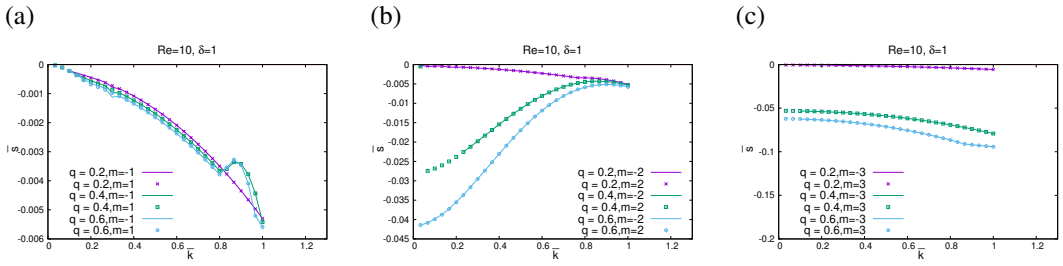

Figure 11.5 – Same as figure 11.4 but for $\delta = 1$ ($Re_B = 10$).

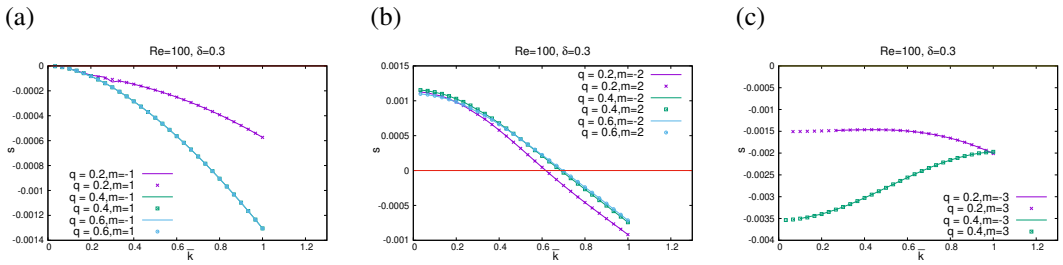

Figure 11.6 – Same as figure 11.4 but for $\delta = 0.3$ and $Re_B = 100$.

Chapter 12

Linear and non-linear evolution using Basilisk flow solver

Contents

In chapter 11, the solutions of the linearized Navier-Stokes equations for the problem were presented. In this chapter we use an existing numerical code, the Basilisk flow solver [Popinet, 2015], to validate these solutions with Direct Numerical Simulations (DNS). We also see the nonlinear evolution of some non-axisymmetric instability mode. The code uses the Volume of Fluid (VOF) method to track the interface position as well as an accurate method for the estimation of forces at the interface [Afkhami et al., 2009].

12.1 Validation of swirling air-column instability

In this section, we compare the growth rates of the instability of a swirling air column obtained using the instability code of chapter 11and a DNS of perturbation growth.

12.1.1 Numerical set-up

We can write the Navier–Stokes equations in the whole fluid domain:

$$\nabla \cdot \boldsymbol{u} = 0 \tag{12.1}$$

$$\rho \left[\frac{\partial \boldsymbol{u}}{\partial t} + (\boldsymbol{u} \cdot \nabla)\boldsymbol{u} \right] = -\nabla p + \mu \nabla^2 \boldsymbol{u} + \gamma \kappa \delta_s(n)\boldsymbol{n} \tag{12.2}$$

where κ is the mean curvature of the interface and δ_s is a delta function centered at the interface location. For a column of radius R_0 and an initial perturbation of wavelength λ, by choosing the characteristic length, time and mass scales as $[L] = \lambda$, $[T] = \sqrt{\rho^{(w)}\lambda^3/\gamma}$, $[M] = \rho^{(w)}\lambda^3$, we get the dimensionless expression as:

$$\nabla \cdot \tilde{\boldsymbol{u}} = 0 \tag{12.3}$$

$$\tilde{\rho}\left[\frac{\partial \tilde{\boldsymbol{u}}}{\partial t} + (\tilde{\boldsymbol{u}} \cdot \nabla)\tilde{\boldsymbol{u}}\right] = -\nabla \tilde{p} + \tilde{\mu}\nabla^2 \tilde{\boldsymbol{u}} + \tilde{\gamma}\kappa\delta_s(n)\tilde{\boldsymbol{n}} \tag{12.4}$$

with $\tilde{\rho} = \rho/\rho^{(w)}$, $\tilde{\gamma} = 1$, $\tilde{\mu} = \frac{\mu}{\mu^{(w)}}\frac{1}{Re}\sqrt{\frac{\lambda}{R_0}}$ where Reynolds number equals $Re = \sqrt{\rho^{(w)}\gamma R_0}/\mu^{(w)}$.

The general simulation setup consists in two immiscible fluids filling a square domain $(\tilde{x}, \tilde{y}) \in [0,1]\times[0,1]$. The equations are written in the axisymmetric configuration (the axis is the x axis, while y denotes the radial direction), with a normal component of velocity (along the azimuth z) allowed. At the symmetry axis, the radial and azimuthal velocity components are set to zero and the axial velocity satisfies a Neumann condition. At the boundary at $\tilde{y} = 1$ (top), we set a Dirichlet condition for the radial velocity and a Neumann condition for pressure. Periodic conditions are applied along x so that finally:

$$\tilde{u}_r(\tilde{y} = 0) = 0\,, \quad \tilde{u}_r(\tilde{y} = 1) = 0\,, \quad \partial_r p(\tilde{y} = 1) = 0\,, \quad \tilde{\boldsymbol{u}}(\tilde{x} = 0, \tilde{y}) = \tilde{\boldsymbol{u}}(\tilde{x} = 1, \tilde{y}).$$

The initial position of the interface is defined by

$$r = \tilde{R}_0(1 + \epsilon\cos(\tilde{k}_0\tilde{x}))\,, \quad \text{with} \quad \tilde{R}_0 = \frac{R_0}{\lambda} = \frac{k}{2\pi}R_0 \tag{12.5}$$

where ϵ is the the amplitude of the initial perturbation relatively to $\tilde{R}_0$ and $\tilde{k}_0 = 2\pi$ is the nondimensional wavenumber. The initial velocity field is set to the base state $\boldsymbol{u}_{BF}$ (usually the states in section 9.2.3). In the following when there is no ambiguity, the bar is removed.

One extracts the nondimensional perturbation amplitude $\eta(t) = \max(r(x,t) - R_0)$, where $r(x,t)$ is the location of the interface. After a transient regime, this quantity should grow exponentially according to the law $\eta(t) = \eta_0 e^{st}$. The growth rate s can be obtained by linear regression of $\log(\eta)$ and should then be scaled with the relation $\bar{s} = s(\lambda/R_0)^{-3/2}$ to be compared with the results of the linear stability analysis. The error on the growth rate is estimated in appendix G:

$$\xi_{tot} = \sqrt{\xi_{\Delta\tilde{x}}^2 + \xi_\epsilon^2} = \sqrt{\frac{140^2}{N^4} + 0.5\,\epsilon^{0.6}} \quad \text{for} \quad N = \frac{\lambda}{\Delta x}\,, \quad \epsilon \in [10^{-3}, 10^{-1}]. \tag{12.6}$$

where $\xi_{\Delta\tilde{x}}$ stand for the error from mesh size and ξ_ϵ stand for the error from initial interface perturbation amplitude. For instance, in the case $kR_0 = 0.7$, $N = 128$, and $\epsilon = 0.01\Delta x/R_0$, one gets error $\xi_{tot} = \sqrt{7.3\times10^{-5} + 4.6\times10^{-4}} = 0.0231$.

12.1.2 Instability: linear regime

We validate the linear stability analysis obtained in section 11.2.3 for an air column in solid body rotation within water. The base state used is the type A with $\delta = 0.1$ (see section 9.2.3). The densities are set to $\rho^{(1)} = 10^{-3}$, $\rho^{(2)} = 1$, the viscosities to $\mu^{(1)} = 10^{-3}$, $\mu^{(2)} = 1$. We choose several values of q and k, in the

axisymmetric case. The growthrates obtained by DNS are represented by red dots in figure 12.1 and are found to fit well with the predictions of the instability code.

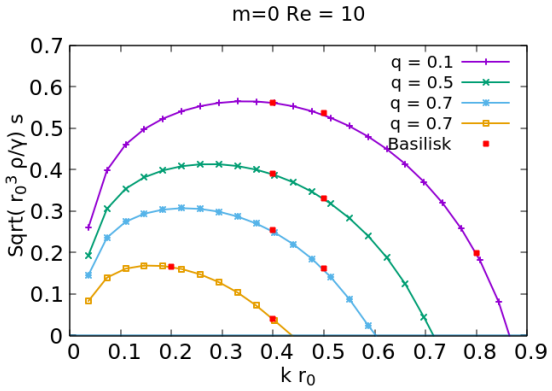

Figure 12.1 – The dispersion relation of axisymmetric mode $m = 0$ for base state of type A with $\delta = 0.1$, $Re = 10$, $\rho^{(1)} = 10^{-3}$, $\rho^{(2)} = 1$, $\mu^{(1)} = 10^{-3}$, $\mu^{(2)} = 1$. Lines: instability code. Red dots: DNS results.

We then perform a second DNS, where we superimpose the base state $\boldsymbol{u}_{BF}$ and the perturbation $\boldsymbol{u}_{mode}$ obtained theoretically (see sec. 10.2.4). The DNS is initiated using the velocity field

$$\boldsymbol{u}_{ic} = \boldsymbol{u}_{BF} + \epsilon \boldsymbol{u}_{mode} \tag{12.7}$$

where ϵ is a small amplitude. The results are shown in figure 12.2, in which a pure exponential growth is found as expected, and the growthrate agrees with the theoretical prediction.

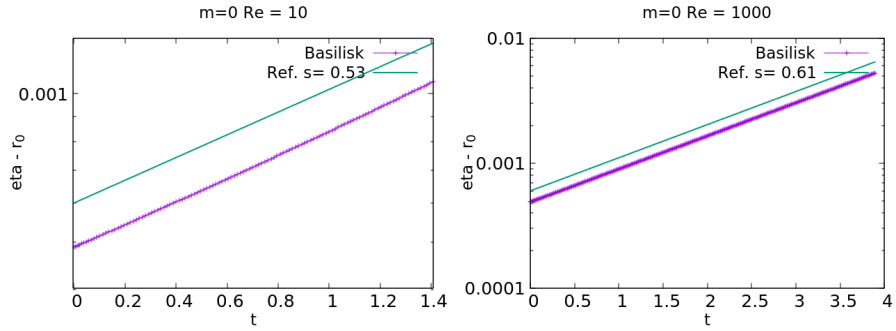

Figure 12.2 – The growth of interface perturbation amplitude for base state A with $\delta = 0.1$, $q = 0.5$, $\rho^{(1)} = 10^{-3}$, $\rho^{(2)} = 1$, $\mu^{(1)} = 10^{-3}$, $\mu^{(2)} = 1$, $\tilde{k}_0 = 0.5$. The initial condition for velocity is given by (12.7). Dotted line: DNS (Basilisk); solid line: theory. Left: $Re = 10$; right: $Re = 10^3$.

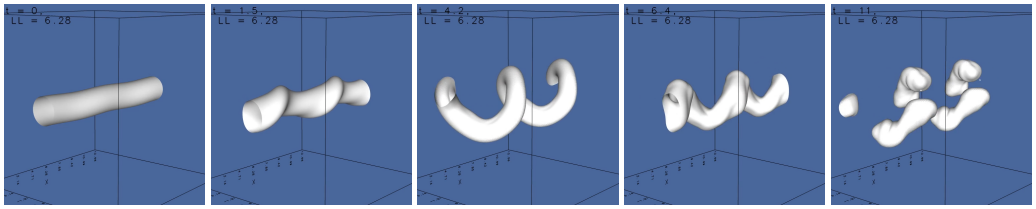

Figure 12.3 – Interface of a swirling water column with base state A at swirl number $q = \sqrt{10}$, $\delta = 0.1$, $Re = 316$ at different times $t = 0, 1.5, 4.2, 6.4, 11$. The initial interface is perturbed with $m = 1$, $\epsilon = 0.05$, $\bar{k} = 1$ and periodic number $L = 2$. Characteristic of two fluids reads $\rho^{(1)} = 1$, $\rho^{(2)} = 10^{-3}$, $\mu^{(1)} = 1$, $\mu^{(2)} = 2 \times 10^{-2}$.

12.2 3D DNS of a rotating water column

We are also interested in non-axisymmetric modes developing naturally in a swirling column of fluid, as presented earlier (see figure 8.1).

The simulations are carried out using Basilisk in a fully 3D configuration. The general simulation setup consists in two immiscible fluids, while the inner column has an initial radius $\bar{R}_0 = 1$, filling a cube domain $(\bar{x}, \bar{y}, \bar{z}) \in [0, L\bar{\lambda}] \times [-L\bar{\lambda}/2, L\bar{\lambda}/2] \times [-L\bar{\lambda}/2, L\bar{\lambda}/2]$, with wavelength perturbation $\bar{\lambda} = \lambda/R_0$, and domain size of L periodic, by default $L = 2$. Periodicity is assumed along x. Conditions at the lateral boundaries are imposed by the base state, namely the velocity profile and swirl intensity q, and one assumes that the perturbations vanish there.

Using polar coordinates (r, θ, x), we then set the initial perturbation for the interface according to:

$$r = R_0(1 + \epsilon \cos(kx + m\theta)), \tag{12.8}$$

where m is the azimuthal mode number considered and $\bar{k} = kR_0$ is the wavenumber closed to maximal growth, predicted by linear stability analysis at the given Reynolds number Re. If there is no ambiguity, the hat will be removed in the following context . The results of 3D simulations from modes $m = 1$ to 4 are plotted in figures 12.3–12.7.

In figure 12.3, the temporal evolution of the perturbation at $m = 1$ is presented. The liquid column is observed to take a helical shape. At a certain helical radius, it breaks into droplets, resulting from both the Rayleigh-Plateau instability and fluid motions inside the column.

In figure 12.4, the evolution of the $m = 2$ perturbation is presented. The dynamics is complex: the column flattens into a twisted sheet ($t < 1.5$), then liquid rims are observed at the edges ($t = 1.5$), the column contracts back ($t = 4$) while secondary perturbations grow: droplets form on the rim while the column is again stretched ($t = 6$); after a second contraction of the column, ligaments are formed that connect to the droplets ($t = 7.6$). In [Kubitschek and Weidman, 2007a] (see figure 8.1 a), the evolution of the perturbation $m = 2$ did not go that far, presumably because of the limited downstream extent of the experimental setup. However, the appearance of rims, sheets, droplets and ligaments observed here is very similar to the process experimentally observed for mode $m = 4$ (see figure 8.1 right).

In figure 12.5 and 12.6, two possible evolutions of mode $m = 3$ are presented. Figure 12.5 corresponds

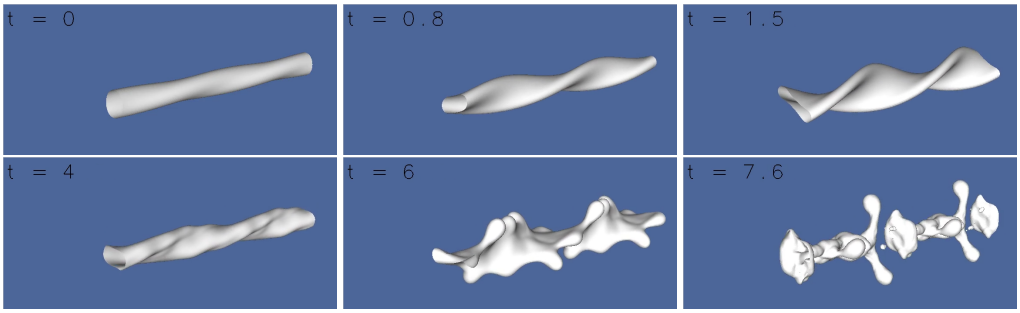

Figure 12.4 – Similar to figure 12.3 for mode $m = 2$ and $Re = 1000$ at $t = 0, 0.8, 1.5, 4, 6, 7.6$. Others parameters are the same, except for $\epsilon = 0.1$, $\bar{k} = 0.5$.

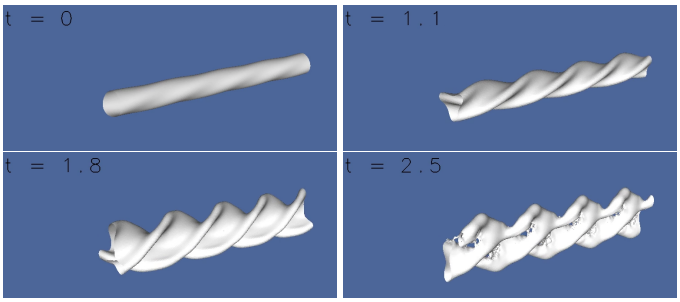

Figure 12.5 – Similar to figure 12.3 for mode $m = 3$ and $Re = 100$ at $t = 0, 0.5, 0.8, 1.1, 1.4, 1.8$. Others parameters are the same, except for $L = 4$, $q = 4.$, $\bar{k} = 1.0$, $\epsilon = 0.01$.

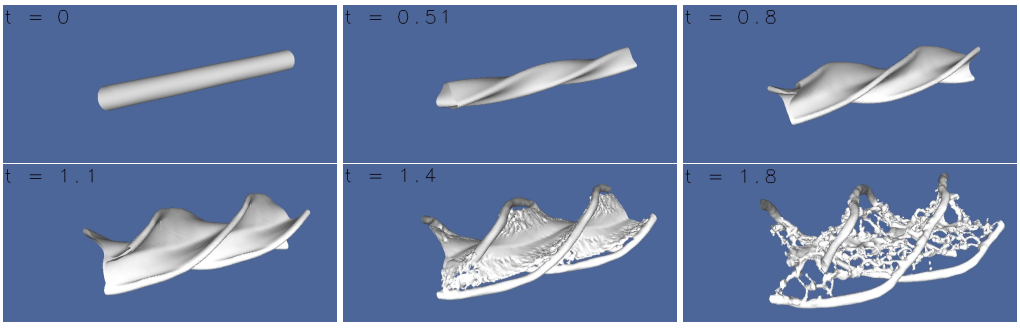

Figure 12.6 – Similar to figure 12.3 for mode $m = 3$ and $Re = 100$ at $t = 0, 0.5, 0.8, 1.1, 1.4, 1.8$. Others parameters are the same, except for $q = 6.$, $\bar{k} = 0.5$, $\epsilon = 0.01$.

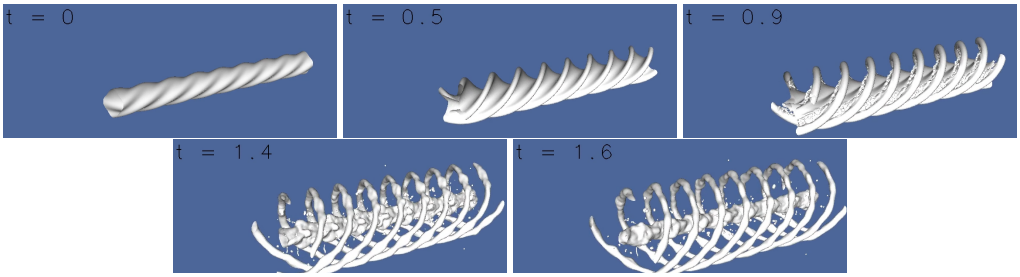

Figure 12.7 – Similar to figure 12.3 for mode $m = 4$ and $Re = 100$ at $t = 0, 0.5, 0.9, 1.4, 1.6$. Others parameters are the same, except for $q = 6.$, $\bar{k} = 2.0$, $\epsilon = 0.1$

to a weak growthrate $s_{th} = 2.02$ for $q = 4$, while figure 12.6 corresponds to a larger growth $s_{th} = 8.1$ for $q = 6$. In this latter case, the formation of helical rims dominates the dynamics, while the central part of the column becomes thinner and disintegrates.

In figure 12.7, an example of perturbation with $m = 4$ at $q = 6$ is presented. Here, helical rims form while a central liquid column persists in the vicinity of the axis.

In the previous cases showing non-axisymmetric dynamics of a swirling water column, a quantitative agreement was found concerning the linear growth rate of instability modes. These simulations then illustrate a rich variety of nonlinear evolution, with rim formation, thinning of the water column which disintegrates, or reforms, or oscillates, sometimes with formation of ligaments... As full 3D simulations cost huge computational resources, we did not go into further quantitative characterizations, for instance of secondary instabilities or nonlinear mode competition.

Chapter 13

Generation and stability of a vortex bubble ring

In this chapter, we study several aspects of the dynamics of a vortex bubble in a liquid environment: the generation of a vortex bubble (or not), the stretching of such a bubble and the investigation of its instability properties, in order to understand its robustness with respect to perturbations. This chapter contains a reprint of an article published in a special issue of the "Compte-Rendus de l'Académie des Sciences" under the title "Instability of a swirling bubble ring", Volume 348, issue 6-7 (2020), p. 519-535.

Comptes Rendus
Mécanique
2020, 348, nº 6-7, p. 519-535
https://doi.org/10.5802/crmeca.22

Tribute to an exemplary man: Yves Couder

Turbulence / *Turbulence*

Instability of a swirling bubble ring

Yonghui Xu [a], Ivan Delbende [b, c], Daniel Fuster [d] and Maurice Rossi [*, d]

[a] Sorbonne Université, UMR 7190, Institut Jean Le Rond d'Alembert, 75005 Paris, France

[b] Sorbonne Université, UFR d'Ingénierie, 4 place Jussieu, 75005 Paris, France

[c] LIMSI, CNRS, Université Paris-Saclay, rue du Belvédère, 91405 Orsay, France

[d] CNRS, UMR 7190, Institut Jean Le Rond d'Alembert, 75005 Paris, France

E-mails: yoghui.xu@sorbonne-universite.fr (Y. Xu), Ivan.Delbende@sorbonne-universite.fr (I. Delbende), daniel.fuster@sorbonne-universite.fr (D. Fuster), maurice.rossi@sorbonne-universite.fr (M. Rossi)

Abstract. A toroidal bubble or a cylindrical gas jet are known to be subjected to the Rayleigh–Plateau instability. Air bubble rings produced by beluga whales and dolphins however are observed that remain stable for long times. In the present work, we analyse the generation of such toroidal bubbles *via* numerical simulations, in particular how the process depends on surface tension. Their stability properties are then briefly analysed. For the estimated Reynolds and Weber numbers relative to the bubbles produced by these animals, the presence of a vortex inside and around the bubble is found to strongly stabilize the Rayleigh–Plateau instability.

Keywords. Instability, Vortex ring, Two-phase flow, Rayleigh–Plateau, Direct numerical simulation.

1. Introduction

This paper is written *in memoriam* Y. Couder. Yves was a colleague of deep thoughts and a humanist. In everyday life, he was prone to enthusiasm and passion for knowledge. He was an extraordinary observer and many of his breakthroughs originated from careful observations. As a modest homage, this paper presents a topic that takes its origin from an observation on Youtube! In his turbulence experiments [1, 2], Yves used bubbles to visualize vortices. The present work concerns a topic somewhat related: the generation and dynamics of an air bubble in the form of toroidal rings. It was some kind of surprise to see dolphins [3] or beluga whales [4] generate bubble rings from their mouth or blowholes and thereafter play for a long period of time with rings in which any sign of instability was absent.

* Corresponding author.

Indeed an axisymmetric columnar jet of fluid 1 embedded in a fluid 2, when slightly disturbed, is known to break into small droplets or bubbles. This subject was first studied by Lord Rayleigh [5, 6]. He computed how infinitesimal perturbations (more specifically normal modes of axial k and azimuthal m wavenumbers) evolve in time and obtained analytically the complex eigenvalue $s(k,m) = s_r + \mathrm{i}s_i$, and precisely s_r their growth rate as a function of wavenumbers k and m. For an inviscid two-phase column of radius a_0, axisymmetric perturbations $m = 0$ are the most dangerous ones and the dimensionless eigenvalue $\bar{s}$ is a function of the dimensionless wavenumber $\bar{k}$:

$$\bar{s}^2\left(1+\frac{\rho^{(2)}}{\rho^{(1)}}\frac{K_0(\bar{k})I_0'(\bar{k})}{K_1(\bar{k})I_0(\bar{k})}\right)=\bar{k}\left(1-\bar{k}^2\right)\frac{I_0'(\bar{k})}{I_0(\bar{k})}\quad\text{with }\bar{s}\equiv\sqrt{\frac{a_0^3\rho^{(1)}}{\sigma}}s,\ \bar{k}\equiv ka_0. \tag{1}$$

For $0 \leqslant \bar{k} \leqslant 1$, $\bar{s}$ is real with the two possible signs, meaning that the jet is unstable. For $\bar{k} \geqslant 1$, $\bar{s} = \mathrm{i}s_i$ is purely imaginary indicating a stable jet. This result can be explained by the theory of minimal energy: a multiphase system tends to possess a minimum capillary energy at rest. This instability known as Rayleigh–Plateau instability is due to a capillary mechanism. It breaks the jet into several drops or bubbles when $\bar{k} \leqslant 1$ so that the interface area is minimized. In order to stabilize Rayleigh–Plateau instability, an added rotation is an interesting possibility for applications, e.g. liquid atomization, spray generation, combustion processes. Previous works on the effect of rotation are those of [7–11]. In our case, we introduce this aspect to understand the video of dolphins playing with ring bubbles!

The present paper covers the three stages observed during the dolphin's video inside three separate sections. First, Section 2 introduces the generation of bubble rings through blowhole or mouth. To do so, one considers an idealized axisymmetric nozzle containing initially a gas bubble which is rapidly expelled. This part uses direct numerical simulation. A second stage in which the toroidal bubble is stretched is analyzed in Section 3 by analytical means. As an end result, this provides the vorticity profile reached after the stretching period. The third stage is discussed in Section 4 in which we study the stability of this new profile. The ring is replaced by a straight columnar bubble embedded in a vortex and a standard linear stability method is employed to investigate how superimposed infinitesimal perturbations evolve in time.

2. Two-phase ring generation

A bubble ring may appear in various ways: a first method consists in generating tiny gas bubbles in advance in a region which is thereafter crossed by a vortex ring produced away from this location [12]. The tiny bubbles migrate because of centrifugal force inside the vorticity ring core and then coalesce to form a toroidal gas bubble transported by the pre-formed vortex ring. In a second method, the vortex is generated at the same spot where tiny bubbles are located [13]. An other method consists in initializing a unique gas bubble inside a nozzle. Ejecting the fluid then causes the bubble to deform and break, yielding a toroidal bubble at the same time and location in which vorticity rolls up, e.g. near the trailing edge of the nozzle. This latter case is probably pertinent for vortex ring bubbles produced through the mouth or blowholes by belugas or dolphins. The presence of the tongue and its motion probably facilitate the toroidal bubble formation as mentioned and demonstrated by a scuba diver [14] but it is shown here not to be an essential feature.

We study below the toroidal bubble production through the mouth or blowholes in an idealized and simplest fashion without introducing the effect of the tongue. The geometry is an axisymmetric nozzle of radius R_0 and of thickness $2b_0 = R_0/4$ with an edge at 26.5° (see Figure 1a). The nozzle edge enables to fix the region of boundary layer separation and ends at $x = 2.8R_0$. Initially the two fluids are at rest and inside the tube, an air bubble of axial length L_B is located

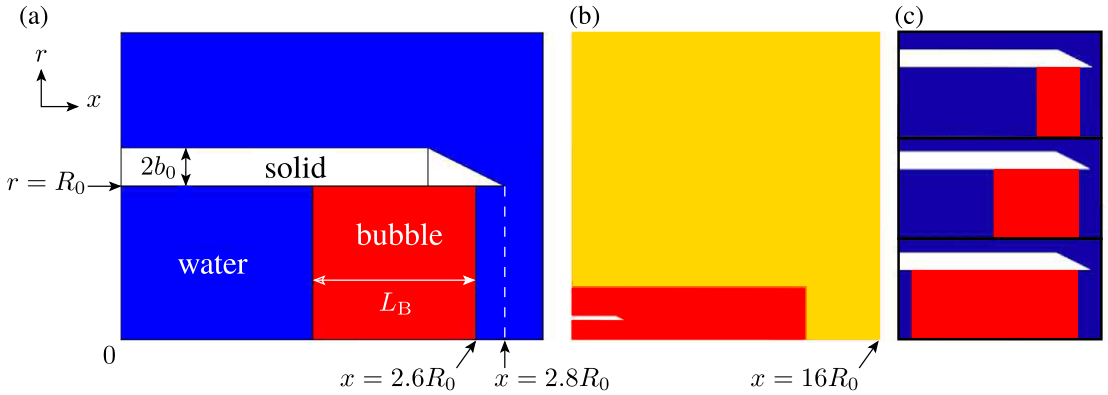

Figure 1. (a) Scheme of the numerical nozzle. (b) The whole numerical domain. In the yellow region, the mesh size is $\Delta_c = 0.125R_0$ and in the red region, $\Delta_c = 0.0078R_0$. (c) The three initial cases: the flow is at rest and a gas bubble (in red) of length L_B is contained in the nozzle. From top to bottom: $L_B = 0.6R_0$, $1.2R_0$ and $2.4R_0$.

within the axial interval $x \in [2.6R_0 - L_B, 2.6R_0]$ (see Figure 1c). The numerical domain (see Figure 1b) has been checked to be large enough to avoid boundary effects during the time of simulation: it is a square box $(x, r) \in [0, 16R_0] \times [0, 16R_0]$. Outflow boundary condition (stress free) are imposed at the downstream domain boundary $x = 16R_0$, impenetrability and slip condition on the lateral wall $r = 16R_0$ and no-slip everywhere else except for the region $x = 0$ and $r \leqslant R_0$ where the velocity is imposed. The air bubble is suddenly expelled from the nozzle and injected inside the ambient water. This occurs *together with* the phenomenon of roll-up of the boundary layer vorticity. The velocity field far inside the nozzle (at $x = 0$) mimics this rapid ejection

$$u_x(x = 0, r, t) = U_0 \operatorname{erf}\left(\frac{t}{\tau}\right) \operatorname{erf}(\eta), \quad u_r = 0 \quad \text{with } \eta = \frac{R_0 - r}{\sqrt{\nu^{(w)} t}} \geq 0, \tag{2}$$

where

$$\operatorname{erf}(x) \equiv \frac{2}{\sqrt{\pi}} \int_0^x \exp(-s^2)\, \mathrm{d}s$$

stands for the error function. The center velocity is changing from rest to a constant value U_0 within a time scale τ. For this problem we assume that $\tau \ll R_0/U_0$: the center velocity reaches its constant value rapidly compared to the time of roll-up itself. In our simulations, this parameter is fixed at $\bar{\tau} \equiv \tau U_0/R_0 = 0.1$. Moreover the flow is almost spatially uniform inside the tube except near the tube border $r = R_0$ where a boundary layer is present to ensure no-slip at the wall. This solution is close to what would be observed in a long tube subjected to a sudden pressure gradient. Kinematical viscosity of air and water are taken to be respectively (dimensional values are given in SI units) $\nu^{(a)} \sim 1.8 \times 10^{-5}$ and $\nu^{(w)} \sim 9 \times 10^{-7}$ and air and water density respectively $\rho^{(a)} = 1$, $\rho^{(w)} = 10^3$. Finally, air-water surface tension is assumed to be $\sigma = 73.4 \times 10^{-3}$.

Based on the nozzle radius R_0 as characteristic length scale and U_0 as the velocity scale, as well as water density and viscosity, this flow is defined by several dimensionless numbers: a *Reynolds* number, a *Weber* number and the relative length r_B of the bubble:

$$Re = \frac{U_0 R_0}{\nu^{(w)}}, \quad We = \frac{\rho^{(w)} U_0^2 R_0}{\sigma}, \quad r_B \equiv \frac{L_B}{R_0}. \tag{3}$$

Note that $Re/We^{1/2} = (\rho^{(w)} \sigma R_0)^{1/2}/\mu^{(w)}$ is independent on velocity and is equal to $Re/We^{1/2} \approx 10^4 {R_0}^{1/2}$ when R_0 is expressed in SI units. The boundary layer thickness δ_0 verifies $\delta_0/R_0 = \sqrt{\bar{t}/Re}$, where a nondimensional time variable $\bar{t} \equiv U_0 t/R_0$ is introduced. This thickness remains small for advective times much less than the Reynolds number $\bar{t} \ll Re$. The largest vorticity

Table 1. Estimated typical Reynolds and Weber numbers for scuba divers, beluga whales or dolphins

SI units	$R_0 = 0.02, U_0 = 0.1$	$R_0 = 0.1, U_0 = 0.1$	$R_0 = 0.02, U_0 = 0.3$	$R_0 = 0.1, U_0 = 0.3$
Re	2222	11111	6666	22222
We	2.72	13.6	24.5	120

occurs at the tube wall. In the bubble, for times such that $\bar{t}$ is of order one, the dimensionless vorticity maximum is of order

$$\frac{R_0}{U_0}\max(\omega) \sim -\frac{2}{\sqrt{\pi}}\frac{\sqrt{Re}}{\sqrt{\nu^{(a)}/\nu^{(w)}}} \sim -\sqrt{\frac{Re}{15.7}}. \tag{4}$$

For $Re = 5000$, the maximum is close to the value 17.8. Using dimensionless quantities, the entrance condition reads

$$u_x = \mathrm{erf}\left(\frac{\bar{t}}{\bar{\tau}}\right)\mathrm{erf}(\eta), \quad u_r = 0, \quad \text{with } \eta = \frac{1-r}{\sqrt{\bar{t}/Re}}. \tag{5}$$

The axisymmetric flow is described by the velocity fields $u_i(x, r, t)$ with $i = 1, 2$ related to the pseudo-scalar vorticity component $\omega_\theta(x, r, t)$, the plane (x, r) being oriented by the normal unit vector $\boldsymbol{e}_z$. In the present work, we focus on the transient period once the ejection has started: we hence study how the roll-up is modified by surface tension. For the formation process of the ring, axisymmetry is an adequate hypothesis but later on, one expects three-dimensional instabilities to appear on the starting bubble ring for a monophasic [15, 16] as for a two-phase vortex [15]. The numerical code we use in the present work is the Basilisk code [17, 18]. It has been largely tested and used to simulate two-phase flow problems. One problematic aspect is the motion of the triple line between bubble, solid and liquid, present during the initial ejection stage. We will not go into numerical details here but let us simply mention *en passant* that Basilisk numerically mimics the presence near the triple line of a Navier condition, i.e. the presence of a slip length condition which is used in the phenomenology of triple line motion. Here the slip length is half the mesh size near the solid boundary, namely $\frac{1}{2}\Delta_c = 0.0039\, R_0$.

The present work is not intended to be an extensive investigation of the parameter space of this problem, which in itself would cover several articles. We simply provide here some evidence about the generation of a bubble ring. Table 1 gives estimated Reynolds and Weber numbers for the toroidal bubble produced by scuba divers, beluga whales or dolphins. As a consequence, we use a realistic Reynolds number which is still affordable by numerical simulations running on a standard workstation. For most simulations, the Reynolds number is set at $Re = 5000$. In the monophasic case, the standard vortex is formed by vorticity sheet roll-up. In the two-phase situation, this mechanism is still active but the bubble expelled from the tube may break up in the same time interval. More importantly, the bubble contains and is surrounded by positive vorticity transported from the boundary layer at the nozzle wall but also from positive and negative vorticity produced at the interface. This interfacial vorticity (related in particular to capillary waves and bubble retraction) is shed in the bulk in the form of vortices. At later times, such vortices may induce a dynamics on the bubble as do the vortices generated by the nozzle wall vorticity roll-up.

The first set of simulations corresponds to a small Weber number $We = 3$. For a length $r_B = 0.6$ (Figure 2), the toroidal vortex is not formed but a bubble remains with vortices inside. This means that when surface tension is too strong, inertial effects are too weak to deform the bubble and thus to generate a toroidal bubble. The second simulation (Figure 3) corresponds to a larger width $r_B = 2.4$. In this instance, the bubble ring is again not formed but the starting period is quite complicated with phase of disconnection followed by reconnection. In this process, multiple

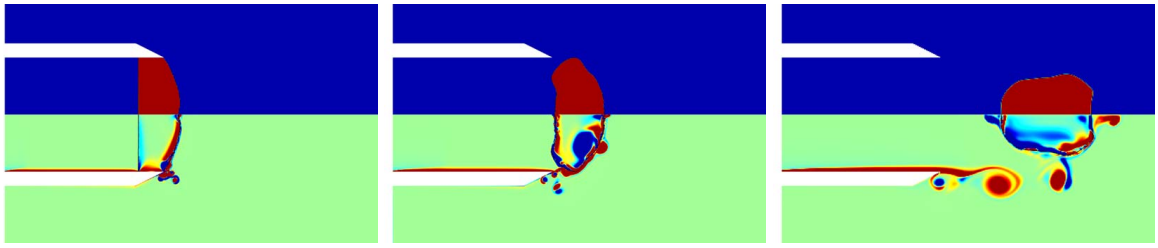

Figure 2. Simulations at $Re = 5000$, $We = 3$ and $r_B = 0.6$. From left to right, the snapshots correspond to times $\bar{t} = 2$, 3.2 and 6.4. The upper half displays phases and interfaces (red is gas and blue water) and the lower half the vorticity field. The vorticity value is colored with a maximum scale of $\omega = 3.75$, which is one fifth of the absolute vorticity maximum at the wall boundary layer (see (4)).

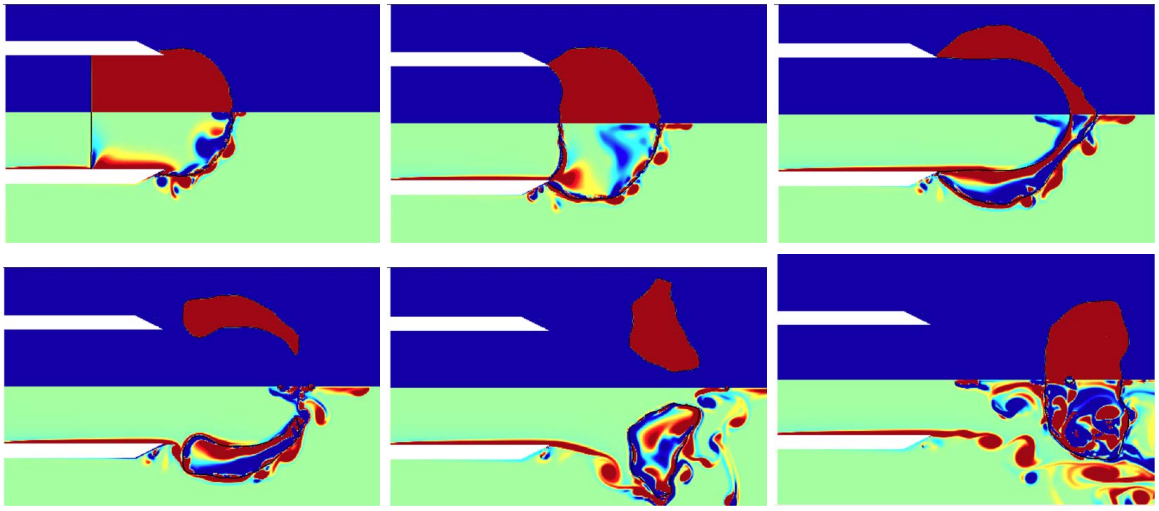

Figure 3. Simulations at $Re = 5000$, $We = 3$ and $r_B = 2.4$. From left to right, first row: $\bar{t} = 4$, 6, 8; second row: $\bar{t} = 8.4$, 10 and 16. Visualizations are similar to Figure 2.

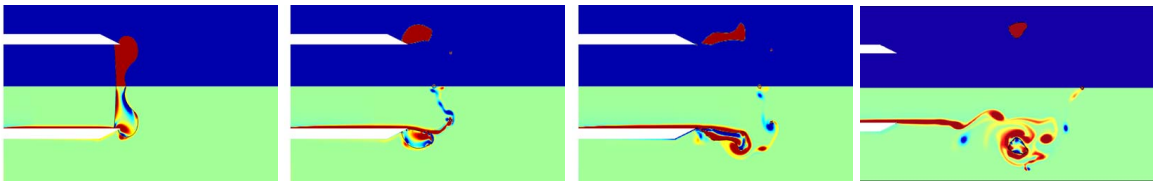

Figure 4. Simulations at $Re = 5000$, $We = 100$ and $r_B = 0.6$. From left to right: $\bar{t} = 2.8$, 4.8, 7.2 and 15.2. Visualizations are similar to Figure 2.

vortices shed at the interface tend to favor this reconnection process. For larger bubbles, the starting vortex is shed inside the air bubble. As a conclusion, it can be checked that for small Weber numbers (e.g. $We = 3$), the bubble that is formed is not toroidal!

The second set displayed on Figures 4–5 corresponds to a large Weber number $We = 100$ for $r_B = 0.6$ and $r_B = 2.4$ respectively. In the first case ($r_B = 0.6$, Figure 4), the bubble becomes a thin layer near the centre and a rim forms near $r = R_0$ with the vorticity roll-up ($\bar{t} = 2.8$). The layer breaks thereafter into small fragments since surface tension is too weak and a toroidal bubble is formed near the edge attached to the nozzle edge ($\bar{t} = 4.8$). The flow then detaches the toroidal bubble ($\bar{t} = 7.2$) and the system evolves through capillary waves dynamics and interactions with

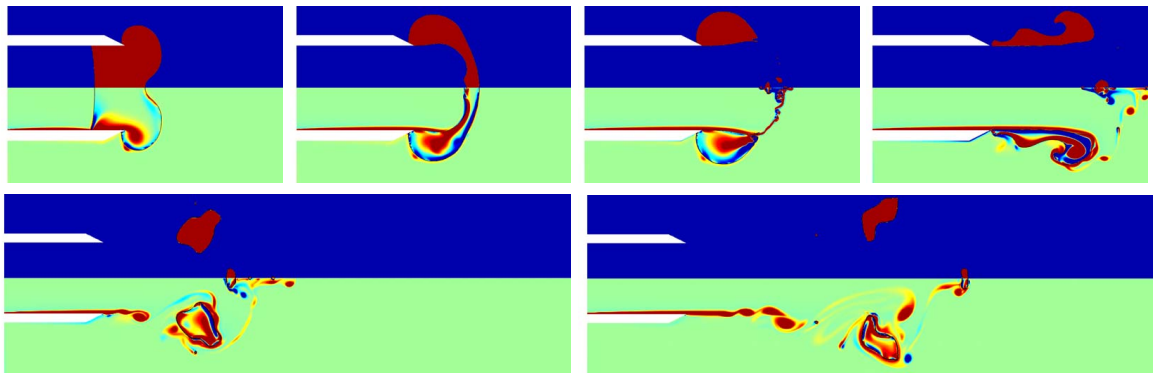

Figure 5. Simulations at $Re = 5000$, $We = 100$ and $r_B = 2.4$. From left to right, first row: $\bar{t} = 4.8$, 7.2, 8, 11.2; second row: $\bar{t} = 13.6$ and 19.6. Visualizations are similar to Figure 2.

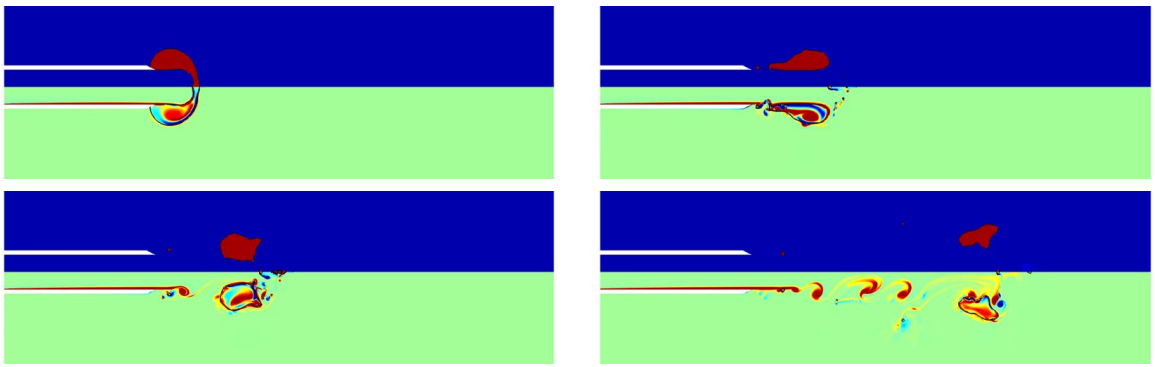

Figure 6. Simulations at $Re = 5000$, $We = 100$ and $r_B = 8$. From left to right: $\bar{t} = 14$, 20, 24 and 40. Visualizations are similar to Figure 2.

vortices ($\bar{t} = 15.2$). For a larger r_B (here $r_B = 2.4$, Figure 5), the boundary layer is not thin but the roll-up of the vortex sheet is still located near $r = R_0$ ($\bar{t} = 4.8$). At the center, the two interfaces get nearby ($\bar{t} = 7.2$) and then reconnect forming a unique toroidal bubble ($\bar{t} = 8$). Later the bubble is stretched ($\bar{t} = 11.2$) before being detached ($\bar{t} = 13.6$). The result is a larger toroidal bubble ($\bar{t} = 19.6$). The process is identical for $r_B = 8$ (Figure 6). For even larger values of r_B, the bubble does not break and the vorticity roll-up occurs inside the gas bubble. The largest toroidal bubble appears for a value of r_B which is clearly dependent on the Weber number.

The intermediate case $We = 20$ is an in-between situation (Figures 7–9) in which a fine balance between the classical roll-up of vorticity and the bubble break-up occurs. For $r_B = 2.4$ (Figure 7), the same process occurs as at larger We: a toroidal bubble is formed, first attached to the edge ($\bar{t} = 9.6$) then detached ($\bar{t} = 14.4$). Thereafter its cross-section becomes almost circular ($\bar{t} = 20$, $\bar{t} = 24$). For $r_B = 1.2$ (Figure 8), the bubble is detached ($\bar{t} = 5.6$) before being broken ($\bar{t} = 9.6$). This is due to the presence of a vortex that was previously shed by the boundary layer. More generally, vorticity production at the interface makes the process quite complex since the toroidal bubble interacts with the vorticity generated at its interface beforehand, or generated by the wall boundary layer (see Figure 8 at times $\bar{t} = 9.6$, 20 and 30). In many simulations for $We = 20$, the chaotic interaction between such vortices and the toroidal bubble brings this bubble towards the symmetry axis, merging it into a simple bubble. This process is seen here on a simulation for $r_B = 0.6$ (Figure 9): the toroidal bubble is formed at $\bar{t} = 4.8$ but its reconnects towards the center at $\bar{t} = 8$. This was also observed for $r_B = 2.4$ by slightly changing the Navier condition for the triple line.

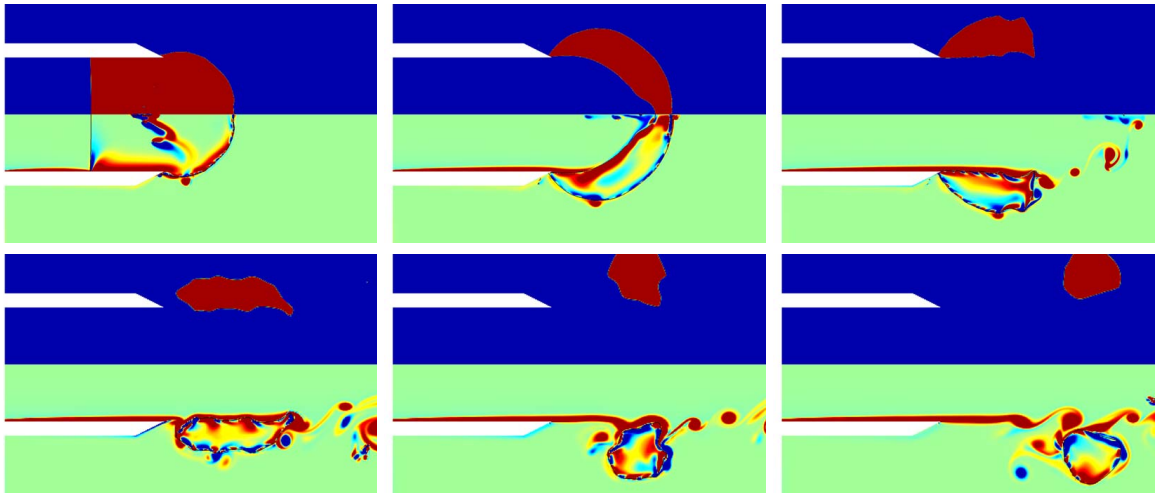

Figure 7. Simulations at $Re = 5000$, $We = 20$ with $r_B = 2.4$. From left to right, first row: $\bar{t} = 4.4, 7.2, 9.6$; second row: $\bar{t} = 14.4, 20$ and 24. Visualizations are similar to Figure 2.

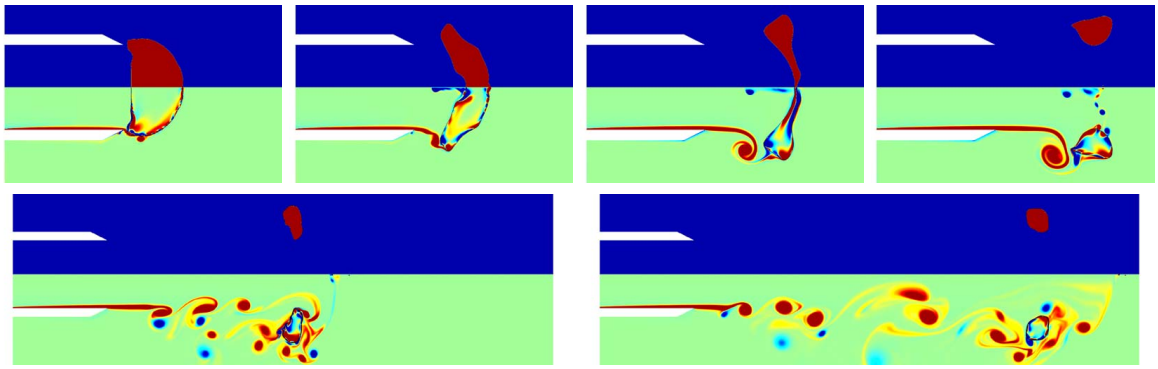

Figure 8. Simulations at $Re = 5000$, $We = 20$ with $r_B = 1.2$. From left to right, first row: $\bar{t} = 4.4, 5.6, 8, 9.6$; second row: $\bar{t} = 20, 30$. Visualizations are similar to Figure 2.

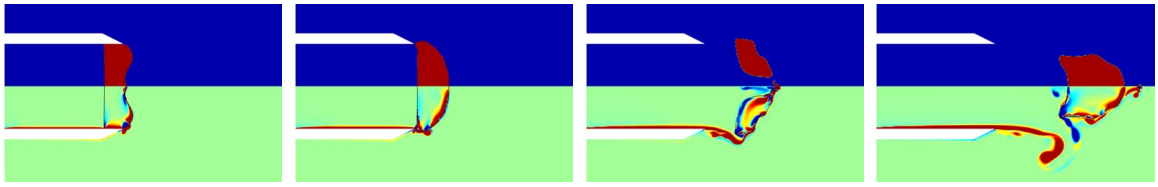

Figure 9. Simulations at $Re = 5000$, $We = 20$ with $r_B = 0.6$. From left to right: $\bar{t} = 2, 3.6, 4.8$ and 8. Visualizations are similar to Figure 2.

It is worth mentioning that modifying the Reynolds number, as illustrated in Figure 10, and/or the position of the bubble may change some dynamical features but does not modify the overall picture described above. When the toroidal bubble is formed in the ejection problem, the structure of the vorticity field is complex inside the bubble and around it (see Figure 11). This is also seen on vorticity profiles (see Figure 12). One may define a bubble-ring total length L_B which is of order $2\pi R_0$, as well as the size a_B of the toroidal bubble section S and the mean circulation Γ_B inside the bubble:

$$a_B = \sqrt{\frac{I_1}{\pi}} R_0 \quad \text{and} \quad \Gamma_B = I_2 U_0 R_0, \quad \text{with } I_1 = \int_S \mathrm{d}x\,\mathrm{d}r,\ I_2 = \int_S \omega\,\mathrm{d}x\,\mathrm{d}r. \tag{6}$$

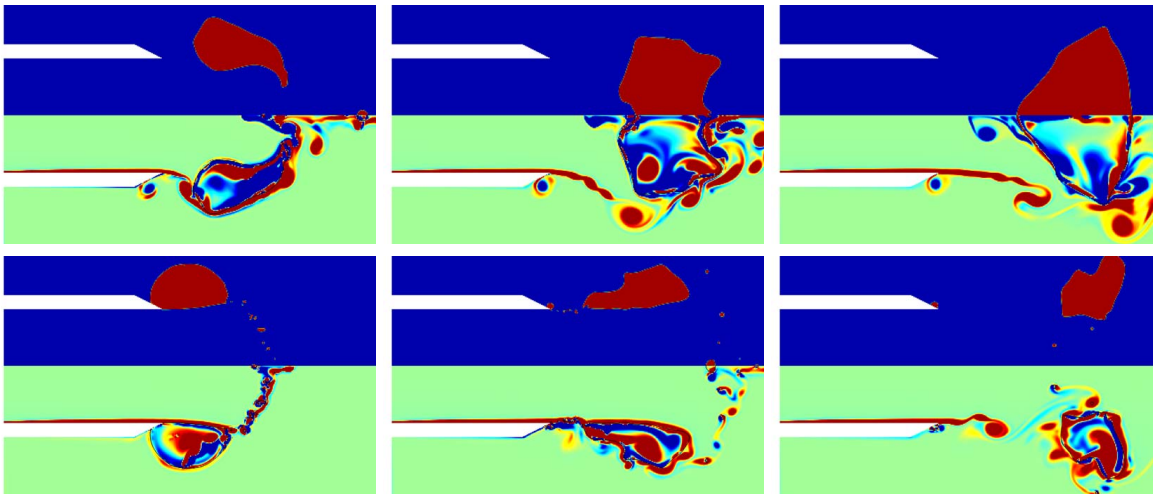

Figure 10. Simulations with $Re = 10000$ and $r_B = 2.4$. From left to right, top row: $We = 3$ at $\bar{t} = 8$, 10, 14.6; bottom row: $We = 100$ at $\bar{t} = 8$, 10 and 14.6. Visualizations are similar to Figure 2.

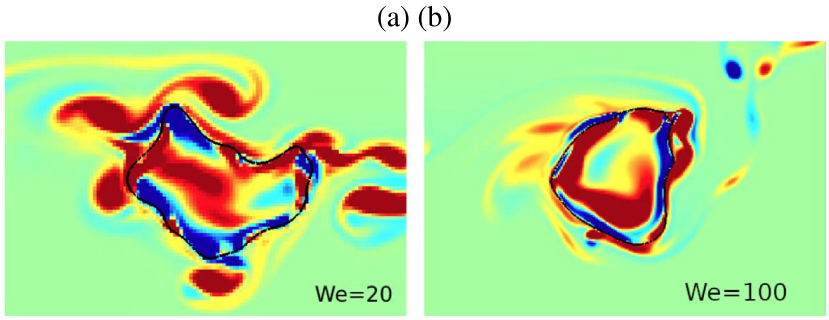

Figure 11. Simulations with $Re = 5000$, $r_B = 4$. Vorticity field near the bubble for (a) $We = 20$ at $\bar{t} = 20$; (b) $We = 100$ at $\bar{t} = 26.4$.

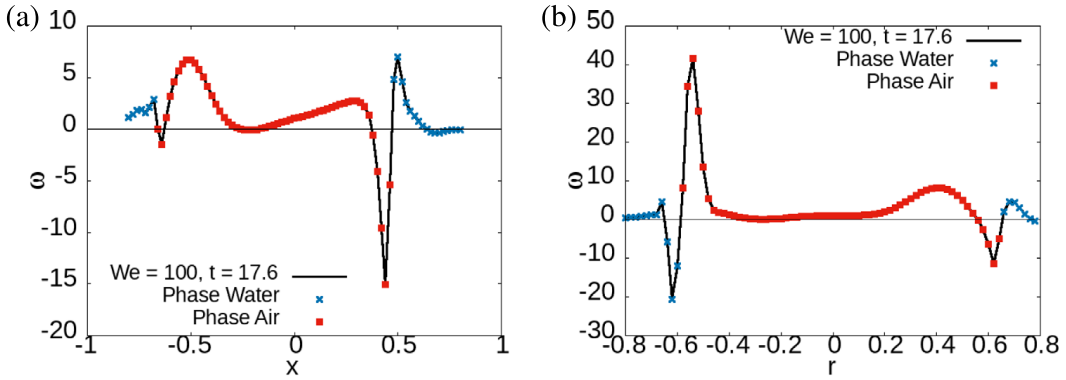

Figure 12. Profiles of vorticity $\omega_\theta(x,r)$ at $Re = 5000$, $We = 100$, $r_B = 4$ and $\bar{t} = 17.6$ (corresponding to the second case of Figure 11) on two orthogonal lines passing through the center of section S: (a) along the x direction, (b) along the r direction. The red dots are located inside the gas bubble, blue dots are outside.

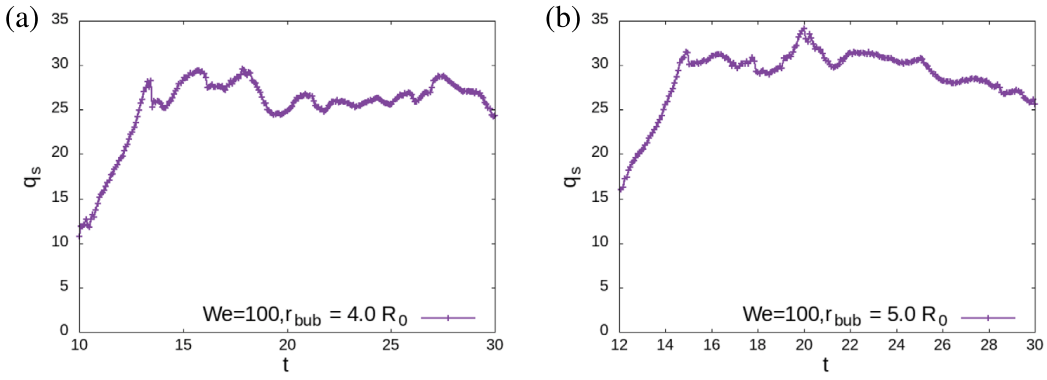

Figure 13. Swirl number q_S as a function of nondimensional time $\bar{t}$. Simulations at $Re = 5000$, $We = 100$ with (a) $r_B = 4$, (b) $r_B = 5$.

Based on such quantities, one computes the mean vorticity inside the bubble $\Gamma_B/(\pi a_B^2)$. For a uniform vorticity inside a bubble of radius a_B, the azimuthal velocity at the interface is equal to $\Gamma_B/(2\pi a_B)$. A dimensionless parameter called the swirl number q_S can thus be defined as the ratio of this azimuthal velocity and the characteristic capillary velocity $U_{cap} \equiv [\sigma/(\rho^{(w)} a_B)]^{1/2}$:

$$q_S \equiv \frac{\Gamma_B}{2\pi a_B U_{cap}}. \tag{7}$$

After a transient period, this swirl seems to fluctuate around an average value, as illustrated in Figure 13.

3. The action of stretching on the bubble ring

In the videos [3, 4], dolphins or beluga whales play with the vortex rings and are able by a motion of their head to increase the bubble length. This is typically known as stretching mechanism of vortex tubes. Starting from a vorticity structure similar to the field obtained numerically at the end of the simulations in the previous section (that is those corresponding to vorticity fields in Figure 11), one should model the effect of the dolphin head. In order to remain simple, we analyse the effect of this stretching mechanism by a simplified model which enables us to use analytical methods. An air column of radius a_B replaces the two-phase bubble ring with a vorticity field vanishing away from the bubble and the effect of stretching for the ring is introduced in the associated columnar bubble *via* an axial axisymmetric unsteady stretching

$$\boldsymbol{u} = \left[\gamma(t)x,\, u_y(y,z,t) - \tfrac{1}{2}\gamma(t)y,\, u_z(y,z,t) - \tfrac{1}{2}\gamma(t)z\right]. \tag{8}$$

The vorticity structure at $t = 0$ is characterized by a unique vorticity component $\omega_x(y,z)$ along x which is identical to $\omega_\theta(r,z)$ obtained at the end of previous simulations (see for instance Figure 11). The stretching occurs during a finite period of time between time $t = 0$ and $t = T_S$. The stretched solution is again characterized by the unique vorticity component $\omega_x(y,z,t)$. This field satisfies the governing equation

$$\frac{D\omega_x}{Dt} = \gamma(t)\omega_x + \nu\Delta_{2D}\omega_x, \tag{9}$$

where Δ_{2D} stands for the two-dimensional Laplacian and $D\cdot/Dt$ for the material derivative:

$$\Delta_{2D} \equiv \frac{\partial^2}{\partial y^2} + \frac{\partial^2}{\partial z^2}, \quad \frac{D}{Dt} \equiv \frac{\partial}{\partial t} - \frac{1}{2}\gamma(t)\left[y\frac{\partial}{\partial y} + z\frac{\partial}{\partial z}\right] + u_y\frac{\partial}{\partial y} + u_z\frac{\partial}{\partial z}. \tag{10}$$

Across any point at the interface, the velocity field is continuous i.e. $u_y^{(1)} = u_y^{(2)}$ and $u_z^{(1)} = u_z^{(2)}$, and the tangential stress is continuous as well. Let us now introduce the following change of variables [19]

$$\tau \equiv \int_0^t S(t')\,\mathrm{d}t', \quad \text{with } S(t) \equiv \exp\left[\int_0^t \gamma(t')\,\mathrm{d}t'\right], \quad \chi = \sqrt{S(t)}\,y, \quad \eta = \sqrt{S(t)}\,z, \tag{11}$$

as well as a rescaling of vorticity and velocity fields

$$\widetilde{\omega}_x(\chi,\eta,\tau) = \omega_x/S(t), \quad \widetilde{u}_y(\chi,\eta,\tau) = u_y/\sqrt{S(t)}, \quad \widetilde{u}_z(\chi,\eta,\tau) = u_z/\sqrt{S(t)}. \tag{12}$$

After such changes, the field $[\widetilde{u}_y(\chi,\eta,\tau), \widetilde{u}_z(\chi,\eta,\tau)]$ has the dynamics of an *unstretched solution* with the same initial condition:

$$\frac{\mathrm{D}\widetilde{\omega}_x}{\mathrm{D}\tau} = \nu\tilde{\Delta}_{2\mathrm{D}}\widetilde{\omega}_x, \quad \text{with } \tilde{\Delta}_{2\mathrm{D}} \equiv \frac{\partial^2}{\partial\chi^2} + \frac{\partial^2}{\partial\eta^2} \text{ and } \frac{\mathrm{D}}{\mathrm{D}\tau} \equiv \frac{\partial}{\partial\tau} + \widetilde{u}_y\frac{\partial}{\partial\chi} + \widetilde{u}_z\frac{\partial}{\partial\eta}, \tag{13}$$

associated to equivalent boundary conditions.

This trick allows one to obtain the effect of stretching on a vortex profile in two steps: first, one solves the pure two-dimensional advection-diffusion equation (13) starting with the velocity field at $\tau = t = 0$ and ending the simulation at $\tau = \tau_S \equiv \int_0^{t=T_S} S(t')\,\mathrm{d}t'$; second, one applies the scalings (11)–(12) back to the initial variables pertinent to describe the physical state. In the videos [3], the bubble ring length L_B increases in a substantial manner: assume this increase to be by a factor of F and γ to be constant, this means that $F = \exp(\gamma T_S)$ and thus $\tau_S \equiv \int_0^{t=T_S} S(t')\,\mathrm{d}t'$ yields $(F-1)/\gamma$. Hence, the ratio $\tau_S/T_S = (F-1)/\ln F$ is large: for a factor $F = 10$, its value is around 4. The first stage of the simulation is thus a pure two-dimensional advection diffusion equation applied during a time τ_S larger than T_S. In the monophasic case, differential rotation in such an equation is known to accelerate diffusion [20], so that the vorticity profile rapidly tends towards a smoother axisymmetric one. More generally, two-dimensional vortical flows localized in a finite region are known to decay towards an axisymmetric monopole or, in case the total circulation is zero, towards a dipole [21, 22]. The present case is slightly different because of the presence of two phases. Since $\nu^{(a)}/\nu^{(w)} = 20$ is large, vorticity actually diffuses much more rapidly inside the bubble than outside. This implies that vorticity tends to become uniform inside the bubble. Vorticity outside becomes smoother than initially and the interface becomes axisymmetric by damping of capillary waves. This evolution is partially seen on Figure 14. In order to go back to the vortex solution at $t = T_S$ (second step), one applies the transformation inverse of (11)–(12). The stretching transformation leaves the vorticity uniform in the bubble, the section of which is now circular with radius $a_\mathrm{new} \ll a(t=0)$. Indeed, by conservation of mass, $a_\mathrm{new}/a(t=0)$ is of the order of $1/\sqrt{F}$. If we assume that the circulation Γ_B inside the bubble is not changing much, this stretched vortex also possesses a new swirl number

$$q_S^\mathrm{new} \sim \sqrt{\frac{a(t=0)}{a_\mathrm{new}}}\,q_S(t=0) \sim \sqrt{F}\,q_S(t=0). \tag{14}$$

The swirl number is thus expected to increase when the bubble ring length increases.

4. Instability of a columnar interface in the presence of surface tension and rotation

After the stretching phase, a toroidal gas bubble inside a vortex with an almost circular section is generated. In order to understand its stability, we proceed again by studying the same simplified problem: an air column of radius $a_0 = a_\mathrm{new}$ replaces a two-phase bubble ring with a vorticity field vanishing away from the bubble. This simplified problem is much more tractable since the base flow is homogeneous in the axial direction x. Whenever necessary, the notation $Q^{(p)}$ is explicitly used to represent the quantity Q in the inner phase $p = 1$ or the outer phase $p = 2$. The jump of a field Q across a point $\boldsymbol{x}$ of the interface is denoted by $[\![Q]\!] \equiv Q^{(1)}(\boldsymbol{x},t) - Q^{(2)}(\boldsymbol{x},t)$.

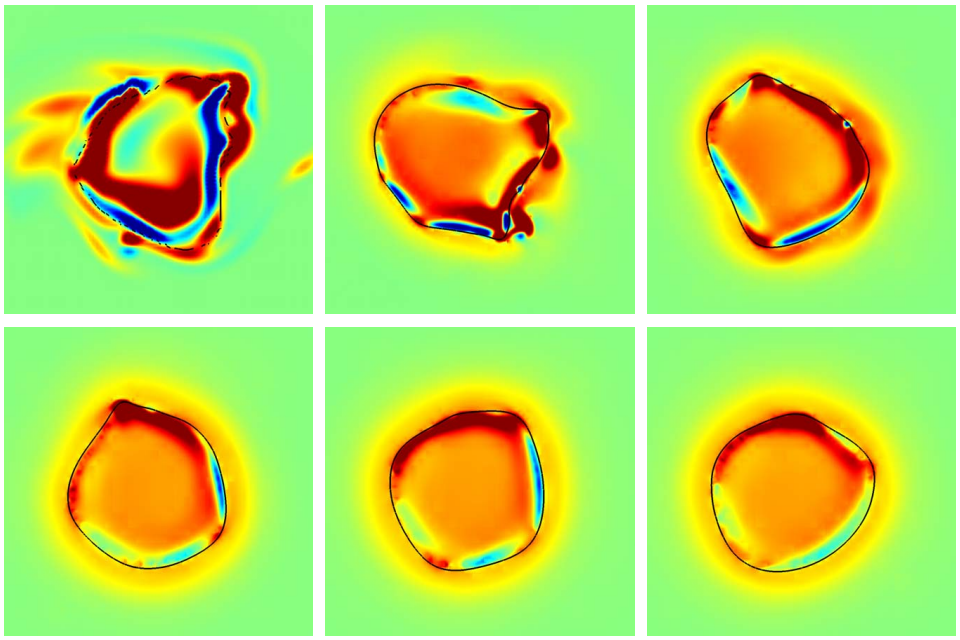

Figure 14. Evolution of the vorticity field $\widetilde{\omega}_x(\chi,\eta,\tau)$ near the bubble, starting from the initial condition corresponding to the second case in Figure 11 and evolving through the two-dimensional advection-diffusion equation (13), represented (left to right and top to bottom) at times $\tau = 0$, 8, 16, 24, 32 and 40.

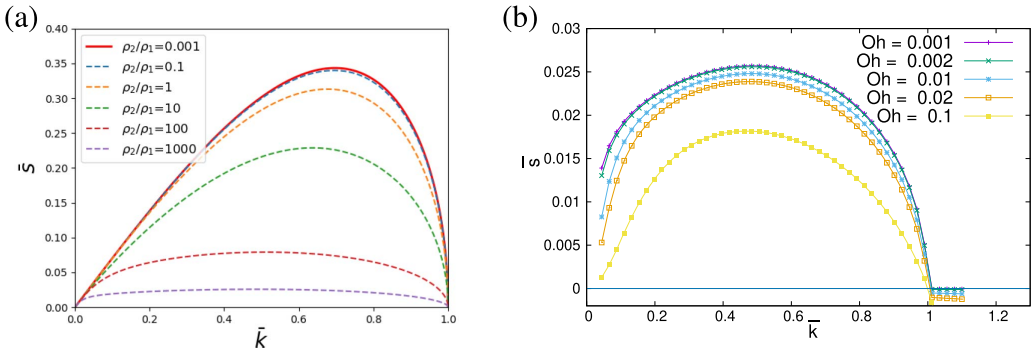

Figure 15. Growth rate $\bar{s}$ as a function of wavenumber $\bar{k}$ for axisymmetric modes $m = 0$. (a) Inviscid column of liquid 1 surrounded by a liquid 2 at various density ratios $\rho^{(2)}/\rho^{(1)} = 10^3$, 10^2, 10, 1, 10^{-1} and 10^{-3}. (b) Viscous air column surrounded by water at various Ohnesorge numbers Oh between 10^{-3} and 10^{-1} with $\mu^{(2)}/\mu^{(1)} = 50$. The inviscid curve almost concides with that of case $Oh = 10^{-3}$.

The theoretical relation (1) indicates that the presence of an external liquid does not change the stability criterion for various density ratios $\rho^{(2)}/\rho^{(1)}$ (Figure 15a). Here, the density ratio is $\rho^{(w)}/\rho^{(a)} = 10^3$, which simply makes the system of a columnar fluid 1 more stable: while the Laplace pressure pushes fluid 1 outward, fluid 2 will oppose a force, which slows down the instability and shift the most unstable wavenumber $\bar{k}$ to a smaller value [23]. The significance of dynamical viscosity $\mu^{(1)}$ (fixing the ratio $\mu^{(2)}/\mu^{(1)}$ to the value $\mu^{(w)}/\mu^{(a)} \approx 50$) compared to surface tension σ is described by the dimensionless *Ohnesorge* number $Oh = \mu^{(1)}/(\rho^{(1)}\sigma a_0)^{1/2}$, a larger Ohnesorge number indicating an increased influence of viscosity. Since $\mu^{(1)}/(\rho^{(1)}\sigma)^{1/2} \approx 6.64 \times 10^{-5}$, $Oh \approx 6.64 \times 10^{-4}$ for a radius $a_0 = 1$ cm. Figure 15b presents the classical dispersion

relation for an air column surrounded by water when viscosity is taken into account. Again it is found that viscosity makes the system less unstable and shifts the most amplified wavelength to a longer on from $Oh = 10^{-2}$ on. The added inertia and viscosity are hence incapable to bring the system from an unstable to a stable configuration.

We assume here that an additional rotational motion stabilizes the toroidal bubble generated by dolphins: with an appropriate azimuthal speed, the centrifugal force stabilizes the Rayleigh–Plateau instability. The stability analysis for a swirling jet has been already studied by Hocking [7]. In the case of an inviscid fluid column with no external fluid and subjected to rotation of constant angular rotation rate Ω_0 (or equivalently of constant vorticity $2\Omega_0$), a stability criterion for azimuthal wavenumber m at $k = 0$ was obtained using the Weber number based on the velocity $\Omega_0 a_0$, i.e. $We = \rho^{(1)} a_0^3 \Omega_0^2/\sigma$ (not to be confused with the Weber number used in (3) which was based on U_0 and R_0). This criterion implies that a mode with $k = 0$ and $m \neq 0$ is stable when $We \leqslant m(m+1)$. The planar mode ($k = 0, m = 1$) being a displacement mode, it is neutral and stability for ($k = 0, m \neq 0$) modes is ensured when $We \leqslant We_c = 6$. In follow-on studies, Gillis [10] provided a general stability criterion for three-dimensional disturbances on a viscous fluid column with no external fluid

$$We \leqslant (ka_0)^2 + m^2 - 1. \tag{15}$$

Weidman [11] showed how the dominant azimuthal mode for a two-phase axisymmetric rotating system depends on the Reynolds number Re. Finally the linear stability of a uniformly rotating viscous liquid column has been investigated by Kubitschek and Weidman [8] and validated experimentally [9]: the dominating mode depends on Re and on the rotation speed. In the present work, we study how perturbations evolve when superimposed on an axisymmetric *air* column in an infinite ambient fluid, namely *water*. We consider the case where surface tension, viscosity, density contrast and centrifugal force act on the instability growth rate, and in which the angular velocity profile $U_\theta(r)/r$ is not uniform outside the bubble. To the best of our knowledge, this stability problem has not yet been performed.

4.1. *The governing equation for a columnar flow with rotation*

We adopt the model of an infinitely long two-phase capillary jet of radius a_0. The inner and outer fluid are both incompressible, immiscible and viscous. Using now radius a_0, $[\rho^{(1)} a_0^3/\sigma]^{1/2}$ and $\rho^{(1)}$ as characteristic scales for length, time and density, we write the Navier–Stokes equations inside each fluid $p = 1$ or 2:

$$\bar{\nabla} \cdot \bar{\boldsymbol{u}}^{(p)} = 0 \tag{16}$$

$$\bar{\rho}^{(p)} \frac{\mathrm{D}}{\mathrm{D}\bar{t}} \bar{\boldsymbol{u}}^{(p)} = -\bar{\nabla} \bar{p}^{(p)} + \frac{\bar{\mu}^{(p)}}{Re_\mathrm{B}} \nabla^2 \bar{\boldsymbol{u}}^{(p)}, \quad \frac{1}{Re_\mathrm{B}} = Oh = \frac{\mu^{(1)}}{\sqrt{\rho^{(1)} \sigma a_0}} \tag{17}$$

where the Reynolds number Re_B of the vortex is the inverse of the Ohnesorge number. Ratios $\bar{\mu}^{(p)} = \mu^{(p)}/\mu^{(1)}$, and $\bar{\rho}^{(p)} = \rho^{(p)}/\rho^{(1)}$ are fixed : $\bar{\mu}^{(2)} = 50$ and $\bar{\rho}^{(2)} = 10^3$ and by definition $\bar{\mu}^{(1)} = \bar{\rho}^{(1)} = 1$. In the following, we use only dimensionless quantities except when specified and the bar notation is assumed. Since the inner fluid $p = 1$ is air and the outer fluid $p = 2$ is water, it is clear that

$$Re_\mathrm{B} = \sqrt{\frac{1}{\rho^{(2)}}} \sqrt{\frac{a_0}{R_0}} \frac{Re}{\sqrt{We}} \approx 300\sqrt{a_0} \tag{18}$$

when a_0 is the bubble radius in SI units. When $a_0 \sim 1$ cm, this implies $Re_\mathrm{B} \sim 30$, and when $a_0 \sim 10$ cm, this implies $Re_\mathrm{B} \sim 100$. Alternatively, if one assumes that $a_0/R_0 \sim 0.1$, for simulations $Re = 10000$ and $We = 100$, one gets $Re_\mathrm{B} = 10$; for simulations $Re = 10000$ and $We = 1$, one gets $Re_\mathrm{B} = 100$.

The Navier–Stokes equations are written in cylindrical coordinates. The radial position of the interface between the two fluids can be described by a function ζ in cylindrical coordinates: $r = \zeta(\theta, x, t)$. This interface is characterized by a outward normal $\boldsymbol{n}$ and two tangential vectors $\boldsymbol{t}_x$ and $\boldsymbol{t}_\theta$:

$$\boldsymbol{t}_x = \frac{\left(\frac{\partial\zeta}{\partial x}, 0, 1\right)}{\sqrt{1+\left(\frac{\partial\zeta}{\partial x}\right)^2}}, \quad \boldsymbol{n} = \frac{\left(1, -\frac{1}{\zeta}\frac{\partial\zeta}{\partial\theta}, -\frac{\partial\zeta}{\partial x}\right)}{\sqrt{1+\left(\frac{\partial\zeta}{\partial x}\right)^2+\left(\frac{1}{\zeta}\frac{\partial\zeta}{\partial\theta}\right)^2}}, \quad \boldsymbol{t}_\theta = \boldsymbol{t}_x \times \boldsymbol{n}, \tag{19}$$

forming an orthonormal basis $(\boldsymbol{t}_x, \boldsymbol{n}, \boldsymbol{t}_\theta)$. The velocity is continuous across the interface $[\![\boldsymbol{u}]\!] = \boldsymbol{0}$. The normal velocity must be compatible with the interface motion

$$\frac{\mathrm{D}\zeta}{\mathrm{D}t} = v_r(\zeta, \theta, x, t). \tag{20}$$

The dynamic conditions express that normal stress and tangential shear must be balanced by the surface tension effect:

$$\left[\!\left[-p + 2\frac{\mu}{Re_\mathrm{B}}\boldsymbol{n}\cdot\mathrm{e}\cdot\boldsymbol{n}\right]\!\right] = \frac{1}{R_1}+\frac{1}{R_2}, \quad [\![2\mu\boldsymbol{t}_\theta\cdot\mathrm{e}\cdot\boldsymbol{n}]\!] = 0 \quad \text{with } e_{ij}^{(p)} = \frac{1}{2}\left(\frac{\partial u_i^{(p)}}{\partial x_j}+\frac{\partial u_j^{(p)}}{\partial x_i}\right). \tag{21}$$

4.2. *The rotating base state*

Here, we mainly study a basic state $\boldsymbol{u} = W_\theta(r,t)\boldsymbol{e}_\theta$ which possesses the feature described in Section 3: it is characterized by a non-uniform angular velocity W_θ/r and a non-uniform axial vorticity $\boldsymbol{\omega} = [W_\theta/r + \partial W_\theta/\partial r]\boldsymbol{e}_x$ in phase 2 only, and the interface is circular $\zeta(x,\theta,t) = 1$. If one neglects the unsteadiness due to bulk viscosity, such profile is a possible solution. In physical terms, this approximation is pertinent since instability occurs *a priori* much faster than the diffusion of the base state. To be mathematically correct, one introduces a body force to counterbalance the bulk diffusion for the basic state. However viscous effects are still present in the boundary conditions at $r = 1$:

$$W_\theta^{(1)}(1) = W_\theta^{(2)}(1), \tag{22}$$

$$\mu^{(1)}\left(\frac{\partial W_\theta^{(1)}}{\partial r}(1) - W_\theta^{(1)}(1)\right) = \mu^{(2)}\left(\frac{\partial W_\theta^{(2)}}{\partial r}(1) - W_\theta^{(2)}(1)\right). \tag{23}$$

This latter condition can be rewritten as well as

$$\omega_x^{(2)}(1) = \frac{\mu^{(1)}}{\mu^{(2)}}\omega_x^{(1)}(1) - 2\left(\frac{\mu^{(1)}}{\mu^{(2)}}-1\right)W_\theta^{(1)}(1). \tag{24}$$

In each phase (p), the basic pressure $\Pi(r)$ should satisfy equation $\rho W_\theta^2(r)/r = \partial\Pi/\partial r$ and a jump condition at $r = 1$. This leads to a pressure of the following form:

$$\Pi^{(1)}(r) = \rho^{(1)}\int_0^r \frac{[W_\theta^{(1)}(r')]^2}{r'}\,\mathrm{d}r', \quad \Pi^{(2)}(r) = \Pi^{(1)}(1) + \rho^{(2)}\int_1^r \frac{[W_\theta^{(2)}(r')]^2}{r'}\,\mathrm{d}r' - 1. \tag{25}$$

The vorticity profile is assumed to be uniform in fluid 1 that is

$$W_\theta^{(1)}(r) = qr, \quad \omega_x^{(1)} = 2q \quad \text{for } r < 1,$$

where the dimensionless parameter q is equal to the ratio of the dimensional azimuthal velocity at the interface with respect to the characteristic capillary velocity $[\sigma/(\rho^{(1)}a_0)]^{1/2}$ — this quantity is equal to $0.27/{a_0}^{1/2}$ when a_0 is expressed in SI units. Note that

$$q \equiv \sqrt{\frac{\rho^{(1)}}{\rho^{(2)}}}\,q_S = \sqrt{\frac{\rho^{(a)}}{\rho^{(w)}}}\,q_S. \tag{26}$$

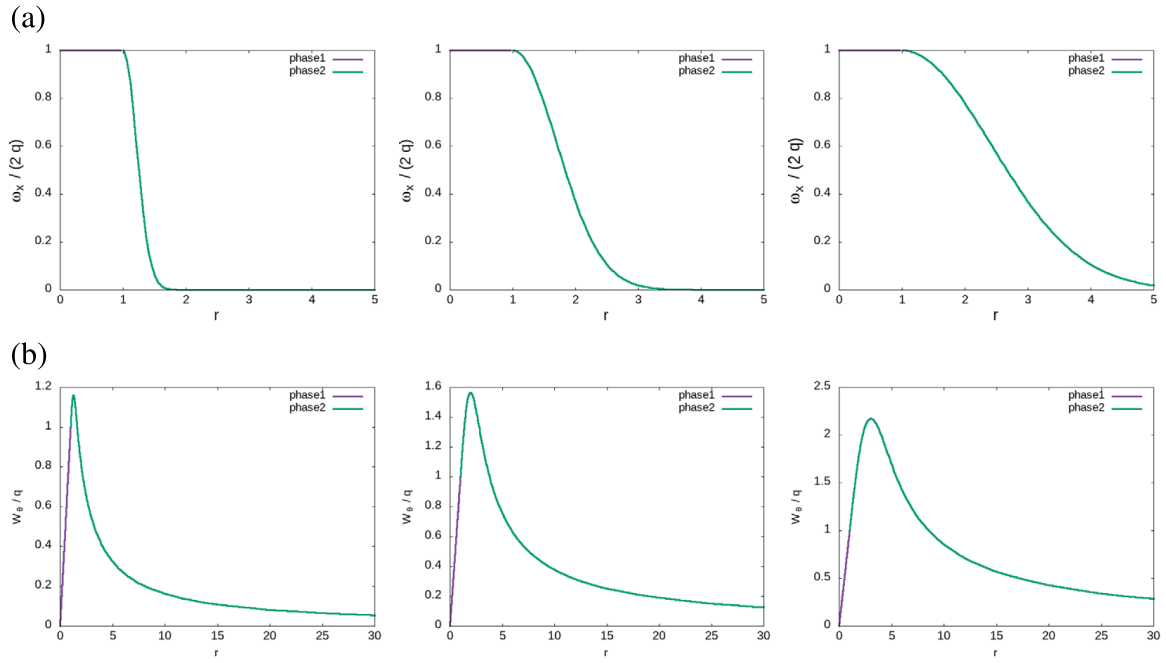

Figure 16. (a) Normalized vorticity $\omega_x(r)/(2q)$ and (b) normalized velocity $W_\theta(r)/q$ profiles for the base state with $\rho^{(2)}/\rho^{(1)} = 10^3$, $\mu^{(2)}/\mu^{(1)} = 50$ for $\delta = 0.3$ (left), $\delta = 1$ (center) or $\delta = 2$ (right).

Vorticity in phase 1 being uniform, Equation (24) imposes that $\omega_x^{(2)}(1) = 2q$. Apart from this constraint, let us assume a vorticity profile $\omega^{(2)}(r) = \omega_x^{(2)}(1) f(r)$ in phase 2, where function f is chosen as $f(r) = \exp[-(r-1)^2/\delta^2]$ and decays in the radial direction, thus generating a vortex ribbon of radial size δ in phase 2 surrounding the interface. It is easily seen that

$$W_\theta^{(2)}(r) = \frac{q}{r} + 2\frac{q}{r}\int_1^r r' f(r')\,\mathrm{d}r', \quad \omega_x^{(2)}(r) = 2q f(r) \quad \text{for } r > 1.$$

This expression, which can be written as well as

$$W_\theta^{(2)}(r) = \frac{q}{r}\left[1 + \delta^2\left(1 - \mathrm{e}^{-(r-1)^2/\delta^2}\right) + \delta\sqrt{\pi}\,\mathrm{erf}\left(\frac{r-1}{\delta}\right)\right] \quad \text{for } r > 1, \tag{27}$$

is displayed in Figure 16.

4.3. *The linear instability results*

We study the linear stability of the above base flow using standard but cumbersome methods. Indeed, the problem is an eigenvalue problem $\bar{s}(\bar{k}, m)$ for given axial $\bar{k}$ and azimuthal m wavenumbers, that contains viscous diffusion in the bulk as well as on the interface. A code has been specifically developed, that solves coupled Orr–Sommerfeld equations in cylindrical coordinates for the two phases. For obvious reasons, details on the implementation will be published elsewhere, and only results for the air-water columnar bubble are presented here.

Figure 17 displays the growthrate $\bar{s}$ as a function of wavenumber $\bar{k}$ for the axisymmetric mode $m = 0$, which is known to be the most unstable mode for $q = 0$. The presence of rotation is found to stabilize axisymmetric modes, and for q larger than a critical value $q_c \approx 0.03$, waves become stable for all wavelengths. This observation holds irrespective of the Reynolds number and δ within the studied interval $\delta \in [0.3, 2]$. Actually the structure in the corona at $r > 1$ seems to play a minor role for the axisymmetric mode.

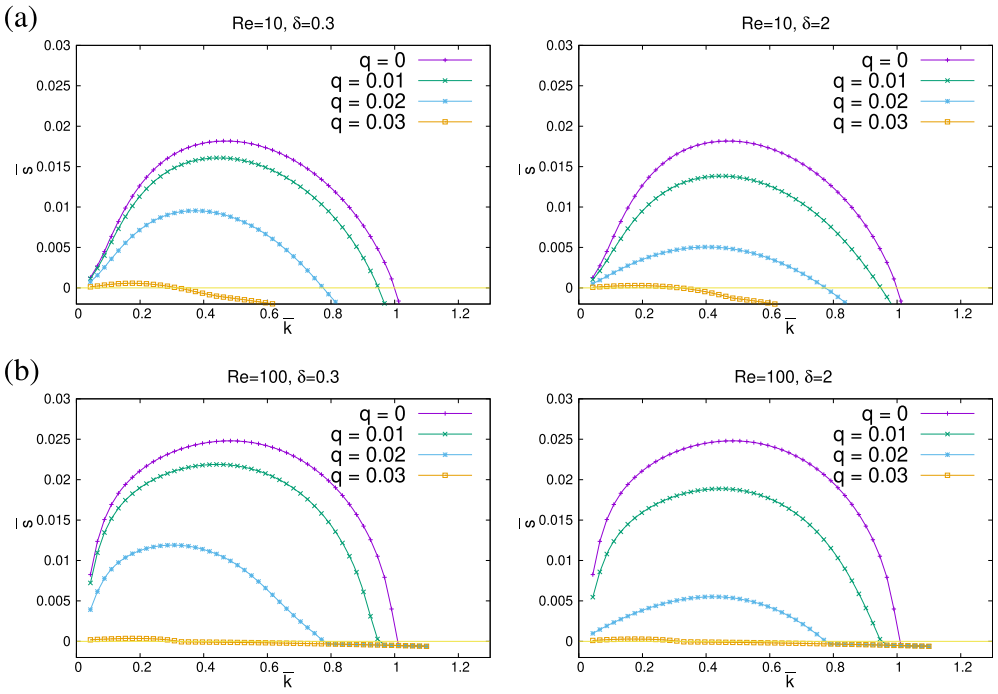

Figure 17. Growth rate $\bar{s}$ as a function of wavenumber $\bar{k}$ for axisymmetric mode $m = 0$ at various swirl numbers $q = 0,\ 0.01,\ 0.02,\ 0.03$. Reynolds number is (a) $Re_B = 10$, (b) $Re_B = 100$. Viscous air column surrounded by water with $\delta = 0.3$ (left) or $\delta = 2$ (right), with $\rho^{(2)}/\rho^{(1)} = 10^3$ and $\mu^{(2)}/\mu^{(1)} = 50$.

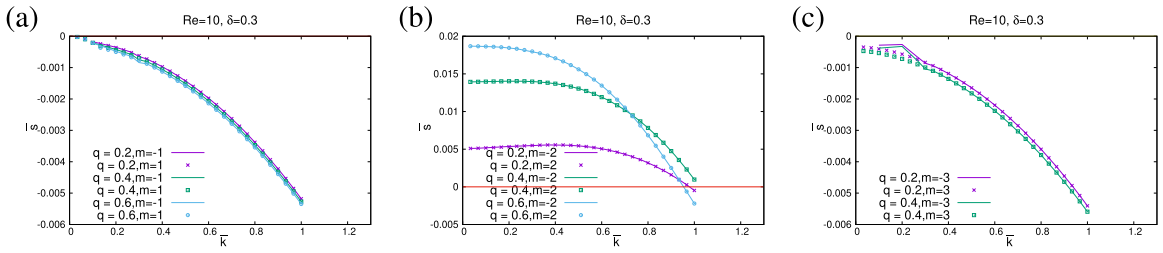

Figure 18. Growth rate $\bar{s}$ as a function of wavenumber $\bar{k}$ for a viscous column of air surrounded by water at $\delta = 0.3$, $Re_B = 10$ and various swirl $q = 0.2, 0.4, 0.6$. (a) $m = \pm 1$; (b) $m = \pm 2$; (c) $m = \pm 3$. Positive m: symbols; negative m: bold line.

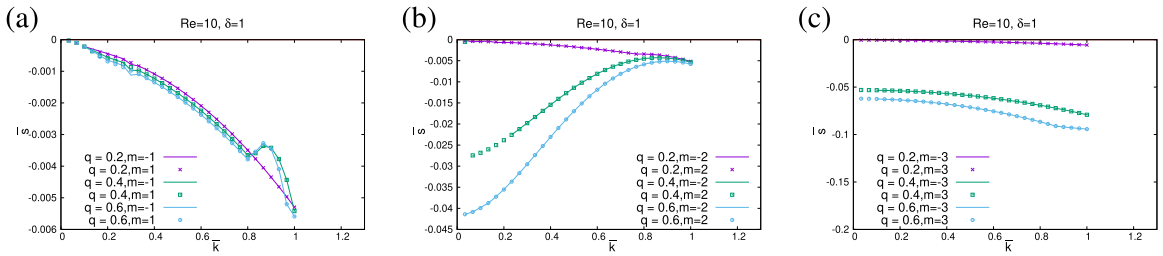

Figure 19. Same as Figure 18 but for $\delta = 1$ ($Re_B = 10$).

Figures 18–21 provide linear instability results for non axisymmetric modes $m \pm 1$, ± 2 and ± 3. The first observation is that, at given $\bar{k}$ and $|m|$ values, the growth rate is found almost the same

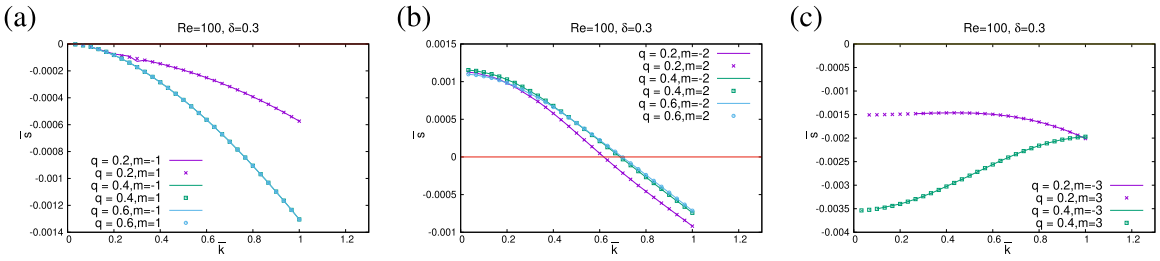

Figure 20. Same as Figure 18 but for $\delta = 0.3$ and $Re_B = 100$.

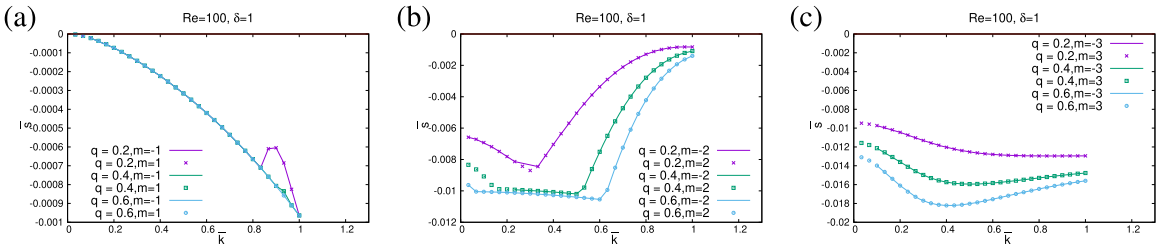

Figure 21. Same as Figure 18 but for $\delta = 1$ and $Re_B = 100$.

for $m > 0$ and $m < 0$. The equality exactly holds when $q = 0$ for symmetry reasons, and the fact that it holds also roughly for $q \neq 0$ can be explained by the uniform vorticity inside the bubble. Interestingly, rotation does not influence mode $|m| = 1$, that remains stable. For sufficiently low Reynolds number and small δ, other azimuthal modes $m \neq 0$ for small k can be destabilized. For instance, the mode $m = 2$ is found unstable for $Re_B = 10$ and $\delta = 0.3$ (Figure 18b). The growth rate decreases as the Reynolds number increases (Figure 20b). This is reminiscent of planar modes $k = 0$ in Ref. [8]. Note that for larger values of δ, this mode is restabilized: for $\delta = 1$, all modes tested are stabilized by rotation, this conclusion holding irrespective of the Reynolds number (Figures 19 and 21).

Finally, going back to the bubble ring, the axisymmetric Rayleigh–Plateau modes are stabilized by rotation. Indeed, from the simulations in Section 2, the pertinent values of q (Figure 13 and (26)) are found to be $q \sim 10^{-3/2} \times 30 \sim 0.94$. When a stretching factor is applied, q generally increases (Equations (14) and (26)) and is thus larger than the stability threshold of $q_c \approx 0.03$.

5. Conclusions

This paper covers three different aspects of the dynamics of toroidal bubbles such as those produced by scuba divers, beluga whales or dolphins. During the initial production of such bubble, vorticity trailing from the nozzle or from the opening rolls up into a toroidal vortex ring able to trap gas in its core; to do so, it has to overcome surface tension which would favor the formation of a single spherical bubble. Simulations show that vortices shed from the nozzle or generated at the bubble interface itself can influence the formation dynamics in a non trivial way. Once formed, the bubble ring may be stretched by an appropriate flow so as to increase its length. A theoretical model where curvature effects are overlooked shows that, during the stretching process, the vorticity in the gas tends to become uniform, the cross-section tends to circular while the core radius is highly reduced and the swirl is enhanced. This latter finding is important since a linear stability study of a gas columnar vortex surrounded by water eventually shows that the dominant axisymmetric Plateau instability is stabilized as swirl increases above a

well-defined critical value. Put all together, these pieces of investigation give some serious clues to physically understand the surprising stability of swirling bubble rings.

References

[1] Y. Couder, "Observation expérimentale de la turbulence bidimensionnelle dans un film liquide mince", *C. R. Acad. Sci. Paris II* **297** (1983), p. 641-645.

[2] O. Cadot, S. Douady, Y. Couder, "Characterization of the low pressure filaments in three-dimensional turbulent shear flow", *Phys. Fluids* **7** (1995), p. 630-646.

[3] Dramaqueen21409, "Dolphin Blowing Rings", Youtube video, last seen 2020, https://www.youtube.com/watch?v=2m6ie3MVIAw.

[4] H. Mind, "Beluga whales blowing bubble rings", Youtube video, last seen 2020, https://www.youtube.com/watch?v=Iiuv2ELttaQ.

[5] Lord Rayleigh, "Xvi. On the instability of a cylinder of viscous liquid under capillary force", *Lond. Edinburgh Dublin Phil. Mag. J. Sci.* **34** (1892), no. 207, p. 145-154.

[6] Lord Rayleigh, "Xix. On the instability of cylindrical fluid surfaces", *Lond. Edinburgh Dublin Phil. Mag. J. Sci.* **34** (1892), no. 207, p. 177-180.

[7] L. M. Hocking, D. H. Michael, "The stability of a column of rotating liquid", *Mathematica* **6** (1959), no. 1, p. 25-32.

[8] J. P. Kubitschek, P. D. Weidman, "The effect of viscosity on the stability of a uniformly rotating liquid column in zero gravity", *J. Fluid Mech.* **572** (2007), p. 261-286.

[9] J. P. Kubitschek, P. D. Weidman, "Helical instability of a rotating viscous liquid jet", *Phys. Fluids* **19** (2007), no. 11, 114108.

[10] J. Gillis, B. Kaufman, "The stability of a rotating viscous jet", *Q. Appl. Math.* **19** (1962), no. 4, p. 301-308.

[11] P. D. Weidman, M. Goto, A. Fridberg, "On the instability of inviscid, rigidly rotating immiscible fluids in zero gravity", *Z. Angew. Math. Phys.* **48** (1997), no. 6, p. 921-950.

[12] TheScubaGuru, "Shooting Underwater Hydro-Rings", Youtube, last seen 2020, https://www.youtube.com/watch?v=5KdsVsiZ6bU.

[13] T. Lee, "Underwater bubble ring", Youtube, last seen 2020, https://www.youtube.com/watch?v=4mbu2ueMe2E.

[14] C. Wedoy, "How To Make Underwater Bubble Rings - Bubble Ring Tutorial", Youtube, last seen 2020, https://www.youtube.com/watch?v=vFbN31EuMvc.

[15] P. G. Saffman, *Vortex Dynamics*, Cambridge University Press, Cambridge, 1992.

[16] T. T. Lim, T. B. Nickels, "Vortex rings", in *Fluid Vortices* (S. I. Green, ed.), Fluid Mechanics and Its Applications, vol. 30, Springer, Dordrecht, 1995, p. 95-153.

[17] S. Popinet, "Basilisk", http://basilisk.fr.

[18] S. Popinet, "A quadtree-adaptive multigrid solver for the Serre–Green–Naghdi equations", *J. Comput. Phys.* **302** (2015), p. 336-358.

[19] J. D. Gibbon, A. S. Fokas, C. R. Doering, "Dynamically stretched vortices as solution of the 3D Navier–Stokes equations", *Physica D* **132** (1999), p. 497-510.

[20] A. J. Bernoff, J. F. Lingevitch, "Rapid relaxation of an axisymmetric vortex", *Phys. Fluids* **6** (1994), no. 11, p. 3717-3723.

[21] J. C. McWilliams, "The emergence of isolated coherent vortices in turbulent flow", *J. Fluid Mech.* **146** (1984), p. 21-43.

[22] R. Robert, J. Sommeria, "Statistical equilibrium states for two-dimensional flows", *J. Fluid Mech.* **229** (1991), p. 291-310.

[23] J. Eggers, E. Villermaux, "Physics of liquid jets", *Rep. Prog. Phys.* **71** (2008), p. 16-18.

Conclusion and perspectives

The work exposed in this manuscript is a contribution to the numerical studies on the dynamics of vortices and their instabilities. Our objective was to estimate the occurrence of different instability modes at given vortex configurations. These instabilities are the source of many applications or the cause of many problems, such as in the context of in a vortex wake after a turbine. The original goal is to study the two-phase helical vortices, however due to time limit, only two simplified models are analyses: the homogeneous helical vortices, which contribute to the part one of the thesis, and the two-phase straight vortices, which lead to the second part of the thesis.

In the first part, by using the DNS code HELIX, we have shown that, when a moderate axial flow is present in a helical vortex, a quasi-equilibrium can be reached with various configurations. We have first exhibited for such a equilibria the existence of two functions f and g, such that $\varpi = f(\Psi^{(\mathrm{T})})$ and $u_B^{(\mathrm{T})}/\alpha = g(\Psi^{(\mathrm{T})})$, where ϖ is defined in (4.15), $\Psi^{(\mathrm{T})}$ is the stream function and $u_B^{(\mathrm{T})}$ is the axial velocity at translating frame. We then developed a more accurate method for computing vortex solutions with all prescribed parameters, namely circulation, helix radius, helical pitch, vortex core size and swirl level. Finally, when the core size is reasonably small with respect to the helical pitch and the curvature radius, the asymptotic theory is shown to adequately describe the structure of the DNS velocity field. Excellent agreement is found between numerics and asymptotic theory. Long- and short-wave instability modes growing on these states are then investigated, for the existence of different elliptical and curvature instability modes as well as the influence of axial jet intensity within the core, helical vortex pitch and core size. Their growth rate are then compared to existing asymptotic theories. Strong evidence shows that torsion modifies the stability properties of helical vortices compared to vortex rings. An improvement of the theoretical solutions is proposed and validated by numerical results. The effect of the direction of axial jet has also been demonstrated in a preliminary way.

In the second part, we study the instabilities occurring in straight two-phase vortices using an original in-house instability code. The code is first validated in a large range of viscosity Re and azimuthal mode m for the homogenize flow by comparing to the theory predictions and the results from other numerical studies. We then validate the growthrate of a uniform rotating gas jet as the results obtained numerically fits well with the theory prediction, in which the stabilizing effect of rotation on capillary instabilities in vortices with a gaseous core is evidenced. The similar results for certain cases are also obtained with tool Basilisk by DNS, during which the code is validate by studying the convergence and performance of error estimation techniques. The code is then used to verify the accuracy of analytical predictions from the in-house instability code, good agreements are found in various cases. The non-linear evolution of a swirling liquid jet are also qualitative studied with full 3D simulation with perturbation predicted by analytical solutions. In the next we investigate the generation of toroidal vortex bubbles as those produced

by direct two-phase simulations: the toroidal bubble is produced by a vortex trailing from the nozzle, which rolls up into a toroidal vortex ring and is able to trap gas in its core by overcoming surface tension. We also proved the bubble ring may be stretched by an appropriate flow so as to increase its length, the section tends to be circular while the core radius is highly reduced and the swirl is enhanced above a well-defined critical value. With the conclusion from second part, a physical explanation is given for the disappearance of the Plateau instability which is usually observed on a classic bubble column.

perspectives

First, for homogeneous helical vortices, due to the complexity of the structure in the vortex core and the requirement of a large simulation domain in some cases, an optimized solver with adaptive mesh refinement (AMR) is a priori required. In addition, many interesting topics remain to be studied: strong axial flow inside the vortex core may alter the quasi-equilibrium state structures of helical vortices ; we have only demonstrated the existence of the effect of torsion on the stability properties, but have not provided a solid theoretical explanation on it; the effect of axial flow direction is also open to discussion, we still have no conclusion on this part. Secondly, an extension to the analysis of two-phase helical vortices can be considered in the future. A priori on a helical vortex, the existence of interface should largely impact its dynamics. This study may be essential to better understand the turbine system of a ship.

Appendix for part one

Appendix A

Appendix: Relation between two planes for helically symmetric flows

Contents

A.1 Relationships between planes Π_0 and $\Pi_\perp$

The vortex characterization requires its local distribution in plane $\Pi_\perp$ which is perpendicular to the vortex centre helical line. The direct numerical simulation in code HELIX is fixed at plane Π_0 orthogonal to the vortex axis. It is necessary to connect the point M in the plane Π_0 to the point $\mathrm{M_h}$ which lies on a the same helical line $\varphi = \varphi_M$ and intersects the plane $\Pi_\perp$, . We called point $\mathrm{M_h}$ the helical projection of point M at plane $\Pi_\perp$. Any point M located in the plane Π_0 in polar coordinates (r_M, φ_M) is given by

$$\overrightarrow{OM} = r_M \cos\varphi_M \boldsymbol{e}_x + r_M \sin\varphi_M \boldsymbol{e}_y, \tag{A.1}$$

where $(\boldsymbol{e}_x, \boldsymbol{e}_y)$ are unitary vectors along x and y respectively. For point $\mathrm{M_h}$, vector $\overrightarrow{OM_h}$ can be expressed by

$$\overrightarrow{OM_h} = z_{M_h} \boldsymbol{e}_z + r_M \cos\theta_{M_h} \boldsymbol{e}_x + r_M \sin\theta_{M_h} \boldsymbol{e}_y \tag{A.2}$$

with $\theta_{M_h} = \varphi_M + z_{M_h}/L$, or else

$$\overrightarrow{OM_h} = \overrightarrow{OA^\star} + \xi_1 \boldsymbol{e}_{r_{A^\star}} + \eta_1 \boldsymbol{e}_{\varphi_{A^\star}} = (r_{A^\star} + \xi_1)\boldsymbol{e}_{r_{A^\star}} + \eta_1 \boldsymbol{e}_{\varphi_{A^\star}} \tag{A.3}$$

where $(\xi_1, \eta_1) = (\rho\cos\psi, \rho\sin\psi)$ are the local Cartesian coordinates of $\mathrm{M_h}$. Using both expressions, one can compute the scalar products $\overrightarrow{O\mathrm{M_h}} \cdot \boldsymbol{e}_x$, $\overrightarrow{O\mathrm{M_h}} \cdot \boldsymbol{e}_y$ and $\overrightarrow{O\mathrm{M_h}} \cdot \boldsymbol{e}_z$. This yields

$$r_M \cos(\theta_{\mathrm{M_h}}) = (r_{\mathrm{A}^\star} + \rho\cos\psi), \tag{A.4}$$

$$r_M \sin(\theta_{\mathrm{M_h}}) = \alpha_{\mathrm{A}^\star}\,\rho\sin\psi, \tag{A.5}$$

$$\varphi_M = \theta_{\mathrm{M_h}} + \alpha_{\mathrm{A}^\star}\,\frac{r_{\mathrm{A}^\star}}{L}\,\frac{\rho}{L}\,\sin\psi \tag{A.6}$$

$$z_{\mathrm{M_h}} = -\alpha_{\mathrm{A}^\star}\,\frac{r_{\mathrm{A}^\star}}{L}\rho\sin\psi. \tag{A.7}$$

From any (ρ, ψ) one gets r_M and $\theta_{\mathrm{M_h}}$ from equations (A.4)–(A.5) and thereafter φ_M from (A.6). When the point M is near $\mathrm{A}^\star$, the local radius is small compared to pitch $\rho/L \ll 1$, the radial and azimuth values are approximated to:

$$r_M^2 = r_{\mathrm{A}^\star}^2 + 2r_{\mathrm{A}^\star}\rho\cos\psi, \qquad \theta_{\mathrm{M_h}} = \frac{1}{r_{\mathrm{A}^\star}}\alpha_{\mathrm{A}^\star}\,\rho\sin\psi\,.$$

It yields the expression of helical line:

$$\varphi_M = \theta_{\mathrm{M_h}} + \epsilon = \frac{1}{r_{\mathrm{A}^\star}}\alpha_{\mathrm{A}^\star}\,\rho\sin\psi + \alpha_{\mathrm{A}^\star}\,\frac{r_{\mathrm{A}^\star}}{L}\,\frac{\rho}{L}\,\sin\psi = \beta_{\mathrm{A}^\star}^2\theta_{\mathrm{M_h}}$$

This yields two expressions

$$\rho^2 = (r_M\cos(\theta_{\mathrm{M_h}}) - r_{\mathrm{A}^\star})^2 + \beta_{\mathrm{A}^\star}^2\,(r_M\sin(\theta_{\mathrm{M_h}}))^2 = (r_M\cos(\varphi_M) - r_{\mathrm{A}^\star})^2 + \alpha_{\mathrm{A}^\star}^2\,(r_M\sin(\varphi_M))^2\,.$$

A.2 Projection of the velocity field on the $\Pi_\perp$ plane

Point A denotes the vortex centre, with the associated Serret–Frenet basis $(\boldsymbol{e}_{r_\mathrm{A}}, \boldsymbol{e}_{\varphi_\mathrm{A}}, \boldsymbol{e}_{B_\mathrm{A}})$ such that

$$\boldsymbol{e}_{\varphi_\mathrm{A}}(r_\mathrm{A}, \theta_\mathrm{A}) = \alpha_\mathrm{A}\left(\boldsymbol{e}_{\theta_\mathrm{A}} - \frac{r_\mathrm{A}}{L}\boldsymbol{e}_z\right), \tag{A.8}$$

$$\boldsymbol{e}_{B_\mathrm{A}}(r_\mathrm{A}, \theta_\mathrm{A}) = \alpha_\mathrm{A}\left(\frac{r_\mathrm{A}}{L}\boldsymbol{e}_{\theta_\mathrm{A}} + \boldsymbol{e}_z\right), \tag{A.9}$$

where $\alpha_\mathrm{A} = (1 + r_\mathrm{A}^2/L^2)^{-1/2}$ (see figure 4.2 for a similar geometry). The plane $\Pi_\perp$ is spanned by the Cartesian basis $(\boldsymbol{e}_{r_\mathrm{A}}, \boldsymbol{e}_{\varphi_\mathrm{A}})$, to which a local polar basis $(\boldsymbol{e}_\rho, \boldsymbol{e}_\psi)$ is associated:

$$\boldsymbol{e}_\rho = \quad \cos\psi\,\boldsymbol{e}_{r_\mathrm{A}} + \sin\psi\,\boldsymbol{e}_{\varphi_\mathrm{A}}\,, \tag{A.10}$$

$$\boldsymbol{e}_\psi = -\sin\psi\,\boldsymbol{e}_{r_\mathrm{A}} + \cos\psi\,\boldsymbol{e}_{\varphi_\mathrm{A}}\,, \tag{A.11}$$

and a normal vector to the plane is $\boldsymbol{e}_b \equiv \boldsymbol{e}_{B_\mathrm{A}}$.

In order to express the velocity field in plane $\Pi_\perp$ using the basis $(\boldsymbol{e}_{r_\mathrm{A}}, \boldsymbol{e}_{\varphi_\mathrm{A}}, \boldsymbol{e}_{B_\mathrm{A}})$, one first determines the intersection M between the helical line passing through $\mathrm{M_0}$ in plane Π_0 and the plane $\Pi_\perp$, which is located at $r_M\boldsymbol{e}_r(\theta_M) + \theta_M\boldsymbol{e}_\theta + z_M\boldsymbol{e}_z$. If O denotes O the origin of plane Π_0, the vector $\overrightarrow{\mathrm{OM}}$ reads

$$\overrightarrow{\mathrm{OM}} = \overrightarrow{\mathrm{OA}} + \overrightarrow{\mathrm{AM}}$$

with $\overrightarrow{\mathrm{OA}} = r_A \boldsymbol{e}_r(\theta_A)$ and $\overrightarrow{\mathrm{AM}} = \xi_1 \boldsymbol{e}_{r_A} + \eta_1 \boldsymbol{e}_{\varphi_A}$, here ($\xi_1$,$\eta_1$) are the components in the local orthogonal basis ($\boldsymbol{e}_{r_A}$,$\boldsymbol{e}_{\varphi_A}$) in plane $\Pi_\perp$. One then obtains

$$\overrightarrow{\mathrm{OM}} = z_M \boldsymbol{e}_z + r_M \boldsymbol{e}_r(\theta_M) = (r_A + \xi_1)\boldsymbol{e}_{r_A} + \eta_1 \boldsymbol{e}_{\varphi_A}\,. \tag{A.12}$$

Quantity z_M can be calculated using the projection:

$$z_M = \overrightarrow{\mathrm{OM}} \cdot \boldsymbol{e}_z = -\frac{\alpha_A r_A}{L}\eta_1\,. \tag{A.13}$$

Equations (A.12)-(A.13) give the radial position:

$$r_M^2 = (r_A + \xi_1)^2 + \alpha_A^2 \eta_1^2\,.$$

The helical symmetric with point M_0 and M can be expressed as:

$$r_M \sin(\theta_M) = (r_A + \xi_1)\sin\theta_A + \eta_1 \alpha_A \cos\theta_A \tag{A.14}$$

$$r_M \cos(\theta_M) = (r_A + \xi_1)\cos\theta_A - \eta_1 \alpha_A \sin\theta_A \tag{A.15}$$

$$\text{where } \theta_M = \theta_{M_0} - \alpha_A \frac{r_A}{L^2}\eta_1 \tag{A.16}$$

For a chosen point M in plane $\Pi_\perp(A)$, the values of (θ_A, ξ_1, η_1, r_M) are known, then the azimuthal location θ_M can be deduced from equations (A.14)–(A.15), then one obtains the value of θ_{M_0} through equation (A.16).

The velocity field at any point M_0 in plane Π_0 is given by

$$\boldsymbol{u}(\mathrm{M}_0) = u_r(\mathrm{M}_0)\boldsymbol{e}_r(\mathrm{M}_0) + u_\varphi(\mathrm{M}_0)\boldsymbol{e}_\varphi(\mathrm{M}_0) + u_B(\mathrm{M}_0)\boldsymbol{e}_B(\mathrm{M}_0)\,.$$

and the velocity at corresponding point M in plane $\Pi_\perp$ reads

$$\boldsymbol{u}(\mathrm{M}) = u_\rho(\mathrm{M})\boldsymbol{e}_\rho(\mathrm{M}) + u_\psi(\mathrm{M})\boldsymbol{e}_\psi(\mathrm{M}) + u_b(\mathrm{M})\boldsymbol{e}_b(\mathrm{M})\,.$$

The helical symmetry implies that $\boldsymbol{u}(\mathrm{M})$ has the same components as $\boldsymbol{u}(\mathrm{M}_0)$ in the helical basis ($\boldsymbol{e}_r$,$\boldsymbol{e}_\varphi$,$\boldsymbol{e}_B$):

$$\boldsymbol{u}(\mathrm{M}) = u_r(\mathrm{M}_0)\boldsymbol{e}_r(\mathrm{M}) + u_\varphi(\mathrm{M}_0)\boldsymbol{e}_\varphi(\mathrm{M}) + u_B(\mathrm{M}_0)\boldsymbol{e}_B(\mathrm{M})\,.$$

Projected on the basis ($\boldsymbol{e}_{r_\mathrm{A}}$,$\boldsymbol{e}_{\varphi_\mathrm{A}}$,$\boldsymbol{e}_{B_\mathrm{A}}$), this yields

$$\begin{pmatrix} u_{r_\mathrm{A}}(\mathrm{M}) \\ u_{\varphi_\mathrm{A}}(\mathrm{M}) \\ u_{B_\mathrm{A}}(\mathrm{M}) \end{pmatrix} = \left[u_r(\mathrm{M}_0)\boldsymbol{e}_r(\mathrm{M}) + u_\varphi(\mathrm{M}_0)\boldsymbol{e}_\varphi(\mathrm{M}) + u_B(\mathrm{M}_0)\boldsymbol{e}_B(\mathrm{M})\right] \cdot \begin{pmatrix} \boldsymbol{e}_{r_\mathrm{A}} \\ \boldsymbol{e}_{\varphi_\mathrm{A}} \\ \boldsymbol{e}_{B_\mathrm{A}} \end{pmatrix}.$$

Using projection relations of vector at point M in direction $\boldsymbol{e}_{r_\mathrm{A}}$

$$\begin{aligned} \boldsymbol{e}_r(\mathrm{M}) \cdot \boldsymbol{e}_{r_\mathrm{A}} &= \cos(\theta_\mathrm{M} - \theta_\mathrm{A}) \\ \boldsymbol{e}_\varphi(\mathrm{M}) \cdot \boldsymbol{e}_{r_\mathrm{A}} &= \alpha_\mathrm{M} \sin(\theta_\mathrm{A} - \theta_\mathrm{M}) \\ \boldsymbol{e}_B(\mathrm{M}) \cdot \boldsymbol{e}_{r_\mathrm{A}} &= \alpha_\mathrm{M} \frac{r_\mathrm{M}}{L} \sin(\theta_\mathrm{A} - \theta_\mathrm{M}) \end{aligned}$$

in direction $\boldsymbol{e}_{\varphi_\mathrm{A}}$

$$\begin{aligned}
\boldsymbol{e}_r(\mathrm{M})\cdot\boldsymbol{e}_{\varphi_\mathrm{A}} &= \alpha_\mathrm{A}\sin(\theta_\mathrm{M}-\theta_\mathrm{A})\\
\boldsymbol{e}_\varphi(\mathrm{M})\cdot\boldsymbol{e}_{\varphi_\mathrm{A}} &= \alpha_\mathrm{M}\alpha_\mathrm{A}\left[\frac{r_\mathrm{M}r_\mathrm{A}}{L^2}+\cos(\theta_\mathrm{M}-\theta_\mathrm{A})\right]\\
\boldsymbol{e}_B(\mathrm{M})\cdot\boldsymbol{e}_{\varphi_\mathrm{A}} &= \alpha_\mathrm{M}\alpha_\mathrm{A}\left[-\frac{r_\mathrm{A}}{L}+\frac{r_\mathrm{M}}{L}\cos(\theta_\mathrm{M}-\theta_\mathrm{A})\right]
\end{aligned}$$

and in direction $\boldsymbol{e}_{B_\mathrm{A}}$

$$\begin{aligned}
\boldsymbol{e}_r(\mathrm{M})\cdot\boldsymbol{e}_{B_\mathrm{A}} &= \alpha_\mathrm{A}\frac{r_\mathrm{A}}{L}\sin(\theta_\mathrm{M}-\theta_\mathrm{A})\\
\boldsymbol{e}_\varphi(\mathrm{M})\cdot\boldsymbol{e}_{B_\mathrm{A}} &= \alpha_\mathrm{M}\alpha_\mathrm{A}\left[-\frac{r_\mathrm{M}}{L}+\frac{r_\mathrm{A}}{L}\cos(\theta_\mathrm{M}-\theta_\mathrm{A})\right]\\
\boldsymbol{e}_B(\mathrm{M})\cdot\boldsymbol{e}_{B_\mathrm{A}} &= \alpha_\mathrm{M}\alpha_\mathrm{A}\left[1+\frac{r_\mathrm{M}r_\mathrm{A}}{L^2}\cos(\theta_\mathrm{M}-\theta_\mathrm{A})\right].
\end{aligned}$$

Using the relation of new local basis $(\rho,\,\psi)$ at point M

$$u_\rho = \cos\psi\; u_{r_A} + \sin\psi\; u_{\varphi_A}\,,\quad u_\psi = -\sin\psi\; u_{r_A} + \cos\psi\; u_{\varphi_A}\,,$$

one obtains the "helical projection relations [Selçuk et al., 2017b] linking point M_0 in plane Π_0 to point M in plane $\Pi_\perp$:

$$\begin{aligned}
u_\rho(\mathrm{M}) = {}& u_r(\mathrm{M}_0)\left[\cos(\theta_\mathrm{M}-\theta_\mathrm{A})\cos\psi+\alpha_\mathrm{A}\sin(\theta_\mathrm{M}-\theta_\mathrm{A})\sin\psi\right]\\
&+u_\varphi(\mathrm{M}_0)\alpha_\mathrm{M}\left[\sin(\theta_\mathrm{A}-\theta_\mathrm{M})\cos\psi+\alpha_\mathrm{A}\left(\frac{r_\mathrm{M}r_\mathrm{A}}{L^2}+\cos(\theta_\mathrm{M}-\theta_\mathrm{A})\right)\sin\psi\right]\\
&+u_B(\mathrm{M}_0)\frac{\alpha_\mathrm{M}}{L}\left[r_\mathrm{M}\sin(\theta_\mathrm{A}-\theta_\mathrm{M})\cos\psi+\alpha_\mathrm{A}(-r_\mathrm{A}+r_\mathrm{M}\cos(\theta_\mathrm{M}-\theta_\mathrm{A}))\sin\psi\right],
\end{aligned}$$

$$\begin{aligned}
u_\psi(\mathrm{M}) = {}& u_r(\mathrm{M}_0)\left[-\cos(\theta_\mathrm{M}-\theta_\mathrm{A})\sin\psi+\alpha_\mathrm{A}\sin(\theta_\mathrm{M}-\theta_\mathrm{A})\cos\psi\right]\\
&+u_\varphi(\mathrm{M}_0)\alpha_\mathrm{M}\left[-\sin(\theta_\mathrm{A}-\theta_\mathrm{M})\sin\psi+\alpha_\mathrm{A}\left(\frac{r_\mathrm{M}r_\mathrm{A}}{L^2}+\cos(\theta_\mathrm{M}-\theta_\mathrm{A})\right)\cos\psi\right]\\
&+u_B(\mathrm{M}_0)\frac{\alpha_\mathrm{M}}{L}\left[-r_\mathrm{M}\sin(\theta_\mathrm{A}-\theta_\mathrm{M})\sin\psi+\alpha_\mathrm{A}(-r_\mathrm{A}+r_\mathrm{M}\cos(\theta_\mathrm{M}-\theta_\mathrm{A}))\cos\psi\right],
\end{aligned}$$

$$\begin{aligned}
u_b(\mathrm{M}) = {}& u_r(\mathrm{M}_0)\alpha_\mathrm{A}\frac{r_\mathrm{A}}{L}\sin(\theta_\mathrm{M}-\theta_\mathrm{A})\\
&+u_\varphi(\mathrm{M}_0)\frac{\alpha_\mathrm{M}}{L}\alpha_\mathrm{A}[-r_\mathrm{M}+r_\mathrm{A}\cos(\theta_\mathrm{M}-\theta_\mathrm{A})]\\
&+u_B(\mathrm{M}_0)\alpha_\mathrm{M}\alpha_\mathrm{A}[1+\frac{r_\mathrm{M}r_\mathrm{A}}{L^2}\cos(\theta_\mathrm{M}-\theta_\mathrm{A})].
\end{aligned}$$

With the coordinates of point M_0 in plane Π_0, the values of all fields can be obtained in plane $\Pi_\perp$ with proper interpolations.

Appendix B

HELIKZ–NL and HELIKZ–LIN

Contents

B.1 Pseudo-spectral method

It is recalled that the non-linear operator **NL** in HELIKZ–NL equals to:

$$\mathrm{NL}_r = \omega_\theta u_z - \omega_z u_\theta \,, \tag{B.1}$$
$$\mathrm{NL}_\theta = \omega_z u_r - \omega_r u_z \,, \tag{B.2}$$
$$\mathrm{NL}_z = \omega_r u_\theta - \omega_\theta u_r \,, \tag{B.3}$$

and the linear operator **LNL** in HELIKZ–LIN equals:

$$\mathrm{LNL}_r \equiv \omega'_\theta u_z^{\mathrm{BF}} + \omega_\theta^{\mathrm{BF}} u'_z - \omega'_z u_\theta^{\mathrm{BF}} - (\omega_z^{\mathrm{BF}} + 2\Omega_0) u'_\theta \,, \tag{B.4}$$
$$\mathrm{LNL}_\theta \equiv \omega'_z u_r^{\mathrm{BF}} + (\omega_z^{\mathrm{BF}} + 2\Omega_0) u'_r - \omega_r^{\mathrm{BF}} u'_z - \omega'_r u_z^{\mathrm{BF}} \,, \tag{B.5}$$
$$\mathrm{LNL}_z \equiv \omega'_r u_\theta^{\mathrm{BF}} + \omega_r^{\mathrm{BF}} u'_\theta - \omega'_\theta u_r^{\mathrm{BF}} - \omega_\theta^{\mathrm{BF}} u'_r \,. \tag{B.6}$$

Both expressions contain the sum of terms, each one being the product of two fields, of the type $f(r,\varphi) = u(r,\varphi)v(r,\varphi)$. Let us define the Fourier modes in φ associated to both quantities:

$$u^{(j)}(r) \equiv \frac{1}{2\pi}\int_0^{2\pi} u(r,\varphi)\exp(-\mathrm{i}j\varphi)\mathrm{d}\varphi \,, \quad v^{(k)}(r) \equiv \frac{1}{2\pi}\int_0^{2\pi} v(r,\varphi)\exp(-\mathrm{i}k\varphi)\mathrm{d}\varphi \,, \tag{B.7}$$

Since f in physical space equals:

$$f(r,\varphi) = \sum_{j=-\infty}^{\infty} \sum_{k=-\infty}^{\infty} \exp[\mathrm{i}(j+k)\varphi] u^{(j)}(r) v^{(k)}(r), \tag{B.8}$$

its Fourier coefficient $f^{(m)}$ reads

$$f^{(m)}(r) = \sum_{k=-\infty}^{\infty} u^{(m-k)}(r) v^{(k)}(r). \tag{B.9}$$

If the value of $f^{(m)}$ was estimated in spectral space by performing the above sums, the number of operations would be of order N^2.

One uses instead the pseudo-spectral method (PSM in short) to accelerate the calculation: it consists in a Fast Fourier Transform (FFT). This algorithm is performed in $N \log_2 N$ operation, and provides quantity $u_N(r,\varphi_j)$ in physical space:

$$u_N(r,\varphi_j) = \sum_{m=0}^{N-1} u_N^{(m)}(r) \exp(\mathrm{i}m\varphi_j) \quad \text{with} \quad \varphi_j = 2\pi j/N\,, \quad j = 0,1,...,N-1\,, \tag{B.10}$$

and a similar transform for v_N. This is followed by N products of $f_N(r,\varphi_j) = u_N(r,\varphi_j) v_N(r,\varphi_j)$ used to evaluate the nonlinear term at the collocation points in physical space. Finally a direct Fourier transform is performed to get the Fourier coefficients of f_N:

$$f_N^{(m)}(r) = \frac{1}{N} \sum_{j=0}^{N-1} \exp(-\mathrm{i}m\varphi_j) f_N(r,\varphi_j). \tag{B.11}$$

For instance, when $N = 256$, this reduces the number of operations by a factor of 32, and hence saves a huge simulation time.

B.1.1 Spectral folding and anti-aliasing

When an arbitrary periodic function f is represented at collocation points φ_j using only a finite number of modes:

$$f(r,\varphi_j) = \sum_{m=-\infty}^{\infty} f^{(m)}(r) \exp(\mathrm{i}m\varphi_j) = \sum_{m=0}^{N-1} f_N^{(m)}(r) \exp(\mathrm{i}m\varphi_j), \tag{B.12}$$

an effect named aliasing occurs. Indeed, since $\exp[\mathrm{i}(m+pN)\varphi_j)] = \exp[\mathrm{i}(m\varphi_j + 2\pi p)] = \exp(\mathrm{i}m\varphi_j)$, all modes $(m+pN)$ become indistinguishable at these collocation points, and one has by identification:

$$f_N^{(m)}(r) = \sum_{p=-\infty}^{+\infty} f^{(m+pN)}(r). \tag{B.13}$$

Here for nonlinear terms $f_N^{(m)}(r)$, the sum can be split into two parts: one involving both modes in the range $]-\frac{1}{2}N, \frac{1}{2}N]$, and one involving modes outside this range (the aliasing error):

$$f_N^{(m)}(r) = \sum_{-\frac{1}{2}N<k\leq\frac{1}{2}N}^{-\frac{1}{2}N<m-k\leq\frac{1}{2}N} u_N^{(m-k)}(r)v_N^{(k)}(r) + \underbrace{\sum_{-\frac{1}{2}N<k\leq\frac{1}{2}N}^{m-k>\frac{1}{2}N \text{ or } m-k\leq-\frac{1}{2}N} u_N^{(m-k)}(r)v_N^{(k)}(r)}_{\text{aliasing error}} . \tag{B.14}$$

In order to prevent aliasing, so-called anti-aliasing (or de-aliasing) methods exist. The general idea is to move the "indistinguishable" spectrum to a non-used range of the spectrum so as to keep the rest of the spectrum that we are interested in free of aliasing. Practically for freeing $-\frac{1}{2}N \leq k \leq \frac{1}{2}N$ from aliasing errors, one performs Fourier transforms on the range $-\frac{1}{2}N_\varphi \leq m \leq \frac{1}{2}N_\varphi$ (rather than N) with

$$\varphi_j = 2\pi j/N_\varphi \,, \quad j = 0, 1, ..., N_\varphi - 1 \,. \tag{B.15}$$

the points number is chosen as $N_\varphi = \frac{3}{2}N$, which indicate the sub-spectrum range $]-\frac{1}{2}N, \frac{1}{2}N]$ is then free of aliasing:

- if $m-k > \frac{1}{2}N_\varphi$, then the coefficient will be aliased to $m-k-N_\varphi$. To prevent aliasing, $m-k-N_\varphi$ should be less than $-\frac{1}{2}N$. The largest value of $m-k$ is $N-1$ reached when $m = \frac{1}{2}N$ and $k = -\frac{1}{2}N+1$: this leads to $N_\varphi > \frac{3}{2}N - 2$.
- if $m-k \leq -\frac{1}{2}N_\varphi$, then the coefficient will be aliased to $m-k+N_\varphi$. To prevent aliasing, $m-k+N_\varphi$ should be greater than $\frac{1}{2}N$. The smallest value of $m-k$ is $-N+1$ reached when $m = -\frac{1}{2}N+1$ and $k = \frac{1}{2}N$: this leads to $N_\varphi > \frac{3}{2}N - 1$.

To summarize, the pseudo-spectral method uses N_φ collocations points. In the spectral domain, which covers modes in the interval $]-\frac{1}{2}N_\varphi, \frac{1}{2}N_\varphi]$, one can keep the sub-range $]-\frac{1}{2}N, \frac{1}{2}N]$ free from aliasing, by choosing $N_\varphi = \frac{3}{2}N$ and setting to zero the amplitude of the modes outside this sub-range.

B.2 Boundary conditions at $r = R_{\rm ext}$

In the following we introduce the quantity

$$\boxed{H_{|m|}(\hat{r}) \equiv \frac{1}{K_{|m|}(\hat{r})}\frac{\partial K_{|m|}(\hat{r})}{\partial \hat{r}}} \,. \tag{B.16}$$

where the simplified expressions for $H_{|m|}$ are given in Appendix C.

B.2.1 for HELIKZ–NL

In the potential region, the velocity field is derived from the potential $\hat{\Phi}$:

$$\hat{\Phi}(r,\varphi,t) = e^{\mathrm{i}m\varphi}\Phi^{(m)}(r,t). \tag{B.17}$$

Boundary conditions to be imposed at $r = R_{\text{ext}}$ are Robin conditions (mixed boundary conditions)

$$\boxed{\frac{\partial\Phi^{(m)}}{\partial r} = C_{\Phi}^{(m)}\Phi^{(m)}, \quad \frac{\partial p^{(m)}}{\partial r} = C_{p}^{(m)}p^{(m)},} \tag{B.18}$$

$$\boxed{\frac{\partial v_r^{(m)}}{\partial r} = C_{r}^{(m)}v_r^{(m)}, \quad \frac{\partial v_\theta^{(m)}}{\partial r} = C_{\theta}^{(m)}v_\theta^{(m)}, \quad \frac{\partial v_z^{(m)}}{\partial r} = C_{z}^{(m)}v_z^{(m)}}, \tag{B.19}$$

where $C_{\Phi}^{(m)}, C_{p}^{(m)}$ and $C_{r}^{(m)}, C_{\theta}^{(m)}, C_{x}^{(m)}$ are constants to be determined in each case. We only give results since computations are similar to those found in appendix F. In the following let us introduce the notations

$$\boxed{\beta \equiv -\frac{m}{L}, \quad \hat{r} \equiv |\beta| r \quad \text{and} \quad \hat{R}_{ext} = |\beta| R_{\text{ext}}.}$$

B.2.2 Conditions for $\beta \neq 0$

$$C_{\Phi}^{(m)} \equiv |\beta| H_{|m|}(\hat{R}_{\text{ext}}), \quad C_{p}^{(m)} \equiv C_{\Phi}^{(m)} + \frac{2m}{R_{\text{ext}}\Big(m - 2\frac{\omega}{\Omega^{B}(R_{\text{ext}})}\Big)}, \tag{B.20}$$

$$C_{z}^{(m)} \equiv C_{\Phi}^{(m)}, \quad C_{r}^{(m)} \equiv \frac{\beta^2 + \frac{m^2}{(R_{\text{ext}})^2}}{C_{\Phi}^{(m)}} - \frac{1}{R_{\text{ext}}}, \quad C_{\theta}^{(m)} \equiv C_{\Phi}^{(m)} - \frac{1}{R_{\text{ext}}}. \tag{B.21}$$

B.2.3 Conditions for $\beta = 0$ and $m = 0$ for HELIKZ–NL

For $\beta = 0, m = 0$, one has a potential flow Φ, the equation $\Delta\Phi = 0$ reads:

$$\frac{\mathrm{d}^2\Phi^{(m=0)}}{\mathrm{d}r^2} + \frac{1}{r}\frac{\mathrm{d}\Phi^{(m=0)}}{\mathrm{d}r} = 0. \tag{B.22}$$

The solutions of equation (B.22) reads:

$$\Phi^{(m)}(r) = A + B\ln r.$$

Since no source is present, one supposes $B = 0$ (so that $v_r^{(0)} = 0$).

The velocities are expressed as:

$$v_r^{(0)} = \frac{\partial \Phi^{(0)}}{\partial r} = 0\,, \qquad v_\theta^{(0)} = \frac{\Gamma}{2\,\pi\,r}\,, \qquad v_z^{(0)} = 0\,, \tag{B.23}$$

assuming that the total circulation Γ is known.

B.3 for HELIKZ–LIN

In the potential region, the velocity field is derived from the potential $\hat{\Phi}$

$$\hat{\Phi}(r,\varphi,t) = e^{\mathrm{i}(m\varphi+kz)}\Phi^{(m)}(r,t). \tag{B.24}$$

From this remark, one can infer that the boundary conditions to be imposed at $r = R_{\text{ext}}$ are Robin conditions (mixed boundary conditions)

$$\boxed{\frac{\partial \Phi^{(m)}}{\partial r} = C_\Phi^{(m)}\Phi^{(m)}} \tag{B.25}$$

$$\boxed{\frac{\partial v_r^{(m)}}{\partial r} = C_r^{(m)}\,v_r^{(m)}\,, \quad \frac{\partial v_\theta^{(m)}}{\partial r} = C_\theta^{(m)}\,v_\theta^{(m)}\,, \quad \frac{\partial v_z^{(m)}}{\partial r} = C_z^{(m)}\,v_z^{(m)}}\,, \tag{B.26}$$

where $C_\Phi^{(m)}, C_p^{(m)}$ and $C_r^{(m)}, C_\theta^{(m)}, C_x^{(m)}$ are constants to be determined in each case. We only give results since computations are similar to those found in appendix F . In the following let us introduce the notations

$$\boxed{\beta \equiv k_z - \frac{m}{L}, \quad \hat{r} \equiv |\beta| r \quad \text{and} \quad \hat{R}_{ext} = |\beta| R_{\text{ext}}.}$$

B.3.1 Conditions for $\beta \neq 0$

$$C_\Phi^{(m)} \equiv |\beta| H_{|m|}(\hat{R}_{\text{ext}}), \quad C_p^{(m)} \equiv C_\Phi^{(m)} + \frac{2m}{R_{\text{ext}}\Big(m - 2\frac{\omega}{\Omega^B(R_{\text{ext}})}\Big)}, \tag{B.27}$$

$$C_z^{(m)} \equiv C_\Phi^{(m)}\,, \quad C_r^{(m)} \equiv \frac{\beta^2 + \frac{m^2}{(R_{\text{ext}})^2}}{C_\Phi^{(m)}} - \frac{1}{R_{\text{ext}}}, \quad C_\theta^{(m)} \equiv C_\Phi^{(m)} - \frac{1}{R_{\text{ext}}}. \tag{B.28}$$

B.3.2 Conditions for $\beta = 0$, $k = m/L$ and $m \neq 0$

$$C_\Phi^{(m)} \equiv -\frac{|m|}{R_{ext}}, \quad C_r^{(m)} \equiv -\frac{|m|+1}{R_{\text{ext}}}, \quad C_\theta^{(m)} \equiv -\frac{|m|+1}{R_{\text{ext}}}, u_x^{(m)} = 0\,. \tag{B.29}$$

The case $\beta = 0$ and $m = 0$ is not pertinent as a perturbation.

B.4 Boundary conditions at the axis $r = 0$

The boundary conditions at the axis $r = 0$ come from **regularity** considerations: while the cylindrical coordinates have a singularity at $r = 0$, all physical quantities, when written in Cartesian coordinates, must remain infinitely differentiable there [Lopez et al., 2002].

The transformation between the Cartesian and cylindrical coordinates reads:

$$x = r\cos\theta\,, \quad y = r\sin\theta\,, \tag{B.30}$$

with $\theta = \varphi + z/L$. Using the complex variable $\zeta = r\exp[\mathrm{i}(\varphi + z/L)]$, one has $x = \frac{1}{2}(\zeta + \bar{\zeta})$, $y = -\frac{\mathrm{i}}{2}(\zeta - \bar{\zeta})$. Any function $f(r,\varphi)$ can be expressed as a function $h(\zeta,\bar{\zeta})$ through the linear change of variables

$$f(r,\varphi) = f\left[\tfrac{1}{2}(\zeta+\bar{\zeta}), -\tfrac{\mathrm{i}}{2}(\zeta-\bar{\zeta})\right] \equiv h(\zeta,\bar{\zeta})\,. \tag{B.31}$$

Function h is infinitely differentiable, especially at $\zeta = \bar{\zeta} = 0$ where its Taylor expansion reads:

$$h(\zeta,\bar{\zeta}) = \sum_{p,q=0}^{+\infty} h_{p,q}\zeta_p\bar{\zeta}_q\,.$$

For a scalar field f, the Taylor expansion of the Fourier coefficient $f^{(m)}$ reads, for $m \geq 0$:

$$\begin{aligned} f^{(m)}(r) &= \frac{1}{2\pi}\int_0^{2\pi} f(r,\varphi)\mathrm{e}^{-\mathrm{i}m\varphi}\mathrm{d}\varphi = \sum_{p,q=0}^{+\infty} h_{p,q}r^{p+q}\frac{1}{2\pi}\int_0^{2\pi} e^{\mathrm{i}(p-q-m)\varphi}\mathrm{d}\varphi \\ &= \sum_{p-q=m;\ p,q=0}^{+\infty} h_{p,q}r^{p+q} = r^m\sum_{q=0}^{+\infty} h_{(q+m,q)}r^{2q}\,. \end{aligned}$$

One defines $F(r) = \sum_{q=0}^{+\infty}(h_{q+m,q})r^{2q}$, which is by construction an even function, then $f^{(m)}(r)$ has the form:

$$f^{(m)}(r) \sim r^m F(r) \quad \text{when} \quad r \to 0\,.$$

For a vector field $\boldsymbol{v}$, one can express $\boldsymbol{v} = v_x\boldsymbol{e}_x + v_y\boldsymbol{e}_y + v_z\boldsymbol{e}_z = v_r\boldsymbol{e}_r + v_\theta\boldsymbol{e}_\theta + v_z\boldsymbol{e}_z$, the transformation between the Cartesian and cylindrical coordinates reads $v_x = v_r\cos\theta - v_\theta\sin\theta$ and $v_y = v_r\sin\theta + v_\theta\cos\theta$. One defines two new variables:

$$v_\pm \equiv v_r \pm \mathrm{i}v_\theta = \exp(\mp\mathrm{i}\theta)(v_x \pm \mathrm{i}v_y)\,. \tag{B.32}$$

The Taylor expansion of Fourier coefficient $v_\pm^{(m)}$ for $m \geq 1$ reads:

$$v_\pm^{(m)}(r) = \sum_{p-q=m\pm1;\ p,q=0}^{+\infty} h_{\pm,p,q}r^{p+q} = r^{m\pm1}\sum_{q=0}^{+\infty}(h_{\pm(q,m\pm1+q)})r^{2q}\,. \tag{B.33}$$

The Fourier coefficients of $v_\pm$ for $|m| \geq 1$ can be expressed as:

$$v_+^{(m)}(r) = r^{|m|+1} K_m(r), \quad v_-^{(m)}(r) = r^{|m|-1} L_m(r), \tag{B.34}$$

where K_m, L_m are regular even functions.

Equation (B.32) reads as $v_r = \frac{1}{2}(v_+ + v_-)$ and $v_\theta = \frac{\mathrm{i}}{2}(v_- - v_+)$. Accordingly, one can express the Fourier coefficients $v_r^{(m)}$ and $v_\theta^{(m)}$ as:

$$v_r^{(m)}(r) = \frac{1}{2}\left(r^{m-1} \sum_{q=0}^{+\infty} h_{-(q,m-1+q)} r^{2q} + r^{m+1} \sum_{q=0}^{+\infty} h_{+(q,m+1+q)} r^{2q} \right), \tag{B.35}$$

$$v_\theta^{(m)}(r) = \frac{\mathrm{i}}{2}\left(r^{m-1} \sum_{q=0}^{+\infty} h_{-(q,m-1+q)} r^{2q} - r^{m+1} \sum_{q=0}^{+\infty} h_{+(q,m+1+q)}) r^{2q} \right). \tag{B.36}$$

The relations between velocity components and potential:

$$v_r = \frac{\partial \Phi}{\partial r}, \quad v_\theta = \frac{1}{r}\frac{\partial \Phi}{\partial \theta}$$

give in the spectral space when r goes to zero:

$$v_r^{(m)}(0) = \left.\frac{\partial \Phi^{(m)}}{\partial r}\right|_{r=0}, \quad v_\theta^{(m)}(0) = \lim_{r\to 0} \mathrm{i}m \frac{\Phi^{(m)}}{r} = \mathrm{i}m \left.\frac{\partial \Phi^{(m)}}{\partial r}\right|_{r=0} = \mathrm{i}m v_r^{(m)}(0).$$

For $m \geq 1$, the Fourier coefficients of field $\boldsymbol{v}$ thus read:

$$v_r^{(m)}(r) = C_m r^{|m|-1} + r^{|m|+1} G_m(r), \tag{B.37}$$

$$v_\theta^{(m)}(r) = \mathrm{i}m C_m r^{|m|-1} + r^{|m|+1} H_m(r), \tag{B.38}$$

$$v_z^{(m)}(r) = r^{|m|} J_m(r), \tag{B.39}$$

where G_m, H_m, J_m are regular even functions.

For $m = 0$, the components are of the form:

$$v_r^{(0)} = r G_0(r), \quad v_\theta^{(0)} = r H_0(r), \quad v_z^{(0)} = J_0(r), \tag{B.40}$$

where G_0, H_0, J_0 are regular even functions.

The behaviour of all velocity components have been determined, so that we can write the boundary conditions at axis $r = 0$ for the different modes m. If $m > 1$, one may introduce $r = 0$ into equations (B.37)–(B.39), leading to Dirichlet zero conditions for all the velocity components:

$$v_r^{(m)} = 0, \quad v_\theta^{(m)} = 0, \quad v_z^{(m)} = 0 \ \text{ at } r = 0. \tag{B.41}$$

If $m = 1$, equations (B.37)–(B.39) at $r = 0$ indicate that the velocity components v_r and v_θ are finite at axis with:

$$v_r^{(1)} = \frac{\partial \Phi^{(1)}}{\partial r}, \quad v_\theta^{(1)} = \mathrm{i}\frac{\partial \Phi^{(1)}}{\partial r}, \quad v_z^{(1)} = 0 \ \text{ at } r = 0.$$

As $\Phi^{(1)}(r) = r\,F(r)$, and $F(r)$ a regular even function such that $F'(0) = 0$, the boundary conditions then read:

$$\frac{\partial v_r^{(1)}}{\partial r} = 0\,, \ \frac{\partial v_\theta^{(1)}}{\partial r} = 0\,, \ v_z^{(1)} = 0 \ \text{ at } \ r = 0. \tag{B.42}$$

If $m = 0$, the boundary conditions read:

$$v_r^{(0)} = 0, \quad v_\theta^{(0)} = 0, \quad \frac{\partial v_z^{(0)}}{\partial r} = 0 \ \text{ at } \ r = 0. \tag{B.43}$$

Appendix C

Appendix: Evaluation of Bessel functions

Contents

Let us evaluate the function

$$\boxed{H_{|m|}(\hat{r}) \equiv \frac{1}{K_{|m|}(\hat{r})} \frac{\partial K_{|m|}(\hat{r})}{\partial \hat{r}}} \,. \tag{C.1}$$

where $K_{|m|}(\hat{r})$ is a modified Bessel function of the second kind [Abramowitz and Stegun, 1964].

Let us introduce one small parameter $\epsilon = 0.01$ and the integer $m_{Large} = 10$

C.1 Expressions for $m = 0$

C.1.1 For $\hat{r} \leq \epsilon$

The asymptotic form of the Bessel function K_0 reads:

$$K_0(\hat{r}) \propto -\log\left(\frac{\hat{r}}{2}\right) - \gamma_c \tag{C.2}$$

with the Euler–Mascheroni constant $\gamma_c \approx 0.58$. As a consequence, the function H_0 behaves as:

$$H_0(\hat{r}) = \frac{K_0'(\hat{r})}{K_0(\hat{r})} \propto \frac{1}{\hat{r}(\gamma_c + \log(\frac{\hat{r}}{2}))} \,. \tag{C.3}$$

C.1.2 For $\epsilon < \hat{r} < \frac{1}{\epsilon}$

One uses a standard algorithm (subroutine IK01A) to compute Bessel function of the second kind $K_0(\hat{r})$ and thus the function H_0

$$H_0(\hat{r}) = \frac{K_0'(\hat{r})}{K_0(\hat{r})}. \tag{C.4}$$

C.1.3 For $\frac{1}{\epsilon} \leq \hat{r}$

For large $\hat{r} \geq \frac{1}{\epsilon}$, an asymptotic expression can be used for the Bessel K_0 function [Abramowitz and Stegun, 1964]

$$K_0(\hat{r})|_{\hat{r}\to+\infty} \propto e^{-\hat{r}}\sqrt{\frac{\pi}{2\hat{r}}}\left(1 - \frac{1}{8}\frac{1}{\hat{r}} + O(\hat{r}^{-2})\right). \tag{C.5}$$

As a consequence, $H_0(\hat{r})$ is expressed as:

$$H_0(\hat{r}) = \frac{K_0'(\hat{r})}{K_0(\hat{r})} \propto -\left(1 + \frac{1}{2\hat{r}}\right). \tag{C.6}$$

C.2 Expressions for $0 < |m| \leq m_{Large}$

For $|m| > 0$ the function $H_{|m|}(\hat{r})$ is such that

$$\boxed{H_{|m|}(\hat{r}) \equiv \frac{1}{K_{|m|}(\hat{r})}\frac{\partial K_{|m|}(\hat{r})}{\partial \hat{r}} = -\frac{K_{|m|-1}}{K_{|m|}} - \frac{|m|}{\hat{r}}}. \tag{C.7}$$

C.2.1 For $\hat{r} < \epsilon$

Since

$$H_1(\hat{r}) = \frac{K_1'(\hat{r})}{K_1(\hat{r})} \propto -\frac{1}{\hat{r}} \quad \text{for } |m| = 1, \tag{C.8}$$

$$\frac{K_{|m|-1}(\hat{r})}{K_{|m|}(\hat{r})} \simeq \frac{\hat{r}}{|m|-1} \quad \text{si } |m| \geq 2, \tag{C.9}$$

then

$$\boxed{H_{|m|}(\hat{r}) \propto -\frac{|m|}{\hat{r}}}. \tag{C.10}$$

C.2.2 For $\epsilon \leq \hat{r} \leq m_{Large}^2$

One uses an iterative standard algorithm to compute the ratio of Bessel functions of the second kind and thus the function $H_{|m|}$. One evaluates $K_0(\hat{r})/K_1(\hat{r})$ using a standard algorithm (the subroutine IK01A) and then computes $K_{|m|-1}(\hat{r})/K_{|m|}(\hat{r})$ using the recurrence

$$\frac{K_{|m|}(\hat{r})}{K_{|m|+1}(\hat{r})} = \left[\frac{K_{|m|-1}(\hat{r})}{K_{|m|}(\hat{r})} + \frac{2|m|}{\hat{r}}\right]^{-1}. \tag{C.11}$$

C.2.3 For $m_{Large}^2 < \hat{r}$

An asymptotic expression can be used for the Bessel $K_{|m|}$ function [Abramowitz and Stegun, 1964]

$$K_{|m|}(\hat{r})\Big|_{\hat{r}\to+\infty} \propto e^{-\hat{r}}\sqrt{\frac{\pi}{2\hat{r}}}\left(1 + \frac{4m^2-1}{8}\frac{1}{\hat{r}} + O(\hat{r}^{-2})\right). \tag{C.12}$$

As a consequence, $H_{|m|}(\hat{r})$ is expressed as:

$$H_{|m|}(\hat{r}) = \frac{K'_{|m|}(\hat{r})}{K_{|m|}(\hat{r})} \propto -\left(1 + \frac{1}{2\hat{r}}\right). \tag{C.13}$$

C.3 Expressions for $|m| > m_{Large}$

C.3.1 For $\hat{r} < \epsilon|m|$

The asymptotic form of the Bessel function $K_{|m|}$ reads:

$$K_{|m|}(\hat{r}) \propto \frac{1}{2}(|m|-1)!\left(\frac{\hat{r}}{2}\right)^{-|m|}, \tag{C.14}$$

$$\frac{K_{|m|-1}(\hat{r})}{K_{|m|}(\hat{r})} \simeq \frac{\hat{r}}{|m|-1}. \tag{C.15}$$

As a consequence, the function $H_{|m|}$ behaves as:

$$H_{|m|}(\hat{r}) \propto -\frac{|m|}{\hat{r}}. \tag{C.16}$$

C.3.2 For $\epsilon|m| < \hat{r} < \frac{|m|}{\epsilon}$

$$H_{|m|}(\hat{r}) = \frac{K'_{|m|}(\hat{r})}{K_{|m|}(\hat{r})} = -\frac{|m|\sqrt{1+\frac{\hat{r}^2}{|m|^2}}}{\hat{r}}\frac{|m|-V}{|m|-U}, \tag{C.17}$$

with

$$V \equiv \frac{1}{24}(-9p + 7p^3)\,, \quad U \equiv \frac{1}{24}(3p - 5p^3)\,, \quad p \equiv \frac{1}{\sqrt{1 + \frac{\hat{r}^2}{|m|^2}}}\,.$$

C.3.3 For $\frac{|m|}{\epsilon} < \hat{r} < |m|^2$

To be solved but never used in our computations.

C.3.4 For $|m|^2 \leq \hat{r}$

An asymptotic expression can be used for the Bessel $K_{|m|}$ function [Abramowitz and Stegun, 1964]

$$K_{|m|}(\hat{r})\Big|_{\hat{r}\to+\infty} \propto e^{-\hat{r}}\sqrt{\frac{\pi}{2\hat{r}}}\left(1 + \frac{4m^2 - 1}{8}\frac{1}{\hat{r}} + O(\hat{r}^{-2})\right). \tag{C.18}$$

As a consequence, $H_{|m|}(\hat{r})$ is expressed as:

$$H_{|m|}(\hat{r}) = \frac{K'_{|m|}(\hat{r})}{K_{|m|}(\hat{r})} \propto -\left(1 + \frac{1}{2\hat{r}}\right). \tag{C.19}$$

Part III

Appendix for part two

Appendix D

Appendix: linearization and modal form

Contents

D.1 Linearization of the conditions at the interface

In order to linearize the boundary conditions at the deformed interface $r = \zeta(\theta, x, t) = 1 + \epsilon\zeta'(\theta, x, t)$, we must at first linearize the expressions (9.10) and (9.11) of the normal and tangential vectors. We introduce the velocity decomposition (10.1), and keep only 1st-order terms $O(\epsilon)$:

$$\boldsymbol{n} = (1,0,0) + \epsilon(0, -\frac{\partial\zeta'}{\partial\theta}, -\frac{\partial\zeta'}{\partial x}) \qquad \boldsymbol{t}_\theta = (0,1,0) + \epsilon(\frac{\partial\zeta'}{\partial\theta}, 0, 0) \qquad \boldsymbol{t}_x = (0,0,1) + \epsilon(\frac{\partial\zeta'}{\partial x}, 0, 0).$$

Using Taylor expansions for $\boldsymbol{u}$ and p at the interface, and again linearizing leads to

$$v_r(\zeta) = \epsilon v_r'(1 + \epsilon\zeta') \simeq \epsilon u_r'(1) \tag{D.1}$$

$$w_\theta(\zeta) = W_\theta(1 + \epsilon\zeta') + \epsilon w_\theta'(1 + \epsilon\zeta') \simeq W_\theta(1) + \epsilon\zeta' \frac{\partial W_\theta}{\partial r}(1) + \epsilon w_\theta'(1) \tag{D.2}$$

$$u_x(\zeta) = U_x(1 + \epsilon\zeta') + \epsilon u_x\prime(1 + \epsilon\zeta') \simeq U_x(1) + \epsilon\zeta' \frac{\partial U_x}{\partial r}(1) + \epsilon u_x'(1) \tag{D.3}$$

$$p(\zeta) = \Pi(1 + \epsilon\zeta') + \epsilon p\prime(1 + \epsilon\zeta') \simeq \Pi(1) + \epsilon\zeta' \frac{\partial \Pi}{\partial r}(1) + \epsilon p'(1). \tag{D.4}$$

The rate of stain tensor (9.18) can be written as the sum of a base state and the linear perturbation $\boldsymbol{e} = \boldsymbol{e}_b + \boldsymbol{e}'$:

$$
\begin{aligned}
2\boldsymbol{e} = &\begin{bmatrix} 0 & \frac{\partial W_\theta}{\partial r}(1) - W_\theta(1) & \frac{\partial U_x}{\partial r}(1) \\ \frac{\partial W_\theta}{\partial r}(1) - W_\theta(1) & 0 & 0 \\ \frac{\partial U_x}{\partial r}(1) & 0 & 0 \end{bmatrix} \\
&+ \epsilon \begin{bmatrix} 2\frac{\partial v_r'}{\partial r} & \frac{\partial v_r'}{\partial \theta} + \frac{\partial w_\theta'}{\partial r} - w_\theta' & \frac{\partial v_r'}{\partial x} + \frac{\partial u_x'}{\partial r} \\ \frac{\partial v_r'}{\partial \theta} + \frac{\partial w_\theta'}{\partial r} - w_\theta' & 2\frac{\partial w_\theta'}{\partial \theta} + 2v_r' & \frac{\partial u_x'}{\partial \theta} + \frac{\partial w_\theta'}{\partial x} \\ \frac{\partial v_r'}{\partial x} + \frac{\partial u_x'}{\partial r} & \frac{\partial u_x'}{\partial \theta} + \frac{\partial w_\theta'}{\partial x} & 2\frac{\partial u_x'}{\partial x} \end{bmatrix} \\
&+ \epsilon\zeta' \begin{bmatrix} 0 & \frac{\partial^2 W_\theta}{\partial r^2}(1) - \frac{\partial W_\theta}{\partial r}(1) + W_\theta(1) & \frac{\partial^2 U_x}{\partial r^2}(1) \\ \frac{\partial^2 W_\theta}{\partial r^2}(1) - \frac{\partial W_\theta}{\partial r}(1) + W_\theta(1) & 0 & 0 \\ \frac{\partial^2 U_x}{\partial r^2}(1) & 0 & 0 \end{bmatrix}.
\end{aligned}
\tag{D.5}
$$

Using (D.1)–(D.5) leads to the linearized expressions

$$
\boldsymbol{t_x} \cdot \boldsymbol{e} \cdot \boldsymbol{n} = \frac{1}{2}\left(\frac{\partial U_x}{\partial r} + \epsilon\zeta' \frac{\partial^2 U_x}{\partial r^2}(1) + \epsilon\left(\frac{\partial v_r'}{\partial x} + \frac{\partial u_x'}{\partial r}\right)\right),
$$

$$
\boldsymbol{n} \cdot \boldsymbol{e} \cdot \boldsymbol{n} = \epsilon\left(\frac{\partial v_r'}{\partial r} - \frac{\partial \zeta'}{\partial \theta}\left(\frac{\partial W_\theta}{\partial r}(1) - W_\theta(1)\right) - \frac{\partial \zeta'}{\partial x}\frac{\partial U_x}{\partial r}(1)\right)
$$

and

$$
\boldsymbol{t_\theta} \cdot \boldsymbol{e} \cdot \boldsymbol{n} = \frac{1}{2}\left[\frac{\partial W_\theta}{\partial r}(1) - W_\theta(1) + \epsilon\zeta'\left(\frac{\partial^2 W_\theta}{\partial r^2}(1) - \frac{\partial W_\theta}{\partial r}(1) + W_\theta(1)\right) + \epsilon\left(\frac{\partial v_r'}{\partial \theta} + \frac{\partial w_\theta'}{\partial r} - w_\theta'\right)\right]
$$

and to the linearized conditions (10.11)–(10.16) at the interface necessary for the linear instability study.

D.2 Linearized equations using v_+ and v_-

Here, we write the set of linearized equations using, instead of v_r' and w_θ', the auxillary variables

$$
v_+' \equiv v_r' + \mathrm{i}w_\theta' \quad v_-' \equiv v_r' - \mathrm{i}w_\theta'. \tag{D.6}
$$

Reciprocally, one has

$$
v_r' = \frac{1}{2}(v_+' + v_-') \quad w_\theta' = \frac{\mathrm{i}}{2}(v_-' - v_+').
$$

The linearized system (10.6)–(10.9) now reads

$$\frac{\partial u_x'}{\partial x} + \frac{v_+' + v_-'}{2r} + \frac{1}{2}\left(\frac{\partial v_+'}{\partial r} + \frac{\partial v_-'}{\partial r}\right) + \mathrm{i}\frac{1}{2r}\left(\frac{\partial v_-'}{\partial \theta} - \frac{\partial v_+'}{\partial \theta}\right) = 0 \tag{D.7}$$

$$\rho\left[\frac{\partial u_x'}{\partial t} + U_x\frac{\partial u_x'}{\partial x} + \frac{(v_+' + v_-')}{2}\frac{\partial U_x}{\partial r} + \frac{W_\theta}{r}\frac{\partial u_x'}{\partial \theta}\right] = -\frac{\partial p'}{\partial x} + \frac{\mu}{Re}\nabla^2 u_x' \tag{D.8}$$

$$\begin{aligned}\rho\left[\frac{\partial v_+'}{\partial t} + U_x\frac{\partial v_+'}{\partial x} + \frac{W_\theta}{r}\frac{\partial v_+'}{\partial \theta} + \mathrm{i}\frac{W_\theta}{2r}(3v_+' - v_-') + \mathrm{i}\frac{(v_+' + v_-')}{2}\frac{\partial W_\theta}{\partial r}\right] \\ = -\frac{\partial p'}{\partial r} - \frac{\mathrm{i}}{r}\frac{\partial p'}{\partial \theta} + \frac{\mu}{Re}\left[\nabla^2 v_+' - \frac{v_+'}{r^2} + \mathrm{i}\frac{2}{r^2}\frac{\partial v_+'}{\partial \theta}\right]\end{aligned} \tag{D.9}$$

$$\begin{aligned}\rho\left[\frac{\partial v_-'}{\partial t} + U_x\frac{\partial v_-'}{\partial x} + \frac{W_\theta}{r}\frac{\partial v_-'}{\partial \theta} + \mathrm{i}\frac{W_\theta}{2r}(v_+' - 3v_-') - \mathrm{i}\frac{(v_+' + v_-')}{2}\frac{\partial W_\theta}{\partial r}\right] \\ = -\frac{\partial p'}{\partial r} + \frac{\mathrm{i}}{r}\frac{\partial p'}{\partial \theta} + \frac{\mu}{Re}\left[\nabla^2 v_-' - \frac{v_-'}{r^2} - \mathrm{i}\frac{2}{r^2}\frac{\partial v_-'}{\partial \theta}\right].\end{aligned} \tag{D.10}$$

In terms of v_+ and v_-, the boundary conditions (10.10)-(10.16) read (variables in capital letters are for $r = 1$):

$$\frac{1}{2}\left(\frac{\partial v_+'}{\partial r} + \frac{\partial v_-'}{\partial r}\right) = \frac{\partial \zeta'}{\partial t} + U_x\frac{\partial \zeta'}{\partial x} + W_\theta\frac{\partial \zeta'}{\partial \theta} \tag{D.11}$$

$$\left\langle\!\left\langle u_x' + \zeta'\frac{\partial U_x}{\partial r}\right\rangle\!\right\rangle = 0 \tag{D.12}$$

$$\langle\!\langle v_+' + v_-'\rangle\!\rangle = 0 \tag{D.13}$$

$$\left\langle\!\left\langle \mathrm{i}(v_-' - v_+') + 2\zeta'\frac{\partial W_\theta}{\partial r}\right\rangle\!\right\rangle = 0 \tag{D.14}$$

$$0 = \left\langle\!\left\langle \mu\left[2\zeta'\frac{\partial^2 U_x}{\partial r^2} + \frac{\partial v_+'}{\partial x} + \frac{\partial v_-'}{\partial x} + 2\frac{\partial u_x'}{\partial r}\right]\right\rangle\!\right\rangle \tag{D.15}$$

$$\zeta' + \frac{\partial^2 \zeta'}{\partial x^2} + \frac{\partial^2 \zeta'}{\partial \theta^2} = \left\langle\!\left\langle -p' - \rho\zeta' W_\theta^2 + \frac{\mu}{Re}\left[\frac{\partial v_+'}{\partial r} + \frac{\partial v_-'}{\partial r} - 2\frac{\partial \zeta'}{\partial \theta}\left(\frac{\partial W_\theta}{\partial r} - W_\theta\right) - 2\frac{\partial \zeta'}{\partial x}\frac{\partial U_x}{\partial r}\right]\right\rangle\!\right\rangle \tag{D.16}$$

$$0 = \left\langle\!\left\langle \mu\left[2\zeta'\left(\frac{\partial^2 W_\theta}{\partial r^2} - \frac{\partial W_\theta}{\partial r} + W_\theta\right) + \frac{\partial v_+'}{\partial \theta} + \frac{\partial v_-'}{\partial \theta} + \mathrm{i}\frac{\partial v_-'}{\partial r} - \mathrm{i}\frac{\partial v_+'}{\partial r} - \mathrm{i}v_-' + \mathrm{i}v_+'\right]\right\rangle\!\right\rangle. \tag{D.17}$$

D.3 Linearized system for $m = 0$ in fluid (1)

The linearized system of equations is given in the main text only for $m \geq 1$ (see 10.23). For axisymmetric modes ($m = 0$), the change of variables (10.22) done for fluid (1) becomes

$$F(r) = f(r), \quad G_+(r) = rg_+(r), \quad G_-(r) = rg_-(r), \quad P(r) = p(r) \tag{D.18}$$

where f, g_+, g_- and p are even functions of r. Introducing (D.18) into (10.20) leads to the linearized equation system valid for $m = 0$ only, involving only even terms:

$$
\begin{aligned}
&\mathrm{i}kf + (g_+ + g_-) + \frac{r^2}{2}\left(\frac{g_+'}{r} + \frac{g_-'}{r}\right) = 0 \\
&\rho^{(1)}\left[(-\mathrm{i}\omega + \mathrm{i}kU_x)f + r^2\frac{(g_+ + g_-)}{2}\frac{U_x'}{r}\right] + \mathrm{i}kp - \frac{\mu^{(1)}}{Re}\left(f'' + \frac{f'}{r} - k^2 f\right) = 0 \\
&\rho^{(1)}\left[(-\mathrm{i}\omega + \mathrm{i}kU_x)g_+ + \frac{\mathrm{i}}{2}(3\frac{W_\theta}{r} + W_\theta')g_+ + \frac{\mathrm{i}}{2}(-\frac{W_\theta}{r} + W_\theta')g_-\right] \\
&\qquad + \frac{p'}{r} - \frac{\mu^{(1)}}{Re}\left(g_+'' + 3\frac{g_+'}{r} - k^2 g_+\right) = 0 \\
&\rho^{(1)}\left[(-\mathrm{i}\omega + \mathrm{i}kU_x)g_- + \frac{\mathrm{i}}{2}(\frac{W_\theta}{r} - W_\theta')g_+ - \frac{\mathrm{i}}{2}(3\frac{W_\theta}{r} + W_\theta')g_-\right] \\
&\qquad + \frac{p'}{r} - \frac{\mu^{(1)}}{Re}\left(g_-'' + 3\frac{g_-'}{r} - k^2 g_-\right) = 0\,.
\end{aligned}
\tag{D.19}
$$

D.4 Linearized system for $m \leq -1$ in fluid (1)

The linearized system of equations is given in the main text only for $m \geq 1$ (see 10.23). For $m \leq -1$, one gets in fluid (1)

$$
\begin{aligned}
&\mathrm{i}kf + \frac{1}{2}\frac{g_+'}{r} + (-m+1)g_- + \frac{r^2}{2}\frac{g_-'}{r} = 0 \\
&\rho^{(1)}\left[(-\mathrm{i}\omega + \mathrm{i}X)f + \frac{1}{2}\frac{U_x'}{r}g_+ + \frac{r^2}{2}\frac{U_x'}{r}g_-\right] + \mathrm{i}kp - \frac{\mu^{(1)}}{Re}\left[f'' + (-2m+1)\frac{f'}{r} - k^2 f\right] = 0 \\
&\rho^{(1)}\left[(-\mathrm{i}\omega + \mathrm{i}X)g_+ + \frac{\mathrm{i}}{2}\left(3\Omega + W_\theta'\right)g_+ - \frac{\mathrm{i}}{2}r^4 Y g_-\right] - 2mp + r^2\frac{p'}{r} - \frac{\mu^{(1)}}{Re}\left[g_+'' + (-2m-1)\frac{g_+'}{r} - k^2 g_+\right] = 0 \\
&\rho^{(1)}\left[(-\mathrm{i}\omega + \mathrm{i}X)g_- - \frac{\mathrm{i}}{2}\left(3\Omega + W_\theta'\right)g_- + \frac{\mathrm{i}}{2}Y g_+\right] + \frac{p'}{r} - \frac{\mu^{(1)}}{Re}\left[g_-'' + (-2m+3)\frac{g_-'}{r} - k^2 g_-\right] = 0\,.
\end{aligned}
\tag{D.20}
$$

D.5 Symmetry of the linearized equations

The following transform

$$
\begin{aligned}
k &\to k \\
m &\to -m \\
F &\to F \\
G+ &\to G_- \\
G_- &\to G+ \\
W_\theta &\to -W_\theta \\
P &\to P
\end{aligned}
$$

leaves the system unchanged if no axial velocity is present. This remark is used to test the validity of the part of the code relative to $m \leq -1$ using the part of the code relative to $m \geq 1$.

Appendix E

Appendix: Differentiation by the Chebychev-collocation method

Contents

In this appendix, the explicit formulas of the matrices $\boldsymbol{A}^r$, $\boldsymbol{A}^*$, $\boldsymbol{B}^r$ and $\boldsymbol{B}^*$ used for first and second differentiation are given. We deal first with arbitrary functions (fluid 2), then with even functions (fluid 1 around the axis).

E.1 Chebychev-collocation method: arbitrary function

One wishes to express the first and second derivative of an arbitrary function Q defined at points $r_i = R(\xi_i)$ where ξ_i are the Gauss-Lobatto points in $[-1;1]$ and R a mapping function. If function ξ designates the reciprocal function of the mapping function ($\xi_i = \xi(r_i)$), then, using the chain rule:

$$Q'(r) = \frac{dQ}{d\xi}\xi'(r) \tag{E.1}$$

$$Q''(r) = \frac{d^2Q}{d\xi^2}\xi'^2(r) + \frac{dQ}{d\xi}\xi''(r). \tag{E.2}$$

The derivative of Q with respect to ξ can be approximated using the Chebychev-collocation method [Canuto et al., 2012]:

$$\frac{dQ}{d\xi}(\xi_i) \approx \sum_{j=0}^{2N} A^*_{ij} Q\left(\xi_j\right), \quad i = 0, 1, \cdots, 2N \tag{E.3}$$

where ξ_i are the $2N+1$ Gauss-Lobatto points

$$\xi_i = \cos\left(\frac{i\pi}{2N}\right), \quad i = 0, 1, \cdots, 2N$$

and matrix $\boldsymbol{A}^*$ is defined by:

$$A^*_{ij} \equiv \begin{cases} \frac{c_i(-1)^{i+j}}{c_j\left(\xi_i - \xi_j\right)} & i \neq j \\ \frac{-\xi_i}{2\left(1-\xi_i^2\right)} & 1 \leq i = j \leq 2N-1 \\ \frac{2(2N)^2+1}{6} & i = j = 0 \\ -\frac{2(2N)^2+1}{6} & i = j = 2N \end{cases}, \quad \text{with } c_i = \begin{cases} 2 & \text{if } i = 0 \text{ or } 2N \\ 1 & \text{otherwise} \end{cases}.$$

The second derivative is given by

$$\frac{d^2Q}{d\xi^2}(\xi_i) \approx \sum_{j=0}^{2N} B^*_{ij} Q\left(\xi_j\right) \quad \text{with} \quad B^*_{ij} \equiv \sum_{k=0}^{2N} A^*_{ik} A^*_{kj}. \tag{E.4}$$

The derivatives of Q with respect to r are then deduced by (10.37). This is used for peripheral fluid (2).

E.2 Chebychev-collocation method: even function

For the inner fluid (1), the equations are written using only even terms. If Q is even in $[-1;1]$, one has the symmetry relation $Q_i = Q_{2N-i}$. Let q be the restriction of Q on $[0;1]$. Using only the $N+1$ positive Gauss-Lobatto points

$$\xi_i = \cos\left(\frac{i\pi}{2N}\right), \quad i = 0, 1, \cdots, N,$$

the derivative of q can be written at these points as:

$$\frac{dq}{d\xi}(\xi_i) = \sum_{j=0}^{2N} A^*_{ij} Q_j \tag{E.5}$$

$$= \sum_{j=0}^{N-1} A^*_{ij} Q_j + A^*_{iN} Q_N + \sum_{j=N+1}^{2N} A^*_{ij} Q_j \tag{E.6}$$

$$= \sum_{j=0}^{N-1} \left(A^*_{ij} + A^*_{i,2N-j}\right) q_j + A^*_{iN} q_N \tag{E.7}$$

Thus the first derivative of q is such that

$$q'(\xi_i) \approx \sum_{j=0}^{N} A^e_{ij} q_j \quad \begin{cases} A^e_{ij} \equiv A^*_{ij} + A^*_{i,2N-j} & (j = 0, \cdots, N-1) \\ A^e_{iN} \equiv A^*_{iN} \end{cases} \tag{E.8}$$

and the second derivative can expressed as:

$$q''(\xi_i) \approx \sum_{j=0}^{N} B^e_{ij} q_j \quad \begin{cases} B^e_{ij} \equiv B^*_{ij} + B^*_{i,2N-j} & (j = 0, \cdots, N-1) \\ B^e_{iN} \equiv B^*_{iN} \end{cases} . \tag{E.9}$$

A last step is needed since only even terms are used, we have to express the ratio $q'(\xi_j)/\xi_j$, rather than $q'(\xi_j)$ which is odd. Eventually one has (formulas (10.36) in main text)

$$\frac{q'(\xi_i)}{\xi_i} \approx \sum_{j=0}^{N_1} A^r_{ij} q_j \,, \quad q''(\xi_i) \approx \sum_{j=0}^{N_1} B^r_{ij} q_j \,, \tag{E.10}$$

with

$$A^r_{ij} \equiv \begin{cases} \dfrac{A^e_{ij}}{\xi_i} & \text{if } \xi_i \neq 0 \;\; (i = 0, \cdots, N-1) \\ B^e_{ij} & \text{if } \xi_i = 0 \;\; (i = N) \end{cases} \tag{E.11}$$

$$B^r_{ij} \equiv B^e_{ij} \,. \tag{E.12}$$

Appendix F

Appendix: Conditions at the outer boundary $r = R_{\text{ext}}$

Contents

If vorticity perturbation remains localized in a region around the vortex axis, the perturbation velocity field becomes potential at large r that is $\boldsymbol{u}' = \boldsymbol{\nabla}\Phi'$. Incompressibility imposes that Φ' satisfies the Laplace equation

$$\boldsymbol{\nabla} \cdot (\boldsymbol{\nabla}\Phi') = \mathbf{0}. \tag{F.1}$$

In turn, this implies that viscous terms vanish at large r since

$$\Delta \boldsymbol{u}' = \Delta(\boldsymbol{\nabla}\Phi') = \boldsymbol{\nabla}(\Delta\Phi') = \mathbf{0}. \tag{F.2}$$

and perturbations thus satisfy:

$$\rho\left(\frac{\partial u_x'}{\partial t} + \Omega^B \frac{\partial u_x'}{\partial \theta}\right) = -\frac{\partial p'}{\partial x}, \tag{F.3}$$

$$\rho\left(\frac{\partial v_r'}{\partial t} + \Omega^B \frac{\partial v_r'}{\partial \theta} - 2\Omega^B w_\theta'\right) = -\frac{\partial p'}{\partial r}, \tag{F.4}$$

$$\rho\left(\frac{\partial w_\theta'}{\partial t} + \Omega^B \frac{\partial w_\theta'}{\partial \theta}\right) = -\frac{1}{r}\frac{\partial p'}{\partial \theta}. \tag{F.5}$$

with Ω^B the angular velocity of base flow

$$\Omega^B \equiv \frac{\Gamma}{2\pi r^2},$$

Γ being the total circulation. For normal modes, the perturbation potential, velocity and pressure take the form:

$$\Phi' = e^{\mathrm{i}(kx+m\theta-\omega t)}\Phi^{(m)}(r), \tag{F.6}$$

$$\boldsymbol{u}' = e^{\mathrm{i}(kx+m\theta-\omega t)}\boldsymbol{u}^{(m)}(r), \tag{F.7}$$

$$p' = e^{\mathrm{i}(kx+m\theta-\omega t)}p^{(m)}(r). \tag{F.8}$$

Under the potential flow condition, a Robin condition (mixed boundary condition) is imposed on the above quantities at $r = R_{\text{ext}}$

$$\boxed{\frac{\partial v_r^{(m)}}{\partial r} = C_r^{(m)} v_r^{(m)}, \quad \frac{\partial v_\theta^{(m)}}{\partial r} = C_\theta^{(m)} v_\theta^{(m)}, \quad \frac{\partial v_x^{(m)}}{\partial r} = C_x^{(m)} v_x^{(m)}}, \tag{F.9}$$

$$\boxed{\frac{\partial \Phi^{(m)}}{\partial r} = C_\Phi^{(m)}\Phi^{(m)}, \quad \frac{\partial p^{(m)}}{\partial r} = C_p^{(m)} p^{(m)},} \tag{F.10}$$

where $C_r^{(m)}, C_\theta^{(m)}, C_x^{(m)}$ and $C_\Phi^{(m)}, C_p^{(m)}$ are constants to be determined in each case.

Since Φ' satisfies Laplace equation, relation (F.6) implies that

$$\frac{\partial^2\Phi^{(m)}}{\partial r^2} + \frac{1}{r}\frac{\partial\Phi^{(m)}}{\partial r} - (k^2 + \frac{|m|^2}{r^2})\Phi^{(m)} = 0. \tag{F.11}$$

F.1 Conditions for $k \neq 0$

In the following we introduce the notations

$$\hat{r} \equiv |k|r \quad \text{and} \quad \hat{R}_{ext} = |k|R_{\text{ext}}.$$

F.1.1 Conditions on potential Φ

Relation (F.11) implies that

$$\frac{\partial^2\Phi^{(m)}}{\partial \hat{r}^2} + \frac{1}{\hat{r}}\frac{\partial\Phi^{(m)}}{\partial \hat{r}} - (1 + \frac{|m|^2}{\hat{r}^2})\Phi^{(m)} = 0. \tag{F.12}$$

The general solution of the above equation is of the sum

$$\Phi^{(m)}(r) = A\, I_{|m|}(\hat{r}) + B\, K_{|m|}(\hat{r}),$$

where $I_{|m|}(\hat{r})$ denotes the modified Bessel function of first kind and $K_{|m|}(\hat{r})$ the modified Bessel function of second kind [Abramowitz and Stegun, 1964]. Since $I_{|m|}$ diverges as $\hat{r} \to +\infty$, A must vanish. One

introduces this condition in the code by enforcing a Robin condition at the outer boundary $r = R_{\text{ext}}$

$$\boxed{C_\Phi^{(m)} \equiv |k| H_{|m|}(|k| R_{\text{ext}}),} \tag{F.13}$$

where $H_{|m|}$ is defined by equation (C.1).

F.1.2 Condition on the pressure perturbation

Equations (F.3)–(F.4) lead to three equations

$$\mathrm{i}\rho\left(\varpi - m\Omega^B\right)\Phi^{(m)} = p^{(m)}, \tag{F.14}$$

$$\mathrm{i}\rho\left(|k| H(\varpi - m\Omega^B) - 2\frac{m\Omega^B}{r}\right)\Phi^{(m)} = \frac{\partial p^{(m)}}{\partial r}, \tag{F.15}$$

$$\mathrm{i}\rho\left(\frac{m}{r}(\varpi - m\Omega^B)\right)\Phi^{(m)} = \frac{m}{r}p^{(m)}. \tag{F.16}$$

which are equivalent providing the pressure condition at $r = R_{\text{ext}}$:

$$\boxed{C_p^{(m)} \equiv C_\Phi^{(m)} + \frac{2m}{R_{\text{ext}}\left(m - 2\frac{\varpi}{\Omega^B(R_{\text{ext}})}\right)}.} \tag{F.17}$$

F.1.3 Condition on axial velocity

Since the axial velocity v_x' satisfies $v_x' = \partial\Phi/\partial x$, equations (F.6)–(F.7) imply that $v_x^{(m)} = \mathrm{i}k\Phi^{(m)}$. The boundary condition for $v_x^{(m)}(r)$ is thus the same as for the potential:

$$\boxed{C_x^{(m)} \equiv C_\Phi^{(m)}.} \tag{F.18}$$

F.1.4 Condition on radial velocity

Since the radial velocity v_r' satisfies $v_r' = \partial\Phi/\partial r$, one has

$$v_r^{(m)}(r) = |k| H_{|m|}(\hat{r})\Phi^{(m)}(r).$$

The mixed boundary condition for $v_r^{(m)}$ reads:

$$\frac{\partial v_r^{(m)}}{\partial r} = |k| H_{|m|}(\hat{r})\frac{\partial\Phi^{(m)}}{\partial r} + |k|\frac{\partial H_{|m|}}{\partial \hat{r}}\frac{v_r^{(m)}}{H_{|m|}(\hat{r})} \tag{F.19}$$

$$\frac{\partial v_r^{(m)}}{\partial r} = |k| H_{|m|}(\hat{r}) v_r^{(m)} + |k|^2 \frac{\partial H_{|m|}}{\partial \hat{r}} \frac{v_r^{(m)}}{|k| H_{|m|}(\hat{r})} \tag{F.20}$$

This yields

$$\frac{\partial v_r^{(m)}}{\partial r} = |k| \left(H_{|m|}(\hat{r}) + \frac{1}{H_{|m|}(\hat{r})} \frac{\partial H_{|m|}}{\partial \hat{r}} \right) v_r^{(m)}, \tag{F.21}$$

The following property [Abramowitz and Stegun, 1964]

$$H_{|m|} + \frac{1}{H_{|m|}} \frac{\partial H_{|m|}(\hat{r})}{\partial \hat{r}} = \frac{(1 + \frac{|m|^2}{\hat{r}^2})}{H_{|m|}} - \frac{1}{\hat{r}}.$$

finally yields at $r = R_{\text{ext}}$,

$$\boxed{C_r^{(m)} \equiv \frac{k^2 + \frac{|m|^2}{(R_{\text{ext}})^2}}{|k| H_{|m|}} - \frac{1}{R_{\text{ext}}} = \frac{k^2 + \frac{|m|^2}{(R_{\text{ext}})^2}}{C_\Phi^{(m)}} - \frac{1}{R_{\text{ext}}}.} \tag{F.22}$$

F.1.5 Condition on azimuthal velocity

Since the azimuthal velocity perturbation satisfies $w'_\theta = (1/r)\partial\Phi'/\partial\theta$, one has

$$w_\theta^{(m)}(r) = \frac{\mathrm{i} m \Phi^{(m)}}{r}.$$

The mixed boundary condition for $w_\theta^{(m)}$ at $r = R_{\text{ext}}$ reads:

$$\boxed{C_\theta^{(m)} \equiv C_\Phi^{(m)} - \frac{1}{R_{\text{ext}}}.} \tag{F.23}$$

F.1.6 Condition on auxilliary variables (v_+, v_-)

We have introduced the velocity components (v'_+, v'_-):

$$v'_+ = v'_r + \mathrm{i} w'_\theta, \quad v'_- = v'_r - \mathrm{i} w'_\theta, \tag{F.24}$$

or reciprocally

$$v'_r = \frac{1}{2}(v'_+ + v'_-), \quad w'_\theta = \frac{1}{2\mathrm{i}}(v'_+ - v'_-). \tag{F.25}$$

One assumes

$$v'_+ = e^{\mathrm{i}(kx+m\theta-\omega t)} v_+^{(m)}(r)$$
$$v'_- = e^{\mathrm{i}(kx+m\theta-\omega t)} v_-^{(m)}(r).$$

Then it is possible to derive boundary conditions for v_+ and v_- since

$$\frac{\partial v_\pm^{(m)}}{\partial r} = \frac{\partial v_r^{(m)}}{\partial r} \pm \mathrm{i} \frac{\partial w_\theta^{(m)}}{\partial r}$$

At $r = R_{\text{ext}}$, one gets

$$\frac{\partial v_\pm^{(m)}}{\partial r} = \frac{\partial v_r^{(m)}}{\partial r} \pm \mathrm{i} \frac{\partial w_\theta^{(m)}}{\partial r} = C_r^{(m)} v_r^{(m)} \pm \mathrm{i} C_\theta^{(m)} w_\theta^{(m)} = C_r^{(m)} \frac{v_+^{(m)} + v_-^{(m)}}{2} \pm \mathrm{i} C_\theta^{(m)} \frac{v_+^{(m)} - v_-^{(m)}}{2\mathrm{i}}$$

$$\boxed{\frac{\partial v_+^{(m)}}{\partial r} = \frac{C_r^{(m)} + C_\theta^{(m)}}{2} v_+^{(m)} + \frac{C_r^{(m)} - C_\theta^{(m)}}{2} v_-^{(m)}} \tag{F.26}$$

$$\boxed{\frac{\partial v_-^{(m)}}{\partial r} = \frac{C_r^{(m)} - C_\theta^{(m)}}{2} v_+^{(m)} + \frac{C_r^{(m)} + C_\theta^{(m)}}{2} v_-^{(m)},} \tag{F.27}$$

The expressions for $H_{|m|}$ are given in Appendix C.

F.2 Conditions for $k = 0$

The case $k = 0$ and $m = 0$ is not pertinent as a perturbation. The case $k = 0$ and $m \neq 0$ is treated below. Variables read

$$\Phi' = e^{\mathrm{i}(m\theta-\omega t)} \Phi^{(m)}(r), \tag{F.28}$$
$$\boldsymbol{u}' = e^{\mathrm{i}(m\theta-\omega t)} \boldsymbol{u}^{(m)}(r), \tag{F.29}$$
$$p' = e^{\mathrm{i}(m\theta-\omega t)} p^{(m)}(r). \tag{F.30}$$

so that the amplitude of the potential $\Phi^{(m)}(r)$ satisfies

$$\frac{\mathrm{d}^2\Phi^{(m)}}{\mathrm{d}r^2} + \frac{1}{r}\frac{\mathrm{d}\Phi^{(m)}}{\mathrm{d}r} - \frac{m^2}{r^2}\Phi^{(m)} = 0. \tag{F.31}$$

If $m \neq 0$, the general solution to (F.31) reads

$$\Phi^{(m)}(r) = A r^{|m|} + B r^{-|m|}. \tag{F.32}$$

one imposes $A = 0$ to avoid the divergence of the solution as $r \to +\infty$.

$$\boxed{C_{\Phi}^{(m)} \equiv -\frac{|m|}{R_{ext}},} \tag{F.33}$$

Concerning axial velocity perturbation $u_x' = \partial\Phi'/\partial x$, one deduces

$$\boxed{u_x^{(m)} = 0}.$$

Concerning on radial velocity perturbation $v_r^{(m)}(r) = -\frac{|m|}{r}\Phi^{(m)}(r)$, condition at $r = R_{\text{ext}}$ imposes

$$\boxed{C_r^{(m)} \equiv -\frac{|m|+1}{R_{\text{ext}}}.} \tag{F.34}$$

Concerning azimuthal velocity, $w_\theta^{(m)}(r) = \frac{\mathrm{i}m\Phi^{(m)}(r)}{r}$ the condition at $r = R_{\text{ext}}$ reads

$$\boxed{C_\theta^{(m)} \equiv -\frac{|m|+1}{R_{\text{ext}}}.} \tag{F.35}$$

Finally, the constants for the auxilliary velocity components $v_\pm^{(m)}$ reads

$$\begin{cases} \frac{1}{2}(C_r^{(m)} + C_\theta^{(m)}) = -\dfrac{|m|+1}{R_{\text{ext}}} \\ \frac{1}{2}(C_r^{(m)} - C_\theta^{(m)}) = 0 \end{cases}. \tag{F.36}$$

Appendix G

Convergence study for Basilisk

This work was performed under the guidance of my supervisor Daniel Fuster.

The accuracy of the code was estimated with the classic Rayleigh-Plateau instability of a liquid jet at rest with $Oh = 0.001$. The ambient liquid is set to be gas ($\rho_2/\rho_1 = \mu_2/\mu_1 = 10^{-3}$) with dimensionless wavenumber $\bar{k} = 2\pi/9 \sim 0.7$. The differences between simulation results and theoretical values can be attributed to two main sources of error:

1. We use the symbols $\xi_{\Delta\bar{x}}$ to denote the errors related to the dimensionless mesh size $\Delta\bar{x} = \frac{\Delta x}{\lambda}$ (with $\Delta x = \lambda/N$), controls the spatial discretization errors.
2. We use the symbol $\xi_{\bar{\lambda}_0}$ to denote the difference between analytic and numerical predictions controlled by the finite size of the domain $\bar{\lambda}_0$.
3. We use the symbol $\xi_{\epsilon t}$ to denote the difference between analytic and numerical predictions due to the finite amplitude of the initial perturbation.

The impact of mesh size and the border effect are first studied with constant regular meshes. We vary the number of discretization points in one spatial period $N = \lambda/\Delta x$, form 32 to 1024, and the simulation domain λ_0 from λ to 5 λ. We calculate the convergence speed with the offset between the discrete solution f and the exact solution f_h for arbitrary variable f. As the scheme we use here is centered, the error should converge at order 2.

$$\xi_{\Delta\bar{x}} = \left|\frac{f_h - f}{f_h}\right| \sim \left(\frac{\Delta x}{\lambda}\right)^2 \tag{G.1}$$

In figure G.1 (right) we find that for $\frac{\lambda}{\Delta x} > 64$, the error almost converges at order 2, while for smaller $\frac{\lambda}{\Delta x}$ it converges at order between 1 and 2. Here we estimate that the offset between the results and the converged

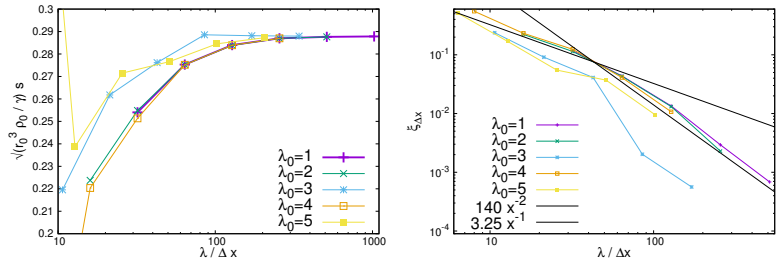

Figure G.1 – The growthrate $\bar{s}$ (left) and the error $\xi_{\Delta x}$ (right) as a function of $\lambda/\Delta x$. With $Oh = 0.001$, initial perturbation $\epsilon = 0.01$ and simulation domain $\bar{\lambda}_0 \in [1, 2, 3, 4, 5]$.

value due to the size of grid can be fitted according to the following empiric formula:

$$\xi(\frac{\Delta x}{\lambda}) \simeq 140\left(\frac{\Delta x}{\lambda}\right)^2 \quad for \quad \frac{\lambda}{\Delta x} \gtrsim 44 \tag{G.2}$$

In figure G.1 (left) we look at the influence of $\bar{\lambda}_0 = [1, 2, 4]$, We see that the error is mainly controlled by the grid size, $\frac{\lambda}{\Delta x}$, thus we conclude that there is no border effect for $\bar{\lambda}_0 \geq 1$.

Then the influence of initial perturbation amplitude ϵ is discussed in Figure G.2. The results are obtained by first keeping the mesh size constant and varying ϵ from order $O(10^{-4})$ to $O(10^{-1})$, and then repeating the same protocol for different resolution levels. As expected, we find that there is a competition between

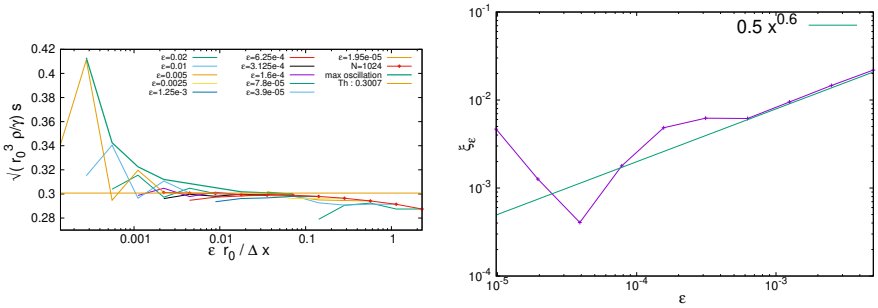

Figure G.2 – (left) The growthrate $\sqrt{\frac{r_0^3\rho}{\gamma}}s$ as a function of $\frac{\epsilon r_0}{\Delta x}$ for different ϵ present by fine lines. Three bold lines: the maximum oscillation values (Green), the analytic growthrate(Yellow), and the convergence results for different ϵ (Red). With $Oh = 0.001$, $\bar{\lambda}_0 = 1$. (right) The error ξ_ϵ as a function of ϵ. With viscosity $Oh = 0.001$, $N = 1024$ and simulation domain $\bar{\lambda}_0 = 1$

the grid resolution and the optimal perturbation amplitude. For very small values of $\epsilon r_0/\Delta x$ we find that the growthrates obtained oscillate due to the poor resolution of the initial perturbation amplitude. In the mean time, there is a limit on the maximum values of ϵ that can be used, as the condition $\epsilon \ll 1$ has to be respected. In figure G.2 left, we see that for $\epsilon \geq 0.1$ the errors induced by the finite size of the initial amplitude are significant. We then conclude that to obtain accurate results we need a nondimensional amplitude that satisfies $0.005\frac{\Delta x}{r_0} < \epsilon < 0.1$. In figure G.2 right we plot the relative error as a function of ϵ.

The offset between analytic and numerical values due to the presence of initial perturbation amplitude can be fitted according to the following empiric formula

$$\xi_{\epsilon t} = \xi_{\epsilon}(\epsilon) \simeq 0.5\,\epsilon^{0.6} \tag{G.3}$$

provided that condition $0.001\frac{\Delta x}{r_0} < \epsilon < 0.1$ is satisfied. Thus, if we choose the minimum ϵ for which we obtain acceptable results, $\epsilon = 0.01\frac{\Delta x}{r_0}$, the error scales as

$$\xi_{\epsilon t} = \xi_{\epsilon}(\epsilon) \simeq 0.0315\left(\frac{\Delta x}{r_0}\right)^{0.2} \tag{G.4}$$

We conclude that for a given grid size and finite amplitude of the perturbation $\epsilon = 0.01\frac{\Delta x}{r_0}$, we can obtain the accuracy of the numerical predictions by the empirical formula:

$$\begin{aligned}
&\xi_{tot}\left(\xi_{\Delta\bar{x}}, \xi_{cfl}, \xi_{\epsilon t}, \xi_{\bar{\lambda}_0}\right) \simeq \xi_{tot}\left(\xi_{\Delta\bar{x}}, \xi_{\epsilon}\right) \\
&\xi_{tot} = \sqrt{\xi_{\Delta\bar{x}}^2 + \xi_{\epsilon}^2} = \sqrt{140^2\left(\frac{\Delta x}{\lambda}\right)^4 + 0.0315^2\left(\frac{\Delta x}{r_0}\right)^{0.4}}
\end{aligned} \tag{G.5}$$

Based on these analyses we calculate the dispersion relation for a classical Rayleigh-Plateau instability of a cylindrical liquid jet at rest. As shown in figure G.3, the DNS results obtained fitted well with the analytic solutions. While the error bar is added, all the values obtained by Basilisk are located inside the the empirical formula G.5 of error prediction.

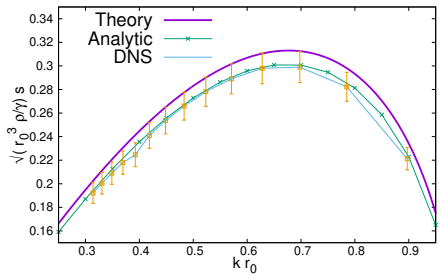

Figure G.3 – the comparison between inviscid theory (line purple), the analytic viscous solution (points line green) and DNS results (line blue) for the dispersion relation of $\bar{s}$ and $\bar{k}$, with N =128, $\epsilon = 0.05\frac{\lambda\Delta x}{r_0}$.

Bibliography

[Abramowitz and Stegun, 1964] Abramowitz, M. and Stegun, I. A. (1964). *Handbook of Mathematical Functions with Formulas, Graphs, and Mathematical Tables*. Mathmatica, New York, ninth dover printing, tenth gpo printing edition.

[Afkhami et al., 2009] Afkhami, S., Zaleski, S., and Bussmann, M. (2009). A mesh-dependent model for applying dynamic contact angles to vof simulations. *Journal of computational physics*, 228(15):5370–5389.

[Ahmed et al., 2020] Ahmed, S., Croaker, P., and Doolan, C. J. (2020). On the instability mechanisms of ship propeller wakes. *Ocean Engineering*, 213:107609.

[Ali and Abid, 2014] Ali, M. and Abid, M. (2014). Self-similar behaviour of a rotor wake vortex core. *Journal of Fluid Mechanics*, 740:R1.

[Batchelor, 1964] Batchelor, G. K. (1964). Axial flow in trailing line vortices. *J. Fluid Mech.*, 20:645–658.

[Batchelor, 1967] Batchelor, G. K. (1967). *An Introduction to Fluid Dynamics*. Cambridge University Press.

[Batchelor, 2000] Batchelor, G. K. (2000). *An Introduction to Fluid Dynamics*. Cambridge Mathematical Library. Cambridge University Press.

[Bayly, 1986] Bayly, B. J. (1986). Three-dimensional instability of elliptical flow. *Physical review letters*, 57(17):2160.

[Bernoff and Lingevitch, 1994] Bernoff, A. J. and Lingevitch, J. F. (1994). Rapid relaxation of an axisymmetric vortex. *Phys. Fluids*, 6(11):3717–3723.

[Blanco-Rodríguez et al., 2015] Blanco-Rodríguez, F. J., Le Dizès, S., Selçuk, C., Delbende, I., and Rossi, M. (2015). Internal structure of vortex rings and helical vortices. *J. Fluid Mech.*, 785:219–247.

[Blanco-Rodríguez and Le Dizès, 2016] Blanco-Rodríguez, F. J. and Le Dizès, S. (2016). Elliptic instability of a curved batchelor vortex. *J. Fluid Mech.*, 804:224–247.

[Blanco-Rodríguez and Le Dizès, 2017] Blanco-Rodríguez, F. J. and Le Dizès, S. (2017). Curvature instability of a curved batchelor vortex. *J. Fluid Mech.*, 814:397–415.

[Bolnot, 2012] Bolnot, H. (2012). *Instabilités des tourbillons hélicoïdaux: application au sillage des rotors*. PhD thesis, Aix-Marseille.

[Brancher et al., 1994] Brancher, P., Chomaz, J.-M., and Huerre, P. (1994). Direct numerical simulations of round jets: Vortex induction and side jets. *Phys. Fluids*, 6(5):1768–1774.

[Brennen, 2005] Brennen, C. E. (2005). *Fundamentals of Multiphase Flow*. Cambridge University Press.

[Brynjell-Rahkola and Henningson, 2020] Brynjell-Rahkola, M. and Henningson, D. S. (2020). Numerical realization of helical vortices: application to vortex instability. *Theoret. Comput. Fluid Dynamics*, 34:1–20.

[Callegari and Ting, 1978] Callegari, A. J. and Ting, L. (1978). Motion of a curved vortex filament with decaying vortical core and axial velocity. *SIAM J. Appl. Math.*, 35(1):148–175.

[Canuto et al., 2012] Canuto, C., Hussaini, M. Y., Quarteroni, A., Thomas Jr, A., et al. (2012). *Spectral methods in fluid dynamics*. Springer Science & Business Media.

[Cheng et al., 2010] Cheng, M., Lou, J., and Lim, T. T. (2010). Vortex ring with swirl: A numerical study. *Phys. Fluids*, 22(9):097101.

[Cruz-Roldán et al., 2002] Cruz-Roldán, F., Amo-López, P., Maldonado-Bascón, S., and Lawson, S. S. (2002). An efficient and simple method for designing prototype filters for cosine-modulated pseudo-qmf banks. *IEEE signal processing letters*, 9(1):29–31.

[De Gennes et al., 2004] De Gennes, P.-G., Brochard-Wyart, F., Quéré, D., et al. (2004). *Capillarity and wetting phenomena: drops, bubbles, pearls, waves*, volume 336. Springer.

[Delbende et al., 2012a] Delbende, I., Rossi, M., and Daube, O. (2012a). DNS of flows with helical symmetry. *Theoret. Comput. Fluid Dynamics*, 26(1):141–160.

[Delbende et al., 2012b] Delbende, I., Rossi, M., and Piton, B. (2012b). Direct numerical simulation of helical vortices. *International Journal of Engineering Systems Modelling and Simulation 46*, 4(1-2):94–101.

[Eggers and Villermaux, 2008] Eggers, J. and Villermaux, E. (2008). Physics of liquid jets. *Reports on Progress in Physics*, 71:16–18.

[enseeiht, 2013] enseeiht (2013). Sujets de stages et de projets en licence 3 physique à bordeaux collège sciences et technologies. http://hmf.enseeiht.fr/travaux/beiepe/book/export/html/114.

[FABRE and JACQUIN, 2004] FABRE, D. and JACQUIN, L. (2004). Viscous instabilities in trailing vortices at large swirl numbers. *Journal of Fluid Mechanics*, 500:239–262.

[Felli et al., 2011] Felli, M., Camussi, R., and Di Felice, F. (2011). Mechanisms of evolution of the propeller wake in the transition and far fields. *Journal of Fluid Mechanics*, 682:5–53.

[Fukumoto and Hattori, 2005] Fukumoto, Y. and Hattori, Y. (2005). Curvature instability of a vortex ring. *Journal of Fluid Mechanics*, 526:77–115.

[Fukumoto and Miyazaki, 1991] Fukumoto, Y. and Miyazaki, T. (1991). Three-dimensional distortions of a vortex filament with axial velocity. *J. Fluid Mech.*, 222:369–416.

[Fukumoto and Moffatt, 2000] Fukumoto, Y. and Moffatt, H. K. (2000). Motion and expansion of a viscous vortex ring. Part 1. A higher-order asymptotic formula for the velocity. *J. Fluid Mech.*, 417:1–45.

[Fukumoto and Okulov, 2005] Fukumoto, Y. and Okulov, V. L. (2005). The velocity field induced by a helical vortex tube. *Phys. Fluids*, 17(10):107101.

[Gallaire and Chomaz, 2003] Gallaire, F. c. and Chomaz, J.-M. (2003). Mode selection in swirling jet experiments: a linear stability analysis. *Journal of Fluid Mechanics*, 494:223–253.

[Gharib et al., 1998] Gharib, M., Rambod, E., and Shariff, K. (1998). A universal time scale for vortex ring formation. *Journal of Fluid Mechanics*, 360.

[Gillis and Kaufman, 1962] Gillis, J. and Kaufman, B. (1962). The stability of a rotating viscous jet. *Quarterly of Applied Mathematics*, 19(4):301–308.

[Gupta and Loewy, 1974] Gupta, B. and Loewy, R. (1974). Theoretical analysis of the aerodynamic stability of multiple, interdigitated helical vortices. *AIAA journal*, 12(10):1381–1387.

[Hall, 1972] Hall, M. (1972). Vortex breakdown. *Annual review of fluid mechanics*, 4(1):195–218.

[Hand et al., 2001] Hand, M. M., Simms, D. A., Fingersh, L. J., Jager, D. W., Cotrell, J. R., Schreck, S., and Larwood, S. M. (2001). Unsteady aerodynamics experiment phase vi: Wind tunnel test configurations and available data campaigns. *United States osti gov*.

[Hardin, 1982] Hardin, J. C. (1982). The velocity field induced by a helical vortex filament. *The Physics of Fluids*, 25(11):1949–1952.

[Hattori et al., 2019] Hattori, Y., Blanco-Rodríguez, F. J., and Le Dizès, S. (2019). Numerical stability analysis of a vortex ring with swirl. *Journal of Fluid Mechanics*, 878:5–36.

[Hattori and Fukumoto, 2003] Hattori, Y. and Fukumoto, Y. (2003). Short-wavelength stability analysis of thin vortex rings. *Physics of Fluids*, 15(10):3151–3163.

[Hattori and Fukumoto, 2009] Hattori, Y. and Fukumoto, Y. (2009). Short-wavelength stability analysis of a helical vortex tube. *Physics of fluids*, 21(1):014104.

[Hattori and Fukumoto, 2014] Hattori, Y. and Fukumoto, Y. (2014). Modal stability analysis of a helical vortex tube with axial flow. *J. Fluid Mech.*, 738:222–249.

[Helmholtz, 1858] Helmholtz, H. (1858). Über integrale der hydrodynamischen gleichungen, welche den wirbelbewegungen entsprechen. *Journal für die reine und angewandte Mathematik*, 55:25–55.

[Hicks, 1884] Hicks, W. M. (1884). Vii. on the steady motion and small vibrations a hollow vortex. *Philos. Trans. R. Soc.*, 175:161–195.

[Hocking and Michael, 1959] Hocking, L. and Michael, D. (1959). The stability of a column of rotating liquid. *Mathematika*, 6(1):25–32.

[Huerre et al., 1998] Huerre, P., Rossi, M., Godrèche, C., and Manneville, P. (1998). Hydrodynamics and nonlinear instabilities. *Aléa Saclay*, pages 160–180.

[IQBAL, 2005] IQBAL, M. I. (2005). Instabilities of vortices with axial flow: an accurate numerical formulation. Master internship report.

[Jiménez et al., 1996] Jiménez, J., Moffatt, H. K., and Vasco, C. (1996). The structure of the vortices in freely decaying two-dimensional turbulence. *J. Fluid Mech.*, 313:209–222.

[Joukowsky and Vetchinkin, 1929] Joukowsky, N. E. and Vetchinkin, V. P. (1929). *Théorie tourbillonnaire de l'hélice propulsive*. Gauthier-Villars.

[Kelvin, 1869] Kelvin, L. (1869). On vortex motion. *Trans. Roy. Soc. Edinb.*, 25:217–260.

[Kerswell, 2002] Kerswell, R. R. (2002). Elliptical instability. *Annual review of fluid mechanics*, 34(1):83–113.

[Kida, 1981] Kida, S. (1981). Motion of an elliptic vortex in a uniform shear flow. *J. Phys. Soc. Japan*, 50(10):3517–3520.

[Korkut and Atlar, 2002] Korkut, E. and Atlar, M. (2002). On the importance of the effect of turbulence in cavitation inception tests of marine propellers. *Proceedings of The Royal Society A: Mathematical, Physical and Engineering Sciences*, 458:29–48.

[Kubitschek and Weidman, 2007a] Kubitschek, J. and Weidman, P. (2007a). The effect of viscosity on the stability of a uniformly rotating liquid column in zero gravity. *Journal of Fluid Mechanics*, 572:261–286.

[Kubitschek and Weidman, 2007b] Kubitschek, J. and Weidman, P. (2007b). Helical instability of a rotating viscous liquid jet. *Physics of Fluids*, 19(11):114108.

[Küchemann, 1965] Küchemann, D. (1965). Report on the iutam symposium on concentrated vortex motions in fluids. *Journal of Fluid Mechanics*, 21(1):1–20.

[Kuibin and Okulov, 1998] Kuibin, P. A. and Okulov, V. L. (1998). Self-induced motion and asymptotic expansion of the velocity field in the vicinity of a helical vortex filament. *Phys. Fluids*, 10(3):607–614.

[Lacaze et al., 2007] Lacaze, L., Ryan, K., and Le Dizes, S. (2007). Elliptic instability in a strained batchelor vortex. *Journal of Fluid Mechanics*, 577:341–361.

[Lamb, 1932] Lamb, H. (1932). Hydrodynamics, 156. *Aufl., Cambridge: Univ. Press1879–1932*, 427.

[Le Dizes et al., 1996] Le Dizes, S., Rossi, M., and Moffatt, H. (1996). On the three-dimensional instability of elliptical vortex subjected to stretching. *Physics of Fluids*, 8(8):2084–2090.

[Le Dizès and Verga, 2002] Le Dizès, S. and Verga, A. (2002). Viscous interactions of two co-rotating vortices before merging. *J. Fluid Mech.*, 467:389–410.

[Lessen et al., 1974] Lessen, M., Singh, P. J., and Paillet, F. (1974). The stability of a trailing line vortex. Part 1. Inviscid theory. *J. Fluid Mech.*, 63:753–763.

[Levy and Forsdyke, 1928] Levy, H. and Forsdyke, A. G. (1928). The steady motion and stability of a helical vortex. *Proc. R. Soc. Lond. A*, 120(786):670–690.

[Leweke et al., 2016] Leweke, T., Le Dizes, S., and Williamson, C. H. (2016). Dynamics and instabilities of vortex pairs. *Annual Review of Fluid Mechanics*, 48:507–541.

[Lopez et al., 2002] Lopez, J., Marques, F., and Shen, J. (2002). An efficient spectral-projection method for the navier–stokes equations in cylindrical geometries: Ii. three-dimensional cases. *J. Comput. Phys.*, 176(2):384–401.

[Lundgren and Mansour, 1991] Lundgren, T. S. and Mansour, N. N. (1991). Vortex ring bubbles. *Journal of Fluid Mechanics*, 224:177–196.

[Maeda et al., 2016] Maeda, T., Kamada, Y., Murata, J., Yamamoto, M., Ogasawara, T., Shimizu, K., Kogaki, T., et al. (2016). Study on power performance for straight-bladed vertical axis wind turbine by field and wind tunnel test. *Renewable Energy*, 90:291–300.

[Marquet et al., 2008] Marquet, O., Sipp, D., and Jacquin, L. (2008). Sensitivity analysis and passive control of cylinder flow. *Journal of Fluid Mechanics*, 615:221–252.

[maurice rossi, 2006] maurice rossi (2006). of vorticies and vortical layers: an overview. http://www.lmm.jussieu.fr/MEMBRES/ROSSI/TELECHARGER/VortexRossi.pdf.

[Mayer and Powell, 1992] Mayer, E. W. and Powell, K. G. (1992). Viscous and inviscid instabilities of a trailing vortex. *J. Fluid Mech.*, 245:91–114.

[Meunier et al., 2005] Meunier, P., Le Dizes, S., and Leweke, T. (2005). Physics of vortex merging. *Comptes Rendus Physique*, 6(4-5):431–450.

[Moffatt, 1969] Moffatt, H. K. (1969). The degree of knottedness of tangled vortex lines. *J. Fluid Mech.*, 35(1):117–129.

[Moore and Saffman, 1971] Moore, D. and Saffman, P. G. (1971). Structure of a line vortex in an imposed strain. In *Aircraft wake turbulence and its detection*, pages 339–354. Springer.

[Moore and Saffman, 1972] Moore, D. W. and Saffman, P. G. (1972). The motion of a vortex filament with axial flow. *Phil. Trans. R. Soc. A*, 272(1226):403–429.

[Müller and Obermeier, 1988] Müller, E.-A. and Obermeier, F. (1988). Vortex sound. *Fluid Dynamics Research*, 3(1-4):43–51.

[Okulov, 2004] Okulov, V. (2004). On the stability of multiple helical vortices. *Journal of Fluid Mechanics*, 521:319–342.

[Okulov and Sørensen, 2007] Okulov, V. and Sørensen, J. N. (2007). Stability of helical tip vortices in a rotor far wake. *Journal of Fluid Mechanics*, 576:1–25.

[Okulov et al., 2019] Okulov, V. L., Kabardin, I. K., Mikkelsen, R. F., Naumov, I. V., and Sørensen, J. N. (2019). Helical self-similarity of tip vortex cores. *Journal of Fluid Mechanics*, 859:1084–1097.

[Okulov and Sørensen, 2020] Okulov, V. L. and Sørensen, J. N. (2020). The self-induced motion of a helical vortex. *J. Fluid Mech.*, 883:A5.

[Pierrehumbert, 1986] Pierrehumbert, R. (1986). Universal short-wave instability of two-dimensional eddies in an inviscid fluid. *Physical review letters*, 57(17):2157.

[Piton, 2011] Piton, B. (2011). *Simulations de tourbillons à symétrie hélicoïdale*. PhD thesis. Thèse de doctorat dirigée par Rossi, Maurice et Delbende, Ivan Mécanique Paris 6 2011.

[Poincaré, 1893] Poincaré, H. (1893). *Théorie des tourbillons: Leçons professées pendant le deuxième semestre 1891-92*. Gauthier-Villars.

[Ponstein, 1959] Ponstein, J. (1959). Instability of rotating cylindrical jets. *Applied Scientific Research, Section A*, 8(1):425–456.

[Popinet, 2015] Popinet, S. (2015). A quadtree-adaptive multigrid solver for the Serre–Green–Naghdi equations. *Journal of Computational Physics*, 302:336–358.

[Popinet and co, 2007] Popinet, S. and co (2007). Basilisk. http://basilisk.fr/.

[Quaranta et al., 2015] Quaranta, H. U., Bolnot, H., and Leweke, T. (2015). Long-wave instability of a helical vortex. *Journal of Fluid Mechanics*, 780:687–716.

[Quaranta et al., 2019] Quaranta, H. U., Brynjell-Rahkola, M., Leweke, T., and Henningson, D. S. (2019). Local and global pairing instabilities of two interlaced helical vortices. *J. Fluid Mech.*, 863:927–955.

[Rayleigh, 1892a] Rayleigh, L. (1892a). Xix. on the instability of cylindrical fluid surfaces. *The London, Edinburgh, and Dublin Philosophical Magazine and Journal of Science*, 34(207):177–180.

[Rayleigh, 1892b] Rayleigh, L. (1892b). Xvi. on the instability of a cylinder of viscous liquid under capillary force. *The London, Edinburgh, and Dublin Philosophical Magazine and Journal of Science*, 34(207):145–154.

[Ricca, 1994] Ricca, R. L. (1994). The effect of torsion on the motion of a helical vortex filament. *J. Fluid Mech.*, 273:241–259.

[Robinson and Saffman, 1984] Robinson, A. and Saffman, P. (1984). Stability and structure of stretched vortices. *Studies in applied mathematics*, 70(2):163–181.

[Rosenhead, 1930] Rosenhead, L. (1930). The spread of vorticity in the wake behind a cylinder. *Proceedings of the Royal Society of London. Series A, Containing papers of a mathematical and physical character*, 127(806):590–612.

[Rossi, 2000] Rossi, M. (2000). Of vortices and vortical layers: an overview. In Maurel, A. and Petitjeans, P., editors, *Vortex structure and dynamics. Lecture notes in Physics.*, pages 40–123. Springer Verlag.

[Ruith et al., 2003] Ruith, M., Chen, P., Meiburg, E., and Maxworthy, T. (2003). Three-dimensional vortex breakdown in swirling jets and wakes: direct numerical simulation. *Journal of Fluid Mechanics*, 486:331–378.

[Saffman, 1970] Saffman, P. G. (1970). The velocity of viscous vortex rings. *Studies in Applied Mathematics*, 49(4):371–380.

[Saffman, 1992] Saffman, P. G. (1992). *Vortex Dynamics*. Cambridge University Press. Cambridge Books Online.

[Saffman, 1995] Saffman, P. G. (1995). *Vortex dynamics*. Cambridge university press.

[Selçuk, 2016] Selçuk, C. (2016). *Numerical study of helical vortices and their instabilities*. Phd thesis, Université Pierre et Marie Curie, Paris, France.

[Selçuk et al., 2017a] Selçuk, C., Delbende, I., and Rossi, M. (2017a). Helical vortices: linear stability analysis and nonlinear dynamics. *Fluid Dynamics Research*, 50(1):011411.

[Selçuk et al., 2017b] Selçuk, C., Delbende, I., and Rossi, M. (2017b). Helical vortices: Quasiequilibrium states and their time evolution. *Physical Review Fluids*, 2(8):084701.

[Shtork et al., 2020] Shtork, S., Suslov, D., Litvinov, I., and Gorelikov, E. Y. (2020). Analysis of the flow structure in the model of a microhydraulic turbine. *Journal of Applied Mechanics and Technical Physics*, 61(5):807–813.

[Sørensen et al., 2002] Sørensen, N. N., Michelsen, J., and Schreck, S. (2002). Navier–stokes predictions of the nrel phase vi rotor in the nasa ames 80 ft× 120 ft wind tunnel. *Wind Energy: An International Journal for Progress and Applications in Wind Power Conversion Technology*, 5(2-3):151–169.

[Strykowski and Sreenivasan, 1990] Strykowski, P. J. and Sreenivasan, K. R. (1990). On the formation and suppression of vortex 'shedding'at low reynolds numbers. *Journal of Fluid Mechanics*, 218:71–107.

[Ting and Tung, 1965] Ting, L. and Tung, C. (1965). Motion and decay of a vortex in a nonuniform stream. *The Physics of Fluids*, 8(6):1039–1051.

[Tryggvason et al., 2011] Tryggvason, G., Scardovelli, R., and Zaleski, S. (2011). *Direct Numerical Simulations of Gas–Liquid Multiphase Flows*. Cambridge University Press.

[Tuckerman, 2018] Tuckerman, L. S. (2018). Polar coordinates. https://blog.espci.fr/laurette/files/2022/01/polar.pdf.

[Venegas and Le Dizès, 2019] Venegas, E. D. and Le Dizès, S. (2019). Generalized helical vortex pairs. *Journal of Fluid Mechanics*, 865:523–545.

[von Ohnesorge, 1937] von Ohnesorge, W. (1937). *Anwendung eines kinematographischen Hochfrequenzapparates mit mechanischer Regelung der Belichtung zur Aufnahme der Tropfenbildung und des Zerfalls flüssiger Strahlen*. Triltsch.

[Waleffe, 1990] Waleffe, F. (1990). On the three-dimensional instability of strained vortices. *Physics of Fluids A: Fluid Dynamics*, 2(1):76–80.

[Weatherburn, 2016] Weatherburn, C. E. (2016). *Differential geometry of three dimensions*, volume 1. Cambridge University Press.

[Weidman et al., 1997] Weidman, P., Goto, M., and Fridberg, A. (1997). On the instability of inviscid, rigidly rotating immiscible fluids in zero gravity. *Zeitschrift für angewandte Mathematik und Physik ZAMP*, 48(6):921–950.

[Widnall, 1972] Widnall, S. E. (1972). The stability of a helical vortex filament. *J. Fluid Mech.*, 54(4):641–663.

[Widnall et al., 1971] Widnall, S. E., Bliss, D., and Zalay, A. (1971). Theoretical and experimental study of the stability of a vortex pair. In *Aircraft wake turbulence and its detection*, pages 305–338. Springer.

[Widnall and Tsai, 1977] Widnall, S. E. and Tsai, C.-Y. (1977). The instability of the thin vortex ring of constant vorticity. *Philosophical Transactions of the Royal Society of London. Series A, Mathematical and Physical Sciences*, 287(1344):273–305.

Numerical studies on vortex dynamics
helical vortices and two-phase vortices

Abstract

Nous présentons des études numériques sur la dynamique des vortex homogènes et diphasiques. Dans une première partie, nous étudions la structure des vortex hélicoïdaux homogènes tels qu'on peut les trouver dans le sillage des hélices ou des turbines. Certaines propriétés des états d'équilibre non visqueux sont dérivées théoriquement et confirmées numériquement sur des états de quasi-équilibre en utilisant des simulations numériques directes dans le cadre de la symétrie hélicoïdale. Les modes d'instabilité de grandes et petites longueurs d'onde qui se développent sur ces états sont ensuite étudiés et comparés aux théories asymptotiques existantes, avec un bon accord. L'intensité du jet axial au cœur du vortex joue un rôle prépondérant, mais l'influence d'autres paramètres tels que le pas des vortex hélicoïdaux et la taille du cœur est également étudiée. Dans une deuxième partie, nous étudions deux problèmes de dynamique des vortex diphasiques. D'une part, on traite les instabilités se produisant dans les tourbillons diphasiques droits en utilisant un code d'instabilité maison. En particulier, l'effet de stabilisation par la rotation sur les instabilités capillaires avec un vortex dans le cœur gazeux est mis en évidence. D'autre part, on étudie la génération de bulles tourbillonnaires toroïdales comme celles produites par les plongeurs, les bélugas ou les dauphins par des simulations directes à deux phases. Les résultats d'instabilité sont utilisés pour expliquer la très grande robustesse de telles structures vis-à-vis des perturbations.

Keywords: 〈 vortex; hélicoïdal; stabilité; écoulement diphasique 〉

Études numériques sur la dynamique des vortex
Vortex hélicoïdaux et Vortex diphasiques

Résumé

We present numerical studies on the dynamics of homogeneous and two-phase vortices. In a first part, we study the structure of homogeneous helical vortices as can be found in the wake of propellers or turbines. Some properties of inviscid steady states are derived theoretically and confirmed numerically on quasi-equilibria using direct numerical simulations in the helical symmetry framework. Long- and short-wave instability modes growing on these states are then investigated and compared favourably to existing asymptotic theories. Axial jet intensity within the core has a prominent role, but the influence of other parameters such as helical vortex pitch and core size are also investigated. In a second part, we study two problems concerning the dynamics of two-phase vortices. On the one hand, we investigate the instabilities occurring in straight two-phase vortices using an original in-house instability code. In particular, the stabilizing effect of rotation on capillary instabilities in vortices with a gaseous core is evidenced. On the other hand, we study the generation of toroidal vortex bubbles as those produced by scuba divers, beluga whales or dolphins by direct two-phase simulations. Previous instability results are used to explain the remarkable robustness of such structures with respect to perturbations.

Mots clés : 〈 vortex ; helical ; stability ; two-phase flow 〉